P-T evolution and High-temperature deformation of Precambrian eclogite, Sveconorwegian orogen

Tual, Lorraine

2016

Document Version:
Publisher's PDF, also known as Version of record

LITHOLUND THESES 26

P–T evolution and high-temperature deformation of Precambrian eclogite, Sveconorwegian orogen

LORRAINE TUAL
LITHOSPHERE AND BIOSPHERE SCIENCE | DEPARTMENT OF GEOLOGY | LUND UNIVERSITY 2016

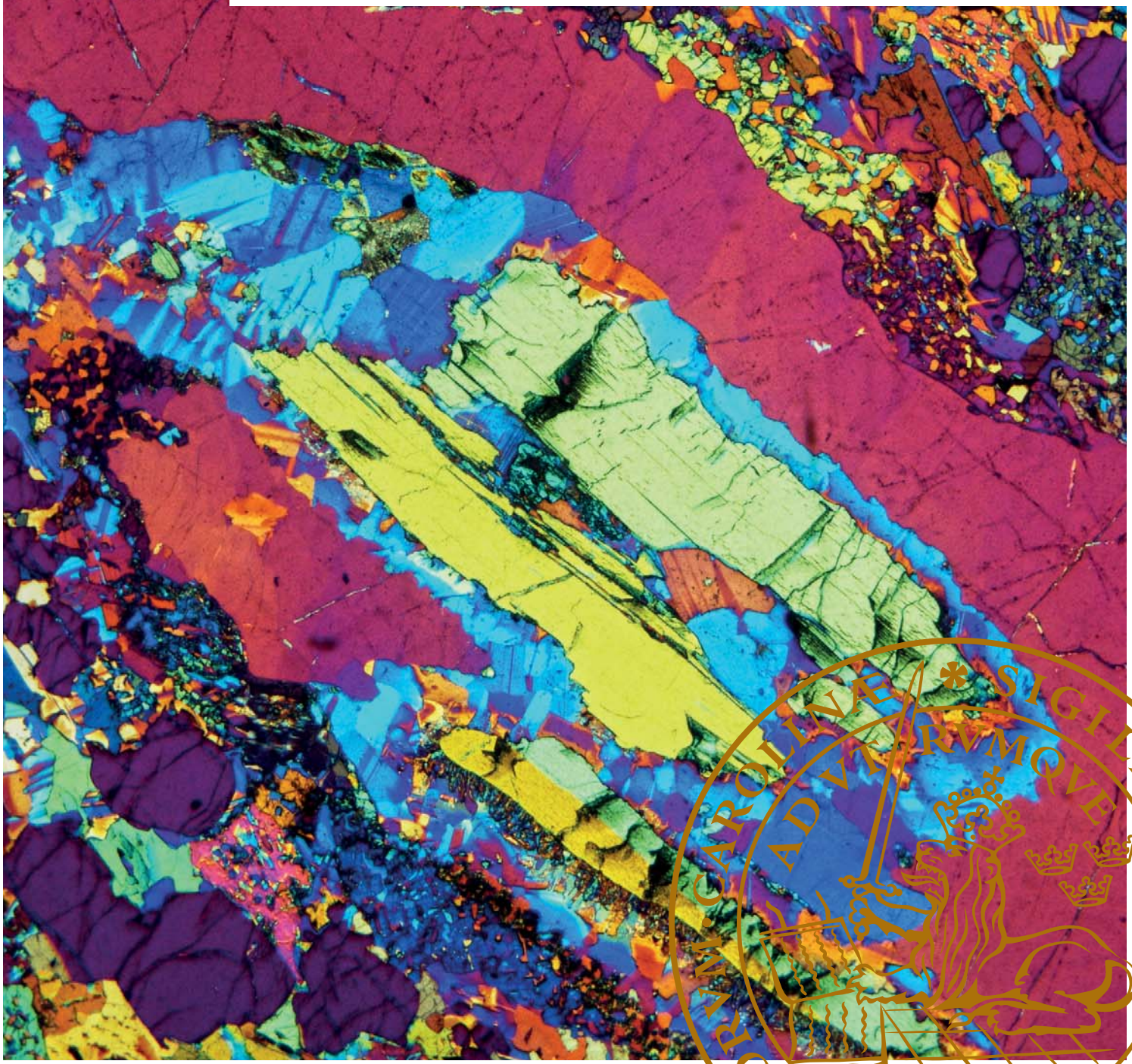

LITHOLUND THESES 26

P–T evolution and high-temperature deformation of Precambrian eclogite, Sveconorwegian orogen

Lorraine Tual

LUND
UNIVERSITY

Lithosphere and Biosphere Science
Department of Geology

DOCTORAL DISSERTATION
by due permission of the Faculty of Science, Lund University, Sweden.
To be defended at the Department of Geology, Lund University on the 4th of May 2016

Faculty opponent
Aphrodite Indares
Memorial University of Newfoundland, Canada

Lithosphere and Biosphere Science
Department of Geology
Faculty of Science

ISBN 978-91-87847-14-1
ISBN 978-91-87847-15-8 (pdf)
ISSN 1651-6648

Printed in Sweden by Media-Tryck, Lund University, Lund 2016

Organization

LUND UNIVERSITY
Department of Geology
Sölvegatan 12
SE-223 62 Lund
Sweden

Author(s) Lorraine Tual

Document name

DOCTORAL DISSERTATION

Date of issue: May 4, 2016

Title and subtitle: *P–T* evolution and high-temperature deformation of Precambrian eclogite, Sveconorwegian orogen

Abstract

The 1.1-0.9 Ga Sveconorwegian orogen is one of several Grenvillian-aged orogenic belts that mark the amalgamation of supercontinent Rodinia. The highest-pressure rocks in the Sveconorwegian orogen are eclogites in the Eastern Segment (SW Sweden). The eclogites occur in a nappe in the high-grade metamorphic level of the Eastern Segment that represents a window into the deepest part of this Precambrian mountain belt. The aim of this thesis is to reconstruct the metamorphic history of the eclogite-bearing nappe by characterizating the deformation associated with exhumation (Paper I) and by reconstructing the P–T evolution (pressure and temperature; papers II and III).

Paper I focuses on the deformation structures in the basal shear zone of the eclogite-bearing nappe. These structures developed during exhumation at high-temperature conditions. Top-to-the-east shear and east-directed flow produced intense folding, interpreted as formed by a combination of simple and pure shear. The interplay of shearing, folding, and melt localization lead to localized shear, high-temperature brittle fracturing, and the formation of high-temperature chevron folds in high-strain zones.

Paper II retraces the metamorphic evolution of the eclogite-bearing nappe by thermodynamic modelling (THERMOCALC©) and construction of P–T pseudosections for two different types of eclogite. One of the samples gave information on both the prograde and the retrograde paths, and an estimate of peak metamorphic conditions of 850–900 °C and ~18 kbar. The first stage of the prograde path, representing a medium P/T gradient, is recorded in the core of garnet grains. The second part of the prograde path and the retrograde path are both steep. The chemical growth zoning of garnet is preserved which, together with the shape of the P–T path, reflects short residence time at high temperatures.

Paper III reports the results of two independent trace element thermometers, which are based on the Zr-contents in rutile and Ti-contents in quartz. The combination of these two methods confirmed the P–T evolution calculated in Paper II. In particular, Ti-in-quartz thermometry are in agreement with the pseudosection estimates at high temperatures, and the minerals appear unaffected by diffusional resetting. A pseudosection model, showing the changes in modal abundance of different phases along the P–T path, demonstrates that rutile grains in the matrix recrystallized from smaller-sized rutile grains, and that this process was simultaneous with the main dehydration reaction in the rock (continuous breakdown of hornblende and formation of clinopyroxene). This study illustrates that Zr-in-rutile and Ti-in-quartz thermometry cannot only robustly constrain a prograde evolution, but when combined with a pseudosection model can also yield information on recrystallization processes. In fact, the combination of these methods provides an unrivalled tool for petrologic interpretation.

The data presented in this thesis testifies to westward tectonic burial of continental crust at ~65 km depth and 890 °C at a late stage of the Sveconorwegian orogenesis. The following foreland-directed tectonic exhumation of the eclogite-bearing nappe was associated with partial melting, ductile flow folding and shearing. The character of both prograde and retrograde P–T paths suggests rapid tectonic burial and exhumation consistent with collision at the end of the Sveconorwegian orogeny.

Key words: *Precambrian, eclogite, P–T path, Sveconorwegian orogen, high-temperature, deformation, basal shear zone, thermometry, pseudosection.*

Classification system and/or index terms (if any)

Supplementary bibliographical information | Language: English

ISSN and key title: 1651-6648 LITHOLUND THESES | ISBN: 978-91-87847-14-1

Recipient's notes | Number of pages 110 | Price

Signature: 

Date: March 3, 2016

For my dad,
you would have loved this.

CONTENTS

LIST OF PAPERS

Paper I

Tual, L., Piñán-Llamas, A. & Möller, C. 2015. High-Temperature Deformation in the Basal Shear Zone of an Eclogite-Bearing Fold Nappe, Sveconorwegian Orogen, Sweden, in: Roberts, N., Viola, G., Slagstad, T. (Eds.), The structural, metamorphic and magmatic evolution of Mesoproterozoic orogens. Precambrian Research, 265, 104-120. Reprinted with permission of Elsevier

Paper II

Tual, L., Pitra, P. & Möller, C. P–T evolution of Precambrian eclogite in the Sveconorwegian orogen, SW Sweden. This is the version of the manuscript submitted to Journal of Metamorphic Geology in January 2016.

Paper III

Tual, L., Möller, C. & Whitehouse, M.J.. Tracking the prograde P–T path of Precambrian eclogite using Ti-in-quartz and Zr-in-rutile thermobarometry. In manuscript

ACKNOWLEDGEMENTS

I has been a long way before I could see a sort of closure to this adventure; both because it was tough and bumpy, but also certainly because I enjoyed so many things doing this PhD and met such wonderful people on the way that I didn't want it to end. Here I would like to thank all these newly met people, along with the ones who always believed in me.

I owe a lifetime gratitude to Lotta Möller for hiring me to do this amazing PhD, and being my supervisor. When I first saw her advertisement for the position, I knew there was no place for a doubt and that it looked like a dreamful project. When a few weeks later, I land for the first time into a forest in Halland County, watching at the soupy, partially molten, complexly folded gneisses, I had a tiny doubt though. But hopefully, the soup is a bit clearer now, at least it is to me, and I indeed still think it was an amazing project. Thank you Lotta; I have not only be able to pursue the dream, but I could also add a few sparkles in it: you generously let me spend a great amount of research money to participate to many conferences and PhD courses around the world, and I truly enjoyed all of them. Thank you for entrusting me with teaching of field and petrology courses. I enjoyed teaching so much, mostly because it was well prepared and about some of my favourite things in the world. The last months were particularly tough, but you've never failed to answer my questions or take part in discussions ten times a day or late in the night with dedication. I am indebted for all the things I have learned thanks to you and the future adventures it may allow me to enjoy.

I also had a great co-supervisor team. Arancha, thanks a lot for the great time on the field, the help at chasing cockroaches in the hut and awful tiny flies in the forest, coping with my stubborn ideas about fold mechanisms and your patience during the 22 first-or-so versions of "Paper I"... Jenny, thanks so much for your limitless and contagious enthusiasm, the nice time on the field during symposiums, all the encouragements and interest in the project. In particular, I will always remember how you took care of my poor person, when I went at Nordsim for the first time and we started realizing I will have to stay there working for a whole night. I managed to stay awake and spot each zircon thanks to all the food you provided me (I had enough for the next couple of days) and the cheering up until late at night. You certainly are a model of positivity to follow. Pavel, thank you for so many things. I am so glad you accepted to embark in this project a couple of years ago, and it wouldn't have been the same if you hadn't. Or maybe it would, because you have always been extremely helpful and cheerful even before that anyway. You are the first one that inspired me and fed my passion for high-grade metamorphic rocks and petrology. It will soon be 10 years since you supervised me the first time, and I know we'll keep being a good team for much longer (and I'll have many occasions to thank you again).

I would like to thank the SGU and the Crafoord fundation for funding large parts of this PhD through generous grants to Charlotte Möller. I also thank the Royal Swedish Academy of Sciences for funding my last project. Thanks are also due to Erasmus program for the teaching mobility grant that allowed me to spend a nice teaching and research time at Rennes University in spring 2015.

I need to broaden the framework here, and thank the teachers I had since I started school. In particular my teachers from high school at the Lycée J. Moulin, Châteaulin, for being inspiring and supportive, in particular when I passed through hell. It did make a difference. Thank you also for all the great students I had during 4 years of metamorphic petrology labs and structural geology fieldwork. I enjoyed teaching very much in your company. Thanks to everyone in Rennes, who made my stay enjoyable, in particular Camille and Caro for being great hosts! Thanks to the wolves, for not showing up doing my many weeks of fieldwork alone in the dark forest. Thank you to those who organized all the conferences, fieldtrips, excursions and PhD courses I attended to. Lucky me, there is a long list, so I cannot cite you all. But special big thank you to Anders and Johan for organizing the first and how memorable one to the western USA, this was such a fantastic trip. I remember it with a happy nostalgia. *Viva Las Vegas!* Thank you Alasdair for showing us cool structures in Iceland, it was as wonderful as it could be without HP rocks around. Thank you David Gee, for kindly inviting me to the Transcand excursion across the Caledonides. This definitely did not help to calm down my passion for high-pressure rocks; I thank you for that, the inspiration from your inexhaustible enthusiasm and the opportunity to meet so many great people in a pleasant atmosphere (yes, good we bought all this wine before crossing the Norwegian border).

Thanks to everyone at the department of Geology, it has been a pleasure to talk with you all during fika or lunch. Thanks in particular to Gert and Michael for saving this project (and me) twice when my first hard drive, then the second plus the time-machine crashed (also, there won't be any thank to you, Apple). If you weren't there, I wouldn't be writing acknowledgements just yet I guess... Thanks Anders for the pep talks and the fun, particularly during the USA fieldtrip. Thank you Leif for all the help, especially in the lab, your inspiring discussions on experimental zircon separation techniques and the emergency assistance on a Sunday afternoon trying to catch them all. Very special thanks to you, Ulf, who rescued me from my very first homeless experience after a couple of months in Sweden. I eventually got used to it, but the first time was really tough and I will never forget the warm welcome I got from you and Pia.

Thanks for all the friends from home, who came to

visit me during the cold winter or lovely spring: Jean-Charles, Emilie, Marion, Carole, Clément, Zoé, Julie, Patrick, Marion, Romain, Marie, Toitoine, Sarah, Élo, Marine, Sylvia. Thanks to the Copenhagen dream-team for such a great time on both sides of the bridge: Quinten, Anouk, Dea, Joan, Robin, Sam, Matthijs...

Living in Sweden was unexpectedly rough, but somehow, all the fun with my new friends here largely overcompensated it. Thank you all (below some details).

When I first arrived two people welcomed me with open arms and I have been feeling grateful almost everyday for this. Mimmi, you've put so much effort to keep me happy and I have so many great memories with you that I cannot list them here; I particularly remember the nice evenings nail-polish-bag-in-box-wine-gin-tonic-til-4-am, which evolved in fika-playing-with-baby-making-plastic-zircon-and-piñata(actually gin-tonic too) that I enjoyed just the same. Thank you so much. Then Vicky. You have been, and certainly will remain the best office mate ever. You're such a brilliant mind; you are such a good person and I enjoyed being near you everyday... until you brought the damn heater in the office! More seriously, I don't know how I will carry on, I got so used chatting with you, asking for your help and wise advice; I will deeply miss you. Thanks to the BGG PhD students for the great time at the department. The fieldtrip to the US (once again) was unforgettable, thanks Johan O., Karolina, Johan G., Johanna, Kristina, Ashley, Anders, Andy, Sanna, and Ingemar. Thanks also to the nice former master students, with whom I enjoyed talking metamorphism, especially Brendan, Birgit and Stephen. Thanks also to the Franska-Svenska diskussion, I enjoyed your company very much.

One of the wisest choice I made as a PhD student is certainly to have climbed to the 4th floor and did not resist to the after work beer on Fridays with the geologists from the quaternary department. You definitely contributed all to improve drastically my mental health by taking me out; although I am pretty sure about the opposite concerning my physical health, considering the thousands of liters of beer we must have had together. Thanks Laurie, Florian, Bryan, Martin, Claire, Anton, Emma, Thorbjorg, Carla, Nadine, Petra, Jesper... With you, soil and water people, I found a safe haven in storms and great friends. Extra thanks to Wim and Patrick, for the nice parties, including the sauna one on the lake and your everyday happiness; Nath, thanks for being so funny and the nice annual summer garden parties; Tom for being so constantly British to your toes tips and used it to generously correct this Kappa. Finally, thanks to my good French buddies, Guillaume and Billy for so, so, so much fun and regrettable parties at the Nations as well. From the raclette parties, les tonnes de Kinder*, to the Ikea furniture building at Valentines Day, I enjoyed every moments I spent with you guys.

I was so happy getting this PhD position that I prepared myself for a nice and smooth adventure. I realized that coming from a lovely remote place in Bretagne also included drawbacks. I wish I were there more often. I am lucky enough to have two wonderful sisters who visited me several times; I will never forget the surprise finding Typhaine with a mojito on my terrace, for my birthday, after an exhausting and lonely field work in the forest. Thank you AirFrance for making a strike (again) and allowed Clémentine to stay by my side a few weeks longer, and thank you Clémentine for the great company in Sweden and at home. Thanks little brother Philippe, I miss you a lot and not only because of your nice cooking performances. Thank you dear little Stephouille & co for being so adorable and refreshing. Thank you Mum and Thierry for also visiting a couple of times, I am so pleased I could show you around and that you truly enjoyed it. My dear Mum, I missed you terribly and I know you did too; nevertheless you never stop encouraging me and showing me how proud you were, which kept me hanging on. I love you for never failing to be right there (on skype) as soon as I needed it, and taking such great care of me at home or at distance. I admire you, and thank you for teaching me to care about others. My dad was the kindest, most inspiring person I will certainly ever meet. As heart breaking as it is each time I realize I accomplish something in my life without one of his bear hug or approving smile, I know that when it is about following a passion with perseverance and humility, it is his voice I can still hear in my mind. I miss you everyday.

The greatest thanks of all, however, go to Thomas. You put your life into brackets for nearly 4 years to be with me, you never complained, kept supporting me and tried to make the best of your time in Sweden. You literally contributed to this thesis by helping me out on the field, happily measuring, peeling moss and cleaning outcrops, picking wild strawberries and huge mushrooms, we're such a great team. You encouraged me sincerely, made me laugh absolutely every day, and I still don't understand how you could understand. You are the shelter and anchor of my life, which it felt just right to decide spending it together. I love you dearly.

1 INTRODUCTION

1.1 Scope of the thesis

Orogenesis is primarily understood from the metamorphic evolutions, the deformation histories, and the magmatic records of different orogens' constituent terranes. Petrology and structural geology, linked to regional geology and tectonic architecture, are the basis of geodynamic interpretation. Key targets of investigation are high-pressure units, containing blueschist, eclogite, or high-pressure granulite, because they carry information on subduction and/or tectonic thickening to great depths. In SW Sweden eclogite occurs in a tectonic unit situated in a high-grade metamorphic domain in the Sveconorwegian orogen, and represents a window into the deepest levels of this Precambrian mountain belt. The aim of this thesis is to understand the significance of the eclogite occurrence in the Sveconorwegian orogen to, retracing in detail the thermal and deformational history of eclogite, sheding light on mountain building processes in Precambrian time.

The first paper of this thesis provides new information on the deformation structures in the basal shear zone of the eclogite-bearing nappe, a key location for the investigation of exhumation mechanisms. The deformation structures related to the main stage of exhumation have been documented, with particular focus on the mutual feedback between shearing, folding and melt localization. The second paper presents the first quantitative *P–T* path for eclogite in the Sveconorwegian orogen, interpreted from phase equilibrium modelling of two samples, and shows that high temperatures were reached both during peak conditions and the exhumation. Both prograde and retrograde paths are steep, implying short episodes of burial and exhumation. The third paper tracks the prograde history of Sveconorwegian eclogite using Zr-in-rutile and Ti-in-quartz thermobarometry. Results are in nearly perfect agreement with the prograde *P–T* path obtained from pseudosection modelling. The combination of the two thermometers, coupled with the *P–T* pseudosection model, allow detailed understanding of the thermal history and crystallization processes in the rock during metamorphism.

1.2 Orogenesis

Each orogen is unique, but comparison of different orogens is necessary in order to obtain a general understanding of orogeny. Systematic differences between Phanerozoic and Precambrian orogens can give information on the evolution of plate tectonics through time. Therefore, beyond the interest of understanding a particular mountain chain, the study of Precambrian orogens provides a wider perspective on Earth history.

Most Precambrian orogens are deeply eroded and form dismembered pieces on Earth. They represent windows into the interior of old mountain chains and allow observation of the results of deep-seated processes, unreachable in most Phanerozoic orogens. Dewey & Bird (1970) defined three classic types of orogens: *Ocean-continent belts* (Fig. 1a), which are characterized by the subduction of an oceanic plate beneath continental lithosphere, often coined as Andean-type orogen; *Arc-continent collisional belts,* formed from the collision between an island arc and continental lithosphere, and *Continent-continent collision belts* (Fig. 1b), which form when two continents collide. This "traditional" view of orogenesis has progressively been nuanced (e.g. Cawood *et al.*, 2009), and orogens are now often separated into (1) collisional, (2) accretionary, and (3) intracratonic. (1) Collisional orogens result from the collision of at least two continental blocks and involve significant crustal thickening, thrusting, and high-grade metamorphism, the latter often associated with partial melting (Condie, 2015). (2) Accretionary orogens form by subduction processes that lead to amalgamation and suturing of partially juvenile crustal blocks and material related to either the subducting or the overriding plate. (3) Intracratonic orogens are less well understood. They are situated far away from continental margins, within a continental plate, and are interpreted to form in response to strain localization in weak lithosphere (e.g. the Peterman orogeny, Walsh *et al.*, 2015), and in situations of flat slab subduction (e.g. the Laramide orogeny, Bird, 1984). Alternatively, as exemplified in the Tianshan in East Asia, they can be related to a distant continent-continent collision, with stress being transmitted through a strong lithosphere.

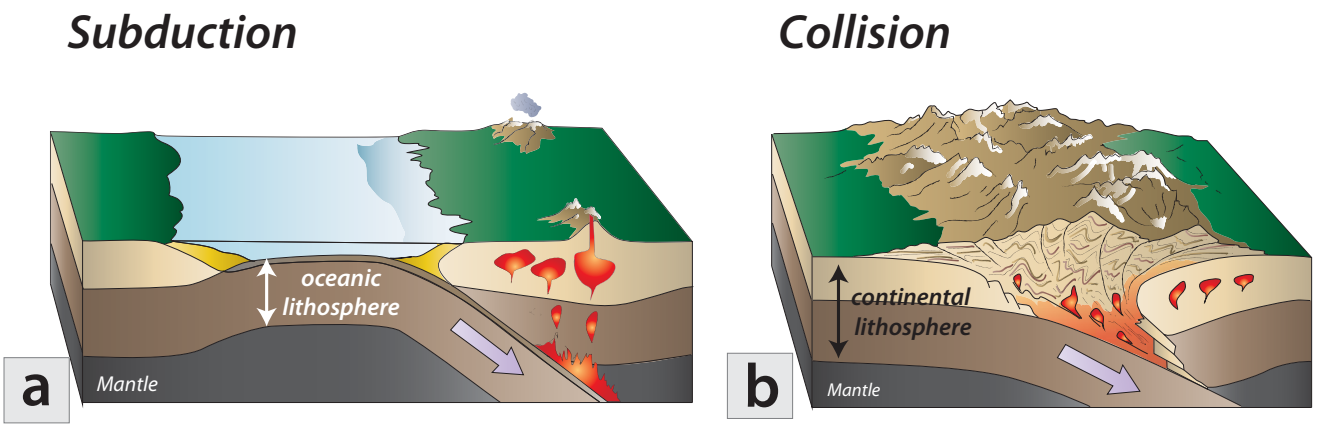

Figure 1: Schematic conceptual models of (a) subduction of oceanic lithosphere beneath a continental margin (right; Andean-type setting), and (b) collision between two continents (Himalayan-type setting).

In these different geodynamic environments, a wide range of magmatic and metamorphic (transformed) rocks is produced. Metamorphic rocks are the result of modification of a pre-existing rock due to changes in temperature (*T*) and pressure (*P*) with time (*t*). In a *P–T* diagram *metamorphic facies* represent the division according to the rocks' main minerals. A classical *P–T* diagram is shown in Fig. 2a. The *metamorphic facies series* represent broad divisions of metamorphic environments according to *P/T* conditions and geodynamic setting (e.g. Turner, 1981; Fig. 2b). Subduction is associated with high *P/T* gradients, whereas island arcs and contact metamorphic settings are associated with low *P/T* gradients. Collisional settings are often described as intermediate *P/T*, but are in reality more complex and can also include elements of high *P/T* (e.g. obducted ophiolites) and low *P/T* (arc material) jammed in the collision zone.

The realm of *P–T* conditions is vast and extends towards high-pressure to the eclogite facies. The occurrence of eclogite implies burial of crustal rocks to great depths in order to reach conditions exceeding ~15 kbar, and for their preservation during exhumation they must escape reequilibration. Hence, the presence of eclogite is the unequivoqual evidence of orogeny, either subduction or collision. When the rocks involved are of continental affinity, this scenario is generally achieved during continental subduction or continent-continent collision. Examples of rocks reaching ultra-high pressure (UH*P*) metamorphism up to 60 kbar and exhuming back to the surface have been documented (e.g. the Kokchetav Massiv, Kazakhstan, Ogasawara *et al.*, 2002).

1.3 Classification of eclogite

H.B. de Saussure provided in *Voyage dans les Alpes* (1779-1796) the first description of eclogite from pebbles found in the Rhône valley. He described the rock as dense, hard, and made of garnet in a matrix consisting of "*jade*" (likely pyroxene) and "*schorl*" (likely amphibole). The first definition of eclogite was made by Haüy in 1822 who derived the name eclogite from the greek word *εκλογη* (choice, election), because the rock contained mostly clinopyroxene and garnet that are not the normal constituents of "*primitive*" rocks (i.e. rocks containing feldspars, mica and amphibole). From the observation that eclogite is derived from gabbro by formation of denser mineral assemblages, Becke (1903) was the first to conclude that eclogite is a high-pressure rock. Consequently, Eskola (1915, 1920) chose the name "eclogite" to define the very-high pressure field in his metamorphic facies scheme. Nowadays, an eclogite is defined as a "*plagioclase-free metamorphic rock composed of ≥75% vol. of omphacite and garnet, both of which are present as major constituents, the amount of neither of them being higher than 75 volume %.*" (Desmons & Smulikowski, 2007).

The realm of eclogite facies rocks is vast. It became necessary to differentiate between different types of eclogite, as eclogite was found in different settings worldwide. Coleman *et al.* (1965) proposed a classification based on garnet composition. Although the composition of garnet is highly dependent on bulk composition, three types of eclogite were defined. Type A eclogite is found together with peridotite or as xenoliths in kimberlite (mantle affinity), Type B represents eclogite enclosed in gneiss (continental crust affinity), and Type C defines eclogite

in subduction settings (oceanic crust affinity). In terms of metamorphic gradient, eclogites fall into two main types. One are H*P*/UH*P* rocks following a "cold", high *P*/*T* gradient, typical for the subduction environment; these eclogites contain characteristic minerals such as coesite and diamond. The other type of eclogite forms at higher temperature, along a medium *P*/*T* gradient typical for collisional metamorphism, and is characteristic of the eclogite–high- pressure granulite (E–HPG) *P*–*T* domain (Fig. 2a). In high-temperature eclogite, clinopyroxene generally contains low or moderate jadeite proportions and instead a significant calcium-tschermak component (CaTs, $CaAl_2SiO_6$). The E-HPG facies represents rocks from the cores of hot, large orogens (e.g. Beaumont *et al.*, 2004), such as the Bohemian Massif (e.g. Schulmann *et al.*, 2008), the Grenville Province (Indares, 2003), and the Himalayas (e.g. Kohn, 2014b). One exceptional example of igneous E-HPG rocks has been documented in Fiordland, New-Zealand, in an exhumed thickened root of a magmatic arc (DePaoli *et al.*, 2009).

1.4 Deformation at depth in orogens

In orogens, thickening and shortening of the crust is accommodated by deformation. The style of deformation depends on different factors, notably temperature, pressure, strain rate, and pore fluid pressure (loosely "water content"). Given a deviatoric stress, a homogeneous rock pile will deform by different mechanisms depending on depth and temperature (Fig. 3). Whereas localized brittle deformation structures such as faults and parallel folds develop in the upper part of the crust, ductile structures dominated by shearing, recumbent folding, and large shear zones develop at depth (Fig. 3).

Ductile shear zones transform rocks to become "mylonitic", i.e. the grain size is so reduced due to dynamic recrystallization that individual grains are no longer visible to the naked eye. Planar and linear deformations are developed in shear zones and give information on finite strain in the rock, in particular the ratio of flattening *versus* elongation.

The geometry of folds also carries information about kinematics and deformation. There are many

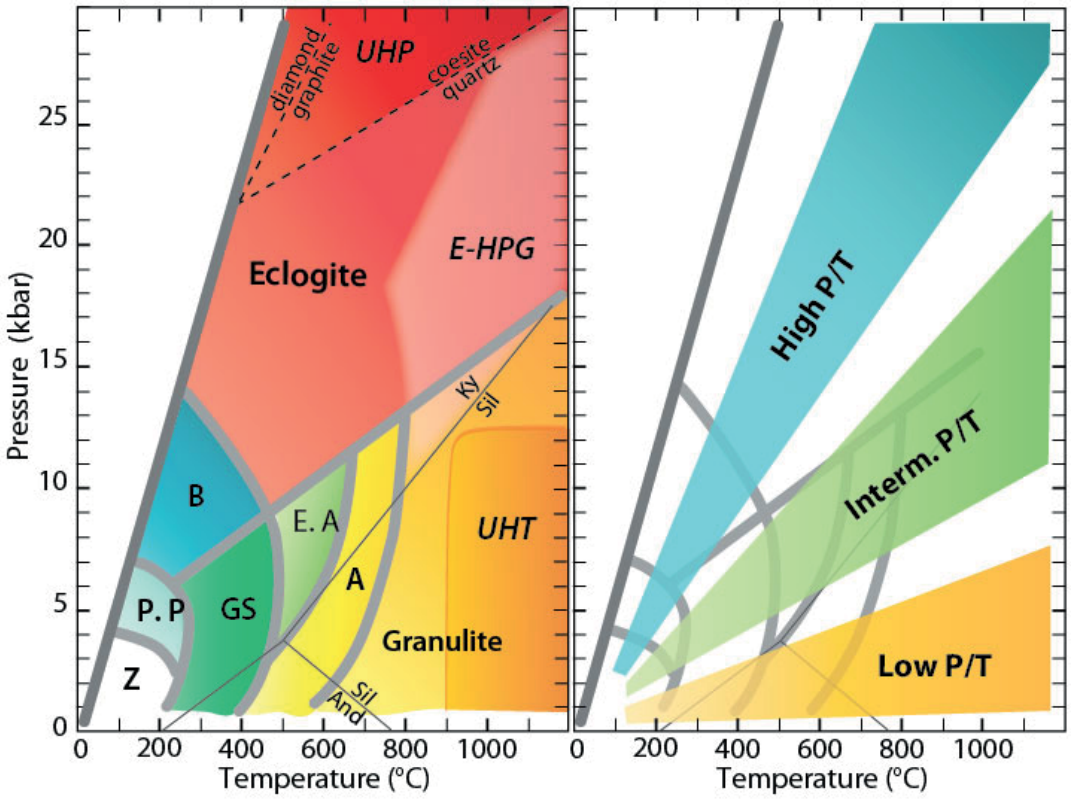

Figure 2: *(a) P–T* diagram showing different metamorphic facies, after Spear (1993). Abbreviations: Z = zeolite -facies; P. P = prehnite–pumpelleyite-facies; GS = greenschist-facies; A = amphibolite-facies; E. A = epidote-amphibolite-facies; B = blueschist-facies. Abbreviation of minerals: Ky = kyanite; Sil = sillimanite; And = andalusite. The eclogite–high-pressure granulite (E–HPG) field is shown in white shade; UHP= ultra-high-pressure metamorphism. UHT = ultrahigh-temperature metamorphism (b) *P–T* field showing the three main metamorphic facies series (after Spear, 1993)..

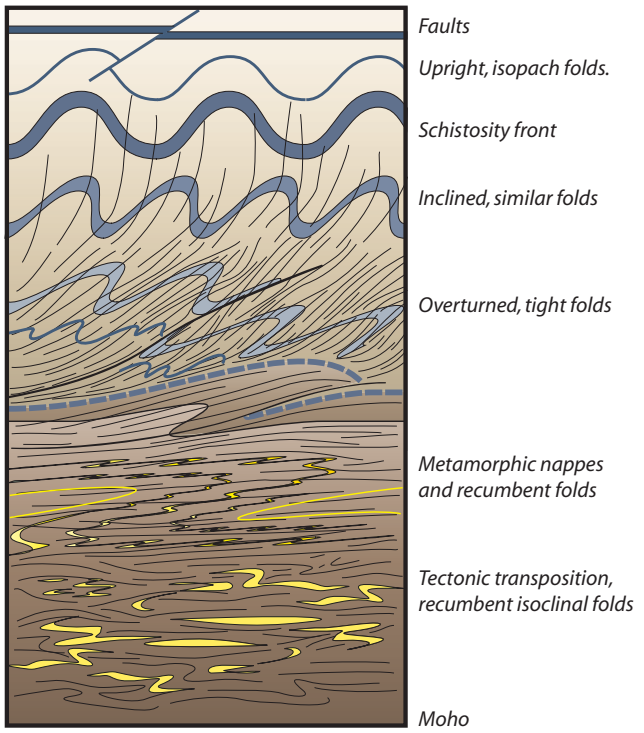

Figure 3:Schematic vertical section through continental crust illustrating the change in style of deformation with depth. Faults and fractures are prominent in the uppermost level, while ductile deformation is near-penetrative at deep crustal levels. Figure from P. Rey, reproduced with permission.

fold shapes (e.g. concentric, sinuous, or chevron folds) and variable orientations (e.g. upright, inclined, or recumbent). Three main fold mechanisms are: (1) active folding (buckling), created by layer-parallel shortening of layers of contrasting rheology, (2) passive folding, generated by simple shear of layers with low rheology contrast and (3) bending, when the stress is applied across the layers (cf. Fossen 2010).

At high-temperature rocks will start to melt in proportions that are largely dependent on the rock's composition and water content. The presence of melt, even in low proportions, will drastically decrease the rock strength (Weinberg and Mark, 2008). Deformation will localize in weak domains that contain melt. Deformation structures may also create sites for melt localization, which eventually result in complex ductile structures.

Systematic mapping of small-scale structures are necessary for reconstruction of large-scale structures. In fact, large deformation structures are often identical in style to those in outcrop-scale.

In a broader framework, because young orogens are generally less eroded they expose structures that are less ductile and characterized by localized deformation; Precambrian orogens expose deep structures, where penetrative ductile deformation is generally homogeneously distributed over large distances.

1.5 Eclogite in the Sveconorwegian orogen

The Sveconorwegian orogen

The Sveconorwegian orogen is part of a global-scale ca. 1 Ga old mountain building event which took place during formation of the supercontinent Rodinia. Other high-pressure regions of ~1 Ga age are present on Earth, e.g. in Scotland (Glenelg; Brewer *et al.*, 2003, Storey *et al.*, 2005) and Canada (the Grenville Province; e.g. Indares & Dunning 1997).

The 1.1-0.9 Ga Sveconorwegian orogen is made up of five crustal segments, from west to east: Telemarkia, Bamble, Kongsberg, and Idefjorden Terranes, and the Eastern Segment (Fig. 4a; Bingen *et al.*, 2005; Bingen *et al.*, 2008a and references therein). These segments are separated by crustal-scale shear-zones. One of these shear zones, the Mylonite Zone, is steep to shallowly west-dipping, 500 km long, and separates the Idefjorden Terrane from the Eastern Segment.

Bingen *et al.* (2008a) described four main tectonometamorphic stages of Sveconorwegian orogeny:

(1) The Arendal phase, c. 1.14 Ga ago, involved granulite- and upper amphibolite-facies metamorphism at intermediate pressure, in Bamble and Kongsberg Terranes (Engvik *et al.*, 2016).

(2) The c. 1.05-1.02 Ga Agder phase reached greenschist- to upper amphibolite-facies metamorphism and affected Telemarkia and Idefjorden Terranes. High-pressure granulite-facies rocks have been recorded locally in the Idefjorden Terrane, just west of the Mylonite Zone (Söderlund *et al.*, 2008). In addition, a granite suite intruded at 1.05-1.02 Ga in Telemarkia (Bingen, 1989; Bingen & van Breemen, 1998; Bingen & Solli, 2009; Slagstad *et al.*, 2012);

(3) The Falkenberg phase, at 0.99-0.97 Ga, caused high-pressure and high-temperature metamorphism of the Eastern Segment (e.g., Johansson *et al.*, 1991; Johansson & Kullerud 1993; Wang & Lindh, 1996; Andersson *et al.*, 1999), and eclogite-facies conditions are recorded in an eclogite-bear-

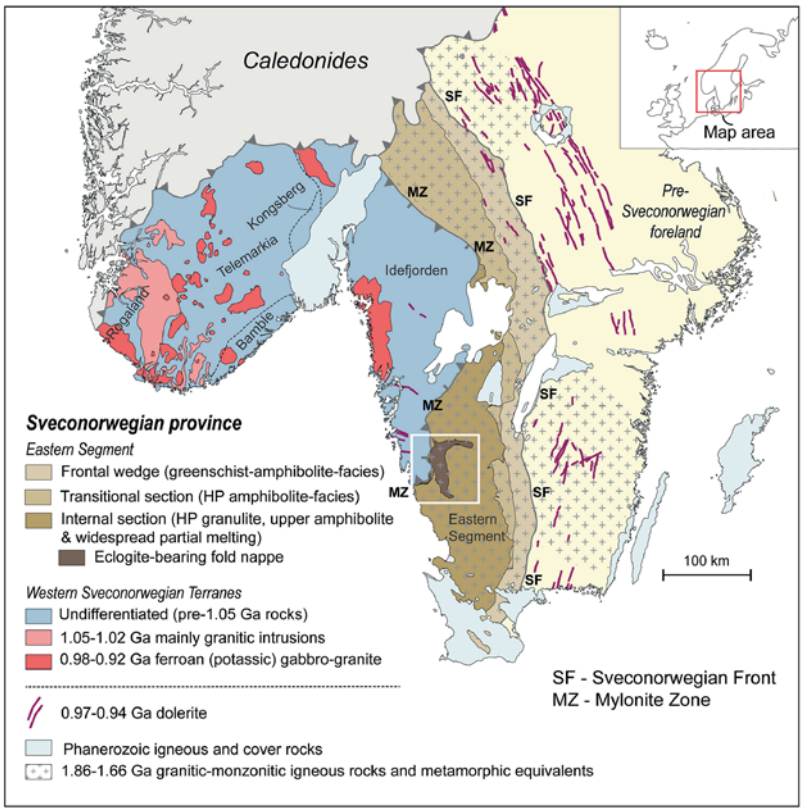

Figure 4: Location of the eclogite-bearing nappe in the Sveconorwegian orogen. Sketch map of the Sveconorwegian orogen showing the Eastern Segment (brown tones) and western Sveconorwegian terranes (bluish grey), separated by ductile deformation zones (terrane divisions after Bingen *et al.,* 2008a; extent of Sveconorwegian magmatism in Telemarkia after Slagstad *et al.*, 2012). Figure from Piñán-Llamas *et al.*, (2015), based on 1:5 M Fennoscandian map database and Geological Survey of Sweden 1:1 M Bedrock map database.

ing nappe (Fig. 4a & b; Möller, 1998, 1999; Möller *et al.*, 1997, 2015a). Partial melting at 0.98–0.96 Ga in the Eastern Segment was followed by intrusion of dolerite and pegmatite dykes (e.g. Möller *et al.*, 2007; Möller *et al.*, 2015a, and references therein);

(4) The Dalane phase is the post-collisional stage after 0.97 Ga and includes an anorthosite–mangerite–charnockite–granite (AMCG) intrusive suite in terranes west of the Mylonite Zone (refs). Finally, c. 0.93-0.92 Ga high- temperature metamorphism associated with these intrusions is recorded in Telemarkia (e.g., Vander Auwera *et al.*, 2011).

The eclogite-bearing fold nappe

During the last decade, a new perspective has arisen from geological mapping in the southern Eastern Segment. Eclogite-bearing associations were mapped out as a tectonically bound metamorphic terrane (Möller *et al.*, 2015a). In order to understand the crustal build-up of the region, it became necessary to constrain the structural and metamorphic history of different units. This thesis has focused on the eclogite bearing nappe that retains information on the deepest buried rocks and their exhumation.

The eclogite-bearing nappe represents a part of the Baltica continental crust that experienced westward tectonic burial at eclogite-facies conditions beneath the Idefjorden Terrane, and was followed by eastward, foreland-directed, tectonic exhumation (Möller *et al.*, 2015a). The nappe is made up of rocks similar to the orthogneisses enclosing it, and do not represent a detached piece of an oceanic slab (Möller 1998, 1999; Johansson *et al.*, 2001; Möller *et al.*, 2015a). The eclogite-bearing fold nappe lies just underneath the contact with the Idefjorden Terrane (The Mylonite Zone, Fig. 5) and is surrounded by upper amphibolite- and high-pressure granulite-facies gneisses (e.g., Johansson *et al.*, 1991; Wang & Lindh 1996; Möller *et al.*, 2015b). Penetrative deformation and polyphasal folding is widespread in the surrounding gneisses (Andersson *et al.*, 1999, 2002; Söderlund *et al.*, 2002; Möller *et al.*, 2007, 2015a; Hansen *et al.*, 2015; Piñán-Llamas *et al.*, 2015). Sveconorwegian migmatization is widespread in the Eastern Segment, but is particularly pervasive in the core of the eclogite nappe (Möller *et al.*, 2015a). The contact of the nappe with the surrounding orthogneisses is marked by semi-continuous 1.4 Ga augen orthogneiss beneath a high temperature basal shear zone (Fig. 5; Möller, 1998, 1999; Möller *et al.*, 2015a; Paper I).

The eclogites generally occur as "classic" eclogite, essentially constituted by garnet and clinopyroxene (and variably retrogressed), but locally decimetre- to metre-thick kyanite- bearing layers and Fe-Ti varieties are also found (Fig. 6). When plotted in a ternary diagram, following the classification of Coleman (1965), garnet from the kyanite- and Fe-Ti-eclogite varieties fall within the B-type eclogite (Fig. 7), in agreement with the field observation that eclogite are enclosed as layers and boudins within felsic gneisses of crustal affinity.

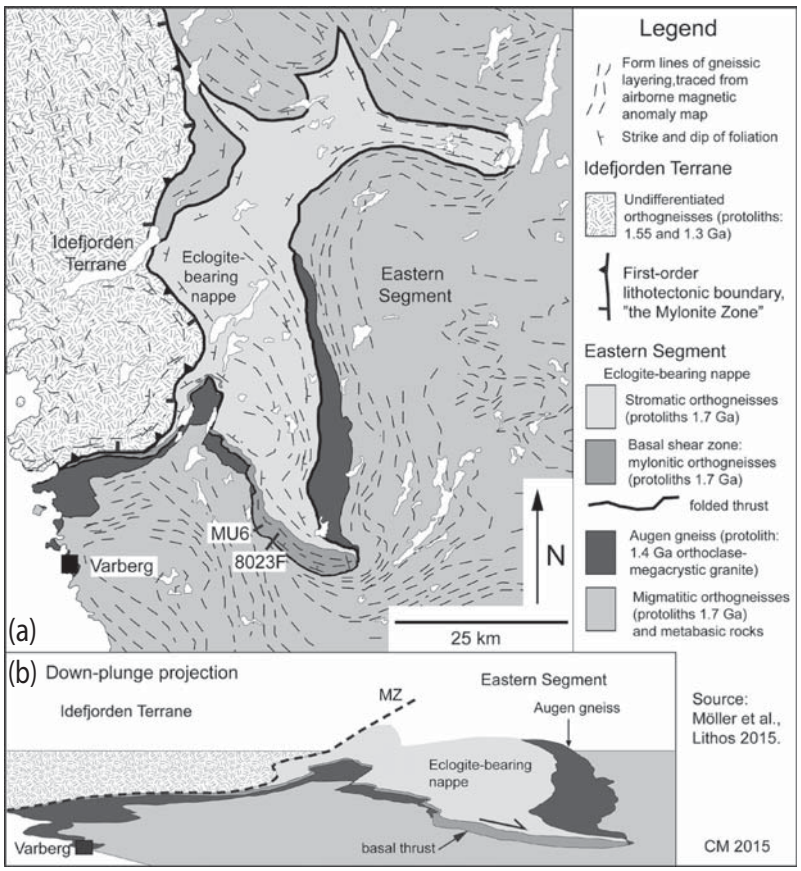

Figure 5: (a) Sketch map showing the location of the eclogite-bearing terrane after Möller *et al.* (2015a). Locations of the investigated samples in this thesis (MU6, 8023F) are indicated. (b) E–W profile across the eclogite-bearing nappe from Möller *et al.*, (2015a; constructed by down-plunge projection)

The bulk composition of the eclogites can potentially indicate the protolith: a norm calculation allows estimation of primary igneous mineral content. The compositions of the Sveconorwegian eclogites point towards plagioclase-rich rocks with olivine and clinopyroxene (kyanite-eclogite), corresponding to olivine gabbro, and anorthite-rich rocks with orthopyroxene, quartz and ilmenite (Fe-Ti eclogite) corresponding to quartz-norite. These rocks may be interpreted as part of a layered igneous complex.

At the start of this project, deformation structures and metamorphic conditions were broadly defined. Peak conditions for the eclogite were estimated at > 15 kbar, with a subsequent reequilibration stage at high-pressure granulite- to upper-amphibolite-facies conditions (Möller *et al.*, 1998, 1999; Austin Hegardt *et al.*, 2005). The deformation was recognized as heterogeneous, with a general orientation of linear structures towards the east (Möller *et al.*, 1997; Andersson *et al.*, 1999, 2002; Söderlund *et al.*, 2002; Möller *et al.*, 2007). Different generations of melt were recognized within the Eastern Segment, some of them associated with Sveconorwegian folding (e.g. Möller *et al.*, 2007). The contact between the eclogite nappe and the surrounding gneisses, i.e. between very-high-pressure (eclogite-bearing) and high-pressure units, was identified as a major deformation zone (Möller *et al.*, 1997, 2015a). The major questions related to the eclogite-bearing nappe were then:

(1) Which deformation structures and fabrics are associated with exhumation and what information can they give?
(2) How deep were the eclogites buried?
(3) What was the thermal evolution from burial to exhumation?

This thesis contributes to the solution of these questions. The first study involved detailed field documentation of the key structure, the basal thrust of the eclogite nappe, and demonstrated how complex ductile structures, involving mutual feedback between melt accumulation and deformation, formed during exhumation of the nappe. The second study constrained the metamorphic history of eclogite and showed that the prograde and the retrograde *P–T* paths were both steep and reached high temperatures, implying rapid tectonic burial and rapid exhumation of the nappe. The third study confirmed, using two independent trace element thermometry methods, the metamorphic history recorded during the burial of the eclogite. This work has important implications for the understanding of the Sveconorwegian orogen, implications that are discussed in section 4.4, before a brief overview of future prospects.

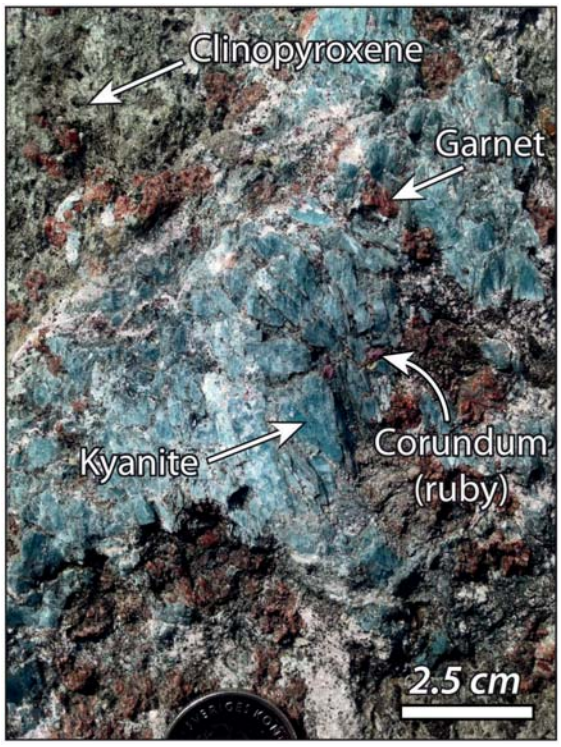

Figure 6: Coarse-grained kyanite-bearing vein in kyanite-bearing eclogite.

2 METHODS

2.1 Fieldwork

Fieldwork was carried out over two extended summer seasons, mostly along a broad N-S profile just east of Ullared (Fig. 2 in Paper I). The main aim was to systematically document the geometry and metamorphic character of different structures, including folds of different generations and shear structures and to collect structural data on the orientations of folds, lineations, and foliations across the basal shear zone, from the gneisses below the nappe to the migmatitic part of the eclogite-bearing nappe above the basal shear zone. Outcrop conditions were variable depending on the state of forest plantation fields. Fold axes were measured where possible, or calculated from the orientations of limbs and axial plane. Particular care was taken to describe the geometry and vergence of the folds to allow extrapolation to larger scale. Kinematic indicators were noted where the orientation of the lineation and the shear sense were both unquestionable. Additional data from C. Möller (earlier observations) and SGU's mapping in the nearby area were integrated. Data were compiled and imported using ArcGis 10.0, only a minor proportion of measurements were presented on the map for clarity. Nevertheless, all data from this part of the basal shear zone are consistent, in agreement with the intense deformation state of the rocks. Although efforts were made to distinguish between the first two stages of deformation, *i.e.* formation of the D1 gneissic layering and the D2 folding and shearing, this distinction was not possible everywhere where folding was absent.

Five key localities were described in detail. A total of nearly 200 thin sections from C. Möller's collection and the two summer's campaigns were observed and described in order to elucidate typical metamorphic assemblages associated with shearing and folding. In addition, one 50x40x30 cm oriented sample was selected for microstructural study, from an area were the folding was described in detail and allowed correlation at a larger scale, in order to confirm macroscopic observations and document kinematic indicators in three dimensions (two perpendicular sections). The sample was oriented after which it was sampled.

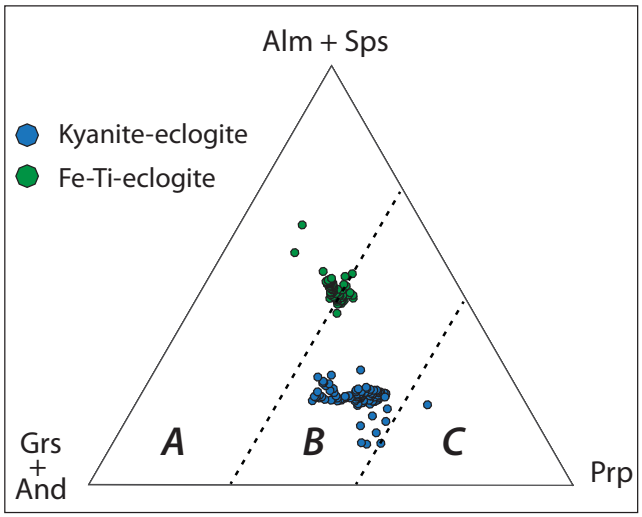

Figure 7: Ternary diagram showing the classification based on garnet composition by Coleman (1965) of different types of eclogite. Type A = eclogite in kimberlite (xenoliths), type B = eclogite in gneiss terrains, type C = eclogite in subduction zones. Alm: almandine; Sps: spessartine; Prp: pyrope; Grs: grossular; And: andradite.

2.2 P–T pseudosection modelling

Phase equilibrium modelling is one of the major techniques used to reconstruct the metamorphic history of a rock. A pseudosection is a phase diagram that is constructed for a specific bulk composition and shows the variation of mineral assemblages as a

function of two variables (typically pressure and temperature, but can also be e.g. temperature and X_{H2O}). Different approaches are used in order to create such diagrams, but the conceptual idea is that rocks tend to achieve equilibrium, i.e. the minimum free energy of the considered system. The THERMOCALC© software (Powell *et al.*, 1998) allows calculation of pseudosections based on the solution of the non-linear equations between the different end-members of considered phases. As pressure and temperature vary the modal proportion of the phases and their respective compositions will change to reach equilibrium; eventually some phases will disappear or new phases appear. The main factors influencing the result are (1) the effective bulk composition of the sample, (2) the chemical system chosen for modelling, and (3) the phases and their solution models. In addition to these factors, careful and thorough petrologic study of the sample is necessary in order to correctly interpret the results.

The first important step is the interpretation in thin section of the prograde, peak-metamorphic, and retrograde sequence of mineral assemblages, which might in some cases prove difficult to identify. In Paper II, for example, it is discussed whether or not corundum was present during the prograde path for one of the samples (8023F). In another sample (MU6), however, used in Papers II and III, microstructural domains with different mineral assemblages could clearly be identified from the start. This sample allowed detailed information because of its early onset of garnet growth and the Ti- and Zr-rich bulk composition. The second important matter is the equilibration volume of the rock. In Paper II and Paper III, we used bulk compositions of small rock pieces (~3x4x1 cm) close to the domain from which the thin section was made. Circa 5g of rock pulp from each sample was analysed by ACME laboratory (Vancouver, Canada) using ICP-Emission spectrometry and determination of FeO-content by titration. The rocks are relatively homogeneous, and a reproducibility test was performed for the two samples. The presence of hydrous minerals like hornblende and the inferred high-temperature conditions for crystallization of the peak (matrix) assemblage in the sample suggest large equilibrium volumes, which is why we consider our approach justified. The choice of the oxides used for calculating pseudosection is also an important point. Phosphorus is considered hosted solely in apatite; we therefore subtracted P and the corresponding amount of Ca as apatite. Similarly, we subtracted MnO as spessartine. Paper II contains an extensive discussion on estimation of both Fe_2O_3 and H_2O, and we show that Fe^{2+} fractionation in sulphides can have significant impact on the pseudosection.

Preservation of chemical zoning in minerals implies gradients of chemical potential and is therefore a disequilibrium feature. Consequently, the interiors of zoned minerals (as well as the inclusions they contain) should be removed from the effective bulk composition when using the pseudosection approach (e.g. Stüwe, 1997; Marmo *et al.*, 2002; Evans, 2004). The estimation and removal of the proportion of the zoned mineral and the inclusions is a delicate task and a possible source of uncertainty. We plan to apply this approach to Fe-Ti eclogite to investigate how it will affect the pseudosection. Nevertheless, in the present case, there is a satisfactory agreement between the observations and the model pseudosection for the Fe-Ti-rich eclogite. For the kyanite-bearing eclogite pseudosection, fractionation of garnet from the bulk composition is considered less significant because garnet started growing at a comparably late stage of the prograde evolution.

The success in interpretation of a *P–T* path lies solely on the quality and rigour of petrological analysis; on a solid basis, equilibrium thermodynamics may be applied in order to retrieve different equilibrium stages in a pseudosection modell (e.g. Powell, 1978).

2.3 Zr-in-rutile and Ti-in-quartz thermometry

Although pseudosection modelling (Paper II) yielded satisfactory results, the results were checked through independent thermometry methods. Recent methods for temperature estimation using trace amounts of Ti and Zr in minerals, based on equilibrium between rutile, quartz, and zircon, had proved to be robust. We applied the Zr-in-rutile and Ti-in-quartz thermometers to the Fe-Ti-rich eclogite sample (MU6) because it contains relatively high amounts of both rutile and quartz (and zircon). Moreover, distinct microstructural domains in garnet core, garnet rim, and in the matrix have the potential of yielding precise constraints on different metamorphic stages.

Because the textural relationship of each single

grain was of primary importance, analyses were performed *in situ*, *i.e.* on rock pieces rather than on separated minerals. Rock slabs of 0.5 mm were prepared and polished by hand. From these slabs garnet grains and their surrounding matrix were selected based on the garnet size, the apparent abundance of rutile and quartz in garnet, and the distinct inclusion pattern in garnet grains. Five garnet grains were selected: four from the Fe-Ti eclogite sample, and one from the kyanite eclogite sample. The selected grains were cut off from the slab and mounted in the centremost part of a 25 mm epoxy disc (Fig. 8), slightly polished and coated with a 30 nm gold layer for SIMS analyses, and coated with carbon for SEM imaging. The sample was also used for other analyses, which is why 5 steps of coating and cleaning were necessary, but this procedure did not affect the analytical results. In the papers presented in this thesis, only three garnet grains (out of five) were used.

Each garnet grain was first imaged using reflected light microscopy, and microphotographs of each rutile and quartz grain was taken from backscattered electron and secondary electron imaging using a Hitachi 3400N Scanning Electron Microscope (SEM). Variation in Ti content in a single quartz grain can result in cathodoluminescence (CL) intensity zoning. Thus CL imaging allows qualitative detection of chemical zoning that may have been produced during crystal growth or diffusion (e.g. Leeman *et al.*, 2012; Spear & Wark. 2009). Cathodoluminescence imaging was performed using a miniGatan CL detector coupled with a Hitachi 3400N Scanning Electron Microscope. Each grain was subsequently imaged again (BSE, SE and CL) in order to document the beam spot.

When the thermometry project started, pseudosection modelling was not yet completed, so precise constraints on the temperature were not available. At high temperature, rutile can contain several hundreds of Zr ppm and could potentially be analysed by electron microprobe, a fast and relatively cheap method. A rough try at the microprobe in Copenhagen confirmed this feasibility. However, analysis of trace amounts of Ti in quartz grains was more complex, as expected Ti content would only reach a few dozen of ppm, and technical issues may arise from heterogeneous quartz sampling using electron microprobe techniques. Moreover, the grains included in garnet are very small. For these reasons, both rutile and quartz grains were analysed using a Secondary Ion Mass Spectrometer (SIMS, Cameca IMS1280) at the Nordsim laboratory at the Museum of Natural History in Stockholm. Analysis was performed using an O^{2-} primary beam, the size of which was set at 10 µm in order to precisely target the centre of the grains. All quartz and rutile inclusions in each of the three selected garnet grains were analysed to avoid any bias. Only analyses that hit outside the grain were discarded. The advantages of SIMS analysis are that both spatial and analytical

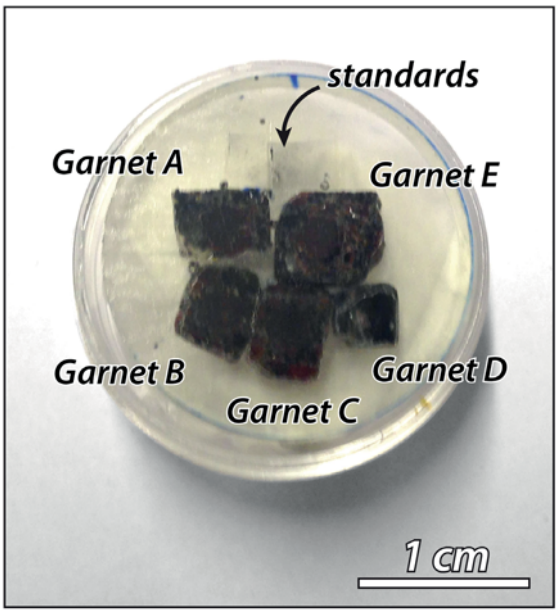

Figure 8: Epoxy mount with garnet grains from eclogite and standard grains of rutile and quartz, used for the study in Paper III. Diameter of the mount ~2.5 cm.

resolutions are high. In the present study the error propagated from standard analyses is the dominant contribution to overall uncertainty (see Paper III).

Temperatures were calculated from the Ti contents in quartz following the calibration by Thomas *et al.* (2010). The Tomkins *et al.* (2007) calibration was chosen for Zr-in-rutile. Three different pressure values (7, 12, and 18 kbar, respectively) were used as input values in the equations, based on pressure values read off the pseudosection for the three corresponding growth zones and textural settings (see Paper III). In addition, intersections in the *P–T* field of the two trace element thermometers allowed independent *P–T* estimation. In Paper III, we show that this technique yielded results in nearly perfect agreement with the pseudosection.

An important point is that all the data were obtained *in situ* and treated equally, and only analyses hitting outside the grain were discarded. This method enabled direct textural correlation and without the bias that may have arisen from analysis of separated grains.

3 SUMMMARY OF THE PAPERS

The statement of authors' contributions in each paper is given in Table 1.

Paper I

Tual, L., Piñán-Llamas, A. & Möller, C. 2015. High-Temperature Deformation in the Basal Shear Zone of an Eclogite-Bearing Fold Nappe, Sveconorwegian Orogen, Sweden, in: Roberts, N., Viola, G., Slagstad, T. (Eds.), The structural, metamorphic and magmatic evolution of Mesoproterozoic orogens. Precambrian Research, 265, 104-120.

The thrust at the base of a nappe is generally the key structure to investigate in order to understand how a nappe has been exhumed. In high-grade terranes, thrust structures can prove very complex, having been formed by polyphasal ductile deformation.This article deals with evidence of the exhumation of the eclogite-bearing fold nappe, with a particular focus on its basal shear zone. It is the first study that documents in detail the structures of this basal shear zone and includes a systematic investigation of kinematics and the links between deformation fabrics and the metamorphic evolution.

We identified D1 as the formation of penetrative gneissic foliation and tectonic layering (S1), stretching lineation (L1), and isoclinal folds (F1). D2 structures include up to km-scale, tight, south-vergent folds (F2) with sheared out limbs (Fig. 9a). F2-folds are associated with an axial planar fabric (S2), defined by upper-amphibolite- and locally granulite-facies mineral assemblages. Shear structures are associated with top-to-the-east kinematic indicators throughout the investigated section. F2 folds are interpreted as transport-parallel folds; these folds have shallowly E-plunging fold axes, parallel to a pronounced stretching lineation (L1-L2) defined by high-grade mineral aggregates.A separate focus was to document the relationships between melt localization and fold geometry in the deformation zone, and the highly ductile style of deformation.

We interpret the D1 episode as the emplacement of the eclogite-nappe into its present structural position. The lineation-parallel folds (F2) are interpreted to have formed by general shear, where the structures reflect the regional E-directed flow of the eclogite-bearing nappe (Fig. 9b).

This paper represents a pathfinder for future studies, and contributes to the understanding of deep-seated thrust structures in orogens in general, and to the understanding of the Sveconorwegian orogeny in particular.

Paper II

Tual, L., Pitra, P. & Möller, C. P–T evolution of Precambrian eclogite in the Sveconorwegian orogen, SW Sweden. Manuscript submitted to Journal of Metamorphic Geology in January 2016.

In this paper, we provide for the first time a quantitative *P–T* path for eclogite in SW Sweden, the only eclogite-bearing terrane described so far in the Sveconorwegian orogen. We present *P–T* pseudosections for two different bulk rock compositions and include precise constraints on the prograde metamorphic path. The influence of the estimated contents of H_2O and Fe_2O_3 is also discussed, and emphasis is given to the effects of Fe^{2+} fractionation in sulphides. We show that the rocks reached conditions ~850–900 °C at 16–19 kbar, beginning at a typical Barrovian gradient, and followed by burial along a steeper *P*/*T* gradient (Fig. 10). Although growth zoning in garnet is preserved, matrix reequilibration during the metamorphic peak and subsequent near-isothermal decompression took place at very high temperatures (810–900 °C).

The new *P–T* path has important implications for the tectonometamorphic evolution of the Eastern Segment, but also for the build-up of the Sveconorwegian orogen. The steepness of both prograde and retrograde paths and the preservation of garnet growth zoning reflect short-lived episodes of burial and exhumation at high pressure and temperature. The eclogite-bearing nappe was part of the underthrusting plate in a collisional setting and was extruded rapidly by tectonic forces.

This paper constitutes a rare case of a well-con-

Table 1: Author's contributions to papers.

	PAPER I	PAPER II	PAPER III
General project design	C. Möller	C. Möller	C. Möller
Litterature study	L. Tual, C. Möller	L. Tual	L. Tual
Field work: documentation, mapping & measurement	L. Tual, C. Möller, A. Pinan-Llamas	C. Möller	-
Sampling	C. Möller, L. Tual	C. Möller	C. Möller
Petrography	L. Tual, C. Möller, A. Pinan-Llamas	L. Tual, C. Möller, P. Pitra	L. Tual
SEM	-	L. Tual	L. Tual
Microprobe analysis	-	L. Tual	-
Trace elements analysis	-	-	L. Tual
Thermodynamic modelling/Thermometry	-	L. Tual	L. Tual
Field photography/Microphotography	L. Tual, C. Möller	L. Tual	L. Tual
Artwork	L. Tual, C. Möller	L. Tual, C. Möller	L. Tual, C. Möller
Data interpretation & discussion	L. Tual, C. Möller, A. Pinan-Llamas	L. Tual, P. Pitra, C. Möller	L. Tual, C. Möller
Manuscript writing	L. Tual, C. Möller, A. Pinan-Llamas	L. Tual, P. Pitra, C. Möller	L. Tual, C. Möller, M. J. Whitehouse
Manuscript review	L. Menegon*, T. Scheiber*	-	*U. Söderlund*

* = Journal reviewer. Italics: not coauthor in the paper.

strained prograde and retrograde *P–T* path for Precambrian eclogite. Rapid burial and exhumation of the eclogite-bearing nappe can conceptually be compared to a Himalayan scenario and demonstrates the modern style of Grenvillian-aged tectonics.

Paper III

Tual, L., Möller, C. & Whitehouse, M.J.. Tracking the prograde P–T path of Precambrian eclogite using Ti-in-quartz and Zr-in-rutile thermobarometry. (Manuscript)

Recently developed trace element thermometry techniques, including Zr-in-rutile and Ti-in-quartz (Zack *et al.*, 2004; Watson *et al.*, 2006; Wark & Watson, 2006; Ferry & Watson 2007, Thomas *et al*, 2010), have proven a robust means for estimation of pressure and temperature. These methods are particularly useful for *T* estimation of high-temperature metamorphic rocks, for which classical thermometry methods based on Fe-Mg exchange are commonly problematic (e.g. Zack *et al.*, 2004; Baldwin and Brown, 2008; Luvizotto and Zack, 2009; Spear & Wark 2009; Zhang *et al.*, 2009; Jiao *et al.*, 2011; Menegon *et al.*, 2011; Kooijman *et al.*, 2012; Ewing *et al.*, 2013; Štípská *et al.*, 2014; Korhonen *et al.*, 2014; Liu *et al.*, 2015).

More often than not prograde stages of metamorphism are overprinted by peak equilibration and/or retrogression, especially in rocks that experienced peak temperatures over 750 °C. Pseudosection calculations presented in Paper II, in particular the one for the Fe-Ti eclogite sample, allowed unusually good constraints on the prograde part of the *P–T* path. Three micro-textural stages were identified, each of them associated with abundant quartz, rutile and zircon, and suitable for both Zr-in-rutile and Ti-in-quartz thermometry. Since metamorphic temperatures were high, high concentrations of Zr in rutile and Ti in quartz were expected. However, since prograde zoning in garnet is preserved, limited chemical diffusion could also be expected (Paper II and references therein). The sample therefore seemed particularly suitable for a comparative study between the two thermometers and the *P–T* pseudosection.

In situ (SIMS) analyses of quartz and rutile in each type of microtextural domain show that whereas Zr-in-rutile records best early stages of the prograde part of the *P–T* path, Ti-in-quartz records best the peak conditions. Pairing results from both thermometers yield a prograde path in nearly perfect agreement with *P–T* pseudosection modelling (Fig. 11). A pseudosection model of the modal proportion of quartz, rutile, and ilmenite shows that the amounts of these minerals varied only during the first part of garnet growth (i.e. the garnet core); dur-

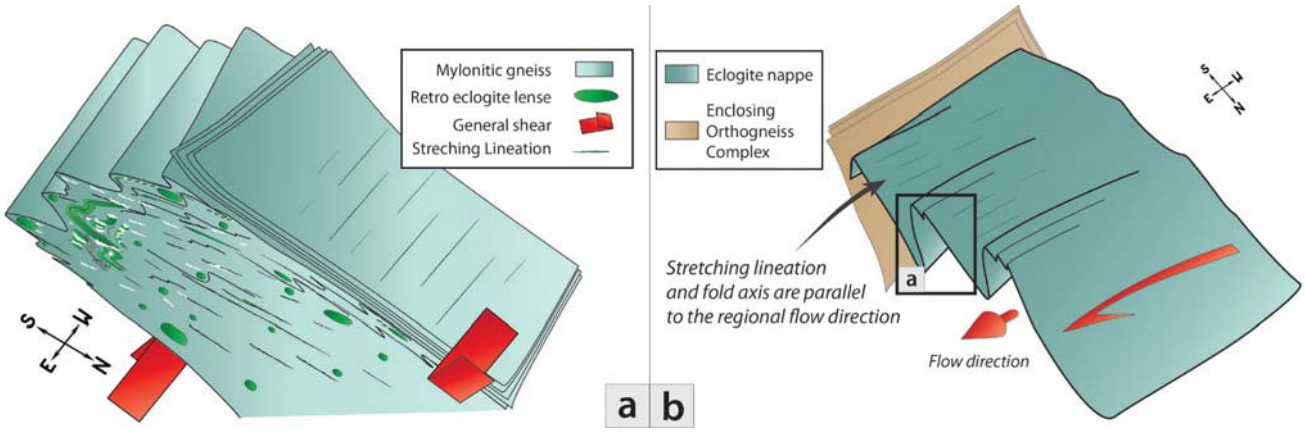

Figure 9: Geometry of and kinematics in F2 folds of the basal shear zone. (a) Sketch summarizing the main characteristics of F2 (close up from (b)). Red arrows mark general shear. The moderate dip of the foliation (i.e. S2) and obliquity of the lineation to strike demonstrate a significant dip-slip component. White trails mark leucosome. (b) Conceptual sketch of development of lineation-parallel folds in a context of regional flow. *Figure from Paper I.*

ing the main part of the *P–T* path these minerals must have reequilibrated by recrystallization of already existing matrix grains. The results from the Zr-in-rutile thermometer are interpreted to reflect major recrystallization of the rock during a continuous dehydration reaction involving breakdown of hornblende and production of clinopyroxene. The presence of fluid produced by this reaction is suggested to have been important for continuous recrystallization and increasing grain size of rutile and other minerals in the matrix. This study demonstrates that the use of three independent methods, Ti-in-quartz thermometry, Zr-in-rutile thermometry, and *P–T* pseudosection modelling, can give robust constrains on temperature and pressure and insights on crystallization process during metamorphism.

4 ONGOING STUDIES AND FUTURE PROSPECTS – A DISCUSSION

4.1 Raman barometry using quartz inclusions in garnet

Conventional geobarometry relies on pressure-dependent equilibria (involving *e.g.* plagioclase or phengite), but at high pressure plagioclase is not stable and phengite is rare in mafic rocks. Some minerals, however, show systematic peak shifts in their Raman spectra as a function of pressure. The main peaks of α-quartz vary with temperature and pressure, a relationship that has been reproduced in experiments (Schmidt & Ziemann, 2000). Because garnet can form robust armour around quartz inclusions, applications of Raman thermobarometry on quartz inclusions in garnet have yielded successful results (e.g., Enami *et al.*, 2007; Ashley *et al.*, 2014).

At the instance quartz grains are trapped in garnet, both minerals are subject to the same pressure. During exhumation, however, the "external" pressure will decrease, and garnet and quartz will behave differently in terms of their relative expansivities and/or compressibilities. For each phase this quantity depends on the entrapment pressure, the elastic properties, and the dependence of molar volume on *P* and *T* (e.g. Guiraud and Powell, 2006). The volume changes of coexisting quartz and garnet can be modelled based on their elastic properties and the residual pressure can thereafter be constrained from *in situ* Raman spectroscopy of quartz. Two main Raman bands of quartz are identified at atmospheric pressure, at 206 and 464 cm^{-1}, but with increasing pressure these bands will shift towards higher wavelengths. Uncertainties are only a few hundred bars, but the Raman shift is significant only at high or low P/T (e.g. Kohn, 2014b, Fig. 12). This is because during cooling quartz expands when crossing isochores from high pressure, and shrinks when crossing from low pressure, this results in two main domains in the

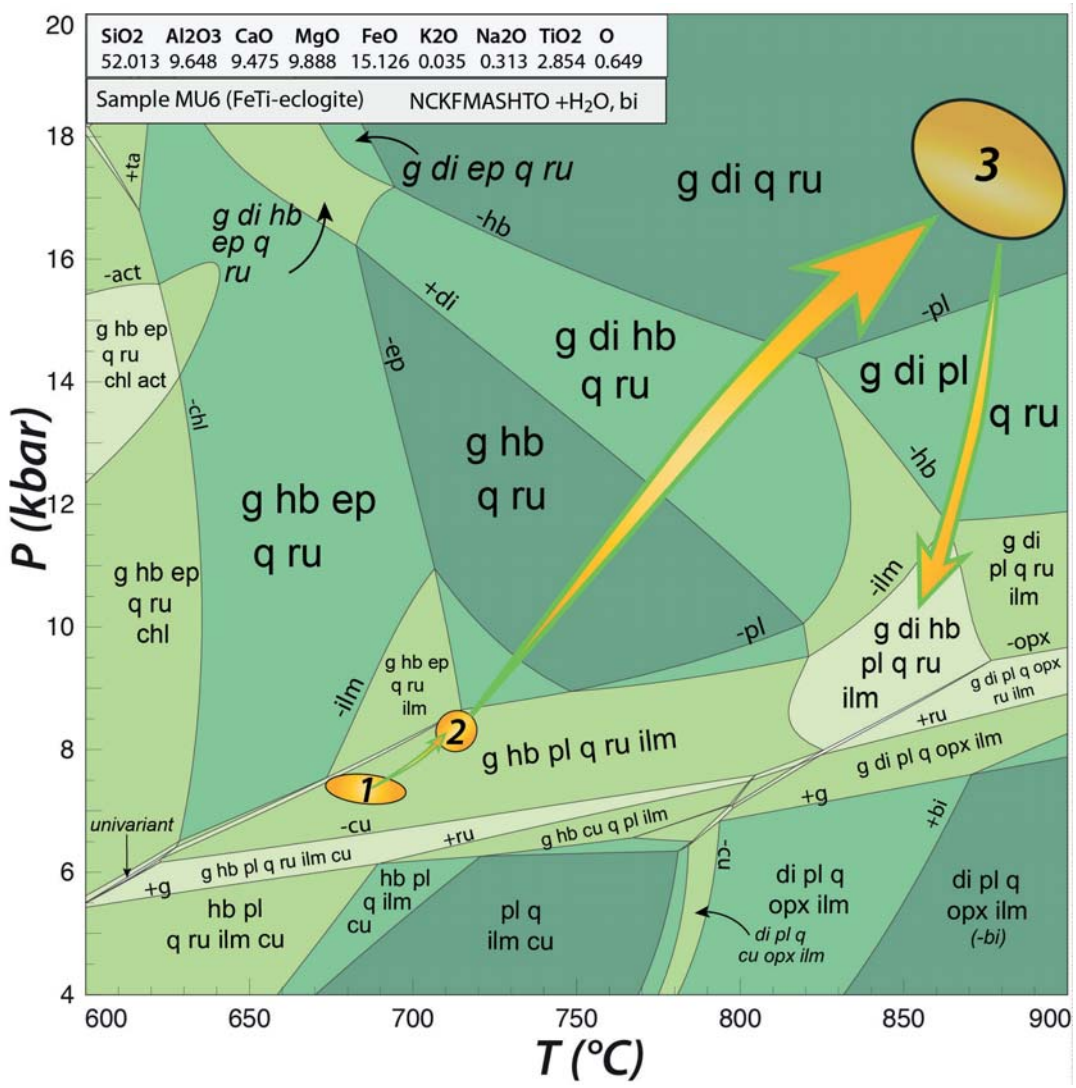

Figure 10: *P–T* pseudosection calculated for sample MU6 (modified from Paper II). The rock composition is given as mole-% oxides. Ellipses correspond to the stages described in Paper II. Mineral abbreviations are from Holland & Powell (2011).

P–T field separated by a zone without significant shift (Fig. 12).

Preliminary application of this technique was undertaken on quartz inclusions in garnet from Fe-Ti-rich eclogite (sample MU6). Raman spectra were collected using a Raman microscope Horiba LabRAM HR Evolution fitted with a detector Sincerity CCD and deep cooled camera (Horiba). The inclusions were focused using x100 objective and a 100 µm hole resulting in high spatial resolution (< 0.5 µm). The grating was set at 1800 lines/mm using a 532 nm laser. Data were collected during a total acquisition time of 150 s with a dwell time of 10 s with three iterations over a spectral range of 80–800 cm^{-1}. Preliminary results of Raman shift were combined into entrapment pressures using the software QuiBCalc® from Ashley *et al.* (2014b).

A total of 80 spectra from small quartz inclusions (5-20 µm) were collected using different sample types: a hand polished slab, a thin section, and an epoxy mount (the same as used for thermometry analysis, Paper III). All spectra were acquired on grains visible at the surface of the sample. Most v_{464} shifts range from 0 to 1 cm^{-1}; assuming an average temperature of 700 °C, and yield entrapment pressures of 9–10 kbar following the calibration of Guiraud and Powell (2006) and 11–12.5 kbar following the calibration of Zhang (1998). Several grains in the rim show shifts ~1.5 and up to 2.9 cm^{-1} which corresponds to entrapment pressures of 13–15.5 kbar (calibration Guiraud and Powell, 2006) and 16–18.5 kbar (calibration Zhang, 1998). Additional analyses are needed to improve statistics. We plan to perform depth profiling of completely encapsulated quartz inclusions to reduce errors introduced by surface grain boundary effects. Nevertheless, our

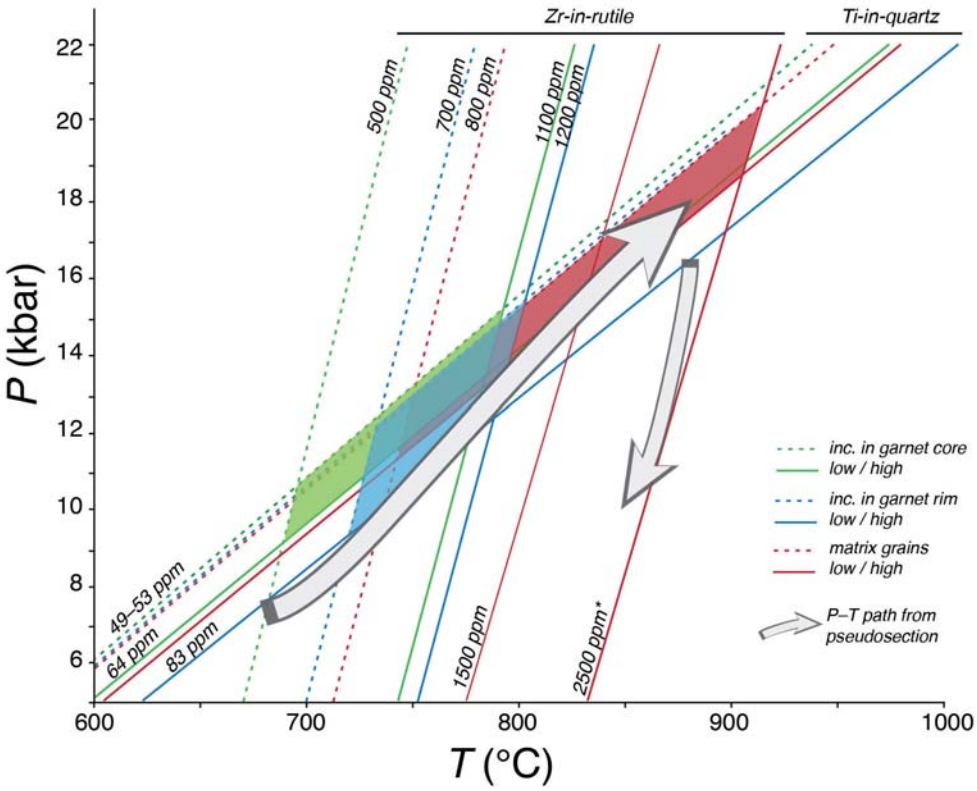

Figure 11: Isopleths calculated for Ti-in-quartz and Zr-in-rutile (method after Thomas *et al.*, 2010) based on the results for inclusions in the cores of garnet (green), inclusions in the rims of garnet (blue), and matrix grains (red). Lower values (dashed lines) correspond to the lower interquartile range of the data; higher values correspond to the upper interquartile range of the data (solid lines). The three highest values of Zr-in-rutile (out of 15 analyses) reached 2500 ppm. The boxes show that the full range of temperature estimates using Zr-in-rutile and Ti-in-quartz in each microstructural setting follows closely the P–T path deduced from pseudosection modelling (white arrows; Paper II.). Figure from Paper III.

preliminary data suggest that retrieval of entrapment pressures from quartz inclusions in garnet may be feasible. Future studies involving quartz-in-garnet Raman barometry might constrain even better the prograde history of Sveconorwegian eclogite.

Few applications of quartz in garnet Raman barometry have yet been undertaken; therefore, beyond the interest of this specific example, this project will allow comparison of different calibrations of a sample for which pressure and temperature are already well known.

4.2 In situ SIMS U-Pb dating, rare earth elements analysis, and Ti thermometry of zircon

Linking time and temperature is needed in order to constrain the metamorphic history and tectonic evolution of different terranes in a mountain belt. Zircon is a key mineral that can record the age of metamorphic events. During the last decade, a wealth of studies has shown that metamorphic zircon may form at different stages of a *P–T* path (e.g. review articles by Harley *et al.* 2007 and Rubatto & Hermann 2007). In metamorphic rocks, zircon may have a compositional zoning that reflects stages of growth. In particular, rare-earth elements (REE) have a preferential distribution between minerals in a metamorphic assemblage. For example, plagioclase is the mineral that will preferentially take up Europium (Eu^{2+}). In contrast, garnet will preferentially fractionate heavy rare earth elements (HREE). The passage to the eclogite facies is characterized by garnet growth and plagioclase breakdown leading to a release of Eu and uptake of HREE. As a result the transition to eclogite facies during the prograde path may be tracked in zircon domains that show Eu enrichment coupled with HREE depletion (e.g. Rubatto, 2002). Consequently comparison of the crystallization ages of zircon domains, REE patterns, and textural interpretation is a key to inference of the metamorphic evolution during zircon growth. Finally, Ti-in-zircon, just as Ti-in-quartz and Zr-in-rutile as presented above, is a thermometer that can yield the temperature of crystallization and provide even further constraints for the *P–T-t* path.

A SIMS study of zircon in eclogite has been initiated together with J, Andersson and C. Möller, involving (1) U-Pb dating of zoned zircon crystals, (2) REE analysis of zircon domains and metamorphic minerals, and (3) Ti-in-zircon thermometry. Four mounts have been prepared for this project. One is the same as used in Paper III, and was used for in situ analysis of zircon grains included in garnet and in matrix minerals of Fe-Ti-rich eclogite (sam-

ple MU6). Separated zircon grains were mounted on a second mount; some grains are from the whole rock and others were carefully handpicked from pure separated and hand-crushed garnet fractions. Zircon grains included in garnet will track the prograde history of the rock (or, alternatively, even older events; cp. the approach by Johansson *et al.*, 2001). Two other mounts with zircon separated from quartz- and kyanite-rich layers in the same eclogite and quartz-bearing eclogite from farther north have been analysed. Each grain has been documented using BSE and CL imaging. U-Th-Pb isotopes, REE contents, and, for sample MU6, Ti contents in zircon, were acquired using the CAMECA at the Nordsim laboratory at the Museum of Natural History in Stockholm.

This project has the potential to yield a high resolution *P–T–t* path by application of the most recent and robust "petrochronologic" tools.

4.3 Fold formation in the eclogite-bearing nappe

Two unsolved but related issues concerning the exhumation of the eclogite-bearing nappe are: 1) the actual deformation mechanism within the nappe and 2) the large-scale structure that is partly hidden beneath the surface. Two good candidates for fold formation are sheath folding and flow-perturbation folding, as discussed in Paper I. Sheath folds and flow-perturbation folds are typical products of high strain ductile deformation and can form structures tens of kilometres in size (e.g. Alsop, 2009; Xypolias & Alsop, 2014). Flow perturbation folds initiate with hinge lines sub-parallel to the main transport direction. Thus, the orientation of hinge lines reflects the flow direction during fold initiation and growth. Depression and culmination surfaces, corresponding to slackening and surging flow, respectively, make up the large-scale structure (Alsop & Holdsworth, 2007). In contrast, sheath folds initiate with fold axes at high angle to the transport direction. Therefore, the formation of sheath folds with parallel stretching lineation and fold axis requires very high finite strain and reorientation of initial fold axes.

Mapping of fold structures in areas other than the basal shear zone is required in order to fully understand the large-scale structure and deformation mechanism of the nappe, this is because strain is high in the basal shear zone. In both cases, opposite strike-slip components are expected on the flanks of the nappe (i.e. sinistral in the north, dextral in the basal shear zone in the south, Fig. 13).

The only way to prove a case of flow folding is to systematically map fold structures within the nappe, where the strain is expected to be most variable. In the case of sheath folding, low-strain zones should be characterized by curvilinear folds and higher variation in fold axis orientation (strain is too low to reach complete fold axis reorientation). Consequently, future systematic mapping of fold orientations within the entire nappe can provide evidence of the nature of the large-scale fold.

Another question concerns the mechanism that triggered exhumation of the eclogite-bearing nappe shortly after its burial. The initiation of shear zones is a challenging issue that has attracted interest (e.g. Mancktelow & Pennachioni, 2005). Sheath folds are commonly initiated around rigid inclusions (e.g. Cobbold & Quinquis, 1980; Marques & Cobbold, 1995; Rosas *et al.*, 2002). Recent studies of Reber *et al.*, (2012, 2013), however, showed that sheath folds can also initiate around slip surfaces and weak inclusions, and yield a recumbent fold structure with a shear zone at its base (Reber *et al.*, 2012, their Fig. 1). We know that we had melt-present conditions during D1 and D2. The drastic rheology contrast that is induced by partial melting and its influence on folding mechanisms and shear zone initiation is demonstrated in Paper I. Consequently, initiation of exhumation and a formation a basal shear zone by partial melting is an appealing scenario for the eclogite-bearing nappe. Basal shear zones of fold nappes are in nature the result of very high-strain, and as a consequence, the initial trigger is obliterated. Hypothesis testing of the large scale folding being triggered by melt initiation may only solely rely on numerical or analogue modelling, an interesting future prospect.

4.4 On the tectonic interpretation of the Sveconorwegian orogen

When trying to elucidate the history of an orogen, it is almost impossible not to keep a conceptual model in mind. Combined petrological, geochronological, structural, and geophysical data for orogens worldwide has been simulated by increasingly complex numerical modelling (e.g. Jamieson *et al.*, 2004; Sizova

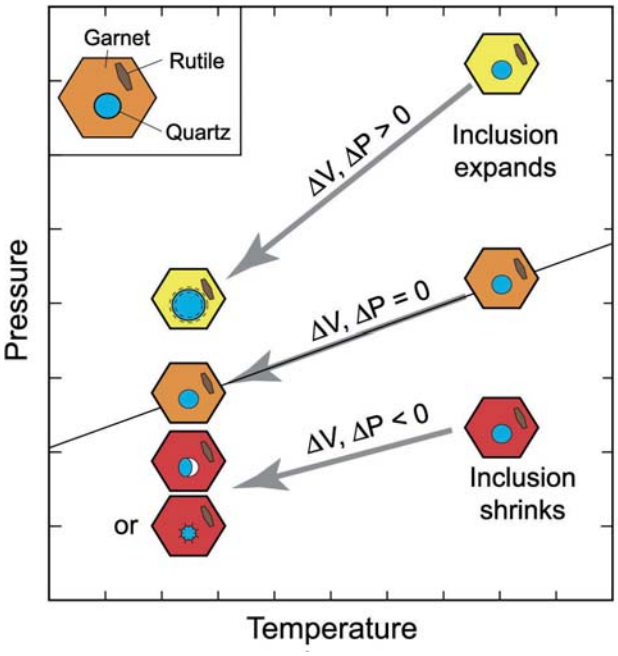

Figure 12: Schematic illustration on how differential pressures develop in mineral inclusions, exemplified by rutile and quartz in garnet. For a specific inclusion–host pair, e.g. quartz-in-garnet, two fields exist in the P–T field. For quartz included at elevated pressure, inclusions expand relative to the host garnet during exhumation, creating positive pressures for both host and inclusion (ΔV, ΔP>0). For quartz included at elevated temperature, inclusions shrink relative to garnet during exhumation, either creating a void space or simultaneously stretching the host and inclusion (ΔV, ΔP<0). The ΔV, ΔP = 0 extrapolates to 1bar, 298 K. Figure and figure text modified from Kohn (2014b) and reproduced with permission from Elsevier.

et al., 2014). Most models are based on Phanerozoic, "modern" orogens, which have not been extensively eroded and in some cases can be coupled with geophysical data to understand structures at depth. As a result, while working on Precambrian orogens that are largely eroded and expose lower levels of the crust, it is crucial to keep in mind that choosing one "classical" model will inevitably induce bold extrapolations. It has, however, the merit to help at identifying key features in order to reconstruct key orogenic events.

The classical view of the Sveconorwegian orogen as a collisional orogen (e.g. Bingen *et al.*, 2008a) was recently challenged, and a model of a non-collisional, Andean-type setting was put forward, based mostly on the presence of granitic 1.05 Ga intrusions in Telemarkia, SW Norway (e.g. Slagstad *et al.*, 2012; Roberts and Slagstad 2014). The Sveconorwegian Province is depicted by these authors as a whole block, accreted 500 Ma before the onset of Sveconorwegian orogeny. An east-dipping subduction zone is proposed, situated west of Norway. Eclogitisation in the Eastern Segment is envisioned as thickening and exhumation in the retro-wedge of an Andean-type belt, without any collisional process.

Presentation of a tectonic model for the entire Sveconorwegian orogen is beyond the scope of this thesis. However, the data presented in our studies imply that a collisional stage took place at the end of the Sveconorwegian orogeny, and that that this event is responsible for westward tectonic burial leading to eclogite-facies metamorphism and subsequent tectonic exhumation. Below are some considerations regarding a general tectonic model of the Sveconorwegian orogen.

The *P–T* history of the eclogite-bearing terrane and surroundings conform to very-high temperature conditions at the end of the Sveconorwegian orogen. Two keys to tectonic interpretation are (1) steep prograde and retrograde paths recorded by eclogite, and (2) partial melting of the eclogite-bearing nappe and associated ductile deformation during the exhumation.

Reaching of the HP-HT conditions recorded for the southern Eastern Segment requires thickening to a ~70-80 km thick crust at c. 1 Ga. An Andean scenario would require this kind of thickening far inside the continent, more than 500 km from the continental margin. Thickening processes in Andean-type orogens generally do not involve tectonic doubling of crust, but instead magmatic underplating. The alternative would be efficient transfer of contractional forces far into the continent.

Magmatic underplating is not the cause of crustal thickening in the Eastern Segment, and magmatism at c. 1 Ga is absent. The alternative explanation (contractional forces reaching far into the continent) requires low-viscosity conditions in order to create high-temperature shearing and regional-scale foreland-directed flow folding, such as found in the Eastern Segment (Paper I; Möller *et al.*, 2015a; Piñán-Llamas *et al.*, 2015). One of the crucial points of the model presented by Roberts and Slagstad (2014) is that the Idefjorden terrane and Eastern Segment accreted 500 Ma prior to eclogite metamorphism. In a case where these blocks had 500 Myr for thermal equilibration before the onset of Sveconorwegian orogeny, it remains unclear how a thick orogenic root could form, and it would be problematic to reach the low-viscosity conditions necessary for the documented foreland-vergent ex-

humation of a deep-seated high-pressure terrane. The case of a flat-slab subduction (e.g. the Laramide orogeny, Bird, 1984) that could drive forces across a margin is an option, although equally elusive. It would be *a priori* difficult to reconcile with a long-lived (500 Myr) subduction history, because flat-slab subduction requires a young, relatively buoyant oceanic slab.

Both options above (magmatic underplating and far-field orogeny) are difficult to reconcile with the setting of eclogite-bearing terrane in the Eastern Segment, which records H*P*-H*T* conditions, ductile thrusting, and deep crustal flow (Johansson *et al.*, 1991; Johansson and Kullerud 1993; Wang and Lindh, 1996; Möller *et al.*, 1997, 2007, 2015a; Möller 1998, 1999; Andersson *et al.*, 1999, 2002; Söderlund *et al.*, 2002; Bingen *et al.*, 2008b; Hansen *et al.*, 2015; Piñán-Lamas *et al.*, 2015; Paper I, II and III). This thesis describes in detail the low-viscosity conditions, deformation, and the *P–T* history of the eclogite-bearing terrane. These constitute major points for consideration when reconstructing a tectonic scenario. Exhumation of H*P* lower crustal rocks following an Andean-type orogeny is not uncommon (e.g. Variscan orogen, Schulmann *et al.*, 2008; the Himalayas, following the formation of the Kohistan arc, Searle *et al.*, 1999), but it requires a major collisional stage less than 100 Ma after terrane accretion, and the formation of an orogenic root.

A critical point is the localization of suture zones in deeply eroded orogens. The Mylonite Zone, just above the eclogite nappe is considered in many respects as a good candidate (see Möller *et al.*, 2015a and references therein). No remnants of mantle or oceanic material have been found, but this is common in collisional Precambrian orogens where suture zones are often just major shear zones. Only some rare cases of Precambrian suture zones have remnants of oceanic or mantle material (the Llano Uplift, USA: Mosher *et al.*, 2008, and the NW Highlands in Scotland: Storey *et al.*, 2005).

Consequently, a more straightforward approach is to interpret the clockwise *P–T* path of the eclogites, associated with near isothermal decompression through granulite-facies conditions (Paper II), as crustal overthickening and subsequent tectonic exhumation during continent collision (cp. reviews of E–HPG settings by Harley, 1989, and O'Brien & Rötzler, 2003). Brown (2014) argues, moreover, that the association of UHT rocks and E-HPG rocks is evidence of collisional suture zones. Only a tectonic scenario involving fast burial and exhumation can account for the steep *P–T* path recorded by Sveconorwegian eclogite, along a high *P/T* gradient, and reaching very high temperature.

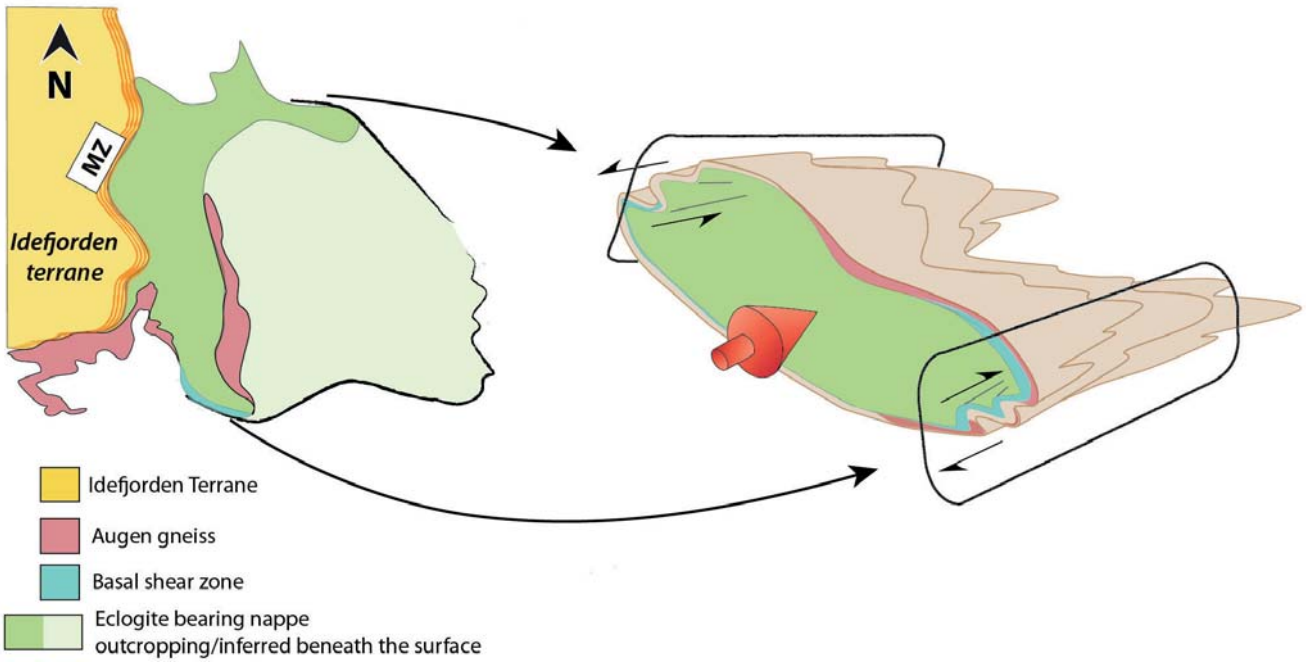

Figure 13: Sketch map of the eclogite-bearing nappe (based on Fig. 5; Möller *et al.*, 2015a) with an (unconfirmed) hypothetical continuation beneath the surface (light green) and a corresponding 3D interpretation (right; figure adapted and redrawn from Alsop & Holdsworth, 2004). The red arrow shows the inferred flow direction; note expected shear sense on each flank of the nappe.

SVENSK SAMMANFATTNING

Bergskedjor är uppbyggda av olika slags berggrund som skjutits samman i de zoner på Jorden där tektoniska plattor möts (konvergerar). Sådana processer sker i dag exempelvis i Himalaya, Alperna eller Anderna, men det finns också gamla, nu inaktiva, bergskedjor som de Skandinaviska Kaledoniderna (ca 400 miljoner år gammal) eller den Svekonorvegiska bergskedjan (ca 1000 miljoner år gammal, i sydvästra Sverige och södra Norge). De komplexa och långdragna processer som skapar bergskedjor kan vi förstå genom att klargöra den geologiska utvecklingen för bergskedjans olika delar. Denna utveckling inbegriper samverkande deformation och metamorfos (omvandling vid ökat tryck och ökad temperatur) samt, i vissa fall, magmatism. Nyckelelement vid rekonstruktion av bergskedjebildning är högtrycksmetamorf berggrund som innehåller blåskiffer, eklogit och/eller högrycksgranulit, därför att sådan berggrund ger information om jordskorpeförtjockning med tektonisk nedtryckning eller subduktion till stora djup.

Min forskning behandlar deformation och metamorfos i den högtrycksmetamorfa delen av den Svekonorvegiska bergskedjan i sydvästra Sverige, med särskilt fokus på en tektonisk enhet (skolla) som innehåller eklogit. Berggrunden här genomgick i sin helhet metamorfos vid mycket stora djup (35-40 km) och är det djupaste snittet av Prekambrisk jordskorpa som finns exponerat i den Fennoskandiska skölden. Berggrunden här är i många avseenden jämförbar med den världsberömda västra gnejsregionen (Western Gneiss Region) i norska Kaledoniderna. Ur ett vetenskapligt perspektiv är berggrunden i sydvästra Sverige ett fönster till de djupa delarna av en bergskedja som för tusen miljoner år sedan var del av en världsomspännande superkontinent, Rodinia. Mitt huvudsakliga mål har varit att karaktärisera den tektoniska och metamorfa utvecklingen av den Svekonorvegiska bergskedjan med utgångspunkt från den eklogitförande skollan i sydvästra Sverige.
Avhandlingen består av tre delar:

Framläggande av en strukturgeologisk och kinematisk modell för deformation i eklogitskollans basala skjuvzon. I denna studie undersökte vi deformationsstrukturer i fält och mätte deras orientering och geometri, i syfte att förstå hur den eklogitförande skollan har lyfts upp från stora djup. Vi kunde visa att skollan transporterades österut längs den basala skjuvzonen och att denna deformation skedde vid minskande tryck (upplyftning) och mycket hög temperatur. I den basala skjuvzonen blev bergarterna mycket starkt deformerade och veckade under hög temperatur, och vi visar exempel på de särskilda deformationsstrukturer som bildas under sådana förhållanden.

Rekonstruktion av den metamorfa utvecklingen för två typer av eklogit. När bergarter pressas ned på djupet och värms upp är de primära mineralen inte längre stabila. Då sker kemiska reaktioner och det bildas nya mineralsällskap som är stabila vid rådande tryck och temperatur. Detta kallas metamorfos. Vi beräknade, genom termodynamisk modellering och utifrån bergarternas kemiska sammansättning, isokemiska fasdiagram som förutsäger vilka mineralsällskap som är stabila vid olika tryck och temperatur för just dessa bergartssammansättningar. Genom att jämföra med faktiska mineralsällskap, hur mineralen förekommer texturellt, samt mineralens kemiska sammansättning, kunde vi jämföra med fasdiagrammet och rekonstruera den progressiva metamorfa utvecklingen: bergartens tryck- och temperaturutveckling (P-T-utveckling). Med denna metod kunde vi visa att eklogiterna tryckts ned till 65 km djup och där värmts upp till nästan 900 °C. Vi kan också se att de lyftes upp till ~35 km djup vid 850 °C. Texturerna, mineralkemin och P-T-utvecklingen visar att nedpressning och upplyftning skedde under en geologiskt sett kort tidsrymd. Denna typ av eklogit och dessa P-T-förhållanden är karaktäristiska för kontinent-kontinent-kollision.

Test, med en helt annan metod, av den P-T-modell som togs fram i studie 2. En del mineral tar upp ökande halter av spårelement vid ökad temperatur. Genom att mäta halterna av zirkonium i rutil och titan i kvarts kan vi "ta temperaturen" på bildningen av dessa mineral i olika texturella positioner i bergarterna. Studien visade på samstämmighet med den P-T-modell som framtogs i studie 2.

REFERENCES

Alsop, G. I. (2009). Unravelling patterns of folding in high-strain zones. Trabajos de geología, 29(29).

Alsop, G. I., & Holdsworth, R. E. (2004). The geometry and topology of natural sheath folds: a new tool for structural analysis. Journal of Structural Geology, 26(9), 1561-1589.

Alsop, G. I., & Holdsworth, R. E. (2007). Flow perturbation folding in shear zones. Geological Society, London, Special Publications, 272(1), 75-101.

Andersson, J., Söderlund, U., Cornell, D., Johansson, L., & Möller, C. (1999). Sveconorwegian (-Grenvillian) deformation, metamorphism and leucosome formation in SW Sweden, SW Baltic Shield: constraints from a Mesoproterozoic granite intrusion. Precambrian Research, 98(1), 151-171.

Andersson, J., Möller, C.A., Johansson, L. (2002). Zircon geochronology of migmatite gneisses along the Mylonite Zone (S Sweden): a major Sveconorwegian terrane boundary in the Baltic Shield. Precambrian Research. 114, 121–147.

Ashley, K. T., Webb, L. E., Spear, F. S., & Thomas, J. B. (2013). P-T-D histories from quartz: A case study of the application of the Ti-in-quartz thermobarometer to progressive fabric development in metapelites. Geochemistry, Geophysics, Geosystems, 14(9), 3821-3843.

Ashley, K. T., Caddick, M. J., Steele-MacInnis, M. J., Bodnar, R. J., & Dragovic, B. (2014a). Geothermobarometric history of subduction recorded by quartz inclusions in garnet. Geochemistry, Geophysics, Geosystems, 15(2), 350-360.

Ashley, K. T., Steele-MacInnis, M., & Caddick, M. J. (2014b). QuIB Calc: A MATLAB® script for geobarometry based on Raman spectroscopy and elastic modeling of quartz inclusions in garnet. Computers & Geosciences, 66, 155-157.

Austin Hegardt, E., Cornell, D.H., Claesson, L., Simakov, S., Stein, H.J., Hannah, J.L. (2005). Eclogites in the central part of the Sveconorwegian, Eastern Segment of the Baltic Shield: support for an extensive eclogite terrane. Geologiska Föreningens i Stockholm Förhandlingar. GFF 127, 221–232.

Baldwin, J. A., & Brown, M. (2008). Age and duration of ultrahigh-temperature metamorphism in the Anápolis–Itauçu Complex, Southern Brasília Belt, central Brazil–constraints from U–Pb geochronology, mineral rare earth element chemistry and trace-element thermometry. Journal of Metamorphic Geology, 26(2), 213-233.

Beaumont, C., Jamieson, R. A., Nguyen, M. H., & Medvedev, S. (2004). Crustal channel flows: 1. Numerical models with applications to the tectonics of the Himalayan-Tibetan orogen. Journal of Geophysical Research: Solid Earth, 109(B6).

Becke, F. (1903). Über Mineralbestand und Struktur der kristallinischen Schiefer. Denkschriften der k. Akademie der Wissenschaften, Mathematisch-Naturwissen-schaftliche Klasse, LXXV, p. 1-53 [Résumé en allemand in Congrès géologique international. Compte rendu de la IXe session, Vienne 1903, p. 553-570].

Bingen, B. (1989). Geochemistry of Sveconorwegian augen gneisses from SW Norway at the amphibolite-granulite facies transition. Norsk geologisk tidsskrift, 69, 177-189

Bingen, B., & van Breemen, O. (1998). U-Pb monazite ages in amphibolite-to granulite-facies orthogneiss reflect hydrous mineral breakdown reactions: Sveconorwegian Province of SW Norway. Contributions to Mineralogy and Petrology, 132(4), 336-353.

Bingen, B. & Solli, A. (2009). Geochronology of magmatism in the Caledonian and Sveconorwegian belts of Baltica: synopsis for detrital zircon provenance studies. Norwegian Journal of Geology, 89 (4).

Bingen, B., Skår, Ø., Marker, M., Sigmond, E. M., Nordgulen, Ø., Ragnhildstveit, J., Mansfeld, J., Tucker, R. D. & Liégeois, J. P. (2005). Timing of continental building in the Sveconorwegian orogen, SW Scandinavia. Norwegian Journal of Geology, 85(1-2), 87-116.

Bingen, B., Nordgulen, Ø., Viola, G. (2008a). A four-phase model for the Sveconorwegian orogeny, SW Scandinavia. Norwegian Journal of Geology 88, 43–72.

Bingen, B., Davis, W.J., Hamilton, M.A., Engvik, A., Stein, H.J., Skår, Ø. & Nordgulen, Ø. (2008b). Geochronology of high-grade metamorphism in the Sveconorwegian belt, S Norway: U-Pb, Th-Pb and Re-Os data. Norwegian Journal of Geology, 88, 13–42.

Bird, P. (1984). Laramide crustal thickening event in the Rocky Mountain foreland and Great Plains. Tectonics, 3(7), 741-758.

Brewer, T. S., Storey, C. D., Parrish, R. R., Temperley, S., & Windley, B. F. (2003). Grenvillian age decompression of eclogites in the Glenelg–Attadale Inlier, NW Scotland. Journal of the Geological Society, 160(4), 565-574.

Brown, M. (2014). The contribution of metamorphic petrology to understanding lithosphere evolution

and geodynamics. Geoscience Frontiers, 5(4), 553-569.

Cawood, P. A., Kröner, A., Collins, W. J., Kusky, T. M., Mooney, W. D., & Windley, B. F. (2009). Accretionary orogens through Earth history. Geological Society, London, Special Publications, 318(1), 1-36.

Cobbold, P.R., Quinquis, H., 1980. Development of sheath folds in shear regimes. Journal of Structural Geology, 119–126.

Coleman, R. G., Lee, D. E., Beatty, L. B., & Brannock, W. W. (1965). Eclogites and eclogites: their differences and similarities. Geological Society of America Bulletin, 76(5), 483-508.

Condie, K. C. (2015). Earth as an evolving planetary system. Academic Press.

Desmons, J., & Smulikowski, W. (2004). A systematic nomenclature for metamorphic rocks: 4. High P–T metamorphic rocks. Recommendations by the IUGS subcommission on the systematics of metamorphic rocks. Web version of, 1(1), 2004.

Dewey, J. F., & Bird, J. M. (1970). Mountain belts and the new global tectonics. Journal of Geophysical Research, 75(14), 2625-2647.

De Paoli, M. C., Clarke, G. L., Klepeis, K. A., Allibone, A. H., & Turnbull, I. M. (2009). The eclogite–granulite transition: mafic and intermediate assemblages at Breaksea Sound, New Zealand. Journal of Petrology, 50(12), 2307-2343.

Enami, M., Nishiyama, T., & Mouri, T. (2007). Laser Raman microspectrometry of metamorphic quartz: A simple method for comparison of metamorphic pressures. American Mineralogist, 92(8-9), 1303-1315.

Engvik, A. K., Bingen, B., & Solli, A. 2016. Localized occurrences of granulite: P–T modeling, U–Pb geochronology and distribution of early-Sveconorwegian high-grade metamorphism in Bamble, South Norway. Lithos, 240, 84-103.

Eskola, P. (1915). Om sambandet mellan kemisk och mineralogisk sammansättring hos Orijärvitraktens metamorfa bergarter. Bulletin de la Commission géologique de Finlande, 8, (44), 145 p.

Eskola, P. (1920). The mineral facies of rocks. Norsk Geologisk Tidsskrift, VI, p. 143-194.

Evans, T. P. (2004). A method for calculating effective bulk composition modification due to crystal fractionation in garnet-bearing schist: implications for isopleth thermobarometry. Journal of Metamorphic Geology, 22(6), 547-557.

Ewing, T. A., Hermann, J., & Rubatto, D. (2013). The robustness of the Zr-in-rutile and Ti-in-zircon thermometers during high-temperature metamorphism (Ivrea-Verbano Zone, northern Italy). Contributions to Mineralogy and Petrology, 165(4), 757-779.

Ferry, J. M., & Watson, E. B. (2007). New thermodynamic models and revised calibrations for the Ti-in-zircon and Zr-in-rutile thermometers. Contributions to Mineralogy and Petrology, 154(4), 429-437.

Fossen, H. (2010). Structural geology. Cambridge University Press.

Guiraud, M., & Powell, R. (2006). P–V–T relationships and mineral equilibria in inclusions in minerals. Earth and Planetary Science Letters, 244(3), 683-694.

Hansen, E., Johansson, L., Andersson, J., LaBarge, L., Harlov, D., Möller, C., & Vincent, S. (2015). Partial melting in amphibolites in a deep section of the Sveconorwegian Orogen, SW Sweden. Lithos, 236, 27-45.

Harley, S. L. (1989). The origins of granulites: a metamorphic perspective. Geological Magazine, 126(03), 215-247.

Harley, S. L., Kelly, N. M., & Möller, A. (2007). Zircon behaviour and the thermal histories of mountain chains. Elements, 3(1), 25-30.

Haüy, R.-J. (1822). Traité de minéralogie. Seconde édition, revue, corrigée et considérablement augmentée par l'auteur. Bachelier et Huzard, Paris, 4 vol. in-8° + atlas [t. II, p. 456 ; t. IV, p. 548].

Holland, T. J. B. & Powell, R. (2011). An improved and extended internally consistent thermodynamic dataset for phases of petrological interest, involving a new equation of state for solids. Journal of Metamorphic Geology, 29, 333–383.

Indares, A. D. (2003). Metamorphic textures and P–T evolution of high-P granulites from the Lelukuau terrane, NE Grenville Province. Journal of metamorphic Geology, 21(1), 35-48.

Indares, A., & Dunning, G. (1997). Coronitic metagabbro and eclogite from the Grenville Province of western Quebec: interpretation of U-Pb geochronology and metamorphism. Canadian Journal of Earth Sciences, 34(7), 891-901.

Jamieson, R. A., Beaumont, C., Medvedev, S., & Nguyen, M. H. (2004). Crustal channel flows: 2. Numerical models with implications for metamorphism in the Himalayan-Tibetan orogen. Journal of Geophysical Research: Solid Earth, 109(B6).

Jiao, S., Guo, J., Mao, Q., & Zhao, R. (2011). Application of Zr-in-rutile thermometry: a case study from ultrahigh-temperature granulites

of the Khondalite belt, North China Craton. Contributions to Mineralogy and Petrology, 162(2), 379-393.

Johansson, L., & Kullerud, L. (1993). Late Sveconorwegian metamorphism and deformation in southwestern Sweden. Precambrian Research, 64, 347-360.

Johansson, L., Lindh, A., & Möller, C. (1991). Late Sveconorwegian (Grenville) high-pressure granulite facies metamorphism in southwest Sweden. Journal of Metamorphic Geology, 9, 283-292.

Johansson, L., Möller, C. & Söderlund, U. (2001). Geochronology of eclogite facies metamorphism in the Sveconorwegian Province of SW Sweden. Precambrian Research, 106, 261-275.

Kohn, M. J. (2014a). Himalayan metamorphism and its tectonic implications. Annual Review of Earth and Planetary Sciences, 42, 381-419.

Kohn, M. J. (2014b). "Thermoba-Raman-try": Calibration of spectroscopic barometers and thermometers for mineral inclusions. Earth and Planetary Science Letters, 388, 187-196.

Kooijman, E., Smit, M. A., Mezger, K., & Berndt, J. (2012). Trace element systematics in granulite facies rutile: implications for Zr geothermometry and provenance studies. Journal of Metamorphic Geology, 30(4), 397-412.

Korhonen, F. J., Clark, C., Brown, M., & Taylor, R. J. M. (2014). Taking the temperature of Earth's hottest crust. Earth and Planetary Science Letters, 408, 341-354.

Leeman, W. P., MacRae, C. M., Wilson, N. C., Torpy, A., Lee, C. T. A., Student, J. J., ... & Vicenzi, E. P. (2012). A study of cathodoluminescence and trace element compositional zoning in natural quartz from volcanic rocks: Mapping titanium content in quartz. Microscopy and Microanalysis, 18(06), 1322-1341.

Liu, Y. C., Deng, L. P., Gu, X. F., Groppo, C., & Rolfo, F. (2015). Application of Ti-in-zircon and Zr-in-rutile thermometers to constrain high-temperature metamorphism in eclogites from the Dabie orogen, central China. Gondwana Research, 27(1), 410-423.

Luvizotto, G. L., & Zack, T. (2009). Nb and Zr behavior in rutile during high-grade metamorphism and retrogression: an example from the Ivrea–Verbano Zone. Chemical Geology, 261(3), 303-317.

Mancktelow, N. S., & Pennacchioni, G. (2005). The control of precursor brittle fracture and fluid–rock interaction on the development of single and paired ductile shear zones. Journal of Structural Geology, 27(4), 645-661.

Marmo, B. A., Clarke, G. L., & Powell, R. (2002). Fractionation of bulk rock composition due to porphyroblast growth: effects on eclogite facies mineral equilibria, Pam Peninsula, New Caledonia. Journal of metamorphic Geology, 20(1), 151-165.

Marques, F. G., & Cobbold, P. R. (1995). Development of highly non-cylindrical folds around rigid ellipsoidal inclusions in bulk simple shear regimes: natural examples and experimental modelling. Journal of Structural Geology, 17(4), 589-602.

Menegon, L., P. Nasipuri, H. Stünitz, H. Behrens, and E. Ravna (2011), Dry and strong quartz during deformation of the lower crust in the presence of melt, Journal of Geophysical Research.

Mosher, S., Levine, J. S. F., & Carlson, W. D. (2008). Mesoproterozoic plate tectonics: A collisional model for the Grenville-aged orogenic belt in the Llano uplift, central Texas. Geology, 36(1), 55-58.

Möller, C. (1998). Decompressed eclogites in the Sveconorwegian (–Grenvillian) orogen of SW Sweden: petrology and tectonic implications. Journal of Metamorphic Geology. 16, 641 656.

Möller, C. (1999). Sapphirine in SW Sweden: a record of Sveconorwegian (–Grenvillian) late-orogenic tectonic exhumation. Journal of Metamorphic Geology. 17, 127–141.

Möller, C., Andersson, J., Söderlund, U., & Johansson, L. (1997). A Sveconorwegian deformation zone (system?) within the Eastern Segment, Sveconorwegian orogen of SW Sweden-a first report.

Möller, C., Andersson, J., Lundqvist, I., Hellström, F.A. (2007). Linking deformation, migmatite formation and zircon U–Pb geochronology in poly-metamorphic orthogneisses, Sveconorwegian Province, Sweden. Journal of Metamorphic Geology. 25, 727–775.

Möller, C., Andersson, J., Dyck, B. & Antal Lundin, I. (2015a). Exhumation of an eclogite terrane as a hot migmatitic nappe, Sveconorwegian orogen. Hirajama, T., Medaris, G. (Eds.), High- and ultrahigh-pressure metamorphism, from microscopic to orogenic scale. Lithos (Special Issue). Lithos, 226, 147–168.

Möller, C., Andersson, J. & Rebay, G. (2015b). Very-high temperature metamorphism and deformation in the footwall of an eclogite-bearing nappe, Sveconorwegian orogen: Meta-leuconoritic and sapphirine-bearing rocks of the Obbhult complex, SW Sweden. Abstract, AGU meeting, Montreal, 3-7 May 2015.

O'brien, P. J., & Rötzler, J. (2003). High-pressure

granulites: formation, recovery of peak conditions and implications for tectonics. Journal of Metamorphic Geology, 21(1), 3-20.

Ogasawara, Y., Fukasawa, K., & Maruyama, S. (2002). Coesite exsolution from supersilicic titanite in UHP marble from the Kokchetav Massif, northern Kazakhstan. American Mineralogist, 87(4), 454-461.

Piñán-Llamas, A., Andersson, J., Möller, C. (2015). Polyphasal foreland-vergent deformation in a deep section of the 1 Ga Sveconorwegian orogen, in: Roberts, N., Viola, G., Slagstad, T. (Eds.), The structural, metamorphic and magmatic evolution of Mesoproterozoic orogens. Special issue of Precambrian Research.

Powell, R. (1978). Equilibrium thermodynamics in petrology: an introduction (p. 295). London: Harper & Row.

Powell, R., Holland, T. J. B. H. & Worley, B. (1998). Calculating phase diagrams involving solid solutions via non-linear equations, with examples using THERMOCALC. Journal of metamorphic Geology, 16, 577-588.

Reber, J. E., Dabrowski, M., Schmid, D. W. (2012). Sheath fold formation around slip surfaces. Terra Nova. 24(5), 417-421, doi:10.1111/j.1365-3121.2012.01081.x.

Reber, J. E., Galland, O., Cobbold, P. R., Le Carlier de Veslud, C. (2013). Experimental study of sheath fold development around a weak inclusion in a mechanically layered matrix. Tectonophysics, 586, 130-144.

Roberts, N. M., & Slagstad, T. (2014). Continental growth and reworking on the edge of the Columbia and Rodinia supercontinents; 1.86–0.9 Ga accretionary orogeny in southwest Fennoscandia. International Geology Review, 1-25.

Rosas, F., Marques, F.O., Luz, A. and Coelho, S. (2002). Sheath folds formed by drag induced by rotation of rigid inclusions in viscous simple shear flow: nature and experiment. Journal of Structural Geology. 24, 45–55.

Rubatto, D. (2002). Zircon trace element geochemistry: partitioning with garnet and the link between U–Pb ages and metamorphism. Chemical Geology, 184(1), 123-138.

Rubatto, D., & Hermann, J. (2007). Zircon behaviour in deeply subducted rocks. Elements, 3(1), 31-35.

Saussure, H.-B. de (1779-96). Voyages dans les Alpes, précédés d'un essai sur l'histoire naturelle des environs de Genève. S. Fauche, Neuchâtel, 4 vol.

Schmidt, C., & Ziemann, M. A. (2000). In-situ Raman spectroscopy of quartz: A pressure sensor for hydrothermal diamond-anvil cell experiments at elevated temperatures. American Mineralogist, 85(11-12), 1725-1734.

Schulmann, K., Lexa, O., Štípská, P., Racek, M., Tajčmanová, L., Konopásek, J., ... & Lehmann, J. (2008). Vertical extrusion and horizontal channel flow of orogenic lower crust: key exhumation mechanisms in large hot orogens?. Journal of Metamorphic Geology, 26(2), 273-297.

Searle, M. P., Khan, M. A., Fraser, J. E., Gough, S. J., & Jan, M. Q. (1999). The tectonic evolution of the Kohistan-Karakoram collision belt along the Karakoram Highway transect, north Pakistan. Tectonics, 18(6), 929-949.

Sizova, E., Gerya, T., & Brown, M. (2014). Contrasting styles of Phanerozoic and Precambrian continental collision. Gondwana Research, 25(2), 522-545.

Slagstad, T., Roberts, N. M., Marker, M., Røhr, T. S. & Schiellerup, H. (2012). A non-collisional, accretionary Sveconorwegian orogen. Terra Nova, 25(1), 30-37.

Spear, F. S., 1993 Metamorphic phase equilibria and pressure-temperature-time paths. Mineralogical Society of America, Washington, 799 pp.

Spear, F. S., & Wark, D. A. (2009). Cathodoluminescence imaging and titanium thermometry in metamorphic quartz. Journal of Metamorphic Geology, 27(3), 187-205.

Storey, C. D., Brewer, T. S., & Temperley, S. (2005). P–T conditions of Grenville-age eclogite facies metamorphism and amphibolite facies retrogression of the Glenelg–Attadale Inlier, NW Scotland. Geological Magazine, 142(05), 605-615.

Štípská, P., Powell, R., & Racek, M. (2014). Rare eclogite-mafic granulite in felsic granulite in Blanský les: precursor of intermediate granulite in the Bohemian Massif?. Journal of Metamorphic Geology, 32(4), 325-345.

Stüwe, K. (1997). Effective bulk composition changes due to cooling: a model predicting complexities in retrograde reaction textures. Contributions to Mineralogy and Petrology, 129(1), 43-52.

Söderlund, U., Möller, C., Andersson, J., Johansson, L., Whitehouse, M.J. (2002). Zircon geochronology in polymetamorphic gneisses in the Sveconorwgian orogen, SW Sweden: ion microprobe evidence for 1.46-1.42 Ga and 0.98-0.96 Ga reworking. Precambrian Research 113, 193-225.

Söderlund, U., Hellström, F. A. & Kamo, S. L. (2008). Geochronology of high-pressure mafic granulite dykes in SW Sweden: tracking the P–T–t path of metamorphism using Hf isotopes in zircon and

baddeleyite. Journal of Metamorphic Geology, 26(5), 539-560.

Thomas, J. B., Watson, E. B., Spear, F. S., Shemella, P. T., Nayak, S. K., & Lanzirotti, A. (2010). Ti-in-quartz under pressure: the effect of pressure and temperature on the solubility of Ti-in-quartz. Contributions to Mineralogy and Petrology, 160(5), 743-759.

Tomkins, H. S., Powell, R., & Ellis, D. J. (2007). The pressure dependence of the zirconium-in-rutile thermometer. Journal of Metamorphic Geology, 25(6), 703-713.

Tual, L., Piñán-Llamas, A. & Möller, C. (2015). High-Temperature Deformation in the Basal Shear Zone of an Eclogite-Bearing Fold Nappe, Sveconorwegian Orogen, Sweden, in: Roberts, N., Viola, G., Slagstad, T. (Eds.), The structural, metamorphic and magmatic evolution of Mesoproterozoic orogens. Precambrian Research, 265, 104-120.

Turner, F. J. (1981). Metamorphic petrology: Mineralogical, field, and tectonic aspects. McGraw-Hill Companies.

Vander Auwera, J., Bolle, O., Bingen, B., Liégeois, J. P., Bogaerts, M., Duchesne, J. C. & Longhi, J. (2011). Sveconorwegian massif-type anorthosites and related granitoids result from post-collisional melting of a continental arc root. Earth-Science Reviews, 107(3), 375-397.

Walsh, A. K., Hand, M., & Kelsey, D. E. (2015). A metamorphic perspective on foreland flexure during intraplate orogeny: evidence for the involvement of weak lithosphere. Terra Nova, 27(5), 329-337.

Wang X.D., & Lindh, A. (1996). Temperature-pressure Investigation of the Southern Part of the Southwest Swedish Granulite Region. European Journal of Mineralogy, 51-68.

Wark, D. A., & Watson, E. B. (2006). TitaniQ: a titanium-in-quartz geothermometer. Contributions to Mineralogy and Petrology, 152(6), 743-754.

Watson, E. B., Wark, D. A., & Thomas, J. B. (2006). Crystallization thermometers for zircon and rutile. Contributions to Mineralogy and Petrology, 151(4), 413-433.

Weinberg, R. F., & Mark, G. (2008). Magma migration, folding, and disaggregation of migmatites in the Karakoram Shear Zone, Ladakh, NW India. Geological Society of America Bulletin, 120(7-8), 994-1009.

Xypolias, P., & Alsop, G. I. (2014). Regional flow perturbation folding within an exhumation channel: A case study from the Cycladic Blueschists. Journal of Structural Geology, 62, 141-155.

Zack, T., Moraes, R., & Kronz, A. (2004). Temperature dependence of Zr-in-rutile: empirical calibration of a rutile thermometer. Contributions to Mineralogy and Petrology, 148(4), 471-488.

Zhang, Y. (1998). Mechanical and phase equilibria in inclusion–host systems. Earth and Planetary Science Letters, 157(3), 209-222.

Zhang, R. Y., Iizuka, Y., Ernst, W. G., Liou, J. G., XU, Z. Q., Tsujimori, T., ... & Jahn, B. M. (2009). Metamorphic P–T conditions and thermal structure of Chinese Continental Scientific Drilling main hole eclogites: Fe–Mg partitioning thermometer vs. Zr-in-rutile thermometer. Journal of Metamorphic Geology, 27(9), 757-772.

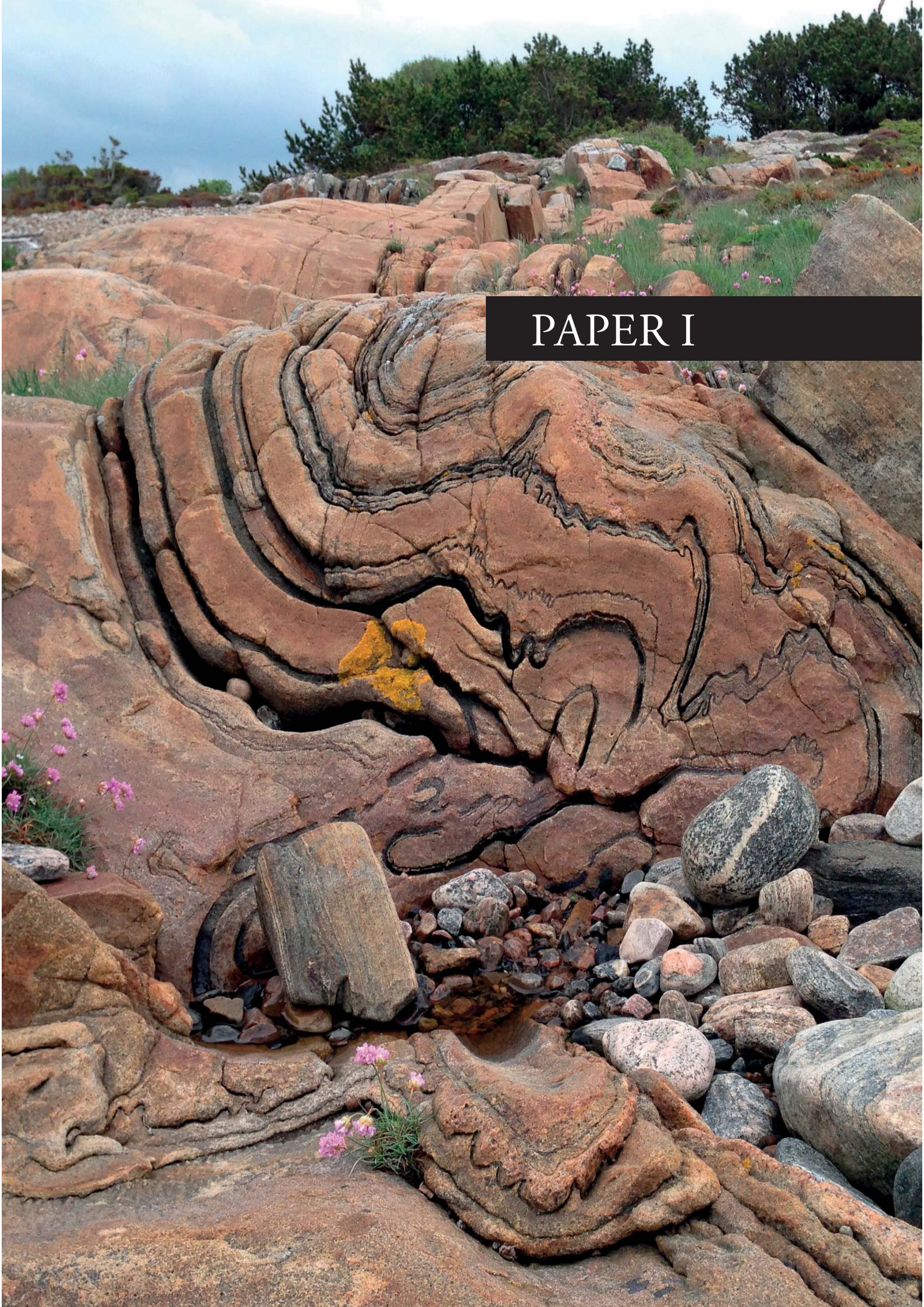

PAPER I

Precambrian Research 265 (2015) 104–120

Contents lists available at ScienceDirect

Precambrian Research

journal homepage: www.elsevier.com/locate/precamres

High-temperature deformation in the basal shear zone of an eclogite-bearing fold nappe, Sveconorwegian orogen, Sweden

Lorraine Tual [a,*], Aránzazu Piñán-Llamas [b], Charlotte Möller [a]

[a] Department of Geology, Lund University, Sölvegatan 12, SE-223 62 Lund, Sweden
[b] Department of Geosciences, IPFW University, 2101 E. Coliseum Blvd, Fort Wayne, IN 46805, USA

ARTICLE INFO

Article history:
Received 2 September 2014
Received in revised form 20 February 2015
Accepted 6 May 2015
Available online 27 May 2015

Keywords:
Sveconorwegian orogen
Basal shear zone
Transport-parallel fold
Melt-enhanced deformation
Eclogite

ABSTRACT

Ductile shear zones associated with emplacement of high-pressure nappes are key features to resolve exhumation mechanisms. The Eastern Segment of the Sveconorwegian orogen hosts an eclogite-bearing fold nappe, whose basal shear zone shows structures associated with emplacement of the eclogite-bearing nappe and decompression under high to intermediate pressure granulite and upper amphibolite facies conditions. Based on detailed structural mapping of a 4 km well-exposed section of the basal shear zone, we describe two major phases of deformation. An early deformation stage (D1) formed a penetrative gneissic foliation and tectonic layering, including isoclinal folds (F1). The sequence was subsequently affected by up to km-scale tight south-vergent folds (F2) with sheared out limbs. At the outcrop scale, asymmetric F2 folds are commonly S-vergent, but symmetric folds with different degrees of tightness are also present. Melt was present at all stages of deformation and the structural relations demonstrate mutual feedback between melt localization and fold formation. F2 folds have shallowly E-plunging fold axis parallel to a stretching lineation defined by high-grade mineral aggregates. Both constitute prominent structures of the basal shear zone. F2-folds are associated with an axial planar fabric (S2), defined by upper-amphibolite- and locally granulite-facies mineral assemblages. D2 shear structures are associated with top-to-the-east kinematic indicators throughout the section. The D1 episode was responsible for emplacement of the eclogite-nappe into its present structural position. The subsequently developed lineation-parallel folds are interpreted to form by general shear, where the structures reflect the regional E-directed flow of the entire eclogite-nappe.

1. Introduction

Largely eroded Precambrian orogens provide exceptional opportunities to understand the records and evidence of exhumation mechanisms that take place at high-temperature conditions in the deepest sections of the crust. In SW Sweden, eclogites have been tectonically emplaced during the Sveconorwegian orogeny, a collisional event that occurred at the end of the Mesoproterozoic and the beginning of the Neoproterozoic. These eclogites, which record evidences of deep burial and rapid exhumation during the last stages of the orogeny (990–970 Ma; e.g. Möller, 1998, 1999; Austin Hegardt et al., 2005; Möller et al., 2015), were exhumed as a partially molten low-viscosity nappe in the Eastern Segment of the Sveconorwegian orogen (Möller et al., 2015). The up to 4 km wide basal shear zone of this fold nappe is a strategic place to study the tectonic emplacement and deformation mechanisms during exhumation of the eclogite-bearing nappe.

In this paper we present new structural, microstructural, kinematic and petrographic data and describe the sequence of deformation events preserved in the basal shear zone of the eclogite nappe. We show the first systematic structural and kinematic study of a section across the basal shear zone and propose a mechanism for the origin of folding. The main exhumation phases, coined as D1 and D2, resulted in the formation of lineation-parallel folds and intense shearing, with an overall top-to-the-east sense of shear. We also demonstrate that the interplay between folding, shearing and melt played an important role during the exhumation process. Based on our data we propose a flow-perturbation model (e.g. Alsop and Holdsworth, 2004) for the exhumation of the eclogite-bearing units. This model implies that the lineation in the basal shear zone reflects the direction of the flow during the nappe's exhumation rather than the direct stress direction.

* Corresponding author. Tel.: +46 729373025.
E-mail addresses: lorraine.tual@geol.lu.se, lorraine.tual@gmail.com (L. Tual).

http://dx.doi.org/10.1016/j.precamres.2015.05.007
0301-9268/

2. Geological setting

The Sveconorwegian orogen consists of different crustal segments separated by roughly N-S trending shear zones: the Telemarkia, Bamble, Kongsberg and Idefjorden terranes in the west and the Eastern Segment in the east (Fig. 1). These terranes were tectonically juxtaposed during the Sveconorwegian orogeny at 1.1–0.9 Ga (Bingen et al., 2008). The Eastern Segment constitutes the reworked margin of Baltica, which experienced ductile deformation and partial melting during the late part of the Sveconorwegian orogeny, at ca. 0.99–0.92 Ga (Söderlund et al., 1999, 2002; Andersson et al., 2002; Möller et al., 2007). The Eastern Segment mainly consists of orthogneisses with protolith ages (1.74–1.66 Ga) and geochemistry similar to igneous rocks east of the Sveconorwegian Front (Transscandinavian Igneous Belt; Connelly et al., 1996; Söderlund et al., 1999, 2002; Petersson et al., 2013).

The Eastern Segment underwent metamorphism and migmatization during a pre-Sveconorwegian tectonometamorphic event, the Hallandian orogeny (1.47–1.38 Ga, Möller et al., 2007; Brander et al., 2012; Ulmius et al., this volume). Dykes and granitic plutons intruded during the Hallandian orogeny (Hubbard, 1975; Åhäll et al., 1997; Christoffel et al., 1999; Andersson et al., 1999; Brander et al., 2012; Ulmius et al., this volume). The youngest Hallandian intrusions (1.41–1.38 Ga) are important structural and metamorphic markers because they record the Sveconorwegian orogenic effects only.

The Eastern Segment is separated from the Idefjorden Terrane to the west by a major tectonic boundary: the several kilometer-wide west-dipping Mylonite Zone (Fig. 1). The Idefjorden and Eastern Segment have different protolith ages and different structural and metamorphic signatures (Andersson et al., 2002; Bingen et al., 2008). Structural investigations along the Mylonite Zone show complex multiphased evolution including top-to-the-east and top-to-the-west movements (Stephens et al., 1996; Berglund, 1997; Viola et al., 2011). Following the interpretation of Andréasson and Rodhe (1990), Viola et al. (2011) proposed the Eastern Segment to be an immature core complex exhumed in a general extensional regime. Eclogite occurences in the Eastern Segment (Möller, 1998, 1999; Johansson et al., 2001) are structurally bound within a 50 km recumbent fold nappe (Fig. 2a) and extrusion is suggested as the main mechanism for their emplacement (Möller et al., 2015). U–Pb SIMS dating of zircon in eclogite constrains the eclogite metamorphism at 990–980 Ma (Möller et al., 2015). The tectonostratigraphy is composed of distinctive units: (a) the eclogite-bearing unit in the core, with stromatic orthogneisses (b) a distinctive heterogeneously deformed 1.4 Ga augen gneiss, which is a tectonostratigraphic marker, outlining the megafold (colored in black in Fig. 2), and (c) an eclogite-free, orthogneisses unit that is enveloping the fold nappe (Möller et al., 2015; Fig. 2). (b) and (c) are hereinafter collectively referred to as enclosing orthogneisses.

The eclogite-bearing nappe has a basal shear zone, the southern part of what was previously coined as the Ullared Deformation Zone by Möller et al. (1997). The tectonostratigraphy has been traced from the coast eastwards along strike for ca. 50 km (Möller et al., 2015; Fig. 2). Deformation in the basal shear zone occurred at high to intermediate pressure granulite and upper amphibolite conditions, post-dating the eclogite facies metamorphism (Möller, 1998, 1999). Geochronology of syntectonic pegmatite suggests that this deformation occurred at ca. 970 Ma (Söderlund et al., 2002), contemporaneous with migmatization in other parts of the nappe (Möller et al., 2015). The tectonostratigraphy, including the eclogite nappe, has been folded into gentle antiforms and synforms trending roughly N-S (Fig. 2).

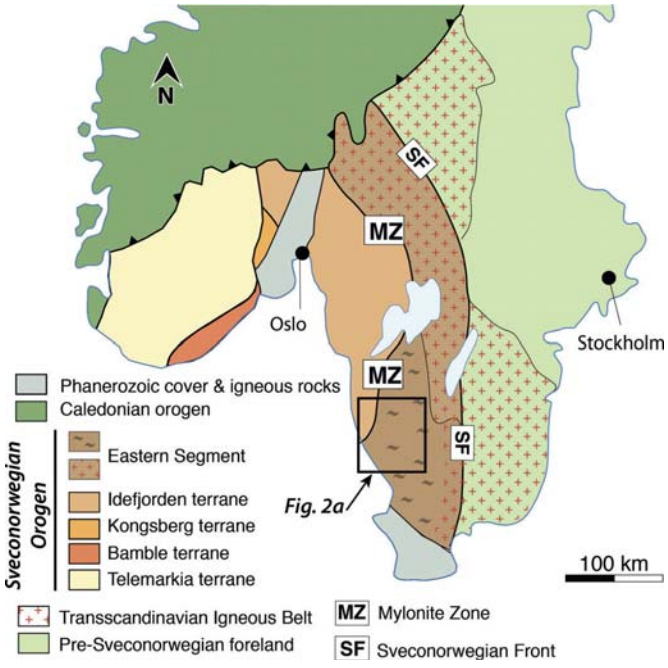

Fig. 1. Overview map of southern Scandinavia (Modified after Möller et al., 2007, Sveconorwegian orogen subdivisions after Bingen et al., 2008). Cross marks for the Transscandinavian Igneous Belt denote undeformed and non-penetratively deformed domains.

3. Section across the basal shear zone

In the following sections we describe the main lithological units present in the study area and the sequence of structures and fabrics observed along a ca. 6 km long profile through the basal shear zone and the underlying part of the enclosing orthogneisses (Figs. 2b and 3). Vertical N-S striking structural sections of the basal shear zone that are rarely accessible elsewhere are exposed along this profile. The cross-section in Fig. 3b was constructed perpendicular to the stretching lineation. Coordinates of key localities are given in Table 1.

3.1. Lithotectonic

Following the lithotectonic components in Möller et al. (2015) for the study area, mappable units from north to south are: (1) the eclogite nappe, inner part (2) eclogite nappe, basal shear zone, and (3) Eastern Segment orthogneiss (herein referred to as enclosing orthogneisses).

The precise contact between the eclogite nappe and the enclosing orthogneisses is not exposed in the studied section, but is located based on the presence of remnant eclogite assemblages in mafic boudins.

3.1.1. Eclogite nappe

The eclogite nappe is divided into a basal shear zone composed of heterogeneous mylonitic gneisses and an inner part dominated by stromatic migmatitic gneiss. Both units contain retroeclogite lenses, but kyanite-bearing varieties were so far been found only in the basal shear zone. The two main types of retroeclogite present in the study area are: (1) kyanite-bearing with local layers of kyanite-free, Fe-Ti-rich, quartz-bearing retroeclogites with higher amount of garnet and (2) a kyanite-free, quartz bearing eclogite. Both types of eclogite are dominated by dark red garnet and dull greenish gray clinopyroxene, and show a wide variation in grain size and degree

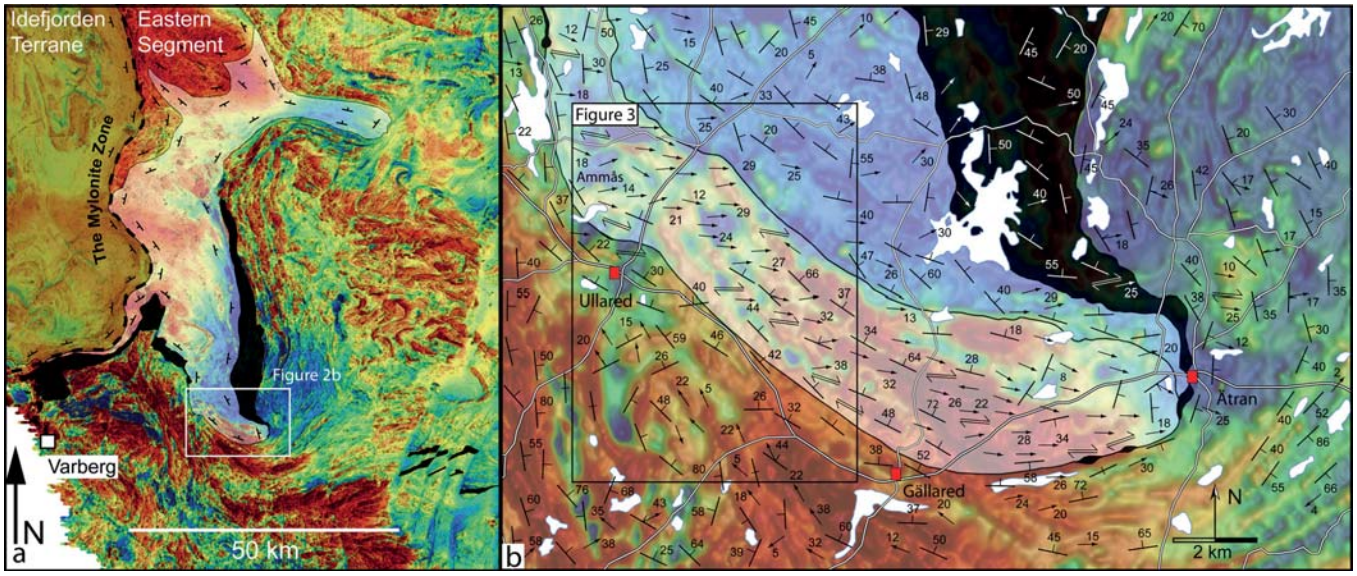

Fig. 2. Location and structure (map section) of the eclogite bearing fold nappe (from Möller et al., 2015). (a) Airborne magnetic anomaly map (total field; data source: Geological Survey of Sweden) illustrating the fold pattern of the Eastern Segment (area marked in Fig. 1). The eclogite-bearing domain is shaded white; augen gneiss (structural marker) is black. (b) Close-up of the basal shear zone. Background is magnetic anomaly map (total field). The inner part of the eclogite nappe is shaded light white, the basal shear zone denser white, 1.4 Ga augen gneiss is black, the enclosing orthogneisses are shaded beige. Symbols represent gneissic foliation/layering and stretching lineation, respectively. Frame marks the location of the section studied in this paper (Fig. 3).

Table 1
Geographic location of key localities.

Referred to in figures	Place name	SWEREF99TM N	SWEREF99TM E
Figs. 4b, c; 5c, f; 6c; 8b	Gläsbacka	6335050	0365360
Figs. 4a; 5a, b, d, e, g, h, i; 6a, g; 8a; 9	Tranabo	6335730	0365460
Fig. 6b and d	Buskabygd	6334230	0366275
	Spetsebo	6332745	0366670
Fig. 7	Skällstorp	6331810	0367255
Fig. 6f	Vräk S.	6337340	0364920
Fig. 6e	Ängaberg	6334690	0363170

of amphibolitization. Meter to cm-thick lenses of retroeclogite are intercalated with orthogneisses (e.g. Fig. 4a and b).

3.1.1.1. Basal shear zone of the eclogite nappe. Heterogeneous mylonitic gneisses dominate in the basal shear zone. They include: (1) gray granitic–intermediate orthogneiss (quartz- and feldspar-rich with variable proportions of amphibole, clinopyroxene, garnet and biotite), containing variable amounts of K-feldspar-rich leucosome, generally parallel to the foliation (2) gray orthogneiss with recrystallized K-feldspar augen and (3) pink leucocratic granitic gneiss with high contents of K-feldspar (4) dark gray orthogneiss grading to intermediate compositions (inferred quartz-monzodioritic).

Cm-thick leucosome is found in variable amounts and structural positions throughout the basal shear zone. These include pink varieties rich in K-feldspar and quartz, and white varieties rich in plagioclase and quartz. The latter is typically found in or at the margin of mafic bodies, and locally carries peritectic amphibole. Leucosome occurs in pre-, syn- or post-tectonic relations to the deformation.

3.1.1.2. Inner part of the eclogite nappe. Orthogneisses in the inner part of the eclogite nappe show a higher degree of partial melting than those in the basal shear zone. They are metatexitic and commonly stromatic. Leucosome is fine to coarse grained with a sugary, unstrained texture. Patch leucosome locally crosscuts layers and folds. The leucosome varies in color, from reddish (inferred granitic composition) in most orthogneisses, to white (inferred tonalitic) in most mafic rocks. Amphibolitization was more pervasive than in the basal shear zone, and in most rocks, including many mafic boudins, garnet grains show partial to complete replacement by hornblende. The inner part of the eclogite nappe corresponds to a low magnetic anomaly (Fig. 2).

The presence of local high strain zones and a local marker of sheared reddish-gray gneiss with recrystallized K-feldspar augen (cm-size) that can be followed for at least 3 km mark the limit between migmatized gneisses of the inner part of the eclogite nappe and the basal shear zone.

3.1.2. Enclosing orthogneisses

The enclosing orthogneisses consist of 1.7 Ga orthogneisses and undifferentiated metabasic rocks and is located structurally below the basal shear zone (Fig. 2b). Remnants of retrogressed eclogites are not present, and mafic rocks in this unit are garnet-rich mafic granulite and migmatitic garnet-amphibolite. Local occurrences of metadolerite and coarse-grained metagabbro have a remnant igneous texture with coronitic, very fine-grained garnet in plagioclase domains. These metadolerites show progressive transitions to fully recrystallized and migmatitic garnet amphibolite. The orthogneisses are gray to reddish migmatitic gneiss with abundant K-feldspar-rich granitic veins (0.5–10 cm in thickness), less-veined augen gneiss rich in recrystallized K-feldspar augen, hornblende-rich gray migmatitic gneiss, and reddish leucocratic granitic gneiss with sparse thin amphibolite layers (<10 cm wide).

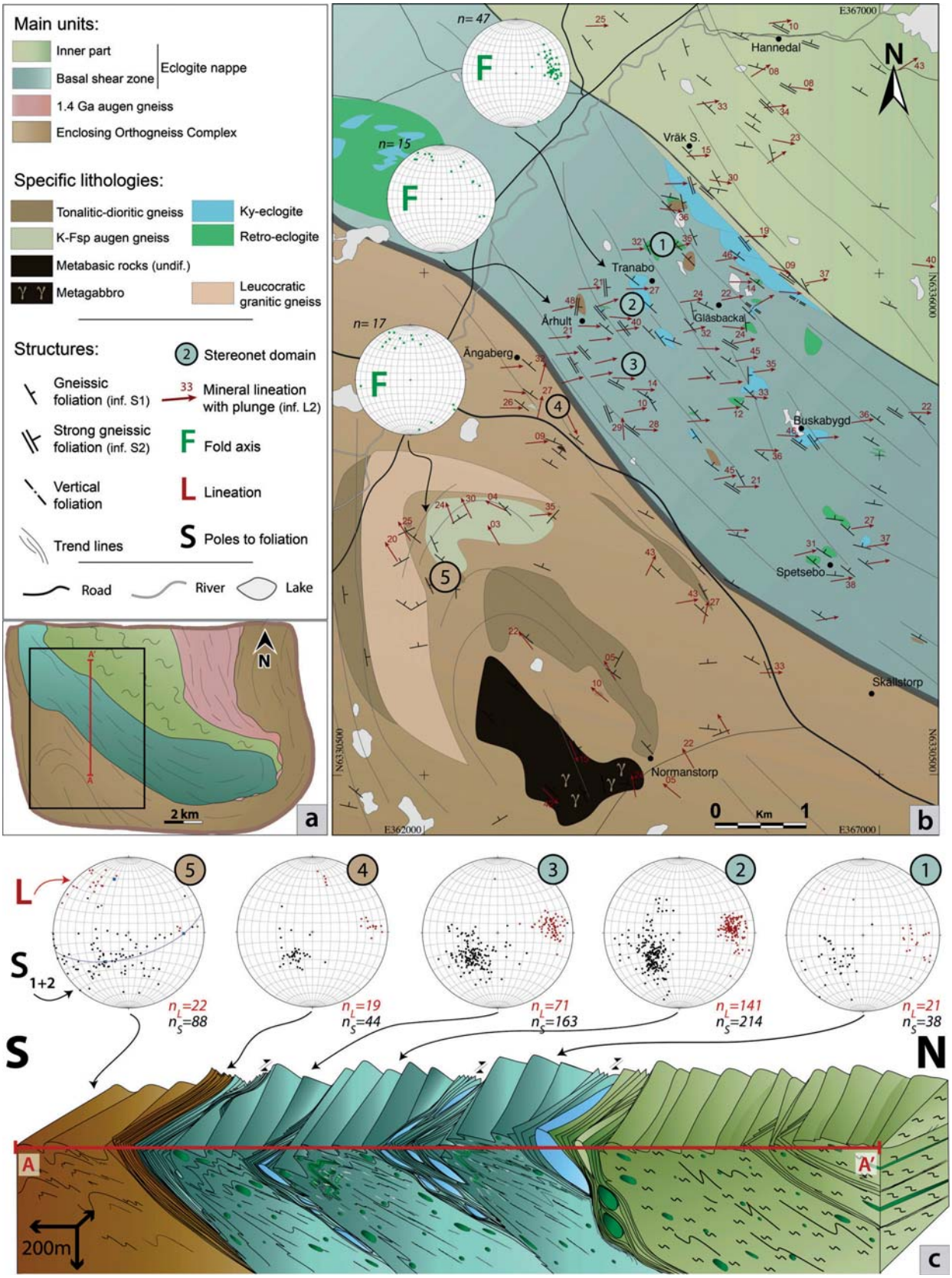

Fig. 3. Map and cross section of the study area. (a) Simplifed map showing the main structural unit. The frame and the red line mark the position of the structural map and the cross section (Fig. 3b and c, respectively). (b) Structural map. Stereograms indicate fold axes from three areas along the investigated profile. (c) Cross section interpreted from observations along the profile marked in (a), and oriented perpendicular to the folds and main transport direction. Stereograms along the profile show lineation (red dots) and poles to foliation (black dots). (For interpretation of the references to color in this figure legend, the reader is referred to the web version of this article.)

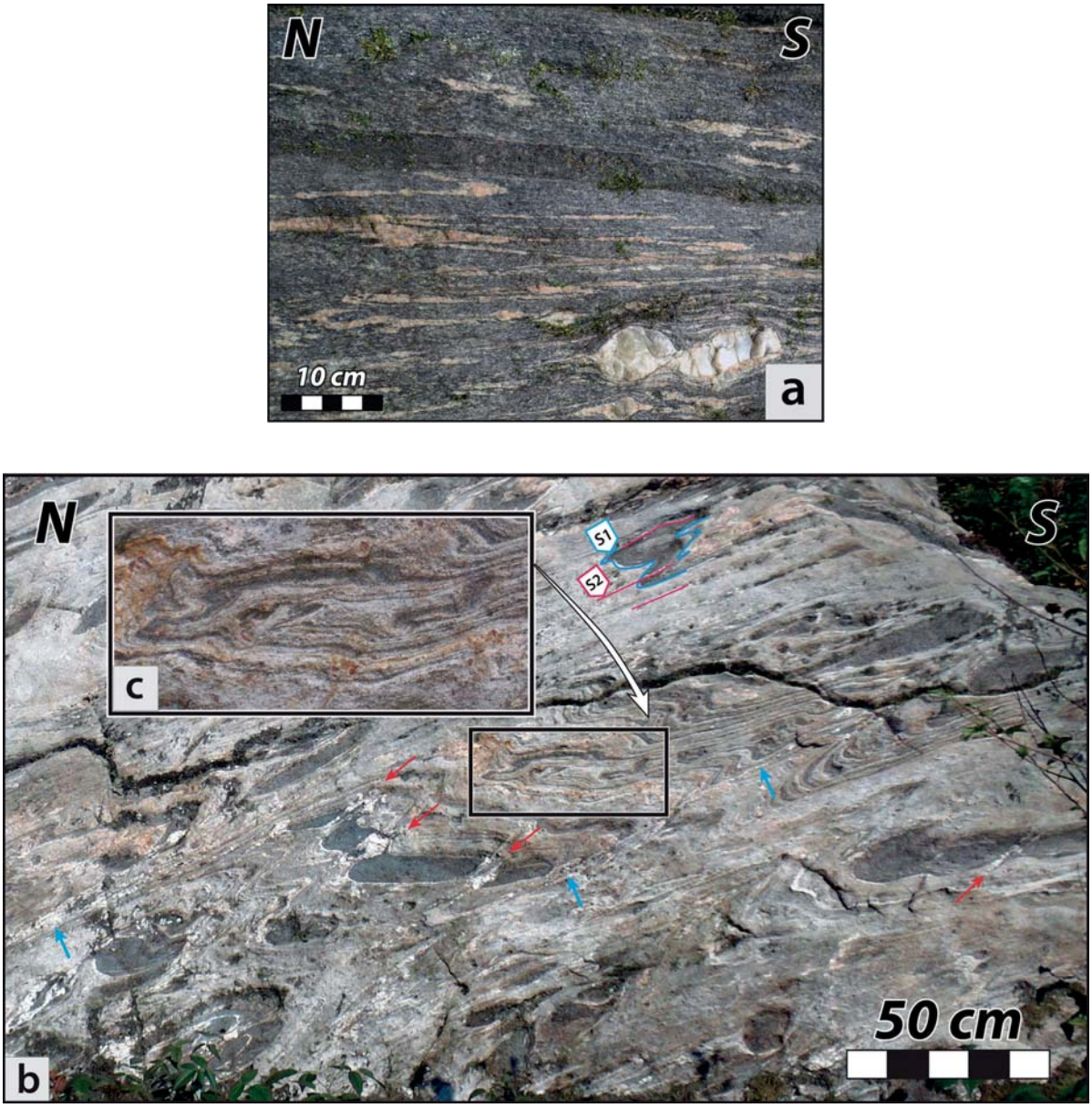

Fig. 4. D1 and D2 structures in the basal shear zone. (a) Isoclinal rootless folds developed during transposition of the gneissic layering (interpreted as F1) in mafic-intermediate gneiss. (b) Thinly-layered (S1) felsic-granitic gray gneiss enclosing lenses and boudins of retrogressed eclogite. F2 folds the gneissic layering (S1), producing a variety of geometries. Synkinematic leucosome (white) is abundant. Shear zones are sub-parallel to F2 axial planes and locally cut layers abruptly (blue arrows). Shear zones are associated with melt and F2 folds. Mafic lenses have been disrupted and have boudin necks filled with leucosome, but also behaved plastically and are folded together with the surrounding gneiss. Boudinage of the mafic lenses can be recognized in fold limbs and along F2 axial planes, associated with melt (red arrows). (c) Closed fold structure. The closing structure is either a consequence of re-folding a F1 structure or, alternatively, a sheath fold developed during D2. (For interpretation of the references to color in this figure legend, the reader is referred to the web version of this article.)

3.2. Structures

Below we describe structural features observed in the research area (Fig. 3). An interpretation of the structural architecture along a N-S cross section is presented in Fig. 3c. We have used fold interference patterns and crosscutting relationships to characterize the sequence of deformational events recorded in the study area. The rocks are affected by at least four deformation events (D1–D4). These events may have been continuous or discontinuous.

3.2.1. Primary and pre-D1 structures

Primary structures consist of intermediate to mafic intrusions and layers within orthogneisses (1.7 Ga). Granitic and pegmatic dykes, as well as foliated K-feldspar-rich leucosome veins are sub-parallel to S1. This particular type of leucosome and dykes are considered as pre-D1 (likely of Hallandian origin; Möller et al., 2007). Early Sveconorwegian fabrics include local oriented kyanite crystals and fabrics found in the core of prograde garnet. These early Sveconorwegian fabrics are found in isolated mafic bodies and are not possible to correlate regionally. We therefore use S1 as the first clear record of a consistent and continuous fabric.

3.2.2. D1

In the basal shear zone and the enclosing orthogneisses the regional gneissic foliation (S1) is defined by alternating intermediate-mafic and felsic layers (Fig. 4b and c). The felsic layers

are quartzo-feldspathic bands, including 1–2 cm-thick leucosome; intermediate-mafic layers include fine-grained dark bands rich in minerals such as amphibole, biotite and locally clinopyroxene (Fig. 4b and c). S1 shows a predominant NW-SE strike (Fig. 3b). The gneissic banding locally preserves cm-scale isoclinal intrafolial folds (F1) and rootless hinges (Fig. 4a) throughout the area, suggesting that S1 formed as a result of tectonic transposition. S1 is axial planar to F1 folds (Fig. 4a).

Fig. 5a and b shows (retrogressed) kyanite-bearing eclogite, in which sapphirine-bearing symplectite formed as pseudomorphs after kyanite grains. These pseudomorphs are embedded within the folded fabric, i.e. S1, suggesting that S1 was associated with kyanite breakdown.

The northernmost part of the enclosing orthogneisses comprises gneissic rocks that are highly strained grading to mylonitic, with the main foliation striking NW-SE (Fig. 3, stereogram 4).The level immediately below the basal shear zone is poorly exposed, hence the limited amount of data from this area.

3.2.3. D2

In the basal shear zone, D1 structures (S1 and intrafolial folds) were affected by intense D2 folding and shearing. F1 folds are folded by F2, which are visible on N-S outcrop sections. Micro- to meso-scale F2 folds (Figs. 4b, c and 5a–i) show different geometries depending on the rock type in which they occur and are locally overprinted by a younger shear. In zones where D2 was more intense the shear F2 folds are isoclinal with sheared limbs.

3.2.3.1. Basal shear zone of the eclogite nappe. In the basal shear zone F2 fold axes generally plunge gently to the E (stereogram in Fig. 3). Also in mylonitic gneisses, F2 fold axes plunge to the E. The location of s- and m-type parasitic folds (Fig. 3c) along the sheared section suggests the presence of three hm-scale south-vergent F2 antiforms separated by NW-SE striking shear zones. Reverse limbs of asymmetric m-scale F2 folds are exposed only locally (i.e. Fig. 5; Spetsebo, Gläsbacka Table 1).

F2 folds are generally asymmetric and south-vergent, or symmetric. Their hinges vary from rounded to chevron-type, and interlimb angles are tight to isoclinal (Fig. 5a–i). Similar folds with thinned limbs (e.g. Fig. 5a and h) are common. Folded mafic layers (F2) often show boudinaged limbs (Figs. 4b and 5c, f). F2 folds with cuspate hinges developed locally (Fig. 5a and d). Chevron folds (Fig. 5g) have developed in highly strained, thinly layered, gneiss.

F2 folds have an axial planar fabric (S2; e.g. Fig. 5h), defined by quartz ribbons, elongated fine-grained feldspar-rich aggregates, and fine-grained aggregates of dark minerals (biotite, hornblende). S2 is sub-parallel to S1 in isoclinal F2 limbs, and crosscuts S1 in F2 hinges. In the investigated cross-section, S2 strikes 310–340° and has moderate dip (double strike symbols, Fig. 3a).

White, coarse-grained leucosome (inferred tonalitic composition; red arrows, Figs. 4b; 5c and f; 6c and g) is in many places associated with mafic lenses and layers. It surrounds mafic boudins, or is located along fractures and F2 axial planes (e.g. red arrows Fig. 4b; blue arrows Fig. 5c).

Locally, F2 folds were strongly sheared with the development of S2 shear planes along their fold limbs and parallel to their axial planes (Fig. 5h). In thinly layered gneisses, formation of axial planar shear resulted in abrupt truncation (e.g. blue arrows, Fig. 4b and 5c). Where shear was particularly intense, F2 folds are isoclinal with sheared-out limbs (Fig. 5i). White, former coarse-grained leucosome veins (inferred tonalitic) were also sheared.

A stretching lineation parallel or subparallel to F2 axes is present in most rocks (Fig. 3), even in domains less affected by D2 shear. This lineation is well clustered around 085/29 (Fig. 3). L2 is ascertained in syn-F2 white leucosome. However, if D1 and D2 are part of a continuous process, we cannot exclude that L2 also includes an older lineation L1. Therefore we describe the lineation as L1–L2. The lineation is defined by elongated

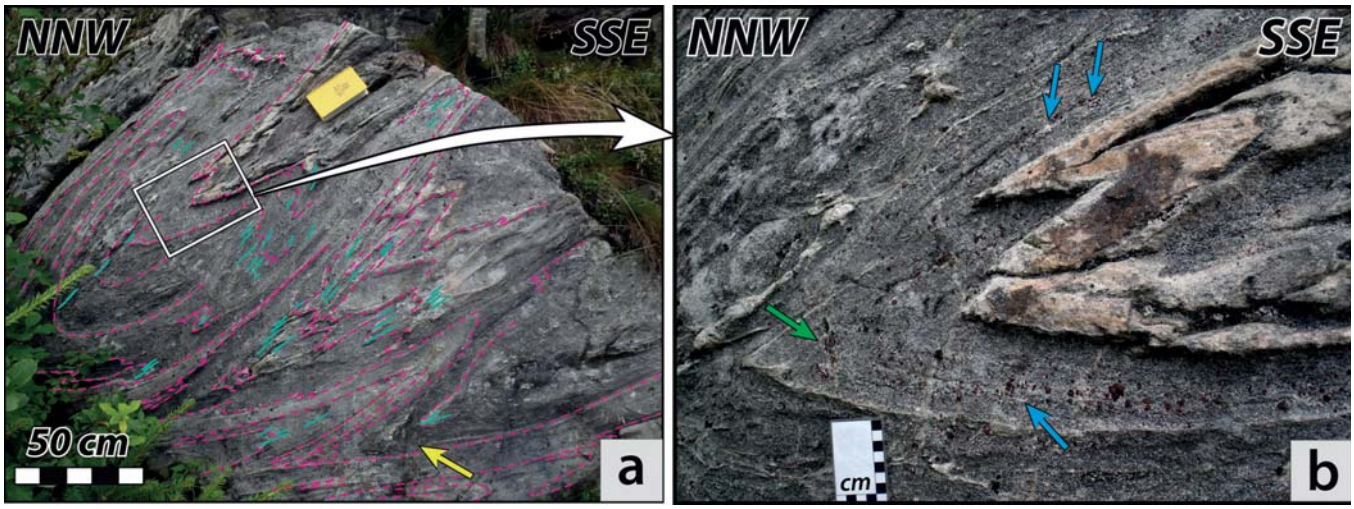

Fig. 5. Structures associated with F2 folding in the basal shear zone. (a) East-plunging F2 folds in kyanite-bearing retroeclogite. Pink dashed represent S1, blue lines S2. Fold geometries vary, from rounded- to chevron-type. An example of cuspate hinge is shown with a yellow arrow. (b) Detail of (a) showing the sharp-crested fold hinges and the folding of the retroeclogite assemblage. F2 folds affect a granitic vein and a fine compositional layering in retroeclogite with thin leucosome, garnet trails (green arrow) and elongated plagioclase-rich domains, which are pseudomorphs after kyanite (blue arrows). (c) South-vergent (F2) fold of felsic gneiss with thin mafic layers. Here the fold shape is not affected by the variable thickness of mafic layers. Some leucosome are localized in fold axial planes and along fractures planes (blue arrows), cross-cutting the fold. (Möller et al., 2015) (d) F2 fold structure illustrating ductile flow in a mafic-intermediate gneiss. Leucosome has localized at the boundaries and within a felsic layer and is surrounded by fine-grained garnet and clinopyroxene. The surface is oblique to the fold axis. (e) Typical F2 fold exposed in two perpendicular sections, i.e. distinctive folds on the N-S section and intensely sheared structures on the E-W section, parallel to the lineation. Mafic-intermediate rock with thin felsic layers. (f) Leucosome in mafic-intermediate retroeclogite pre-, syn- and post-dating F2 folds. (g) F2 fold with rounded hinge (upper left) developed within a thick mafic layer and chevron-like fold with thinned limbs (lower-right) developed in gray gneiss with reddish leucosome veins. The hinge is extremely sharp, slightly thicker than the limbs, and the fold wavelength is 30–50% of that of the nearby fold. In this case, local competency contrasts influence the fold shape. (h) Pronounced S2 axial planar fabric, parallel to the F2 fold limbs in a similar fold. (i) Sheared F2 fold cross-cut by discrete shear plane in a felsic gneiss containing thin mafic layers, indicating intense shearing during late D2 deformation. (S1 in pink dashed lines; S2 in blue; shear plane in orange). (For interpretation of the references to color in this figure legend, the reader is referred to the web version of this article.)

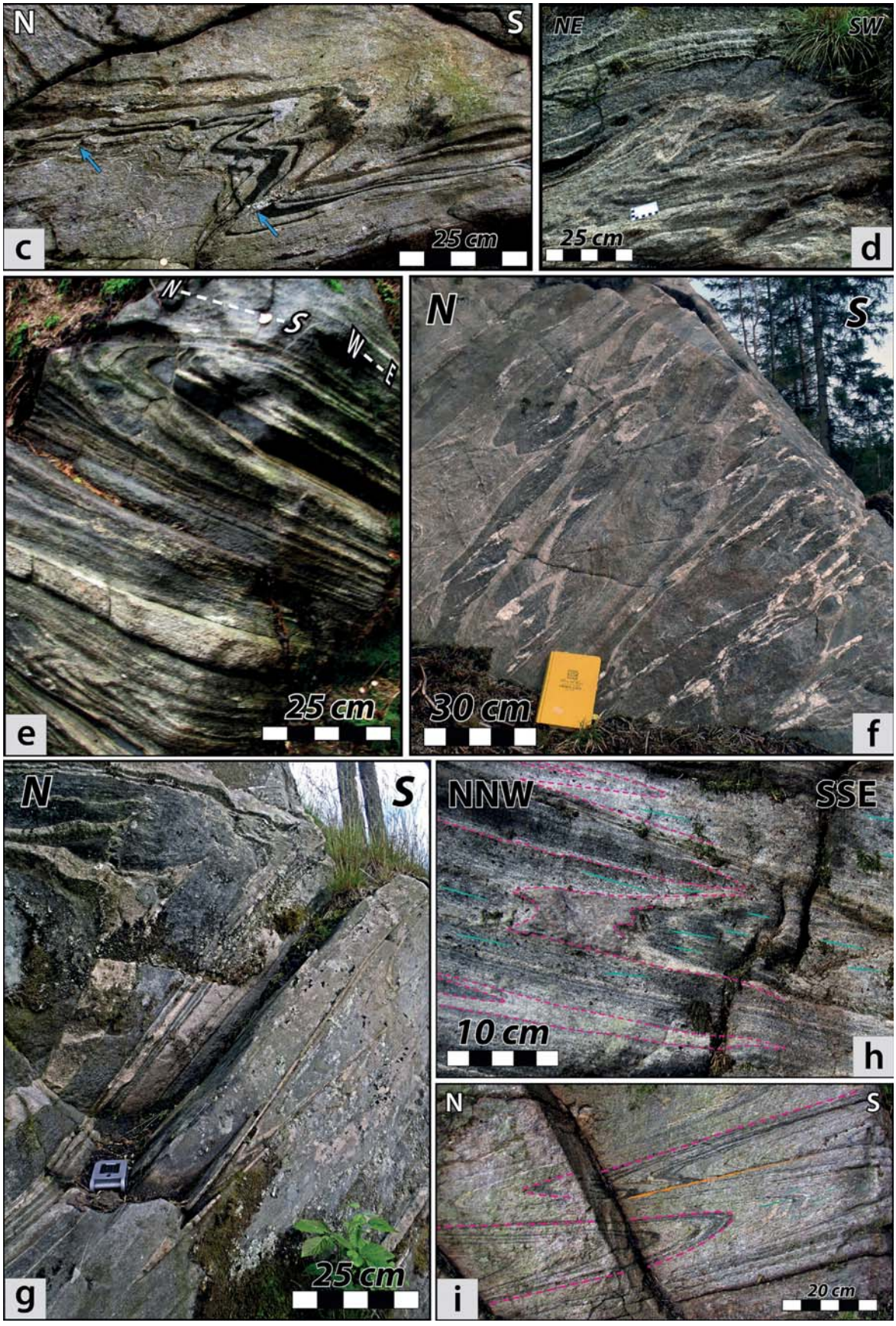

Fig. 5. (*Continued*)

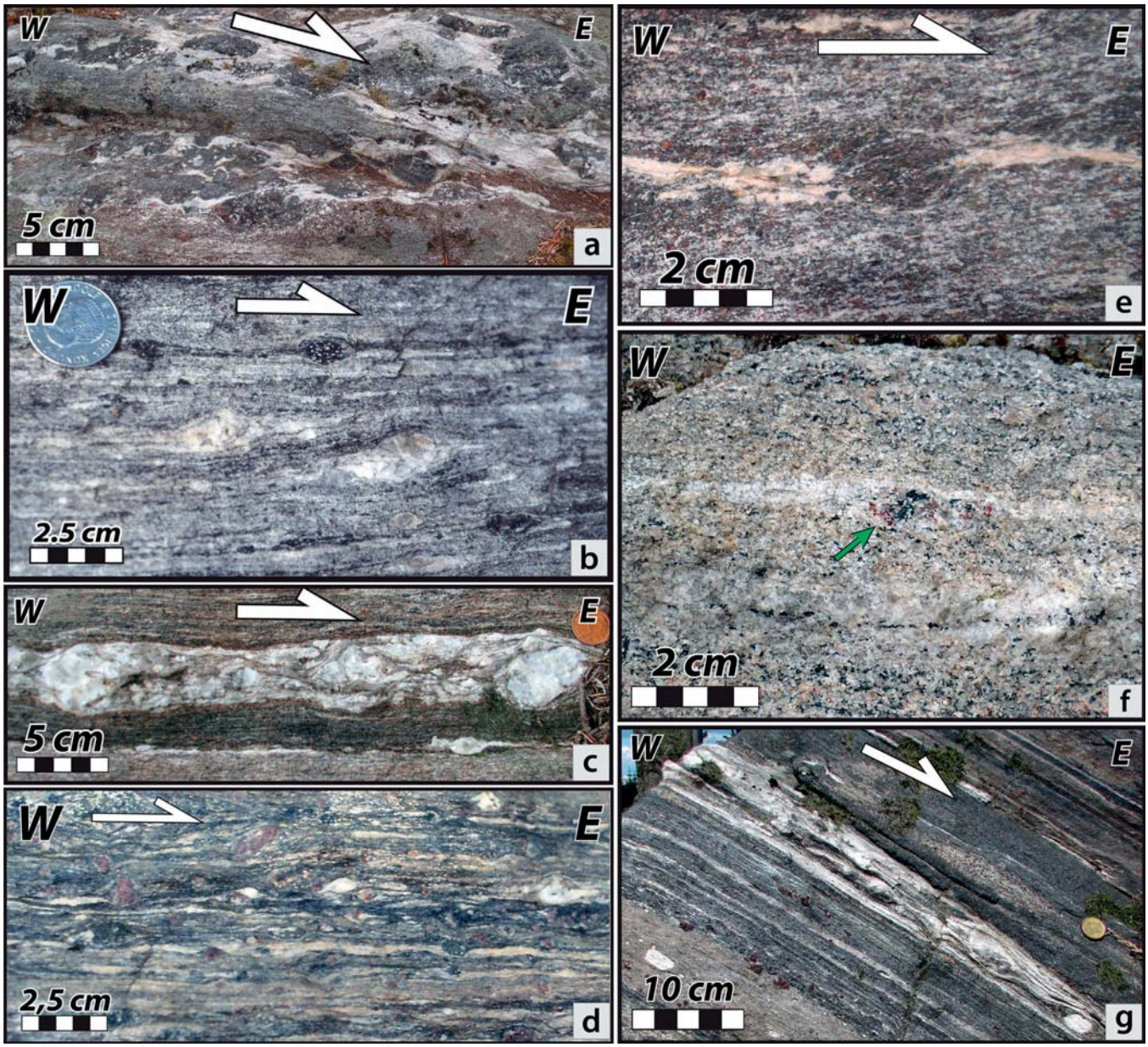

Fig. 6. Kinematic indicators along the profile in Fig. 3c. (a) Deformed leucosome with porphyroclastic hornblende blasts (b) Winged feldspar (white) and amphibole (black) porphyroclasts in a mylonitic gneiss. (photograph from Möller, 1999). (c) Late-D2 leucosome vein sheared after solid-state crystallization. This photograph comes from the same outcrop as Figs. 5f and 6g and the rock is a mylonitic retroeclogite of intermediate-mafic composition. (d) Asymmetric wings on porphyroclasts of garnet (red) and feldspar (white) in a mylonitic mafic to intermediate type of rock (photograph from Möller et al., 1997) (e) Deformed leucosome and a garnet- and hornblende-rich aggregate in a metatexitic garnet amphibolite. Leucosome crystallized in strain shadows. (f) Recrystallized granoblastic aggregate of garnet, amphibole, quartz and plagioclase from the inner part of the eclogite nappe. The green arrow points at the recrystallized lower wing of the clast. (g) Strongly sheared, originally coarse-grained, white leucosome in compositionally layered and mylonitized retroeclogite. (For interpretation of the references to color in this figure legend, the reader is referred to the web version of this article.)

mineral aggregates of quartz, feldspar, and dark minerals, or preferentially oriented amphibole grains in mafic to intermediate rocks.

Although small-scale structures are in many places symmetric in sections parallel to L1–L2, local asymmetric structures including winged porphyroclasts (garnet, feldspar and amphibole, mineral fish (amphibole, quartz); Fig. 6a–g) indicate a consistent top-to-the-east sense of shear along the investigated profile (Fig. 3c). Although particular attention was paid to reversed limbs of F2 folds, no clear reversed kinematic indicators were found at the outcrop scale. Kinematic indicators including deformed mafic lenses surrounded by melt, leucosome veins (Fig. 6c), cm-sized S/C shear bands (S2) and recrystallized winged porphyroclasts (Fig. 6b and d) indicate a top-to-the-east sense of shear.

3.2.3.2. Inner part of the eclogite nappe. In the inner part of the eclogite-bearing nappe the same sequence of deformation is observed: stromatic banding (S1) is folded by tight to open folds (F2), with E-plunging fold axes and associated with syn-tectonic leucosome. Boudinage of mafic layers is common. Strain is overall lower than in the basal shear zone, although local high-strained zones occur (double-strike symbols Fig. 3b). A generally E-plunging stretching lineation (L1–L2) is present locally.

The boundary between the inner part and the basal shear zone is marked by a high strain zone (Fig. 3b) that contains two traceable lithologies: a kyanite-bearing eclogite body and a recrystallized K-feldspar augen gneiss, the strain being strongly localized in the latter. This shear zone also includes migmatitic rocks, which show an increasing degree of mylonitization toward the basal shear zone. The general trend of the shear zone is subparallel to S2 and contains a mineral lineation (amphibole biotite). This shear zone is an example of overprint of shear deformation on anatexis.

3.2.3.3. Enclosing orthogneisses. In the enclosing orthogneisses, F2 folds are similar in geometry to those in the eclogite nappe, although strain is not as high and chevron folds are not present. F2 folds axes show a wider spread than in the eclogite nappe, and plunge moderately to NNW (Fig. 3). Poles to S1 foliations fall on a girdle with calculated β-axis 345/27 suggesting that NNW-trending folds (F2) reoriented the foliations. This axis is subparallel to the main stretching lineation in the same domain (Fig. 3). In a few localities (mafic body at Normanstorp, Fig. 3b), L1–L2 plunges to the SE.

3.2.4. Post-D2 structures

Effects of post-D2 deformation are only local in the study area, but post-D2 structures can be linked to regional observations.

One locality within the basal shear zone exposes a meter-scale cylindrical open S-vergent fold (F3; Skällstorp, Table 1). Its calculated β-axis is 108/03 (Fig. 7). The fold refolds F2 sharp-crested tight–isoclinal folds and earlier structures. An asymmetric crenulation cleavage (S3) developed subparallel to the axial plane (Fig. 7b). At Buskabygd (Table 1), a discrete S3 crenulation cleavage is also present, however with fold axis oriented approximately N-S.

Locally, meter-scale upright, gentle, symmetric folds (F4) with NNE-SSW to N-S trending axes have reoriented D1–D3 structures. These folds can be linked to regional folds with N-S trending axes (Fig. 2; e.g., F4 of Möller et al., 2015; Pinan-Llamas et al., this volume).

Additionally, north-plunging lineation has been locally observed (Fig. 3, stereogram 4). This lineation (defined by recrystallized quartz and feldspar aggregates and preferred orientation of amphibole grains) is less prominent than the E-plunging lineation, and no clear relationship was observed between the two. N-plunging lineations are, however, restricted to the westernmost part of the profile, an area which is affected by later upright folding (F3–4; Fig. 3b).

4. Microstructures and petrography of tectonites

In this section we present petrographic and microstructural observations from localities in the basal shear zone. A list of these localities and the analyzed thin sections is provided in Table 1. Table 2 presents a summary of the petrology and P-T evolution of kyanite-bearing (retro-)eclogites based on previously published data (Möller, 1998, 1999). The aim is to link folding and shearing to the metamorphic evolution of the eclogite nappe. The analyzed samples are felsic and intermediate mylonitic gneisses, hosting kyanite-bearing and kyanite-free retroeclogite layers (Gläsbacka, Tranabo, and Buskabygd, Fig. 3b). Finally, we analyzed oriented thin sections cut from a mesoscale F2-fold to document D1 and D2 microfabrics fabrics and kinematics related to F2-folding.

4.1. Early structures and fabrics

Eclogite-facies fabric is recognizable in local, well-preserved kyanite-bearing eclogite bodies, where preferentially oriented kyanite crystals define a foliation. Corresponding high-pressure fabrics are not preserved outside these competent isolated eclogite bodies. This eclogite facies fabric formed earlier than the pervasive D1 fabrics and structures in the host gneisses.

4.2. Structures and fabrics related to decompression and retrogression

S1 and S2 fabrics are associated with high-pressure granulite to upper amphibolite facies assemblages, hence corresponding to post-eclogite facies decompression.

4.2.1. S1 and S2

Penetrative S1 (gneissic banding) is present in all rock types. In deformed kyanite-bearing eclogite (Fig. 5a and b), sapphirine-bearing pseudomorphs of kyanite outline a folded D1 fabric (lineation or foliation), suggesting that D1 was associated with the breakdown of eclogite facies assemblages. In thin section, the mylonitic layering (S1) is defined by quartzo-feldspathic bands alternating with mafic bands (Fig. 8b and e–h). In E-W sections (e.g. Fig. 6b and c), quartz ribbons wrap around porphyroclastic feldspar. Aggregates of fine-grained feldspar and quartz fill pressure shadows.

In layered intermediate-mafic mylonitic gneiss, S1 is defined by preferentially oriented dark green hornblende (0.2–1 mm), long quartz ribbons (up to 4 cm in length), aggregates of plagioclase, and local fine-grained neoblastic clinopyroxene (Fig. 8a) and scapolite (Fig. 9). This foliation wraps around porphyroclasts of eclogite facies minerals (garnet or clinopyroxene + plagioclase pseudomorphs after omphacite; Fig. 8a and c). In sections parallel to the lineation, plagioclase and biotite crystallized in garnet pressure shadows. Former omphacitic clinopyroxene occurs as lens-shaped remnants, while neoblasts of clinopyroxene occur in trails together with plagioclase and hornblende. Remnants of former omphacitic clinopyroxene show micro-scale blebs of expelled plagioclase along crystallographic planes, which in some tectonites are oriented parallel to the main foliation (Fig. 8c).

S1 and S2 are subparallel in F2 limbs, so S2 is best observed in F2 hinges, where it crosscuts S1 at a high angle. In thin section, the S2 axial planar 0.1–0.5 mm wide foliation is defined by quartz ribbons and preferentially oriented dark mineral aggregates (Fig. 8e and h; Table 1). S1 and S2 fabrics developed at high temperature, and show similar metamorphic assemblages representative of upper amphibolite- and high-pressure granulite-facies, i.e. at temperatures exceeding 750 °C.

Grains of biotite and hornblende are found as small inclusions in quartz ribbons (Fig. 8d). Quartz lobate grains boundaries are common in our samples (e.g. window and left-over grains microstructures, e.g. Passchier and Trouw, 2005) and are consistent with high-temperature grain-boundary migration.

Dynamic recrystallization during D1 and D2 was followed by grain boundary area reduction (c.f. Passchier and Trouw, 2005), which resulted in polygonal grain shapes, smooth to straight grain boundaries, and coarse quartz ribbons segmented into a few different grains (Fig. 8d and f). This high-temperature grain coarsening texture overprints the original deformation fabrics.

4.2.2. Post-D2

Locally, chlorite is found in garnet fractures in otherwise well preserved retroeclogite. Chlorite formed during retrogression at low metamorphic conditions (post-D2).

4.3. Microstructures in F2 fold

Twenty thin sections were made from a 20 × 12 × 10 cm sample of folded gray gneiss rich in thin intermediate-mafic retroeclogite bands (Table 1; Fig. 9a, b; c–h), in order to investigate sections

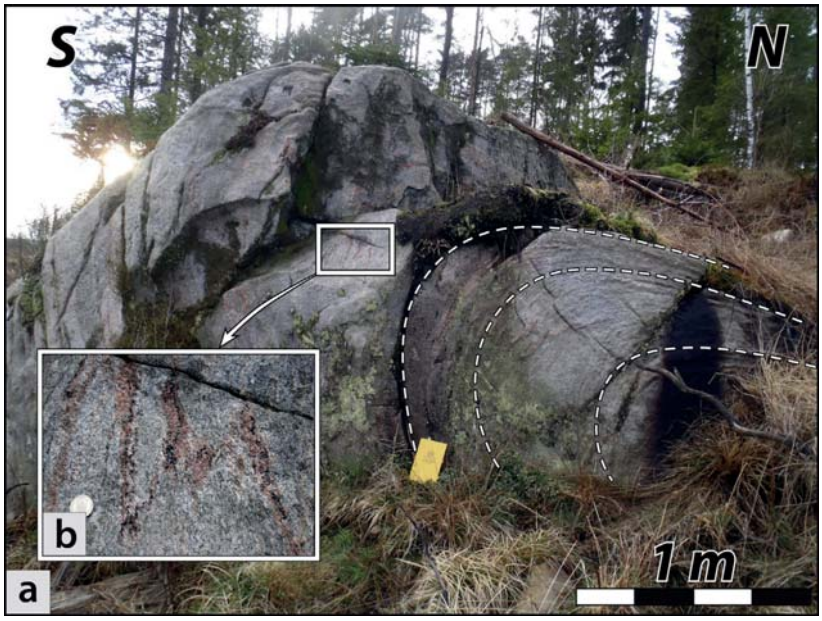

Fig. 7. F3 fold. (a) F3 fold in a granitic gray gneiss with reddish leucosome. (b) Detail of refolded isoclinal F2 fold of K-feldspar-rich leucosome with elongated dark quartz ribbons. The overprinting asymmetric crenulation is sub-parallel to the F3 axial surface.

Table 2
Table summarizing metamorphic and deformation stages, deduced from observed mineral assemblages, and based on Möller (1998, 1999) for a kyanite bearing eclogite. Dashed lines represent a stable mineral, but not general growth.

Deformation stage	*Pre- D1*	*D1 - D2*	*Post- D2*
Metamorphic stage	*Eclogite*	*Granulite to upper-amphibolite*	
Grt	———	- - - - - - - - - - - -	
Ky	———		
Cpx	———	——— - - - - - - -	
Rt	———	- - - - - -	
Zo	———		
Pl		(s) ———	———
Opx		(s) ———	
Spr		(s) ——— - - - - - - - - - -	
Crn	- - - -	(s) - - - - - - - - - - - - - - - -	
Sca		- - - - ———	
Ttn			- - - -
Am	- - - - - - - -	- - - - - - - - ———	———
Chl			- - - -
Bt	- - - - - - - -	- - - - ———	———
		(s) *symplectitic*	

perpendicular and parallel to the fold axis in both limbs and hinge zones.

These thin sections illustrate that high-temperature recrystallization (annealing) was prominent. In contrast to lower-temperature deformation fabrics, micro-scale kinematic indicators are largely lacking in these high-temperature tectonites.

Sections parallel to the macroscopic stretching lineation (L1–L2) show strongly elongated mineral aggregates (Fig. 9e compared to g) and gently asymmetric structures such as mineral fish, asymmetric wings on clasts, and shear bands (C or C′). Wings around garnet porphyroclasts are relatively well developed in E-W sections; the wings are made up of biotite, plagioclase, quartz, hornblende, and opaque minerals. Hornblende and biotite aggregates locally resemble shear-band boudins. A limited number of asymmetric structures are present, however they do not show a consistent sense of shear in the same thin section (Fig. 9). Thus further strain analysis is required in order to document the kinematic vorticity of deformation within these samples and the relative contributions of pure and simple-shear during non-coaxial deformation.

Sections perpendicular to the lineation show folded and recrystallized quartz ribbons (Fig. 9g; similar to Fig. 8e), and locally include remnants of omphacitic clinopyroxene. Folded trails of clinopyroxene, amphibole, biotite and scapolite are common (Fig. 9g and h). Folded garnet is visible in Fig. 9h. In contrast with

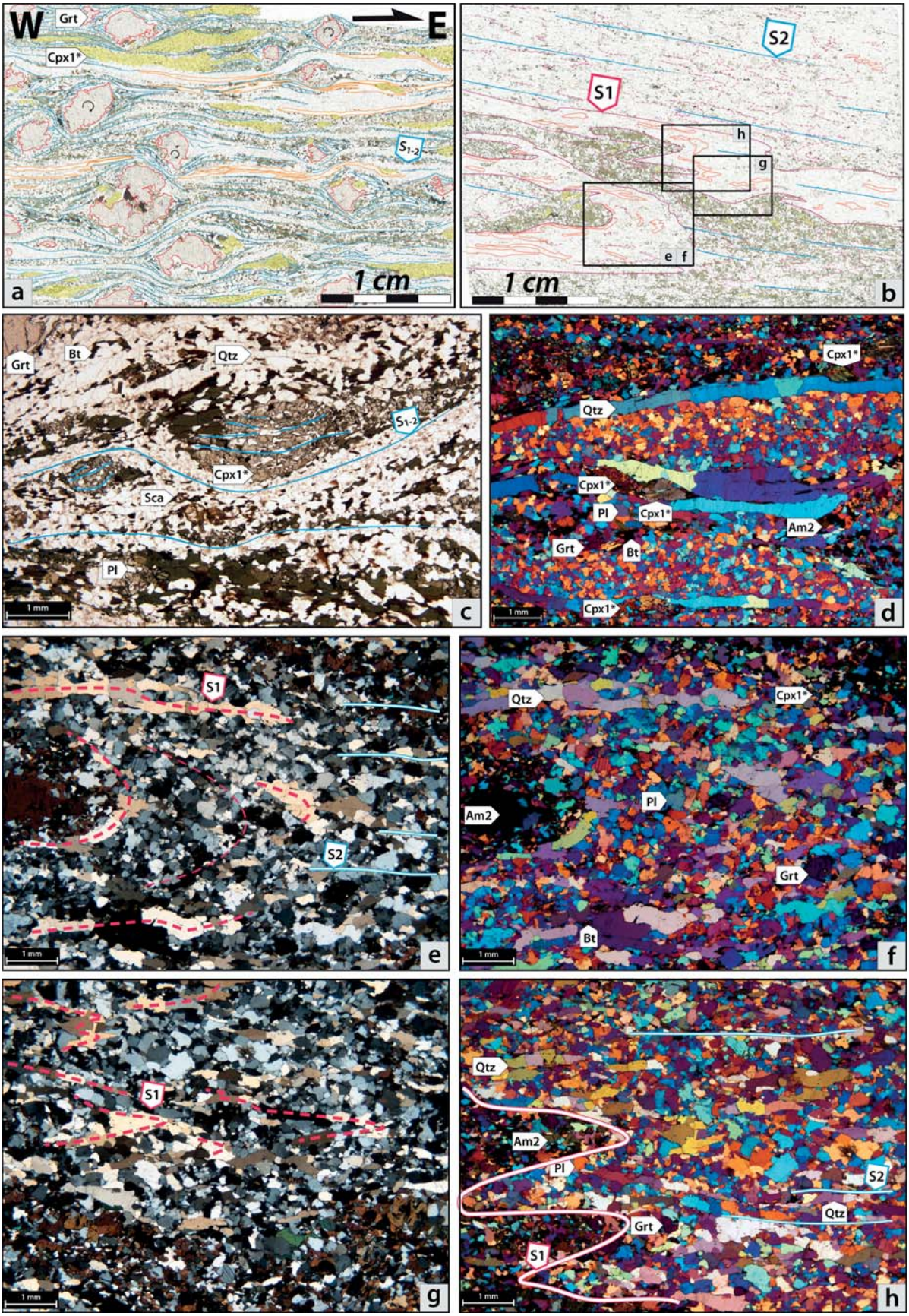

Fig. 8. Photomicrographs illustrating the microstructures of tectonites in the basal shear zone. XPL: cross-polarized light; PPL: plane polarized light. (a) Interpretive sketch of thin section from a mafic-intermediate mylonitic retroeclogite. Former high-pressure assemblage is represented by clinopyroxene-rich domains (Cpx1), which subsequently

lineation-parallel sections, wings around porphyroclasts are rare. An axial planar foliation is marked by trails of biotite and minor hornblende (Fig. 9g and h).

5. Discussion

Our structural, petrographic, and kinematic observations demonstrate that the basal shear zone of the eclogite nappe accommodated polyphase deformation during exhumation and nappe emplacement. Structures developed during simultaneous folding and shearing in the presence of melt.

5.1. Conditions and mechanism of deformation (D1 + D2) in the basal shear zone

D1 ductile deformation postdated eclogite-facies metamorphism and therefore records an early stage of exhumation. S1 fabrics in the basal shear zone of the eclogite nappe and the enclosing orthogneisses are concordant and parallel to the contact between these two units. S1 is defined by similar mineral parageneses in both units. Thus, D1 structures are interpreted as related to the juxtaposition of the eclogite nappe with the enclosing orthogneisses unit. While deformation was localized in the basal shear zone of the eclogite nappe, the enclosing orthogneisses are on average less strained. The boundary between the eclogite nappe and the enclosing orthogneisses is primarily a metamorphic discontinuity. Subsequent (D2) deformation took place at similar metamorphic conditions (high-pressure granulite- to upper amphibolite-facies), producing cm-scale to map-scale south-vergent F2 folds (Figs. 2, 3 and 5c) with geometries that range from angular to similar. This type of similar folds is common in high-grade rocks (e.g. Hudleston and Treagus, 2010) and typically develops by shear. F2 folds are characterized by gently to steeply NE-dipping axial planes, and fold axes parallel and sub-parallel to the L1–L2 stretching lineation. Fig. 10a summarizes the main characteristics of F2.

In the present study area, the stretching lineation has not been seen refolded by F2 folds. However, the stretching lineation may have formed as early as during D1 and persistedly developed throughout D2, so that L2 would include L1. L1 lineation has been described as folded by F2 in other parts of the southern Eastern Segment (Pinan-Llamas et al., this volume).

In sections perpendicular to the stretching lineation (N-S sections parallel to the YZ principal plane of finite strain), F2 hinge zones of folded mafic layers show boudinage with necks filled by leucosome (red arrows Fig. 4b). There are also fractures filled by leucosome and axial planar parallel discrete shear-zones within thin leucosome (red and blue arrows, respectively, Fig. 4b). The presence of F2 south-vergent folds and their associated S2 axial planar cleavage, their boudinaged limbs, and melt migration toward F2 fold hinges are consistent with a south-directed shortening component (pure shear) of the deformation during D2 (Fig. 10a).

In the southernmost area of the basal shear zone (Århult, Table 1), tight to open folds crosscut by cm-thick shear-zones are exposed. These folds with NNW plunging axes are interpreted as F2 based on qualitative criteria (i.e. low-viscosity deformed mafic layers similar to D2, interlimb angle, relative crosscut by NNW-SSE shear zones). Their different orientation is explained by reorientation into a regional N-S-trending F3–4 fold limb (Fig. 2; Figs. 3 and 6a in Möller et al., 2015).

5.1.1. High temperature microtextures

At the microscale, F2 folds have affected D1 structures (quartz ribbons, amphibole- and pyroxene-rich trails) and even elongated garnet grains appear folded (Fig. 9h). Fractures filled with feldspar and biotite cutting the hinge of a garnet may be a small-scale equivalent of axial planar melt (cp. Figs. 4b and 5c). Garnet was overall stable, although it demonstrably did not grow and was instead partially resorbed (volume decrease) during D2 deformation. In Fig. 9h, garnet is folded and pressure shadows show products of garnet breakdown during a late stage of D2 (biotite and feldspar).

Rocks in the basal shear zone experienced partial melting during D1–D2. High temperatures (estimated at c. 750–850 °C, Möller, 1998, 1999) lead to the formation of a coarse gneissic fabric, and near-complete annealing of previous structures. The formation of <mm-thick and several cm long quartz ribbons, annealed and segmented into a few large grains, is evidence of high-temperature dynamic recrystallization followed by grain-boundary area reduction (Fig. 9).

5.2. Late D2 shear

Several meters wide foliation-parallel ductile high strain zones have been documented along the profile (double strike symbols in Fig. 3b). They often contain dm-scale F2 isoclinal folds and asymmetric F2 folds with intensely sheared limbs (Figs. 4b and 5g). These strain zones are localized in overturned limbs of F2 km-scale folds (see cross section Fig. 3c). These map-scale D2 shear zones have diffuse boundaries, showing a gradational decrease in the intensity of S2 mylonitic foliation toward the surrounding lower strain domains.

Narrow shear planes often crosscut F2 reverse limbs. In areas were late D2 shear was localized, F2 folds were partly transposed along shear planes sub-parallel to their axial planes (Fig. 5i). Melt injections of F2 white leucosome along the F2 axial planes, sheared under late D2 solid-state conditions, confirms that folding and shearing took place under high-temperature conditions (upper-amphibolite facies; Table 2).

5.3. D2 melt-present deformation structures and formation of chevron folds

Variations in melt distribution and rock competence, and leucosome migration in response to local pressure variations during folding, contributed to the layered sequence behaving heterogeneously. The geometry and significance of magma and leucosome segregation and their structural relationship with tectonic deformation have been described in different settings (e.g. Sawyer et al., 1999; Vernon and Paterson, 2001; Weinberg and Mark, 2008).

The diverse structural relations of leucosome testify that partial melting persisted during different stages of D2. F2 axial-planar white coarse-grained leucosome (Fig. 5f) formed syn- to post-kinematic with respect to F2 folding, and F2 folds actually created sites for melt segregation. Localization of leucosome in shear zones

expelled plagioclase and partly disrupted during D1–D2, yellow domains) and garnet (red). Garnet grains are wrapped by a foliation (S1–S2, blue lines), marked by recrystallized quartz ribbons (orange), clinopyroxene amphibole, plagioclase and biotite. Garnet porphyroclasts rotated during D2 (and possibly D1) and indicate a dextral sense of shear (sample CM10-11). (b) Thin section from a folded (F2) felsic and mafic mylonitic gneiss containing leucosome, showing folded S1 (pink dashed and plain lines) with S2 developed as axial planar foliation (blue; sample CM10-06C4). (c) Photomicrograph showing a clinopyroxene (Cpx 1) with expelled plagioclase inclusions locally aligned with S1–S2 (Close up of Fig. 8a, PPL). (d) Recrystallized quartz ribbons wrapping clinopyroxene (Cpx1). Grain boundary area reduction is evident from the coarse quartz ribbons and sub-granoblastic texture of feldspar domains (Close up of Fig. 8a, XPL using a retardation plate). (e-f; g-h) Close-up of the hinge zone of F2 fold from Fig. 8b, showing quartz ribbons parallel to S1 (pink dashed lines) and locally disrupted by S2 (blue lines) marked by fine-grained biotite plagioclase and quartz. Images are taken using XPL (e, g) with retardation plate (f, h). (For interpretation of the references to color in this figure legend, the reader is referred to the web version of this article.)

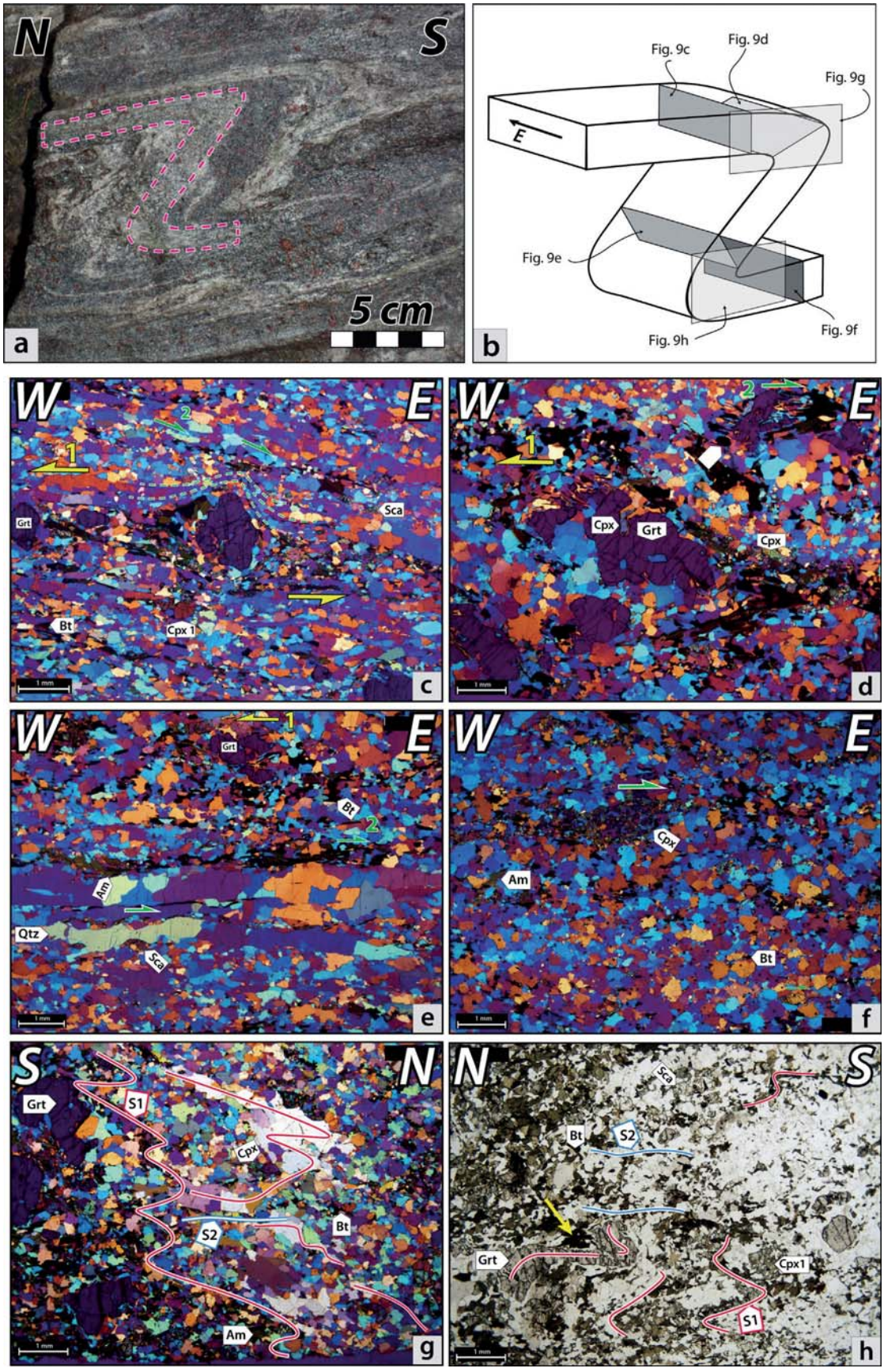

Fig. 9. Sample of F2 fold (LT12055, Table 1) from a mylonitic mafic-intermediate retroeclogite (a) before sampling; (b) sketch of the fold showing location of thin sections studied. (c–h) Photomicrographs of thin sections selected from sample LT12055. The black arrow (upper part of each picture) marks the eastward plunge of the lineation. (g)

parallel to F2 axial planes indicates melt-enhanced deformation, where the concentration of melt was responsible for strain localization and strength reduction. Melt localization in fractures (e.g. Fig. 5c) suggest that the presence of melt also lead to fracturing (blue arrows, Fig. 5c). Stress release by migration of melt thus took place via axial planes, shear zones and local fractures. Melt extraction and axial plane-parallel shearing likely helped to transfer mass within the folded rock so as to allow shortening perpendicular to the fold axis.

Some high-strain areas (e.g. Gläsbacka, Fig. 3b) show features characteristic of mutual feedback between folding, shearing and partial melting (cp. Weinberg and Mark, 2008). Folds show extreme cases of contrasting styles of ductile deformation and including sheared limbs, axial planar shear zones (Fig. 4b, blue arrows; Figs. 5c and f; 6) and local cuspate fold hinges (Fig. 5a, yellow arrow). Other typical structures include migrated melt toward fold hinges and truncation of layers by axial planar shear zone. Similar features are described from other migmatite terranes (e.g. the Karakoram Shear Zone in Ladakh, Weinberg and Mark, 2008). The difference between fold shapes and geometries is locally induced by competency contrast between layers, although the general style of F2 is more consistent with passive folding than buckling. Fig. 5g illustrates how weakened competency in layered rock has lead to high-temperature chevron foldsin zones of very high strain and localized shear. Chevron style folds develop in slaty sequences by flexural slip or flexural flow deformation mechanisms at low grade metamorphic conditions (e.g. Bastida et al., 2007). However, in the high-grade basal shear zone of the eclogite nappe they are also common. A model for chevron fold formation was proposed by Carreras et al. (2005), who suggested that they form in layered rocks with a high competency contrast, where shear-induced flattening is extremely high. In the basal shear zone, chevron fold shapes may have been produced by shear-induced flattening. The presence of melthas however likely also been important in their formation, allowing for mechanical disconnection between different lithologies and layers. Cuspate hinge zones in some chevron folds (yellow arrows, Fig. 5a) are typical features of melt migration and mass loss (Weinberg and Mark, 2008).

5.4. Kinematics

Mesoscopic kinematic indicators (Fig. 6) such as asymmetric pressure shadows on sheared rigid mafic lenses, mineral fish (hornblende), and asymmetric sigma and delta porphyroclasts are consistent with top-to-the-E shear. No change in shear sense across F2 fold axial planes suggests that the penetrative top-to-the-east directed ductile shear was syn- or post-kinematic with respect to this folding.

In sections parallel to the stretching lineation and perpendicular to the S1 and S2 foliation (inferred XZ-principal plane of finite strain) symmetric structures are predominant, although few kinematic indicators that are consistent with a dominant top-to-the-east occur. These observations were also made on outcrops, where F2 folds with axes subparallel and parallel to the X direction of the finite strain ellipsoid are present. At microscale, most kinematic indicators do not show a clear sense of shear due to effects of static recrystallization (Fig. 9).

5.5. Lineation and fold axis variations

In the investigated section, F2 folds in the eclogite nappe generally have subhorizontal to shallowly E-plunging axes (Fig. 3). In the enclosing orthogneisses structurally beneath the basal shear zone, F2 axes and L1–2 are predominantly NW or SE-plunging (i.e. subparallel to the actual contact between the two units) and their orientations are generally less clustered than in the basal shear zone. The stronger clustering of L1–2 and F2 orientations in the basal shear zone likely is an effect of a stronger shear component of the deformation acting on this unit.

5.6. Formation of lineation-parallel folds

The mechanism of formation of typical F2 lineation-parallel folds is important in the interpretation of the transport mechanism of the eclogite nappe. Although we acknowledge that the data presented in this study permit preliminary conclusions only, we discuss our data in the context of different models for the development of lineation-parallel folds. This summary will serve as a base for further studies.

Several studies document field examples of high-strain zones where fold axes and lineation are at small angles or sub-parallel to each other (Ridley, 1986; Foreman et al., 2005; Morales et al., 2011; Xypolias and Alsop, 2014). Different mechanisms have been proposed to explain the development of this parallelism:

(1) Flow-perturbation folding, acting especially at high-temperatures (e.g. Alsop and Holdsworth, 2007, and references therein). Asymmetric folds with axes at a very low angle to the transport direction initiate in response to wrench-dominated differential shearing.
(2) Regional constrictional deformation (Passchier et al., 1997; Zulauf and Zulauf, 2005) may result in co-linearity between fold hinges and lineation.
(3) Pre-existing penetrative linear anisotropies (Watkinson and Cobbold, 1981) can also control the development of folds subparallel to the lineation.
(4) Rotation of initially oblique fold hinges under very high strain (e.g. Escher and Watterson, 1974; Bell, 1978).

(1) Folds with an axis parallel to the stretching lineation can develop in the flanks and base of flow perturbation zones (Fig. 10b; e.g. Ridley, 1986; Alsop and Holdsworth, 2012), also described as regions of layer-normal differential shear (Coward and Potts, 1983). Folds will passively develop or rotate toward the main transport direction. Consistent with this model, in the basal shear zone we observe asymmetric south-vergent transport-parallel folds associated with a dextral and top-to-the-east sense of shear. The geometry of the folds is in many places indicating little competency contrast between layers, suggesting passive folding as the primary folding mechanism.

and (h) are from sections perpendicular to the lineation (L1–L2). All thin sections shows alternating mafic layers of garnet porphyroclasts together with hornblende, biotite, scapolite and clinopyroxene and felsic layers of quartz ribbons and fine grained feldspar and quartz, with similar textures to those in Fig. 8. Photomicrographs (c-g) in XPL with retardation plate, (h) in PPL. (c) Upper horizontal limb of the fold (B22YA). The garnet at the center mainly shows a top-to-the-west (arrow yellow), but a slight component of back-rotation is visible (green dashed lines and arrow). (d) Upper hinge (B2HA1). Top-to-the-west sense of shear is shown from the garnet-rich aggregate in the center, but top-to-the-east shear is shown from a garnet pressure shadow filled with biotite (upper right). (e) Overturned steep limb of the fold (E2YB1). Elongated quartz ribbons are bordered by scapolite fishes showing a top-to-the-east sense of shear (green arrow). Contrastingly, a winged garnet (upper center) shows a top-to-the-west shearing. (f) Lower horizontal limb (E2XA). Top-to-the-east shear from an aggregate of clinopyroxene and feldspar (likely remnant of former omphacite). (g) Section perpendicular to L1–L2 from the upper hinge zone (B23X), where S2 develop axial planar to the folded (F2) quartz ribbons and compositional layering. Garnet porphyroclasts (left side) do not show asymmetric shape nor wings but follows, as trails, the trend of S1. (h) Photomicrograph of thin section E2H2 from the perpendicular section to the lineation (L1–L2) of the lower hinge of the fold. Similar features to (g) are shown, and garnet is also folded (lower left). (For interpretation of the references to color in this figure legend, the reader is referred to the web version of this article.)

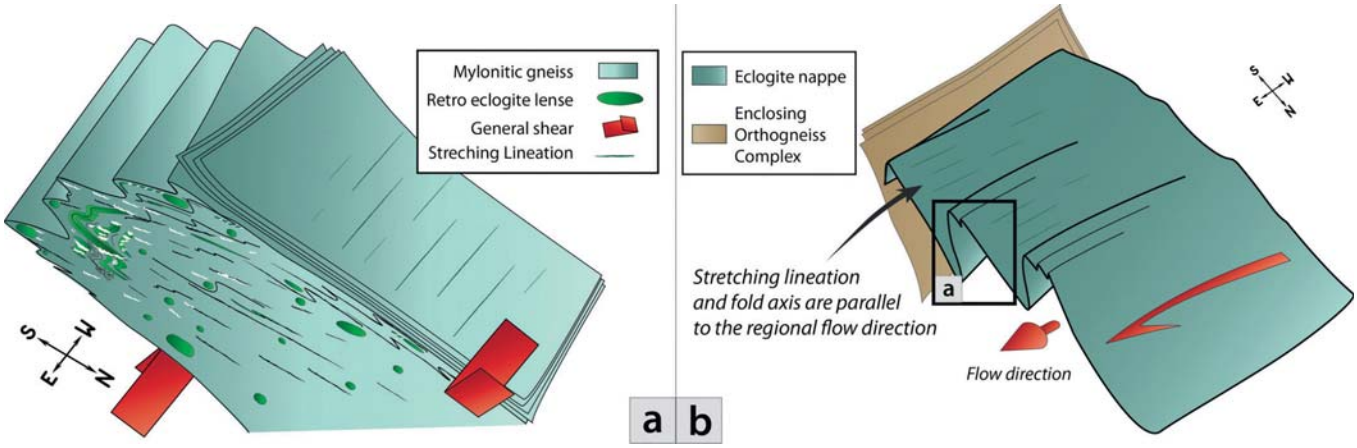

Fig. 10. Geometry of and kinematics in F2 folds of the basal shear zone. (a) Sketch summarizing the main characteristics of F2 (close up from (b)). Red arrows mark general shear. The moderate dip of the foliation (i.e. S2) and obliquity of the lineation to strike demonstrate a significant dip-slip component. White trails mark leucosome. (b) Conceptual sketch of development of lineation-parallel folds in a context of regional flow. (For interpretation of the references to color in this figure legend, the reader is referred to the web version of this article.)

In flow-perturbation folds non-coaxial shearing can result in fold hinge rotation toward the shear direction (e.g. Alsop, 1992; Alsop and Holdsworth, 2004). Sheath folds are typically associated to flow perturbation folds at the outcrop-scale. However, no clear sheath folds have been observed in the research area. They could be absent, or alternatively this could be the result of poor three-dimensional exposures of folds. Large-scale sheath folds with no associated small sheath-folds are rare but have been described (Henderson, 1981; Lacassin and Mattauer, 1985; Fowler and El Kalioubi, 2002). If the model that accounts for the structures in the area is flow perturbation, the stretching lineation L1–L2 will not directly reflect the orientation of the stress directions, but instead represent the direction of flow.

(2) A pure constrictional strain field would produce lineation-parallel folds (e.g. Krabbendam and Dewey, 1998; Passchier et al., 1997). If the main mechanism is constrictional forces, vergence and axial plane of folds are expected to be more irregular than what we have observed (e.g. Ghosh et al., 1995). Constrictional strain commonly produces dominantly L-tectonites in the most ductile and deformed areas, which is not the case in the investigated area. Constrictional deformation in a transtensional regime is also characterized by hinge-parallel boudinage and interference patterns in the fold limbs (Fossen et al., 2013). These features are not characteristic of the investigated basal shear zone.

(3) Lineation-parallel folds may also form in rocks with an initial strong linear fabric, controlling the localization of subsequent folds hinge lines (e.g. Cobbold and Watkinson, 1981). This model is problematic to discuss here, as early structures are largely obliterated in the basal shear zone. An argument in favor of this model is possible rod geometries formed prior to D2 and that influenced F2-fold initiation. Rod structures can form by stretching (parallel to X), by boudinage (parallel to Y), or by folding (parallel to fold axis). This is compatible with field observations where competent mafic layers (>10 cm thick) are boudinaged in directions parallel to the YZ-section of the strain ellipsoid (e.g. Gläsbacka locality, Fig. 4b). The gneissic layering (S1) is an important planar anisotropy in the studied rocks, and although we suggest passive folding as the main mechanism, folds were also controlled by local competency contrasts (e.g. Fig. 5f and g). The abundance of pre-D2 competent retroeclogite bodies may have locally exerted mechanical control and played a role in fold nucleation and orientation in the basal shear zone. However, model (3) would reverse kinematic indicators on overturned limbs if this mechanism played a major role in the folding process. This has not been systematically observed in the investigated section, but detailed kinematic analyses remain to be investigated in other parts of the shear zone.

(4) A common model to explain the formation of lineation-parallel fold hinges is by rotation of initially oblique fold hinges under very high strain (e.g. Escher and Watterson, 1974; Bell, 1978). In this model, systematic variations are expected in different domains since the strain is not homogeneous from one outcrop to another. This is not the case within the basal shear zone. Variations in fold axis orientations would systematically diverge from the lineation orientation in less-strained areas and converge in the highly-strained areas (basal shear zone). Reorientation of folds due to high strain in the basal shear zone may apply to the scale of several kilometers. In domains above and below the basal shear zone, fold axes have clearly a more variable orientation (Fig. 2b). Detailed strain analysis is, however, required to estimate vorticity values and the relative importance of the rotational component of deformation in the basal shear zone.

Based on our data, flow-perturbation folding (model 1) is here interpreted as the most probable mechanism to generate lineation-parallel folds in the basal shear zone. Preexistent rod structures (model 3) may also have locally influenced in the development of D2 structures. Border effects of the flowing nappe on the major tectonometamorphic boundary (hinge rotation, model 4) could explain the prominent cluster of lineation and fold axis orientation in the basal shear zone. A conceptual sketch is proposed in Fig. 10b to show the influence and the coherence of the E-directed regional flow on the fold and lineation development.

5.7. Reorientation of D2 structures

Post-D2 deformation was documented only locally in the research area (e.g. Skällstorp, Fig. 7; Buskabygd Fig. 3b). The open-style of D3–D4 folds and their less penetrative associated fabrics suggest that D3–D4 strain was considerably less intense than D1-D2. Variable trends of F3 and N-S trends of F4 have been recorded in other areas (Möller et al., 2015; Pinan-Llamas et al., this volume). D1 and D2 structures are refolded, and therefore their original orientations are not preserved, but only their relative relationships. Recognition of the reorientation of D1–D2 structures by post-D2 folding is thus important for understanding of the tectonic transport and geometry related to the main deformation (D1–D2).

5.8. Regional extension and tectonic significance of D1 + D2 in a recumbent fold nappe

D1 and D2 structures are not unique to the basal shear zone, but outside this shear zone they have not developed at such high strain and mylonitic gneisses occur only locally. Similar F2 folds with axes parallel to stretching lineations and the same sequence of folding (F1–F4) have been documented throughout the southern Eastern Segment, e.g. in the inner part of the eclogite nappe and in the gneiss complex surrounding it (Möller et al., 2015; Pinan-Llamas et al., this volume). S1 is the regional gneissic layering represented as the banding in the magnetic anomaly map (Fig. 2). The main orientation of the S1 gneissic layering changes gradually across tectonic contacts.

The basal shear zone of the eclogite nappe has been traced for 50 km from the west coast and eastwards (Möller et al., 2015; Fig. 2); the basal shear zone is a thrust, along which the eclogite nappe was emplaced into a high-pressure granulite to upper amphibolite facies complex. The basal shear zone varies in thickness from a few hundred meters to more than three kilometers (as the part investigated in the present study). Shear strain in fold nappe is commonly heterogeneously distributed (Bastida et al., 2014), with marked strain localization in the lower limb (e.g. Ramsay and Huber, 1983). The consistent orientation of lineation and fold axes, together with kinematic indicators suggest E-directed transport, toward the foreland. The stretching lineation is present throughout the investigated area, but more strongly developed and more strongly clustured in the basal shear zone. In the basal shear zone, the strain is strongly localized, so the lineation not only reflects the X-axis of the finite strain ellipsoid, but also likely coincide with the transport direction of the nappe. Although asymmetric structures show a top-to-the-east sense of shear, the abundance of symmetric structures together with chevron-type folds demonstrate that a combination of simple and pure shear originated D2 structures.

Generally, recumbent folds formed at high-grade conditions are believed to initiate in response to a perturbation. An obstacle (i.e. contrasting rheology of a wall buttress) was proposed to be one of the main mechanisms to initiate such folds (e.g. review by Bastida et al., 2014). The forced extrusion of rocks through a recumbent fold has been successfully modeled in several studies (e.g. Bucher, 1956, 1962; Brun and Merle, 1988; Vacas Peña and Martínez Catalán, 2004; Warren et al., 2008; Duretz et al., 2011). If we regard D1–D2 as part of a continuum primarily initiated by regional compression, the extrusion of the eclogite nappe through a recumbent fold (D1) that would propagate and form F2 folds (D2) is an attractive scenario. However, mafic dykes emplacement (Blekinge-Dalarna Dolerites) at 0.97–0.94 (Söderlund et al., 2005), demonstrates a regional E-W extensional regime shortly after eclogite exhumation (D1), and this extensional regime appears to coincide with D2–D4 ,(Möller et al., 2015; Pinan-Llamas et al., this volume). Nevertheless, the D1–D2 structures in the basal shear zone suggest continuous east-vergent flow. Border effects at the base of the flowing nappe could explain the local transpressional character of the basal shear zone in an overall extensional regime during D2. The folding mechanism of F2 in the basal shear zone appears then compatible with a model of flow perturbation, a common setting for the development of recumbent folds in high-grade terranes (e.g. Bastida et al., 2014). Flow-perturbation mechanism requires an initial perturbation, and is commonly described to initiate passively around a rigid inclusion (e.g. Rosas et al., 2002). However, recent studies by Reber et al. (2012, 2013) demonstrate that sheath folds can also initiate around weak inclusions, e.g. a fault. Although the initial basal shear zone itself reflects a possible initial weak and planar anisotropy, the role of partial melting must have had a great influence because it induces a dramatic loss of strength of the partially molten material. Recent U–Pb SIMS metamorphic zircon ages carried out in the eclogite nappe constrain the time of eclogitization at 0.99–0.98 Ga, while dated stages of migmatization are slightly younger, 0.97–0.95 Ga (Möller et al., 2015). Inception of partial melting at depth at the earliest stage of exhumation is an attractive trigger for flow perturbation, but remains to be demonstrated.

6. Conclusions

- The basal shear zone records polyphase deformation during emplacement and exhumation of the eclogite-bearing nappe, from eclogite to high-pressure granulite and upper amphibolite facies conditions.
- Interplay between folding, shearing and partial melting produced the structures in the basal shear zone.
- Structures during the main deformation events (D1 + D2) include lineation-parallel passive folds, locally of chevron type. They are interpreted as formed during a continuous top-to-the-east shearing and local shear-induced flattening at the base of the eclogite-bearing fold nappe.
- The lineation-parallel folds formation in the basal shear zone is proposed to reflect E-directed flow of the nappe during its extrusion.

Acknowledgments

Research was funded by grants from the Geological Survey of Sweden (60-1655/2009, 61-1420/2010) and the Crafoord Foundation (20110817) to C. Möller. Jenny Andersson provided unpublished map data (bedrock map project Falkenberg) and practical and moral support throughout the project. Inger Lundqvist is thanked for generous hospitality during fieldwork. Discussions with Jenny Andersson, Brendan Dyck, Inger Lundqvist, Anders Scherstén, and Mike Stephens are greatly acknowledged. Constructive and thorough reviews by T. Scheiber and L. Menegon improved the manuscript. Editorial handling by G. Viola is greatly appreciated.

References

Alsop, G.I., 1992. Progressive deformation and the rotation of contemporary fold axes in the Ballybofey Nappe, north-west Ireland. Geol. J. 27, 271–283, http://dx.doi.org/10.1002/gj.3350270305

Alsop, G.I., Holdsworth, R.E., Alsop, G.I., Holdsworth, R.E., 2004. The geometry and topology of natural sheath folds: a new tool for structural analysis. J. Struct. Geol. 26, 1561–1589, http://dx.doi.org/10.1016/j.jsg.2004.01.009

Alsop, G.I., Holdsworth, R.E., 2007. Flow perturbation folding in shear zones. Geological Society, London, Special Publications, vol. 272(1)., pp. 75–101.

Alsop, G.I., Holdsworth, R.E., 2012. The three dimensional shape and localisation of deformation within multilayer sheath folds. J. Struct. Geol. 44, 110–128.

Andersson, J., Söderlund, U., Cornell, D., Johansson, L., Möller, C., 1999. Sveconorwegian (Grenvillian) deformation, metamorphism and leucosome formation in SW Sweden, SW Baltic Shield: constraints from a Mesoproterozoic granite intrusion. Precambrian Res. 98, 151–171.

Andersson, J., Möller, C.A., Johansson, L., 2002. Zircon geochronology of migmatite gneisses along the Mylonite Zone (S Sweden): a major Sveconorwegian terrane boundary in the Baltic Shield. Precambrian Res. 114, 121–147.

Andréasson, P.G., Rodhe, A., 1990. Geology of the Protogine Zone south of Lake Vättern, southern Sweden: a reinterpretation. Geol. Föreningens Stockh. Förh. GFF 112 (2), 107–125.

Austin Hegardt, E., Cornell, D.H., Claesson, L., Simakov, S., Stein, H.J., Hannah, J.L., 2005. Eclogites in the central part of the Sveconorwegian, Eastern Segment of the Baltic Shield: support for an extensive eclogite terrane. Geol. Föreningens Stockh. Förh. GFF 127, 221–232.

Åhäll, K.I., Samuelsson, L., Persson, P.O., 1997. Geochronology and structural setting of the 1.38 Ga Torpa granite; implications for charnockite formation in SW Sweden. Geol. Föreningens Stockh. Förh. GFF 119 (1), 37–43.

Bastida, F., Aller, J., Toimil, N.C., Lisle, R.J., Bobillo-Ares, N.C., 2007. Some considerations on the kinematics of chevron folds. J. Struct. Geol. 29, 1185–1200, http://dx.doi.org/10.1016/j.jsg.2007.03.010

Bastida, F., Aller, J., Fernández, F.J., Lisle, R.J., Bobillo-Ares, N.C., Menéndez, O., 2014. Recumbent folds: key structural elements in orogenic belts. Earth-Sci. Rev. 135, 162–183.

Bell, T.H., 1978. Progressive deformation and reorientation of fold axes in a ductile mylonite zone: the Woodroffe thrust. Tectonophysics 44, 285–321.

Berglund, J., (Ph.D. thesis) 1997. Mid-Proterozoic evolution in southwestern Sweden. Earth Sciences Centre, Göteborg University. Publication A16, pp. 132.
Bingen, B., Davis, W.J., Hamilton, M.A., Engvik, A., Stein, H.J., Skår, Ø., Nordgulen, Ø., 2008. Geochronology of high-grade metamorphism in the Sveconorwegian belt, S Norway: U–Pb, Th–Pb and Re–Os data. Nor. J. Geol. 88, 13–42.
Brander, L., Appelquist, K., Cornell, D., Andersson, U.B., 2012. Igneous and metamorphic geochronologic evolution of granitoids in the central Eastern Segment, southern Sweden. Int. Geol. Rev. 54 (5), 509–546.
Brun, J.P., Merle, O., 1988. Experiments on folding in spreading-gliding nappes. Tectonophysics 145 (1–2), 129–139, http://dx.doi.org/10.1016/0040-1951(88)90321-6
Bucher, W.H., 1956. Role of gravity in orogenesis. Bull. Geol. Soc. Am. 67, 1295–1318.
Bucher, W.H., 1962. An experiment of the role of gravity in orogenic folding. Geol. Rundsch. 52, 804–810.
Carreras, J., Druget, E., Griera, A., 2005. Shear zone-related folds. J. Struct. Geol. 27, 1229–1251.
Christoffel, C.A., Connelly, J.N., Åhäll, K.I., 1999. Timing and characterization of recurrent pre-Sveconorwegian metamorphism and deformation in the Varberg–Halmstad region of SW Sweden. Precambrian Res. 98, 173–195, http://dx.doi.org/10.1016/S0301-9268(99)00046-7
Cobbold, P., Watkinson, A., 1981. Bending anisotropy: a mechanical constraint on the orientation of fold axes in an anisotropic medium. Tectonophysics 72, T1–T10.
Connelly, J.N., Berglund, J., Larson, S.Å., 1996. Thermotectonic evolution of the Eastern Segment of southwestern Sweden: tectonic constraints from U–Pb geochronology. Geological Society, London, Special Publications, vol. 112., pp. 297–313, http://dx.doi.org/10.1144/GSL.SP.1996.112.01.16
Coward, M.P., Potts, G.J., 1983. Complex strain patterns developed at the frontal and lateral tips to shear zones and thrust zones. J. Struct. Geol. 5, 383–399.
Duretz, T., Kaus, B.J.P., Schulmann, K., Gapais, D., Kermarrec, J.J., 2011. Indentation as an extrusion mechanism of lower crustal rocks: insight from analogue and numerical modelling, application to the Eastern Bohemian Massif. Lithos 124 (1), 158–168.
Escher, A., Watterson, J., 1974. Stretching fabrics, folds and crustal shortening. Tectonophysics 22, 223–231, http://dx.doi.org/10.1016/0040-1951(74)90083-3
Fowler, A.R., El Kalioubi, B., 2002. The Migif–Hafafit gneissic complex of the Egyptian Eastern Desert: fold interference patterns involving multiply deformed sheath folds. Tectonophysics 346 (3), 247–275.
Foreman, R., Andersen, T.B., Wheeler, J., 2005. Eclogite-facies polyphase deformation of the DrØsdal eclogite, Western Gneiss Complex, Norway, and implications for exhumation. Tectonophysics 398, 1–32.
Fossen, H., Teyssier, C., Whitney, D.L., 2013. Transtensional folding. J. Struct. Geol. 56, 89–102.
Ghosh, S.K., Khan, D., Sengupta, S., 1995. Interfering folds in constrictional deformation. J. Struct. Geol. 17, 1361–1373.
Henderson, J.R., 1981. Structural analysis of sheath folds with horizontal X-axes, northeast Canada. J. Struct. Geol. 3 (3), 203–210.
Hubbard, F.H., 1975. The Precambrian crystalline complex of south-western Sweden. The geology and petrogenetic development of the Varberg region. Geol. Föreningens Stockh. Förh. GFF 97.3 (1975), 223–236.
Hudleston, P.J., Treagus, S.H., 2010. Information from folds: a review. J. Struct. Geol. 32 (12), 2042–2071.
Johansson, L., Möller, C., Söderlund, U., 2001. Geochronology of eclogite facies metamorphism in the Sveconorwegian Province of SW Sweden. Precambrian Res. 106, 261–275.
Krabbendam, M., Dewey, J.F., 1998. Exhumation of UHP rocks by transtension in the Western Gneiss Region, Scandinavian Caledonides. In: Holdsworth, R.E., Strachan, R.A., Dewey, J.F. (Eds.), Continental Transpressional and Transtensional Tectonics, vol. 135. Geological Society of London Special Publication, pp. 159–181.
Lacassin, R., Mattauer, M., 1985. Kilometre-scale sheath fold at Mattmark and implications for transport direction in the Alps. Nature 315, 739–774, http://dx.doi.org/10.1038/315739a0739-742
Morales, L.F., Casey, M., Lloyd, G.E., Williams, D.M., 2011. Kinematic and temporal relationships between parallel fold hinge lines and stretching lineations: a microstructural and crystallographic preferred orientation approach. Tectonophysics 503, 207–221.
Möller, C., Andersson, J., Söderlund, U., Johansson, L., 1997. A Sveconorwegian deformation zone (system?) within the Eastern Segment, Sveconorwegian orogen of SW Sweden-a first report. Geol. Föreningens Stockh. Förh. GFF 119, 73–78.
Möller, C., 1998. Decompressed eclogites in the Sveconorwegian (–Grenvillian) orogen of SW Sweden: petrology and tectonic implications. J. Metamorph. Geol. 16, 641–656.
Möller, C., 1999. Sapphirine in SW Sweden: a record of Sveconorwegian (–Grenvillian) late-orogenic tectonic exhumation. J. Metamorph. Geol. 17, 127–141.
Möller, C., Andersson, J., Lundqvist, I., Hellström, F.A., 2007. Linking deformation, migmatite formation and zircon U–Pb geochronology in poly-metamorphic orthogneisses, Sveconorwegian Province, Sweden. J. Metamorph. Geol. 25, 727–775.
Möller, C., Andersson, J., Dyck, B., Antal Lundin, I., 2015. Exhumation of an eclogite terrane as a hot migmatitic nappe, Sveconorwegian orogen. Lithos 226 (June), 147–168, http://dx.doi.org/10.1016/j.lithos.2014.12.013, ISSN 0024-4937.
Passchier, C.W., Trouw, R.A.J., 2005. Microtectonics. Springer-Verlag, Berlin, 366 pp.
Passchier, C.W., den Brok, S.W.I., van Gool, J.A.M., Marker, M., Manatschal, G., 1997. A laterally constricted shear zone system – the Nordre Strømfjord steep belt, Nagssugtoqidian Orogen, W. Greenland. Terra Nova 9, 199–202.
Petersson, A., Scherstén, A., Andersson, J., Möller, C., 2013. Zircon U–Pb and Hf–isotZircon U–Pb and Hf–isotopes from the eastern part of the Sveconorwegian Orogen, SW Sweden: implications for the growth of Fennoscandia. Geological Society, London, Special Publications, vol. 389., pp. SP389–SP392.
Pinan-Llamas, A., Andersson, J., Möller, C., 2015. Polyphasal foreland-vergent deformation in a deep parautochthonous section of the 1 Ga Sveconorwegian orogen. In: Roberts, N., Viola, G., Slagstad, T. (Eds.), The structural, metamorphic and magmatic evolution of Mesoproterozoic orogens. Special issue of Precambrian Res. (this volume).
Ramsay, J.G., Huber, M.I., 1983. The Techniques of Modem Structural Geology. Strain Analysis, vol. 1. Academic Press, London.
Reber, J.E., Dabrowski, M., Schmid, D.W., 2012. Sheath fold formation around slip surfaces. Terra Nova 24 (5), 417–421, http://dx.doi.org/10.1111/j.1365-3121.2012.01081.x
Reber, J.E., Galland, O., Cobbold, P.R., Le Carlier de Veslud, C., 2013. Experimental study of sheath fold development around a weak inclusion in a mechanically layered matrix. Tectonophysics 586, 130–144.
Ridley, J., 1986. Parallel stretching lineations and fold axes oblique to a shear displacement direction – a model and observations. J. Struct. Geol. 8, 647–653.
Rosas, F., Marques, F.O., Luz, A., Coelho, S., 2002. Sheath folds formed by drag induced by rotation of rigid inclusions in viscous simple shear flow: nature and experiment. J. Struct. Geol. 24, 45–55.
Sawyer, E.W., Dombrowski, C., Collins, W.J., 1999. Movement of melt during synchronous regional deformation and granulite-facies anatexis: an example from the Wuluma Hills, central Australia. Special Publication – Geological Society Of London, vol. 168., pp. 221–238.
Stephens, M.B., Wahlgren, C.A.-H., Weijermars, R., Cruden, A.R., 1996. Left-lateral transpressive deformation and its tectonic implications, Sveconorwegian orogen, Baltic Shield, southwestern Sweden. Precambrian Res. 79, 261–279.
Söderlund, U., Jarl, L.G., Persson, P.O., Stephens, M.B., Wahlgren, C.A.-H., 1999. Protolith ages and timing of deformation in the eastern, marginal part of the Sveconorwegian orogen, southwestern Sweden. Precambrian Res. 94, 29–48.
Söderlund, U., Möller, C., Andersson, J., Johansson, L., Whitehouse, M.J., 2002. Zircon geochronology in polymZircon geochronology in polymetamorphic gneisses in the Sveconorwgian orogen, SW Sweden: ion microprobe evidence for 1.46–1.42 Ga and 0.98–0.96 Ga reworking. Precambrian Res. 113, 193–225.
Söderlund, U., Isachsen, C.E., Bylund, G., Heaman, L.M., Patchett, P.J., Vervoort, J.D., Andersson, U.B., 2005. U–Pb baddeleyite ages and Hf, Nd isotope chemistry constraining repeated mafic magmatism in the Fennoscandian Shield from 1.6 to 0.9 Ga. Contrib. Mineral. Petrol. 150 (2), 174–194.
Ulmius, J., Andersson, J., Möller, C., 2015. Hallandian high temperature metamorphism at 1.45 Ga in continent Baltica: P-T evolution and SIMS U–Pb zircon ages of aluminous gneisses, SW Sweden. In: Roberts, N., Viola, G., Slagstad, T. (Eds.), The structural, metamorphic and magmatic evolution of Mesoproterozoic orogens. Special issue of Precambrian Research (this volume).
Vacas Peña, J.M., Martínez Catalán, J.R., 2004. A computer program for the simulation of folds of different sizes under the influence of gravity. Comput. Geosci. 30 (1), 33–43.
Vernon, R.H., Paterson, S.R., 2001. Axial-surface leucosomes in anatectic migmatites. Tectonophysics 335 (1), 183–192.
Viola, G., Henderson, I.H.C., Bingen, B., Hendriks, B.W.H., 2011. The Grenvillian–Sveconorwegian orogeny in Fennoscandia: back thrusting and extensional shearing along the "Mylonite Zone". Precambrian Res. 189, 368–388.
Warren, C.J., Beaumont, C., Jamieson, R.A., 2008. Modelling tectonic styles and ultra-high pressure (UHP) rock exhumation during the transition from oceanic subduction to continental collision. Earth Planet. Sci. Lett. 267 (1), 129–145.
Watkinson, A.J., Cobbold, P.R., 1981. Axial directions of folds in rocks with linear/planar fabrics. J. Struct. Geol. 3 (3), 211–217.
Weinberg, R.F., Mark, G., 2008. Magma migration, folding, and disaggregation of migmatites in the Karakoram Shear Zone, Ladakh, NW India. Geol. Soc. Am. Bull. 120 (7–8), 994–1009.
Xypolias, P., Alsop, G.I., 2014. Regional flow perturbation folding within an exhumation channel: a case study from the Cycladic Blueschists. J. Struct. Geol. 62, 141–155, http://dx.doi.org/10.1016/j.jsg.2014.02.001
Zulauf, J., Zulauf, G., 2005. Coeval folding and boudinage in four dimensions. J. Struct. Geol. 27 (6), 1061–1068.

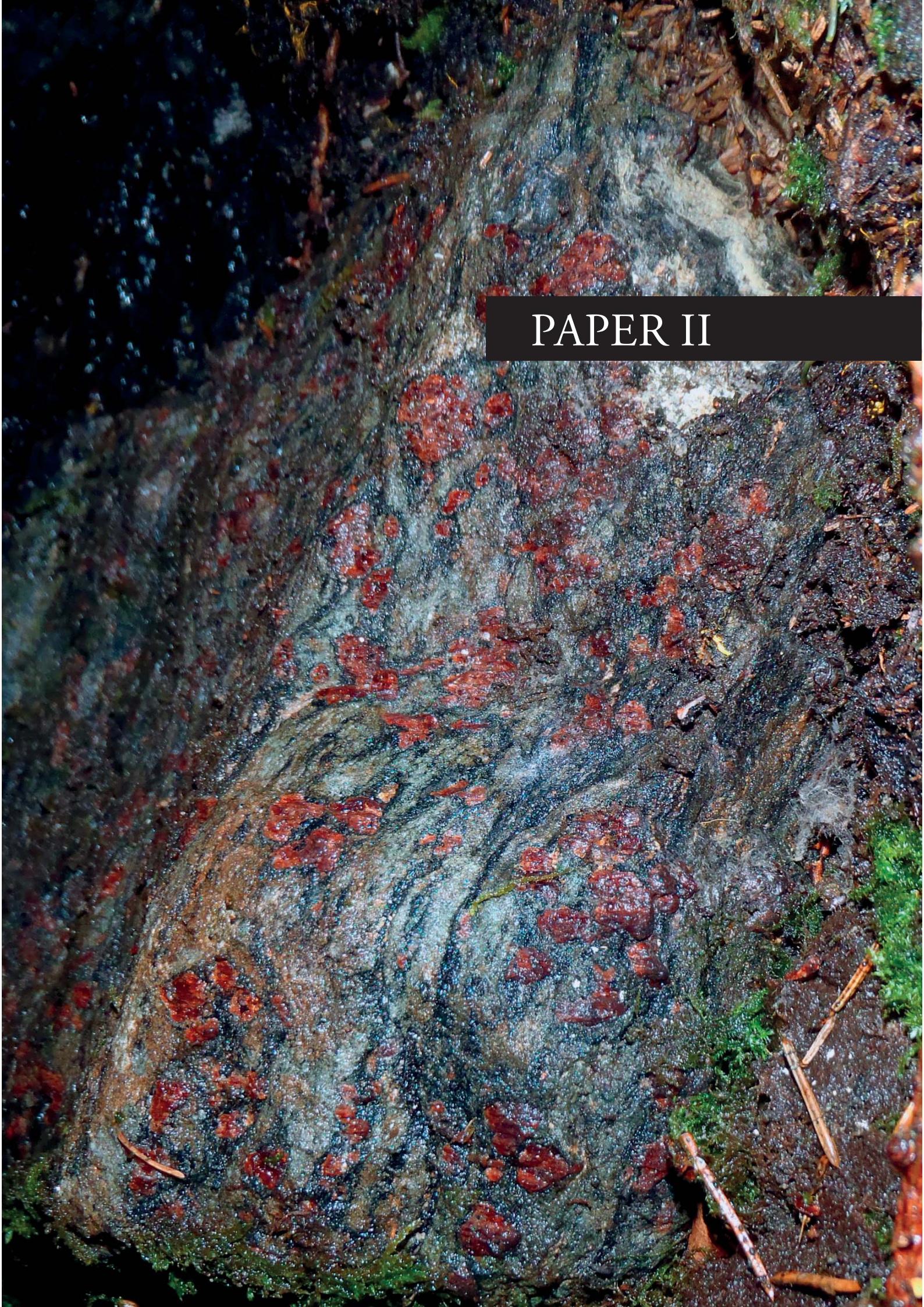

PAPER II

P–T evolution of Precambrian eclogite in the Sveconorwegian orogen, SW Sweden.

Lorraine Tual [1]*, Pavel Pitra [2], Charlotte Möller [1]

[1] Department of Geology, Lund University, Sölvegatan 12, SE-223 62 Lund, Sweden

[2] Géosciences Rennes, UMR CNRS 6118, Université Rennes 1, 35042 Rennes, Cedex, France

Short title: *P–T* evolution of Precambrian eclogite, SW Sweden.

** Corresponding author: lorraine.tual@gmail.com; +46729373025*

ABSTRACT

Precambrian eclogites in the eastern Sveconorwegian orogen are evidence of deep tectonic burial of the continental crust at c. 1Ga. We have determined the prograde and decompressional *P–T* path for Sveconorwegian eclogite using a pseudosection approach together with microtextural analysis. Cores of garnet record a first prograde and syn-deformational stage along a Barrovian geothermal gradient from ~690 °C 7.5 kbar to 710 °C 8.5 kbar. Garnet rims grew during further burial to ~850–900 °C at 16-19 kbar, along a steep d*P*/d*T* gradient. Matrix reequilibration associated with subsequent near-isothermal decompression and partial exhumation is estimated at ~810–870 °C and 8–11.5 kbar. Whereas the assumption of H_2O saturation and the use of analysed value of FeO/Fe_2O_3 yield results that account for the petrologic observations, it is argued that the fractionation of FeO in sulfides influences strongly the calculated phase diagrams and must be taken into account. Fast burial, exhumation and subsequent cooling are supported by the steepness of both the prograde and the retrograde *P–T* paths as well as the preservation of garnet growth zoning and the symplectitic reaction textures. These features are compatible with burial of the eclogite-bearing crust as part of the underthrusting plate (Eastern Segment, continent Baltica) in a collisional setting that led to an effectively doubled crustal thickness and subsequent exhumation of the eclogites through tectonic extrusion. Our results are in accordance with regional structural and petrologic relationships, which demonstrate foreland-vergent partial exhumation of the eclogite-bearing nappe along a basal thrust zone and support a major collisional stage at c. 1 Ga.

***Keywords*:** *P–T path, pseudosection, Precambrian, eclogite, Sveconorwegian.*

INTRODUCTION

Pressure–temperature (*P–T*) paths of exhumed high-pressure rocks place fundamental constraints on the tectonothermal evolution of an orogen. Eclogites are markers of collision zones, in particular important for old orogens, which today occur as dispersed fragments over the Earth. The eclogite-bearing region of SW Sweden represents such a zone, critical for the interpretation of the Sveconorwegian orogen and global-scale Precambrian geodynamics.Eclogites in the Sveconorwegian orogen are structurally confined to a regional recumbent fold nappe in the eastern part of the orogen (Möller *et al.*, 2015), with the base of the nappe marked by a high-temperature shear zone (Tual *et al.*, 2015). They form lenses within migmatitic felsic gneisses, and are interpreted as an original part of the continental crust (e.g. Möller *et al.*, 2015). The general *P–T* path for the Sveconorwegian eclogites has been outlined by Möller (1998, 1999). The *P–T* conditions of reequilibration during decompression were bracketed at ~ 770 ± 50 °C and 10.5 ± 2 kbar; the peak-pressure conditions were only broadly estimated at *P* >15 kbar (Möller, 1998; Austin Hegardt *et al.*, 2005). The prograde eclogite-facies metamorphism was first dated by Johansson *et al.* (2001; 972 ± 14 Ma, U-Pb on zircon), and later refined at c. 988 ± 6Ma (SIMS U-Pb on zircon, Möller *et al.*, 2015).

In this study we calculate the *P–T* path of two eclogite samples of different bulk composition, and discuss the constraints on the geodynamic evolution. Our *P–T* data show burial of the continental crust to ~18 kbar (~65 km depth) at 860 °C, implying a doubled thickness of the continental crust at the end

of the Sveconorwegian orogeny, and subsequent tectonic exhumation of the eclogites – a scenario similar to the Himalayas.

GEOLOGICAL SETTING

The Sveconorwegian orogen

The 1.1-0.9 Ga Sveconorwegian orogen is part of the global Grenvillian-aged orogenic belt (Rodinia supercontinent). It is composed of five crustal segments, which are separated by roughly N-S-trending crustal shear zones; from west to east these are the Telemarkia, Bamble, Kongsberg, and Idefjorden Terranes, and the Eastern Segment (Fig. 1; Bingen *et al.*, 2005; Bingen *et al.*, 2008a and references therein). A west-dipping belt of intense ductile deformation, the Mylonite Zone, separates the Idefjorden Terrane from the Eastern Segment. Four main tectono-metamorphic events have been identified (Bingen *et al.*, 2008a): The c. 1.14 Ga Arendal phase in the Bamble and Kongsberg Terranes involved metamorphism at granulite- and upper amphibolite-facies at intermediate pressures (Engvik *et al.*, 2016). The c. 1.05-1.02 Ga Agder phase is recorded in the Telemarkia and Idefjorden Terranes, as mostly greenschist- to upper amphibolite-facies metamorphism. High-pressure granulite-facies conditions have however been recorded locally in the Idefjorden Terrane just west of the Mylonite Zone (Söderlund *et al.*, 2008). In Telemarkia, a granite suite intruded at 1.05-1.02 Ga (Bingen, 1989; Bingen & van Breemen, 1998; Bingen & Solli, 2009; Slagstad *et al.*, 2012). The subsequent Falkenberg phase at 0.99-0.98 Ga caused high-pressure and high-temperature metamorphism of the southern Eastern Segment, reaching eclogite-facies conditions preserved in an eclogite-bearing nappe (Figs. 1 & 2; Möller *et al.*, 2015). In the Eastern Segment, partial melting at 0.98-0.96 Ga was followed by intrusion of pegmatite and mafic dykes (e.g. Möller *et al.*, 2007; 2015). The post-collisional Dalane phase includes the intrusion of an Anorthosite-Mangerite-Charnockite-Granite (AMCG) suite in terranes west of the Mylonite Zone, and associated high-temperature metamorphism in Telemarkia at c. 0.93-0.92 Ga (e.g., Vander Auwera *et al.*, 2011).

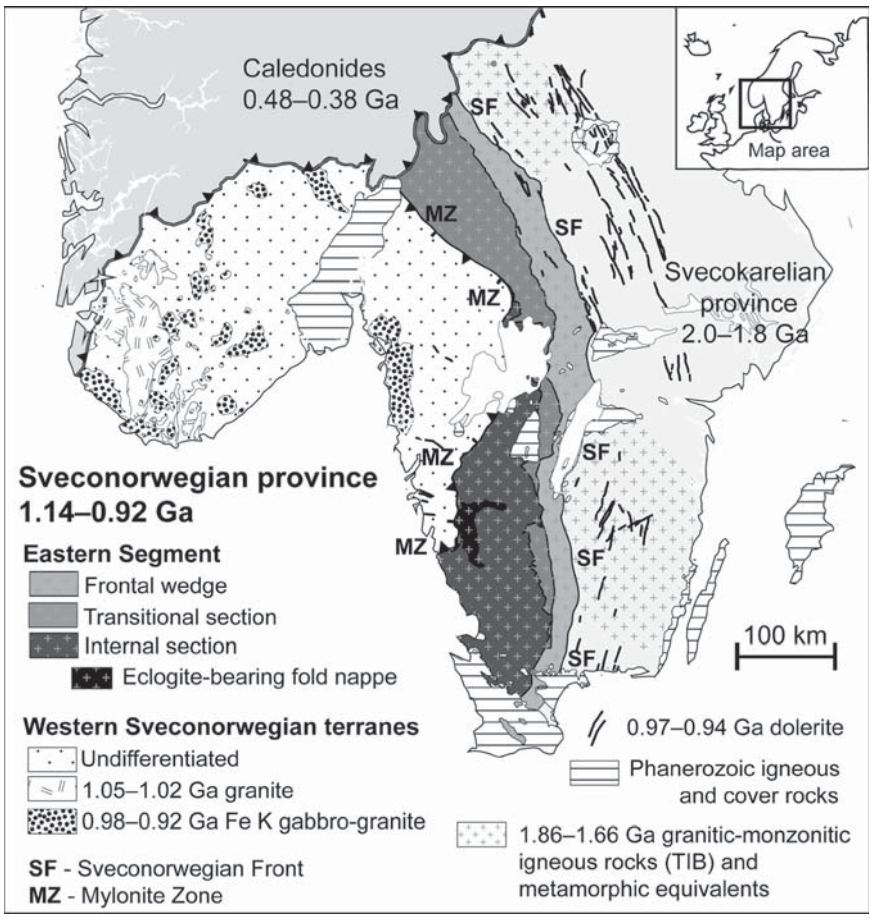

Figure 1: Sketch map of the Sveconorwegian orogen showing the Eastern Segment (dark grey tones) and western Sveconorwegian terranes (white), separated by ductile deformation zones (terrane divisions after Bingen et al., 2008a; extent of Sveconorwegian magmatism in Telemarkia after Slagstad et al., 2012). Figure based on 1:5 M Fennoscandian map database and Geological Survey of Sweden 1:1 M Bedrock map database, template provided by J. Andersson. TIB – Transcandinavian Igneous Belt

The Eastern Segment and the eclogite-bearing nappe

The bedrock east of the Sveconorwegian orogen (Fig. 1) comprises 2.0-1.8 Ga Svecofennian igneous and meta-igneous rocks (e.g. Stephens *et al.*, 2009; Stephens & Andersson, 2015) and rocks of the 1.85–1.65 Ga Transcandinavian Igneous Belt (TIB). These lithologies can be followed westwards into the Eastern Segment where they become increasingly deformed. Most of the Eastern Segment is made up of c. 1.7 Ga orthogneisses equivalent to the TIB intrusions (e.g. Wahlgren *et al.*, 1994; Söderlund *et al.*,

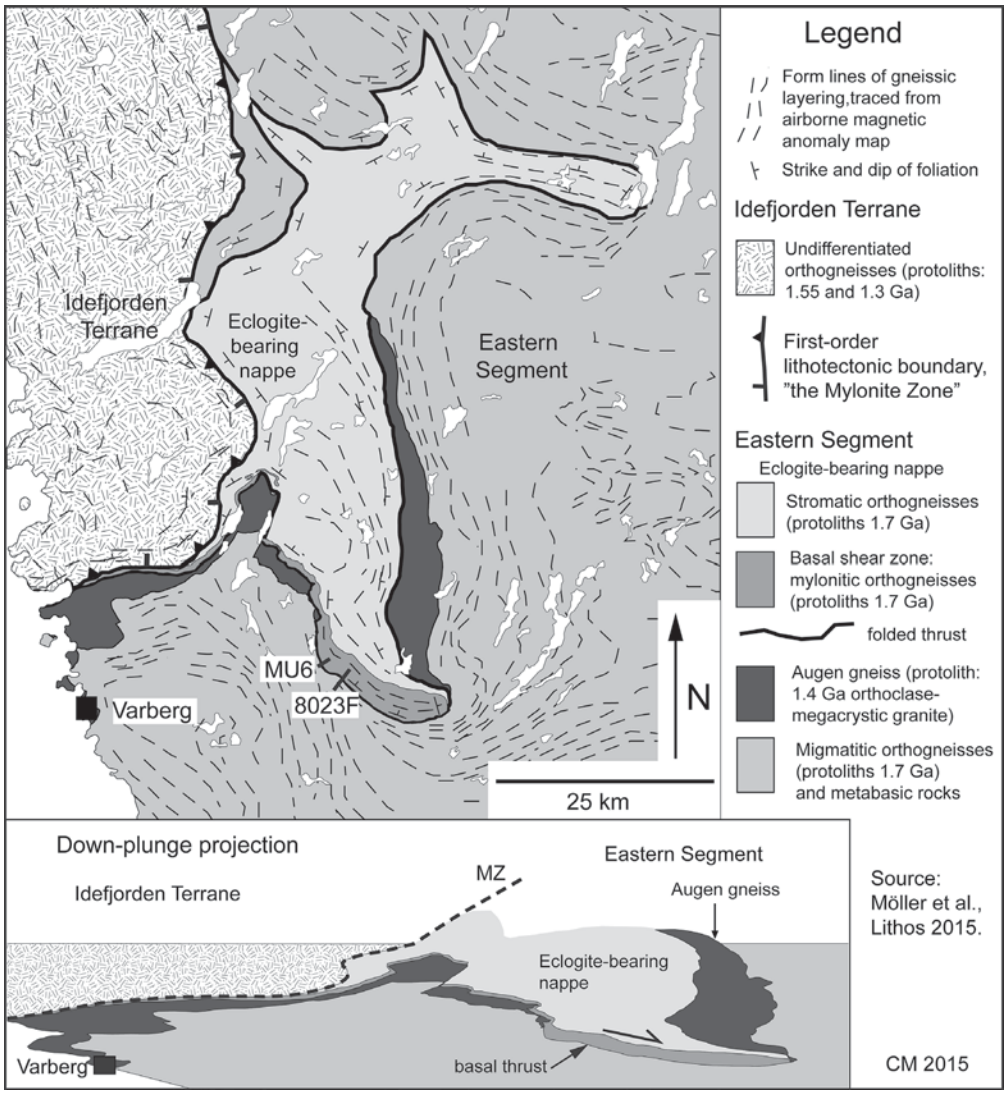

Figure 2: (a) Sketch map showing the eclogite-bearing terrane in light grey; black= augen gneiss, after Möller et al. (2015); parts of this map are based on regular bedrock map data from the Geological Survey of Sweden). Locations of the investigated samples (MU6, 8023F) are indicated. (b) E–W profile across the eclogite-bearing nappe from Möller et al., (2015; constructed by down-plunge projection).

1999, 2002; Andersson *et al.*, 2002; Möller *et al.*, 2007, 2015; Petersson *et al.*, 2015). The eastern limit of Sveconorwegian ductile deformation is marked as the Sveconorwegian Front in Figure 1.

A 50 x 75 km large eclogite-bearing fold nappe is situated in the internal section of the Eastern Segment, at the contact with the overlying Idefjorden Terrane (Figs. 1 & 2; Möller *et al.*, 2015). Rocks enclosing this nappe are upper amphibolite- and high-pressure granulite-facies gneisses (Johansson *et al.*, 1991; Wang & Lindh, 1996), which are in most places migmatitic and show penetrative deformation and polyphasal folding (Andersson *et al.*, 1999, 2002; Söderlund *et al.*, 2002; Möller *et al.*, 2007, 2015; Hansen *et al.*, 2015; Piñán-Llamas *et al.*, 2015). The contact of the nappe with the surrounding orthogneisses is marked by semi-continuous 1.4 Ga augen orthogneiss (Fig. 2; Möller *et al.*, 2015).

Eclogite occurs as lenses in stromatic migmatite gneisses within the fold nappe, and in the basal high-temperature shear zone (Fig. 2; Möller, 1998, 1999; Austin Hegardt *et al.*, 2005; Möller *et al.*, 2015; Tual *et al.*, 2015). Orthogneisses within the eclogite-bearing nappe have been dated at 1.74-1.66 Ga, demonstrating that the nappe is indigenous to the Eastern Segment. The nappe represents a part of the continental crust that experienced westward tectonic burial at eclogite-facies conditions beneath the Idefjorden Terrane, and was followed by eastward, foreland-directed, tectonic exhumation (Möller *et al.*, 2015). The eclogites were part of the Baltica continental crust prior to the onset of the Sveconorwegian orogeny and consequently do not represent a detached piece of an oceanic slab (Johansson *et al.*, 2001; Möller *et al.*, 2015).

The prograde metamorphism leading to eclogitization was first dated at 972 ± 14 Ma (Johansson *et al.*, 2001) and recently refined at 988 ± 6 Ma (Möller *et al.*, 2015). The high-temperature tectonites from the basal thrust zone testify to tectonic exhumation of the eclogite-bearing nappe and stalling at a mid-crustal orogenic level at ~10 kbar (~40 km; Möller *et al.*, 2015; Tual *et al.*, 2015). Syn-deformational leucosomes indicate that nappe emplacement was aided by the presence of melt. The crystallization of leucosome has been bracketed between 976 ± 6 Ma and 956 ± 7 Ma (Möller *et al.*, 2015).

Various types of eclogite are present in the nappe. The field relations, petrology and structural geology of the eclogites and their country rocks have been documented in detail in Möller (1998, 1999), Austin Hegardt *et al.*, 2005, Möller *et al.* (2015), and Tual *et al.* (2015). The samples studied in this paper were taken from mafic bodies in the basal shear zone (Fig. 2a), and represent rare varieties, with limited retrogression, of Fe-Ti-rich eclogite (sample MU6) and kyanite-bearing eclogite (sample 8023F).

METHODS

Mineral X-ray maps and analyses were performed using a JEOL JXA-8200 Superprobe, fitted with five wavelength dispersive spectrometers (WDS) and an energy dispersive spectrometer (EDS) at the University of Copenhagen. The analytical conditions were set at 15.0 kV acceleration voltage and 15 nA probe current. Complementary analyses and imaging were made using a Hitachi 3400N scanning electron microscope equipped with an Oxford EDS. Bulk rock compositions and FeO (vs. Fe_2O_3) determination were analyzed in ACME Vancouver (Canada), from powders prepared at the Lund University using a tungsten-carbide mill.

Mineral abbreviations are those used by THERMOCALC (Holland & Powell, 2011). Pseudosections were calculated using THERMOCALC 3.4 (Powell *et al.*, 1998) and the dataset ds55 (updated Nov. 2003; Holland & Powell, 1998) in the system NCKFMASHTO (Na2O - CaO - K2O - FeO - MgO - Al2O3 - SiO2 - H2O - TiO2 - O). Mixing models for solid solutions were taken from Diener *et al.* (2007; amphibole, clinopyroxene), White *et al.* (2007; garnet, biotite), Holland *et al.* (1998; chlorite), Coggon & Holland (2002; paragonite, muscovite), Holland & Powell (2003; plagioclase, K-feldspar), White *et al.* (2002; magnetite, spinel), Holland & Powell (1998; talc, epidote), White *et al.* (2000; hematite, ilmenite). Epidote was modeled as a solid solution rather than the pure end-member (clino)zoisite, to account for the small amount of Fe^{3+} in the analyzed crystals. In the phase diagrams, the term hornblende (hb) is used *sensu lato* (cf. Dale *et al.*, 2005) rather than in the strict sense of Leake *et al.* (1997).

Mineral compositions are given in mole % unless stated otherwise. Cpfu = cations per formula unit. X_{Fe} = $Fe^{2+}/(Fe^{2+}+Mg)$; *Grs* = 100xCa/(Ca+Fe^{2+}+Mg+Mn); *Prp* = 100xMg/(Ca+Fe^{2+}+Mg+Mn); *Alm* = 100xFe^{2+}/(Ca+Fe^{2+}+Mg+Mn); *Sps* = 100xMn/(Ca+Fe^{2+}+Mg+Mn); *An* = 100xCa/(Ca+Na+K); *Jd* = 100xNa/(Na+Ca). The symbol "→" is used to describe the core to rim evolution.

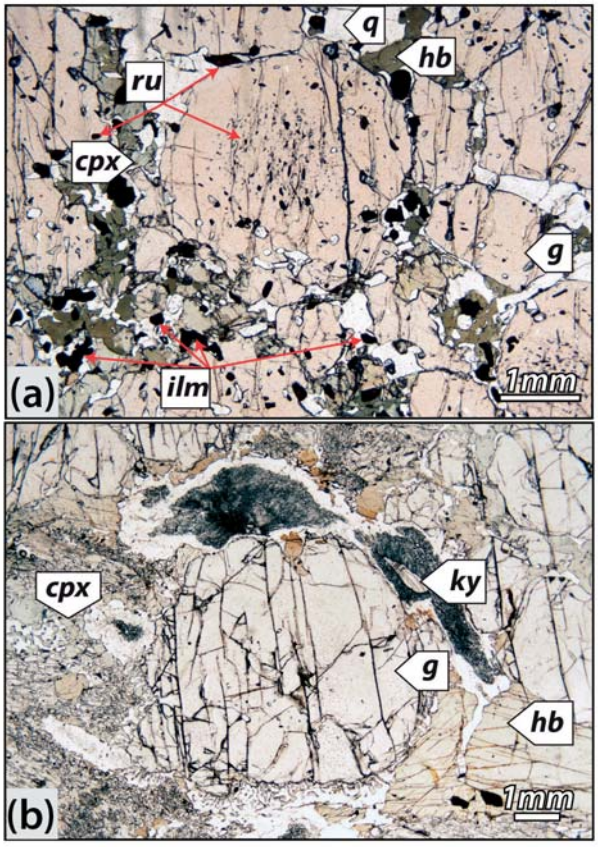

Figure 3: Photomicrographs of texures in the investigated samples. (a) Fe-Ti eclogite (MU6) with high-pressure assemblage garnet + quartz + clinopyroxene + rutile. Clinopyroxene (cpx) is partly replaced by amphibole (hb; dark brown-green). Rutile (ru) is partly to completely replaced by ilmenite (ilm) in the matrix. (b) Kyanite eclogite (8023F) with a relict high-pressure assemblage kyanite + garnet + clinopyroxene + pargasitic amphibole (hb). Dark fine-grained domains are symplectite of sapphirine + plagioclase ± corundum. They locally rim relict kyanite and are surrounded by plagioclase.

PETROGRAPHY AND MINERAL CHEMISTRY

Two samples of different bulk rock composition were selected for a detailed petrological analysis: Fe-Ti-rich quartz-bearing eclogite and Mg-Al-rich kyanite-bearing eclogite (Fig. 3 a, b). Textures and mineral compositions, including detailed zoning patterns, of these rock types are documented in Möller (1998, 1999); here we focus on the two samples that were selected for thermodynamic modeling. Table 1 shows representative analyses of minerals; Table 2 shows whole-rock composition of the two samples in wt. %.

Fe-Ti eclogite (sample MU6)

Sample MU6 represents a Fe-Ti-rich layer from a 2.5 x 1.5 km large eclogite-bearing mafic body (Fig. 2a; WGS84: 57°09'21.3"N 12°42'49.4"E, locality: Ammås). The dominant mineral assemblage is garnet (c. 45%) + quartz (15–30%) + clinopyroxene (c. 15-35%) + rutile (c. 5%; Fig. 3a). Accessory minerals include apatite, zircon and ilmenite.

Garnet generally has a distinct core-and-rim structure. Elongated inclusions in the core define straight, gently bent or locally sigmoidal trails, and comprise rutile, quartz, plagioclase and locally hornblende (Fig. 4). A nearly inclusion-free inner rim separates the core from the outer rim, where rutile and quartz grains are 5-10 times larger and unoriented or their orientation follows the garnet rim (Fig. 4c-e). There is a smooth rimward decrease of almandine, spessartine, and X_{Fe} (*Alm*55→46, *Sps*3→1, X_{Fe}0.76→0.61) balanced by a smooth increase of pyrope (*Prp*17→32). There is a slight increase in grossular from the garnet core to the inner rim (*Grs*25→28), followed by a plateau in the inner rim, and a decrease towards the outermost rim (*Grs*25-26; Fig. 4b-e; Table 1a).

Clinopyroxene grains are generally 2-10 mm large. They commonly contain inclusions of plagioclase (up to 50 vol.%; Fig. 5a) and have the composition of diopside with low jadeite content (X_{Fe}0.10-0.22 but cluster around 0.18-0.20, *Jd*2-10, Al = 0.05-0.32 cpfu; Fig. 4a; Table 1). Area analyses (covering ~ 2 x 1 mm) of diopside + plagioclase gave, however, approximate values of X_{Fe}0.29 and *Jd*15-19. Clinopyroxene inclusions in garnet rims are more magnesian (X_{Fe}0-0.13). The Ca-Tschermak component ranges between 0 and 10% regardless of textural position (Table 1a). Clinopyroxene is locally partly replaced by amphibole (Fig. 5b).

Table 1a: Representative mineral analyses from the Fe-Ti eclogite (MU6): garnet and clinopyroxene.

Mineral	g	g	g	g	g	g	cpx	cpx	cpx	cpx	cpx	cpx
Sample	MU6	MU6	MU6	MU6	MU6	MU6	MU6	MU6	MU6	MU6	MU6	MU6
Name	6p245	6p251	6p225	6p270	6p205	6p299	6i3	6i4	6a123	6a215	6a208	6acp3
Location	core	core	outer core	outer core	rim	rim	inc g rim	inc g rim	mat	mat	mat	reint.
SiO_2	37.87	37.59	37.75	38.14	38.46	38.89	51.32	51.57	48.69	49.94	50.57	53.17
TiO2	0.09	0.05	0.30	0.08	0.04	0.04	0.36	0.33	0.82	0.52	0.45	0.33
Al_2O_3	20.62	20.76	21.20	21.39	21.72	22.03	4.02	3.64	6.21	5.89	5.51	11.4
Cr_2O_3	0.00	0.00	0.00	0.07	0.00	0.03	0.00	0.00	0.03	0.00	0.00	0.06
FeO*	25.51	26.58	25.84	26.04	23.33	22.88	7.34	7.07	9.56	8.30	8.78	6.42
MgO	4.30	4.39	4.98	5.11	7.40	7.58	13.62	13.94	13.55	12.67	12.38	8.73
MnO	1.45	1.55	0.98	1.07	0.19	0.26	0.06	0.01	0.03	0.05	0.03	0.00
CaO	8.99	8.76	9.08	9.03	8.91	8.89	23.13	23.21	20.28	22.01	22.24	17.63
Na_2O	0.07	0.02	0.02	0.02	0.03	0.02	0.90	0.85	0.87	0.81	0.89	2.24
K_2O	0.05	0.01	0.01	0.00	0.00	0.00	0.01	0.01	0.07	0.01	0.02	0.10
Sum	98.96	99.71	100.14	100.96	100.09	100.62	100.76	100.63	100.10	100.21	100.86	100.08
Si	3.00	2.96	2.94	2.95	2.95	2.96	1.88	1.89	1.80	1.84	1.86	1.96
Ti	0.01	0.00	0.02	0.01	0.00	0.00	0.01	0.01	0.02	0.01	0.01	0.01
Al	1.92	1.93	1.95	1.95	1.96	1.98	0.17	0.16	0.27	0.16	0.14	0.49
Cr	0.00	0.00	0.00	0.00	0.00	0.00	0.00	0.00	0.00	0.00	0.00	0.00
Fe^{2+}	1.60	1.60	1.55	1.54	1.35	1.36	0.11	0.10	0.14	0.17	0.19	0.20
Fe^{3+}	0.09	0.15	0.13	0.14	0.15	0.10	0.12	0.11	0.15	0.08	0.08	0.00
Mg	0.51	0.52	0.58	0.59	0.85	0.86	0.74	0.76	0.75	0.70	0.68	0.48
Mn	0.10	0.10	0.07	0.07	0.01	0.02	0.00	0.00	0.00	0.00	0.00	0.00
Ca	0.76	0.74	0.76	0.75	0.73	0.73	0.91	0.91	0.80	0.87	0.88	0.70
Na	0.01	0.00	0.00	0.00	0.01	0.00	0.06	0.06	0.06	0.06	0.06	0.16
K	0.01	0.00	0.00	0.00	0.00	0.00	0.00	0.00	0.00	0.00	0.00	0.00
Sum	8.00	8.00	8.00	8.00	8.00	8.00	4.00	4.00	4.00	4.00	4.00	4.00
X_{Fe}	0.76	0.76	0.73	0.72	0.62	0.61	0.13	0.12	0.16	0.20	0.22	0.29
XAlm	0.54	0.54	0.53	0.52	0.46	0.46						
XPrp/XJd	0.17	0.17	0.20	0.20	0.29	0.29	0.05	0.04	0.07	0.06	0.06	0.19
XGrs	0.26	0.25	0.26	0.25	0.25	0.25						
XSps/XCaTs	0.03	0.03	0.02	0.02	0.00	0.01	0.00	0.00	0.00	0.04	0.04	-

(* Total Fe oxide as FeO). inc. = inclusion in; out. = outer; coro. = corona; sy. = symplectite; exp. = expelled; c. = close to; reint = reintegrated clinopyroxene (domanial composition of diopside + plagioclase). $X_{Fe} = Fe^{2+}/(Fe^{2+}+Mg)$; XGrs = Ca/(Ca+$Fe^{2+}$+Mg+Mn); XPrp = Mg/(Ca+$Fe^{2+}$+Mg+Mn); XAlm = Fe^{2+}/(Ca+Fe^{2+}+Mg+Mn); XSps = Mn/(Ca+Fe^{2+}+Mg+Mn); XJd = Na/(Na+Ca); XCaTs= Al^{IV}-XJd; XAn= Ca/(Ca+Na+K); XOr = K/(Ca+Na+K)

Table 1b: Representative mineral analyses from the Fe-Ti eclogite (MU6): plagioclase and amphibole.

Mineral	pl	pl	pl	pl	am	am
Sample	MU6	MU6	MU6	MU6	MU6	MU6
Name	6i25	6i26	6a110	6a121	6a124	6i34
Location	inc g core	inc g core	exp. cpx core	exp. cpx core	inc cpx core	inc g
SiO_2	47.76	48.22	55.26	54.43	42.26	42.47
TiO2	0.00	0.00	0.00	0.01	2.03	1.82
Al_2O_3	33.47	32.99	28.48	27.98	10.86	14.02
Cr_2O_3	0.01	0.00	0.00	0.01	0.00	0.02
FeO*	0.25	0.25	0.27	0.15	13.21	12.17
MgO	0.00	0.00	0.00	0.00	13.41	13.05
MnO	0.02	0.00	0.00	0.00	0.04	0.03
CaO	17.03	16.31	10.94	10.43	11.75	12.27
Na_2O	2.18	2.57	5.79	6.04	1.52	1.77
K_2O	0.04	0.01	0.03	0.04	0.17	0.47
Sum	100.76	100.35	100.77	99.09	95.25	98.09
Si	2.18	2.21	2.48	2.48	6.30	6.15
Ti	0.00	0.00	0.00	0.00	0.23	0.20
Al	1.80	1.78	1.51	1.50	1.91	2.40
Cr	0.00	0.00	0.00	0.00	0.00	0.00
Fe^{2+}	0.01	0.01	0.01	0.01	0.94	1.06
Fe^{3+}	0.00	0.00	0.00	0.00	0.71	0.42
Mg	0.00	0.00	0.00	0.00	2.98	2.82
Mn	0.00	0.00	0.00	0.00	0.01	0.00
Ca	0.83	0.80	0.53	0.51	1.88	1.91
Na	0.19	0.23	0.50	0.53	0.44	0.50
K	0.00	0.00	0.00	0.00	0.03	0.09
OH					2.00	2.00
Sum	5.02	5.02	5.02	5.04	17.65	17.68
XAn/X_{Fe}	0.81	0.78	0.51	0.49	*0.24*	*0.27*
XAb/XNa_{M4}	0.19	0.22	0.49	0.51	*0.03*	*0.03*
XOr/$Na+K_A$	0.00	0.00	0.00	0.00	*0.40*	*0.53*

(* Total Fe oxide as FeO). XAn= Ca/(Ca+Na+K); XAb= Na/(Ca+Na+K); XOr = K/(Ca+Na+K)

Table 1c: Representative mineral analyses from the Kyanite eclogite (8023F): garnet and clinopyroxene.

Mineral	g	g	g	g	g	g	cpx	cpx	cpx	cpx	cpx	cpx	cpx
Sample	8023F	8023F	8023F	8023F	8023F	8023F	8023F	8023F	8023F	8023F	8023F	8023F	8023F
Name	2pf446	2pf443	2pf422	2pf414	2pf404	2pf469	8Faird13	8Faird14	8pf913	8pf920	8pf937	8pf956	3pf118
Location	core	core	out. core	in. rim	rim	rim	inc. g	inc. g	core	out. core	out. rim	rim	rim
SiO_2	39.34	39.01	39.29	38.74	39.52	40.01	51.10	50.59	52.41	52.78	52.38	52.75	52.41
TiO2	0.05	0.05	0.05	0.00	0.04	0.00	0.26	0.24	0.29	0.27	0.23	0.24	0.30
Al_2O_3	21.95	22.12	22.1	22.21	22.22	22.79	7.78	8.00	7.83	7.94	7.53	7.50	8.00
Cr_2O_3	0.07	0.04	0.04	0.03	0.10	0.07	0.02	0.07	0.04	0.08	0.08	0.05	0.07
FeO*	20.12	19.95	19.25	18.51	15.98	15.60	4.87	4.31	2.76	2.86	2.81	2.97	3.74
MgO	18.67	18.23	17.19	15.35	13.65	13.36	13.94	12.69	12.51	12.48	12.44	13.02	12.91
MnO	1.86	1.84	1.37	1.13	0.36	0.18	0.08	0.02	0.01	0.02	0.00	0.01	0.03
CaO	8.00	8.19	8.59	8.73	8.59	8.44	19.8	21.7	19.59	19.63	19.62	21.02	20.84
Na_2O	0.01	0.02	0.02	0.03	0.04	0.02	1.33	1.48	2.91	2.98	2.98	2.16	2.29
K_2O	0.01	0.00	0.01	0.00	0.00	0.02	0.00	0.01	0.02	0.01	0.01	0.01	0.01
Sum	100.50	100.19	100.45	99.77	99.24	100.23	99.66	99.14	98.37	99.06	98.08	99.75	100.58
Si	2.97	2.96	2.95	2.92	2.95	2.94	1.87	1.86	1.91	1.92	1.92	1.91	1.88
Ti	0.00	0.00	0.00	0.00	0.00	0.00	0.01	0.01	0.01	0.01	0.01	0.01	0.01
Al	1.96	1.98	1.96	1.97	1.95	1.98	0.34	0.35	0.34	0.34	0.33	0.32	0.34
Cr	0.00	0.00	0.00	0.00	0.01	0.00	0.00	0.00	0.00	0.00	0.00	0.00	0.00
Fe^{2+}	1.18	1.16	1.08	0.97	0.85	0.82	0.15	0.1	0.06	0.06	0.05	0.09	0.08
Fe^{3+}	0.09	0.11	0.13	0.20	0.15	0.14	0.01	0.03	0.02	0.02	0.03	0.00	0.03
Mg	1.02	1.01	1.09	1.16	1.38	1.44	0.76	0.69	0.68	0.67	0.68	0.70	0.69
Mn	0.12	0.12	0.09	0.07	0.02	0.01	0.00	0.00	0.00	0.00	0.00	0.00	0.00
Ca	0.65	0.67	0.69	0.70	0.69	0.67	0.77	0.85	0.77	0.76	0.77	0.82	0.80
Na	0.00	0.00	0.00	0.01	0.01	0.00	0.09	0.11	0.21	0.21	0.21	0.15	0.16
K	0.00	0.00	0.00	0.00	0.00	0.00	0.00	0.00	0.00	0.00	0.00	0.00	0.00
Sum	8.00	8.00	8.00	8.00	8.00	8.00	4.00	4.00	4.00	4.00	4.00	4.00	4.00
X_{Fe}	0.54	0.53	0.50	0.45	0.38	0.36	0.16	0.13	0.08	0.09	0.07	0.11	0.10
XAlm	0.4	0.39	0.37	0.33	0.29	0.28							
XPrp/XJd	0.34	0.34	0.37	0.4	0.47	0.49	0.11	0.11	0.21	0.22	0.22	0.16	0.17
XGrs	0.22	0.23	0.23	0.24	0.23	0.23							
XSps/XCaTs	0.04	0.04	0.03	0.02	0.01	0.00	0.11	0.09	0.04	0.04	0.03	0.08	0.06

(* Total Fe oxide as FeO). inc. = inclusion in; out. = outer; coro. = corona; sy. = symplectite; exp. = expelled; c. = close to; reint = reintegrated clinopyroxene (domanial composition of diopside + plagioclase). $X_{Fe} = Fe^{2+}/(Fe^{2}++Mg)$; XGrs = Ca/(Ca+$Fe^{2+}$+Mg+Mn); XPrp = Mg/(Ca+$Fe^{2+}$+Mg+Mn); XAlm = Fe^{2+}/(Ca+Fe^{2+}+Mg+Mn); XSps = Mn/(Ca+Fe^{2+}+Mg+Mn); XJd = Na/(Na+Ca); XCaTs= Al^{IV}-XJd; XAn= Ca/(Ca+Na+K); XOr = K/(Ca+Na+K)

Table 1d: Representative mineral analyses from the kyanite eclogite (8023F): orthopyroxene, spinel, sapphirine, plagioclase, epidote and amphibole.

Mineral	opx	opx	sp	sa	sa	pl	pl	pl	pl	pl	pl	pl	ep	ep	bi	am	am
Sample	8023F	8023F	8023F	8023F	8023F	8023F	8023F	8023F	8023F	8023F	8023F	8023F	8023F	8023F	8023F	8023F	8023F
Name	8f817	8Fa461	8Fa443	8Fa176	8Fa445	8Fa170	8Fa181	8Fir24	8Fa242	8Fa228	8Fa229	8Fa435	8Fa111	8Fa402	8Fa212	8Fa535	8Fir19
Location	cpx coro.	cpx coro.	sy close ru	sy. close g	sy.	sy. close g	sy. close ky	exp. cpx	exp. cpx	sy. g	sy. g	c. opx	inc. g	inc. g	grt core	inc. g	inc/exp. cpx
SiO_2	54.37	54.35	0.02	11.71	10.68	54.38	46.38	62.7	57.73	45.95	45.21	45.82	39.1	39.55	36.28	42.38	45.03
TiO2	0.09	0.04	0.07	0.06	0.07	0.00	0.00	0.00	0.01	0.00	0.00	0.12	0.04	0.03	0.73	0.23	0.57
Al_2O_3	2.69	1.64	61.06	66.11	67.12	29.43	34.54	23.00	26.09	34.38	35.13	34.62	32.51	32.21	19.62	16.90	15.04
Cr_2O_3	0.07	0.12	4.27	0.20	0.69	0.00	0.02	0.02	0.00	0.01	0.00	0.02	0.01	0.01	0.00	0.00	0.17
FeO*	13.13	14.23	20.27	5.42	5.55	0.21	0.14	0.07	0.11	0.13	0.11	0.15	1.86	1.98	8.75	5.45	4.85
MgO	29.26	29.68	14.38	16.75	16.03	0.00	0.01	0.01	0.00	0.00	0.07	0.08	0.07	0.06	18.39	16.22	15.82
MnO/Mn_2O_3	0.09	0.09	0.08	0.02	0.00	0.00	0.00	0.00	0.02	0.03	0.02	0.00	0.07	0.10	0.04	0.06	0.00
CaO	0.19	0.30	0.03	0.19	0.08	11.76	17.87	4.96	8.46	18.16	18.71	17.91	24.72	24.61	0.05	11.78	12.12
Na_2O	0.02	0.01	0.04	0.01	0.00	5.31	1.62	8.98	7.22	1.45	0.99	1.53	0.01	0.02	0.12	2.79	2.82
K_2O	0.00	0.01	0.00	0.00	0.01	0.05	0.04	0.31	0.12	0.00	0.03	0.05	0.00	0.00	10.5	0.55	0.02
Sum	99.94	100.49	100.21	100.48	100.23	101.14	100.61	100.04	99.77	100.11	100.26	100.31	98.41	98.57	94.54	96.45	96.51
Si	1.93	1.92	0.00	0.69	0.63	2.43	2.12	2.78	2.60	2.12	2.08	2.11	2.97	2.99	2.66	6.08	6.43
Ti	0.00	0.00	0.00	0.00	0.00	0.00	0.00	0.00	0.00	0.00	0.00	0.00	0.00	0.00	0.04	0.03	0.06
Al	0.11	0.07	1.89	4.56	4.65	1.55	1.86	1.20	1.38	1.87	1.91	1.88	2.91	2.87	1.70	2.86	2.53
Cr	0.00	0.00	0.09	0.01	0.03	0.00	0.00	0.00	0.00	0.00	0.00	0.00	0.00	0.00	0.00	0.00	0.02
Fe^{2+}	0.37	0.34	0.43	0.21	0.22	0.01	0.01	0.00	0.00	0.01	0.00	0.01			0.54	0.37	0.58
Fe^{3+}	0.02	0.08	0.02	0.06	0.05	0.00	0.00	0.00	0.00	0.00	0.00	0.00	0.12	0.13	0.00	0.29	0.00
Mg	1.55	1.57	0.56	1.46	1.41	0.00	0.00	0.00	0.00	0.00	0.01	0.01	0.01	0.01	2.01	3.47	3.37
Mn/Mn^{3+}	0.00	0.00	0.00	0.00	0.00	0.00	0.00	0.00	0.00	0.00	0.00	0.00	0.00	0.01	0.00	0.01	0.00
Ca	0.01	0.01	0.00	0.01	0.01	0.56	0.88	0.24	0.41	0.9	0.92	0.88	2.01	2.00	0.00	1.81	1.85
Na	0.00	0.00	0.00	0.00	0.00	0.46	0.14	0.77	0.63	0.13	0.09	0.14	0.00	0.00	0.02	0.78	0.78
K	0.00	0.00	0.00	0.00	0.00	0.00	0.00	0.02	0.01	0.00	0.00	0.00	0.00	0.00	0.98	0.10	0.00
OH													1.00	1.00	2.00	2.00	2.00
Sum	4.00	4.00	3.00	7.00	7.00	5.02	5.02	5.01	5.03	5.02	5.01	5.02	9.02	9.01	9.95	17.77	17.63
X_{Fe}/XAn	*0.19*	*0.18*	*0.43*	*0.13*	*0.14*	0.55	0.86	0.23	0.39	0.87	0.91	0.86			*0.21*	*0.10*	*0.15*
XAb/XNa_{M4}						0.45	0.14	0.75	0.60	0.13	0.09	0.13				*0.06*	*0.08*
XOr/$Na+K_A$						0.00	0.00	0.02	0.01	0.00	0.00	0.00				*0.77*	*0.62*

(* Total Fe oxide as FeO). XAn= Ca/(Ca+Na+K); XAb= Na/(Ca+Na+K); XOr = K/(Ca+Na+K)

Table 2: Bulk composition of the two studied samples (wt. %).

Sample	SiO_2	Al_2O_3	Fe_2O_3*	FeO	MgO	CaO	Na_2O	K_2O	TiO_2	P_2O_5	MnO	Cr_2O3	Sum
MU6	46.99	14.99	18.06	14.86	5.96	8.75	0.29	0.05	3.41	0.61	0.29	0.01	99.66
8023F	45.81	18.22	8.24	6.14	11.89	12.34	1.60	0.25	0.34	0.05	0.17	0.10	99.83

Fe2O3* – total Fe expressed as Fe2O3.

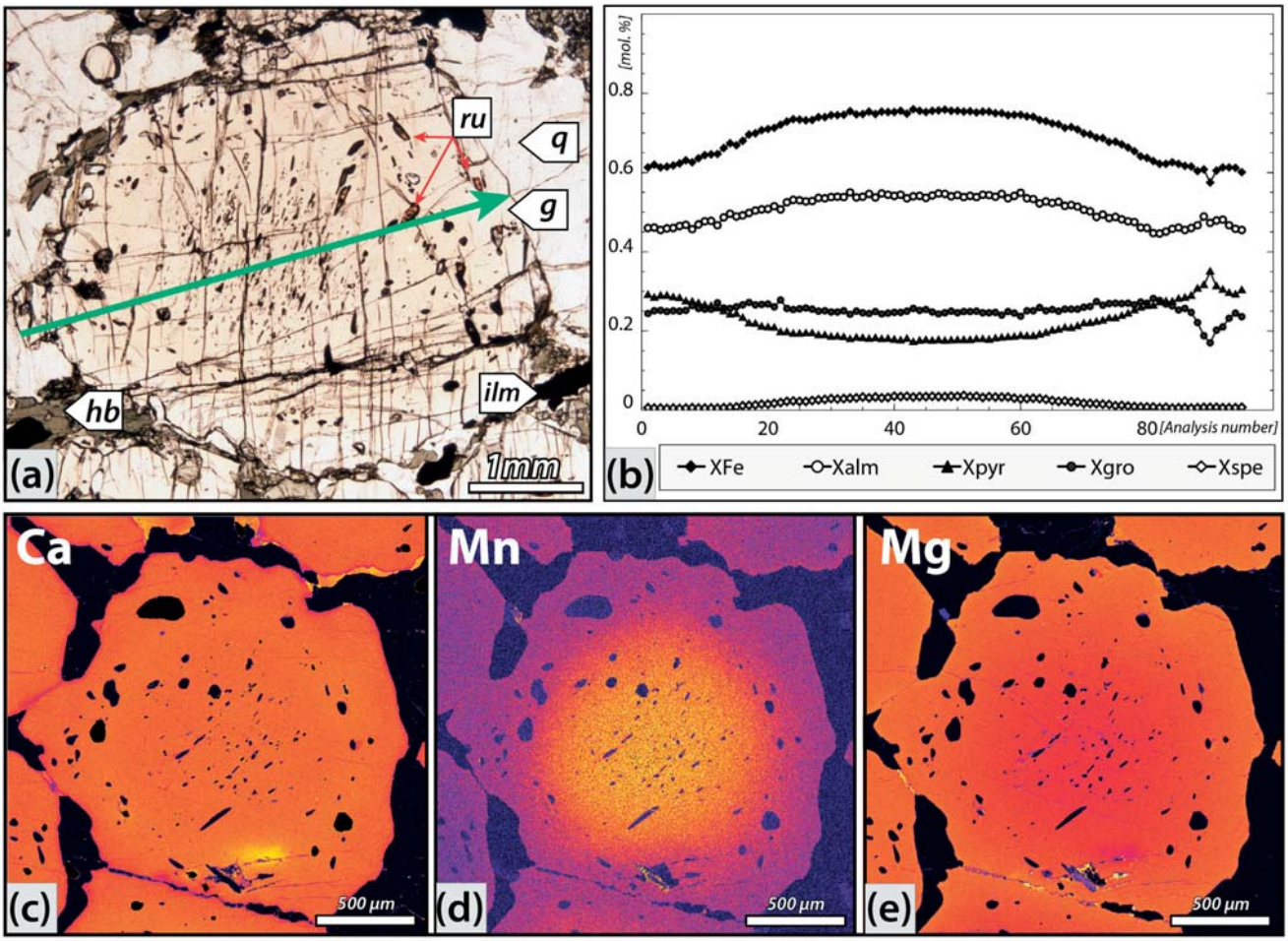

Figure 4: Texture and chemical composition of garnet in Fe-Ti rich eclogite sample MU6. (a) Photomicrograph of garnet grain with oriented inclusion trails of rutile and quartz in the core (internal foliation Si) and unoriented inclusions in the rim. The green arrow marks the garnet profile in (b). (b) Profile across garnet in (a) showing chemical zonation in garnet. (c, d, e) X-ray maps of garnet showing the relative concentration in major elements. Inclusion trails in the core show a slight bend.

Amphibole occurs as early inclusions in garnet cores (Fig. 5c), but also as partial replacements of clinopyroxene in the matrix (Fig. 5b). The composition corresponds in general to hornblende, although some inclusions in garnet classify as pargasite or tschermakite (Fig. 5d). X_{Fe} is generally close to 0.30 but is up to 0.73 in grains included in garnet; XNa_{M4} ($[Na/(Na+Ca)]_{M4}$) = 0.03–0.04; K = 0.01–0.09 cpfu but generally around 0.03; Fe^{3+} ranges between 0.12 and 0.31 cpfu ; Ti = 0.14-0.28 cpfu (Fig. 5d; Table 1b).

Plagioclase occurs as abundant inclusions in the garnet core (Fig. 5e) and in clinopyroxene (up to 50%; Fig. 5a). The composition of the inclusions in clinopyroxene is *An*45-55 (Figs. 5a,f), inclusions in garnet core vary strongly from *An*40 to *An*81 (Fig. 5f).

Quartz forms large grains (up to 3 mm) that constitute up to 30% of the matrix (Figs. 3a, 5b & g). It also occurs as oriented inclusions in the garnet core (0.01-0.1 mm wide; Fig. 5e) and unorientated crystals in the rim (0.05-0.3 mm).

Rutile occurs as inclusions in garnet, quartz and clinopyroxene (Figs 3a, 4a, 5b,c,e,g & h) and as a relatively abundant matrix phase. A few rutile grains included in garnet core are associated with ilmenite. The grain size of rutile progressively increases from a few µm in garnet cores, up to a few hundred µm in garnet rims (Fig. 5g), and up to 2 mm in the matrix (Fig. 5h). Matrix rutile is in general partly replaced by ilmenite (Figs 3a & 5h).

Minor chlorite and sericite are present only locally, overprinting the minerals described above.

We interpret the chemical zoning of garnet, in concordance with the regular decrease of spessartine, as growth zoning formed during prograde metamorphism. Inclusions in the garnet core suggest that plagioclase was part of the early metamorphic assemblage together with hornblende, quartz and rutile. The inclusion pattern, which is locally bent in garnet cores, testifies to the growth of garnet cores during deformation

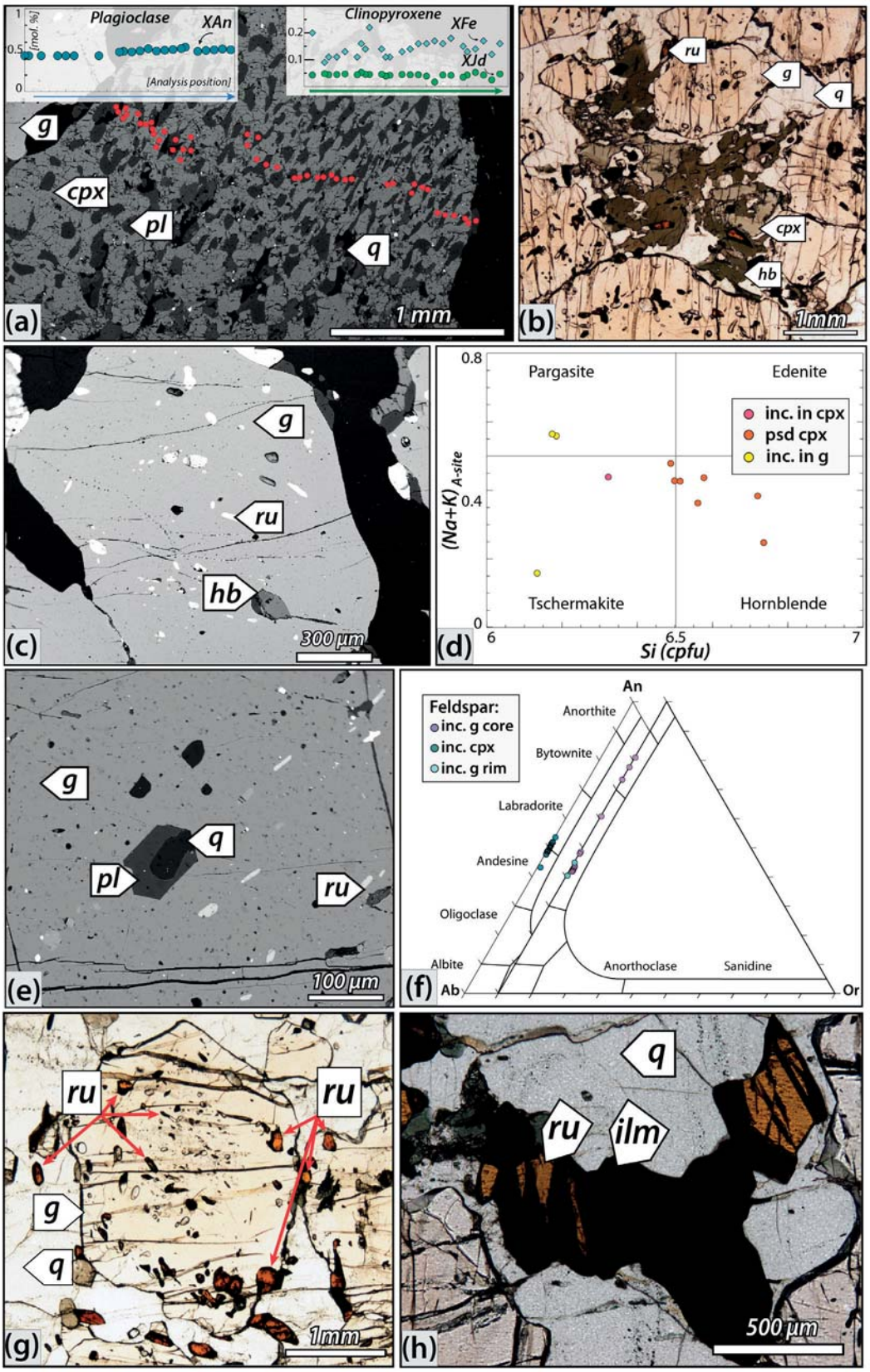

Figure 5: Textures and mineral compositions in Fe-Ti eclogite sample MU6. (a) Back-scattered electron (BSE) image of clinopyroxene with expelled plagioclase. Compositions of clinopyroxene (upper right) and plagioclase (left) analyzed at the red dots. (b) Photomicrograph showing replacement of matrix clinopyroxene by amphibole (hb). Rutile, originally hosted in clinopyroxene, is surrounded by ilmenite. (c) BSE image of rutile and amphibole (hb) inclusions in garnet. (d) Amphibole compositions in different textural settings: amphibole replacing clinopyroxene (psd cpx) is hornblende, while inclusions in clinopyroxene and garnet (part of the prograde assemblage) are more pargasitic or tschermakitic. Classification after Leake et al., (1997; 2004). (e) BSE image of quartz and plagioclase inclusion in garnet core. (f) Ternary plot showing the variation of plagioclase composition according to their textural settin. The composition of plagioclase inclusions in garnet cores varies from bytownite to andesine; plagioclase expelled from clinopyroxene varies from labradorite to andesine. (g) Photomicrograph illustrating the increase of rutile grain size from garnet core to rim and matrix. (h) Photomicrograph showing partial replacement of matrix rutile by ilmenite.

The numerous regularly distributed plagioclase inclusions in clinopyroxene suggest that they are late expulsions from an originally more sodic (i.e. omphacitic) pyroxene. Pyroxene in the matrix is inferred to be roughly contemporaneous with the crystallisation of the garnet rim, matrix quartz and rutile, close to the metamorphic pressure peak. Ilmenite replacing matrix rutile, and hornblende replacing matrix clinopyroxene, are interpreted as secondary, retrograde features. Chlorite and sericite are late phases, formed by small-scale local fluid infiltration at low temperature.

Kyanite eclogite (8023F)

Sample 8023F represents a layer of kyanite-bearing eclogite in an eclogite body of unknown size (Fig. 2a; WGS84: 57° 9′ 9,99″N, 12° 46′ 8,91″E; locality: Tranabo). The sample is composed of garnet (~ 30 vol.%), clinopyroxene (~ 35 vol.%), kyanite (~ 10 vol.%), amphibole (~ 20 vol.%) and locally quartz, rutile and sulphides (pyrite, chalcopyrite; Fig. 3b). Kyanite is in most places surrounded by sapphirine-plagioclase symplectite, locally containing corundum and spinel.

Garnet crystals are 3-8 mm in diameter and contain unoriented inclusions of kyanite, zoisite, biotite, clinopyroxene, quartz and minor apatite (Figs 3b & 6a). There is a rimward decrease of almandine, spessartine, and X_{Fe} (*Alm*40→29, *Sps*4→1, X_{Fe}*0.*54→0.37), which is balanced by an increase of pyrope (*Prp*35→48). There is a slight increase in grossular from the core to the inner rim (*Grs*21→24), and a decrease towards the outer rim (*Grs*21; Fig. 6b-e; Table 1c).

Clinopyroxene grains are up to 8 mm large. They contain inclusions of plagioclase ± amphibole and quartz, commonly elongated along crystallographic planes (Fig. 7). In the inner, inclusion-poor, part the jadeite content (*Jd*) is generally 20-22. In plagioclase inclusion-rich rims *Jd* decreases to 5 (Fig. 7). Inclu-

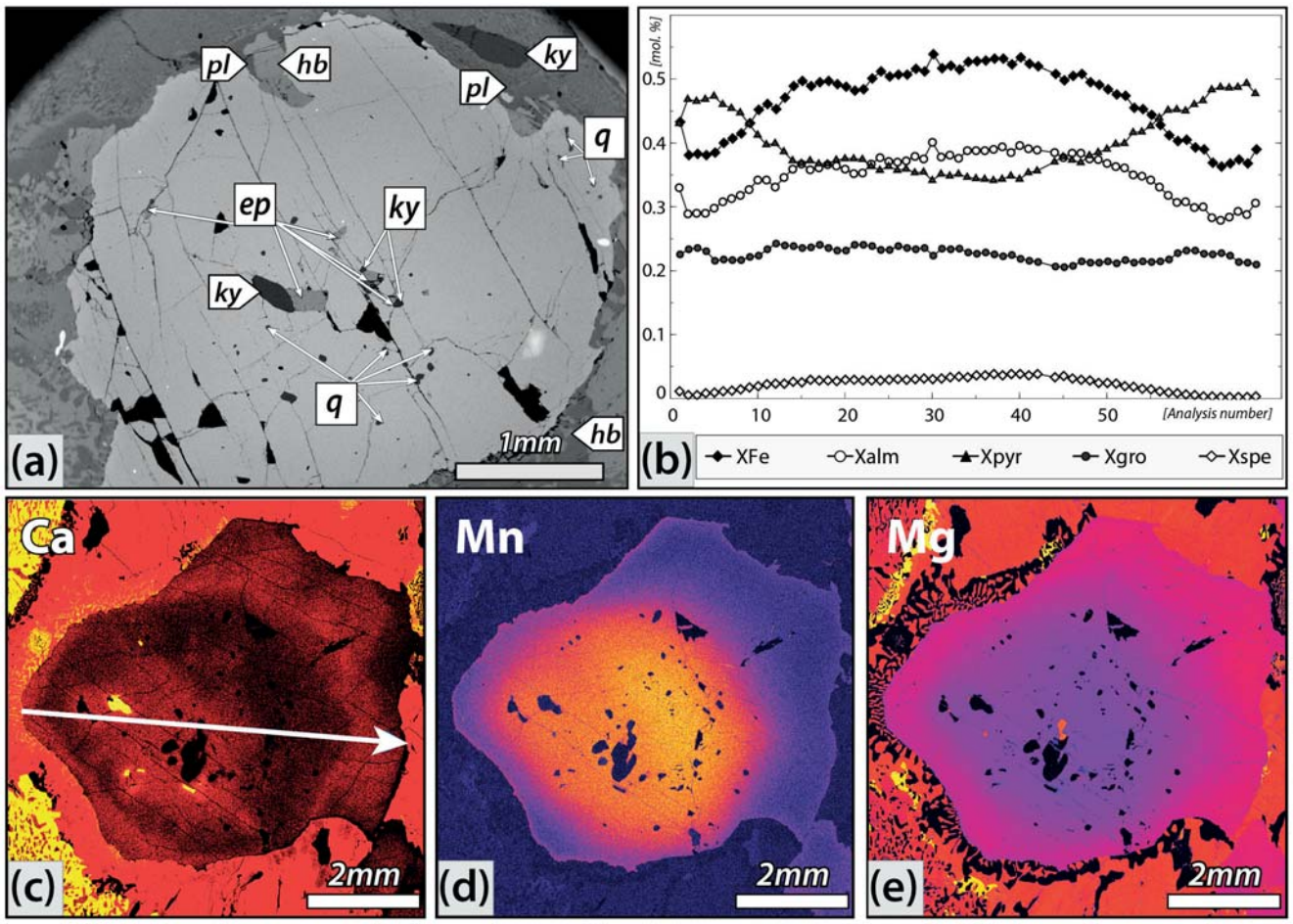

Figure 6: Texture and chemical composition of garnet in kyanite eclogite sample 8023F. (a) BSE image of garnet grain with inclusions of kyanite, zoisite (ep), and quartz. Garnet is locally rimmed by an amphibole + plagioclase corona. (b) Profile across garnet showing chemical zonation. (c, d, e) X-ray maps of garnet showing the relative concentration of major elements. White arrow in (c) marks the profile in (b).

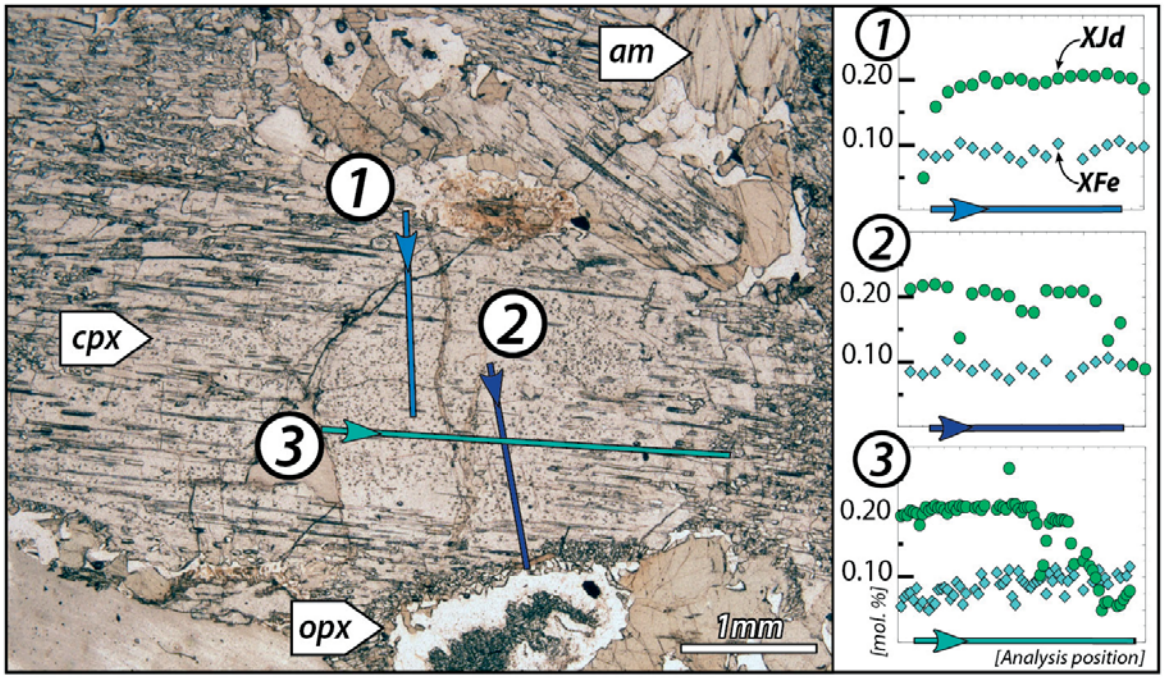

Figure 7: Photomicrograph (PPL) of clinopyroxene grain with plagioclase expelled along crystallographic planes (less abundant in the core of the crystal). Three profiles show the compositional variation across the grain, notably a decrease of jadeite content from core to rim.

sions of clinopyroxene in garnet have *Jd*9-12. X_{Fe} varies from ~ 0.05 to 0.16, most values clustering between 0.09 and 0.11 (Fig. 7; Table 1c).

Kyanite is preserved as inclusions in garnet cores, and in the matrix (0.6 mm long) in cores of plagioclase + sapphirine ± corundum symplectites (Figs 6a, 8a & b). The symplectite domains have locally a rectangular shape and are interpreted as pseudomorphs after kyanite, the initial length of which have been up to 7 mm (see also Möller 1998, 1999).

(Clino)zoisite/epidote is only found as inclusions in garnet cores, as up to 0.3 mm large grains, sometimes in direct contact with kyanite (Fig. 6a). It does not contain significant amounts of Ti or Cr, and the pistachite (epidote *sensu stricto*) content [XFe^{3+} = $Fe^{3+}/(Fe^{3+}+Al-2)$] is ~ 0.12 (Table 1d).

Amphibole forms subhedral grains up to 5 mm in the matrix. Some grains appear to have been in former textural equilibrium with clinopyroxene and garnet. A reaction rim of amphibole + plagioclase is however found in many places between clinopyroxene and garnet (Figs 3b & 6a), and locally between clinopyroxene and sapphirine symplectites. Amphibole also occurs as inclusions in garnet and clinopyroxene (Fig. 9b) Amphibole is pargasite to edenite regardless of the textural setting: $(Na+K)_A$ varies between 0.5 to 0.8 and Si varies from 6 to 6.7 cpfu (Fig. 9b; Table 1d). X_{Fe} varies between 0.12 and 0.16; XNa_{M4} < 0.1; recalculated Fe^{3+} ranges between 0.10 and 0.30 cpfu; K clusters between 0.12 and 0.16 cpfu; Ti = 0.03-0.30 cpfu (Fig. 9b; Table 1d).

Plagioclase is present in a variety of textural settings (Fig. 10a) and the composition varies accordingly. *An* ranges from 91 (in symplectites with sapphirine) to 41 (intergrown with symplectitic orthopyroxene along clinopyroxene rims). *An* of inclusions in clinopyroxene ranges from 39 to 45 (Figs 9a & 10b).

Sulphides are form up to 2 vol.% of the rock and mostly comprise chalcopyrite partly replaced by covellite + goethite, and locally pyrite. Sulphide grains are commonly found in the cores of the large subhedral amphibole crystals.

Orthopyroxene forms symplectitic intergrowths with plagioclase, up to 300 µm wide, along the rims of clinopyroxene (Figs 10a & b). One inclusion (~ 0.3 x 0.1 mm) in garnet made of plagioclase + orthopyroxene + quartz is interpreted as the replacement product of a former inclusion of clinopyroxene (Fig. 10c). X_{Fe} varies from 0.18 to 0.30 (Table 1d). Al content varies from 0.05 to 0.09, but is generally around 0.07.

Sapphirine is intergrown with plagioclase within symplectites after kyanite (Figs 8a, b & 10a). Individual grains are up to 0.3 mm wide, but generally ~ 10 x 100 µm or smaller. X_{Fe}=0.10-0.14 (Table 1d).

Corundum is situated in the symplectite domains after kyanite, generally forming clusters of acicular crystals in plagioclase (Fig. 8b). Traces of Cr and Fe are common but <0.01 cpfu. In the center of one symplectitic micro-domain after kyanite, blocky corundum grains occur together with rutile and spinel; these grains are likely former inclusions in kyanite.

Spinel is only found locally in symplectite domains after kyanite, exclusively in contact with rutile. X_{Fe} = 0.45, Mn and Ti = 0, Cr ~ 0.1 cpfu.

In summary, the regular rimward decrease of spessartine and X_{Fe} in garnet is interpreted to reflect growth zoning, attributable to a prograde metamorphic evolution. Inclusions in the garnet core suggest that kyanite and zoisite were part of the primary mineral assemblage together with clinopyroxene, quartz, rutile, and minor biotite. Large clinopyroxene crystals are interpreted to have crystallized in equilibrium with garnet. The rimward increase of the proportion of jadeite can be attributed to the growth along an up-pressure prograde *P–T* path. The numerous inclusions of plagioclase in some low-jadeite clinopyroxene rims are interpreted as the consequence of decompression-related plagioclase expulsion from a former omphacitic pyroxene. Zoisite is restricted to inclusions in garnet core, whereas quartz inclusions are present even in the very rim. Large subhedral matrix crystals of amphibole are interpreted to have been in equilibrium with garnet and clinopyroxene and belong to the dominant matrix mineral assemblage. Orthopyroxene, sapphirine, and corundum are exclusively located within symplectitic coronas after omphacite and kyanite, respectively, and are interpreted as reaction products related to decompression.

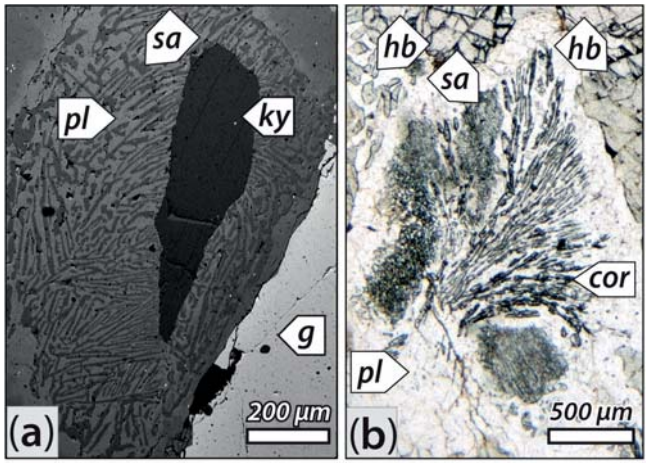

Figure 8: Textures in kyanite eclogite sample 8023F. (a) BSE image of typical reaction textures involving replacement of kyanite. A remnant grain of kyanite is present in the core of a fine-grained symplectite of sapphirine + plagioclase. (b) PPL photomicrograph of symplectitic sapphirine + plagioclase + corundum. Late saussurite appears as faint clouding of plagioclase.

P–T CONDITIONS

P–T pseudosections have been calculated in the framework (chemical system, mixing models etc.) described above, and are presented in Figs 11 & 12. The bulk rock compositions of the two samples (Table 2) were converted to mol.% and adapted to the model system (P_2O_5 was removed as apatite and MnO as spessartine).

In the absence of an appropriate melt model for metabasic systems, the assemblages on the high-temperature side of the pseudosections may be metastable with respect to assemblages involving melt, or at least coexist with melt. However, experimental work, calculations and natural observations suggest that the topology of the phase relationships is similar when

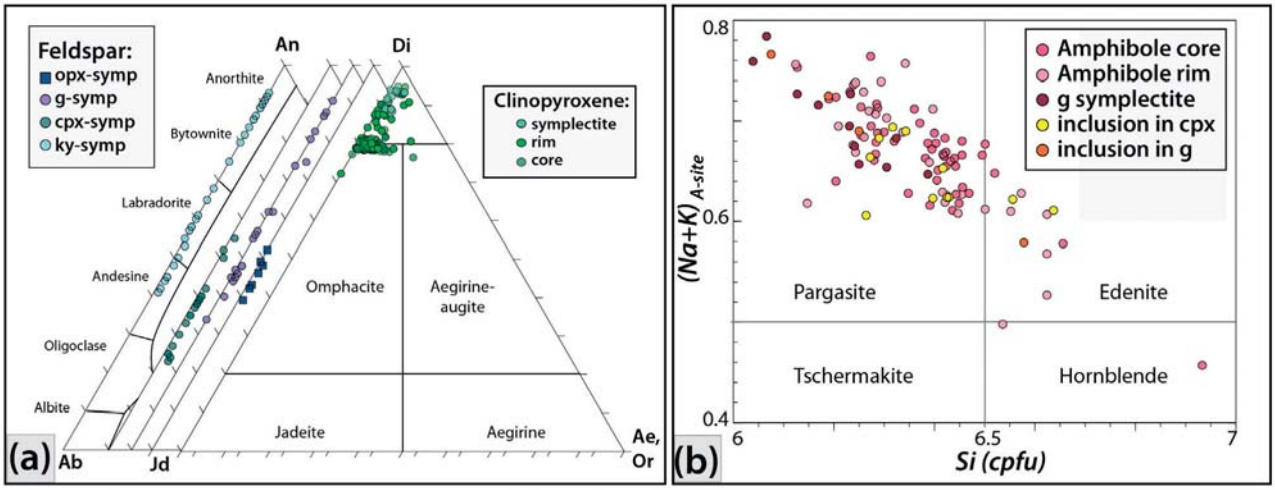

Figure 9: Mineral compositional diagrams of plagioclase, clinopyroxene and amphibole from the kyanite-eclogite sample 8023F. (a) Ternary plots show the variation of plagioclase and clinopyroxene composition in different textural settings. See text for details. (b) Amphibole composition in different textural settings. Classification after Leake et al., (1997; 2004).

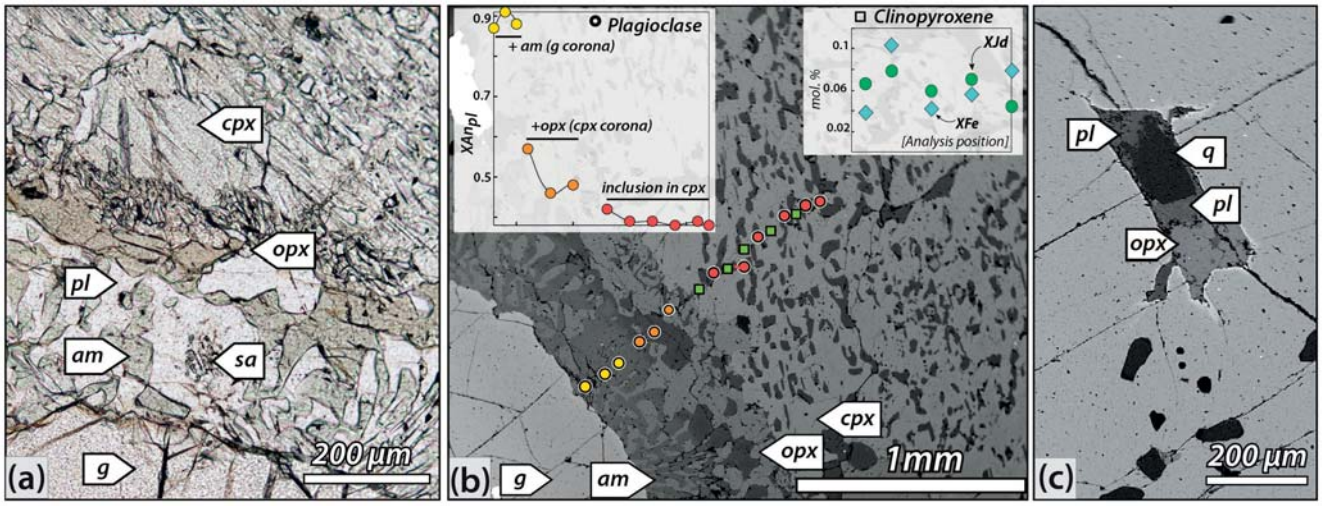

Figure 10: Textures in kyanite eclogite 8023F. Photomicrograph (a) and BSE image (b) of typical reaction rim between garnet and clinopyroxene. Symplectite of plagioclase + amphibole surrounds garnet, while plagioclase + orthopyroxene rims clinopyroxene. Clinopyroxene contains expelled plagioclase blebs. A sapphirine + plagioclase symplectite in (a) is indicates the former presence of kyanite. The graphs in (b) show the composition of plagioclase (An; upper left, from garnet rim to clinopyroxene core) and the composition of clinopyroxene (*Jd*, X_{Fe}; upper right). (c) BSE image of a rare "secondary" inclusion in garnet showing orthopyroxene + plagioclase + quartz, inferred as a pseudomorph of a clinopyroxene inclusion in garnet.

mineral assemblages coexist with fluid or melt and that the field boundaries may not move significantly (e.g. Wolf & Wyllie, 1994; Vielzeuf & Schmidt, 2001; Pattison, 2003). Moreover, the two modeled rocks are not of typical basaltic compositions (Table 2), and no indications of the presence of melt were observed. Biotite is stable throughout the pseudosections (with the exception of the H*P*-L*T* and L*P*-H*T* corners), in very low modal proportions (less than 0.5 mol.%), and it is scarce or absent in our samples. This is the consequence of including K (potassium) in the chemical model system. In nature, K is taken in small quantities in amphibole (cf. Table 1b), but this is not accounted for in the existing mixing models.

Pseudosection for Fe-Ti eclogite (MU6)

The first recorded metamorphic stage corresponds to the assemblage g + hb + pl + q + ru + ilm, which is preserved as inclusions in the garnet core. In the pseudosection, this assemblage is located at 620-820 °C, 6-9 kbar (Fig. 11a). The inferred matrix peak assemblage g + di + q + ru is stable at pressures higher than 15 kbar. This suggests that the sample preserved a prograde *P–T* evolution dominated by a pressure increase and peaked in the eclogite facies. However, the preserved garnet zoning and the chemical composition of the phases bring further constraints to this first order information.

Garnet core: The isopleths corresponding to the composition of the garnet core (X_{Fe}*0.76*, *Grs* ~ z(g)25) intersect in the low-temperature part of the g + hb + pl + q + ru + ilm field (Fig. 11b) and suggest conditions of ~ 670-700 °C at 7-7.5 kbar for the first metamorphic stage (ellipse 1, Fig. 11a). The observed decrease in X_{Fe} and increase of *Grs* towards the outer part of the garnet core (X_{Fe}*0.72*, *Grs*27) suggest a (syndeformational) prograde evolution to 700-720 °C at 8-8.5 kbar (ellipse 2, Fig. 11a).

Garnet rim: Further decrease in X_{Fe} (0.72→0.67) associated with a constant grossular content (*Grs*28) in the garnet inner rim is compatible with continuous garnet growth along a prograde path to ~12 kbar, 770 °C (Fig. 11b). This part of the path is mostly located in the g + hb + q + ru field, which is characterised by a constant value of grossular of ~28 mol.% (Fig. 11b). The absence of plagioclase inclusions in the inner rim is compatible with the absence of plagioclase in this field. A continuous evolution along this *P–T* path (to ellipse 3, Fig. 11a) predicts that garnet X_{Fe} continues to decrease (0.67→0.61), whereas the grossular content slightly decreases (28→24 mol.%), which is in agreement with the observations. This unusual, yet well-modeled, pattern of isopleths supports the good agreement between the inferred *P–T* path and the petrological and chemical features of the sample.

The garnet composition varies little across the relatively large field g + di + q + ru corresponding to the inferred peak matrix assemblage (X_{Fe}*0.61*-0.62, *Grs*26). Consequently, the analyzed garnet composition (X_{Fe}0.61, *Grs*25-26), although in good agreement with these values, does not give strong constraints on the *P–T* conditions. Best fit is obtained at ~ 17-18 kbar, 880 °C (ellipse 3, Fig. 11a).

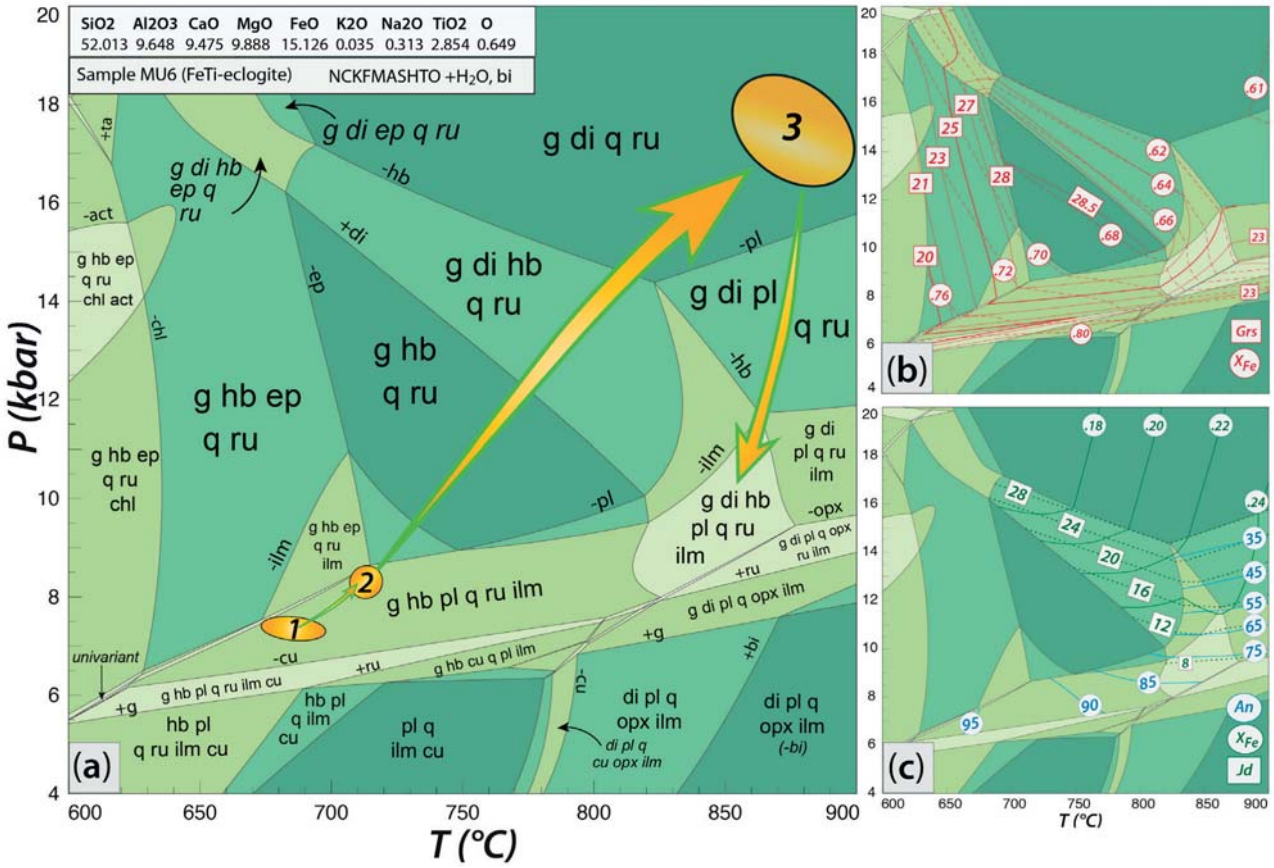

Figure 11: Pseudosection calculated for the Fe-Ti eclogite (MU6). The rock composition is given as mole-% oxide. Ellipses correspond to steps described in the text. (b) Compositional isopleths of the grossular-content and the X_{Fe} ratio in garnet. (c) Compositional isopleths of clinopyroxene (X_{Fe} and *Jd*) and plagioclase (*An*).

The composition of clinopyroxene modelled in this domain (*Jd* ~ 28, X_{Fe} ~ 0.20-0.24; Fig. 11c) does not fit very well with the analysed one (*Jd*2-10, X_{Fe} 0.18-0.22), in particular with respect to the proportion of the jadeite endmember. It may be argued that this is due to late reequilibration (expelled plagioclase) and hence an initial composition richer in jadeite. However, even compositions reintegrated from area analyses (*Jd*15-19, X_{Fe}0.29) are less omphacitic than the calculated ones. We suggest that the Ca-tschermak component in clinopyroxene (up to 10% in the analysed crystals), which is not taken into account in the mixing model used, is the origin of this discrepancy.

Plagioclase, hornblende, ilmenite, and the clinopyroxene-plagioclase intergrowths, are interpreted as reaction products due to post-peak partial reequilibration. Classically, these features are associated with decompression and cooling. In the framework of the present pseudosection, plagioclase stabilization, and in particular the expulsion from omphacitic clinopyroxene after the pressure peak is compatible with a decompression below ~ 16 kbar, in the plagioclase-bearing field g + di + pl + q + ru (12-16 kbar, >825 °C). In this field, the modelled composition of plagioclase agrees with that of the inclusions in clinopyroxene (*An*45-55; Fig. 11c). Further decompression below c. 12 kbar to the field g + di + hb + pl + q + ru + ilm (810-870 °C, 8-12 kbar) accounts for the partial replacement of rutile by ilmenite and the crystallization of amphibole at the expense of clinopyroxene. The presence of amphibole suggests temperatures below 875 °C (Fig. 11a) and thus slight cooling during decompression.

Pseudosection for kyanite-eclogite (8023F)

The inferred first metamorphic assemblage g + di + hb + ky + ep + q + ru, preserved as inclusions in the garnet core, is stable within a narrow trivariant field (highlighted, Fig. 12a) located from 710 °C at 18 kbar to 830 °C at 15 kbar. The dominant matrix assemblage is represented in the adjacent epidote-absent field g + di + hb + ky + q + ru, at higher temperature and pressure, suggesting a prograde *P*–*T* evolution. The local presence of quartz in the matrix and as inclusions in garnet rims suggests that the *P*–*T* evolution did not go significantly beyond the quartz-out line, at ~ 18 kbar.

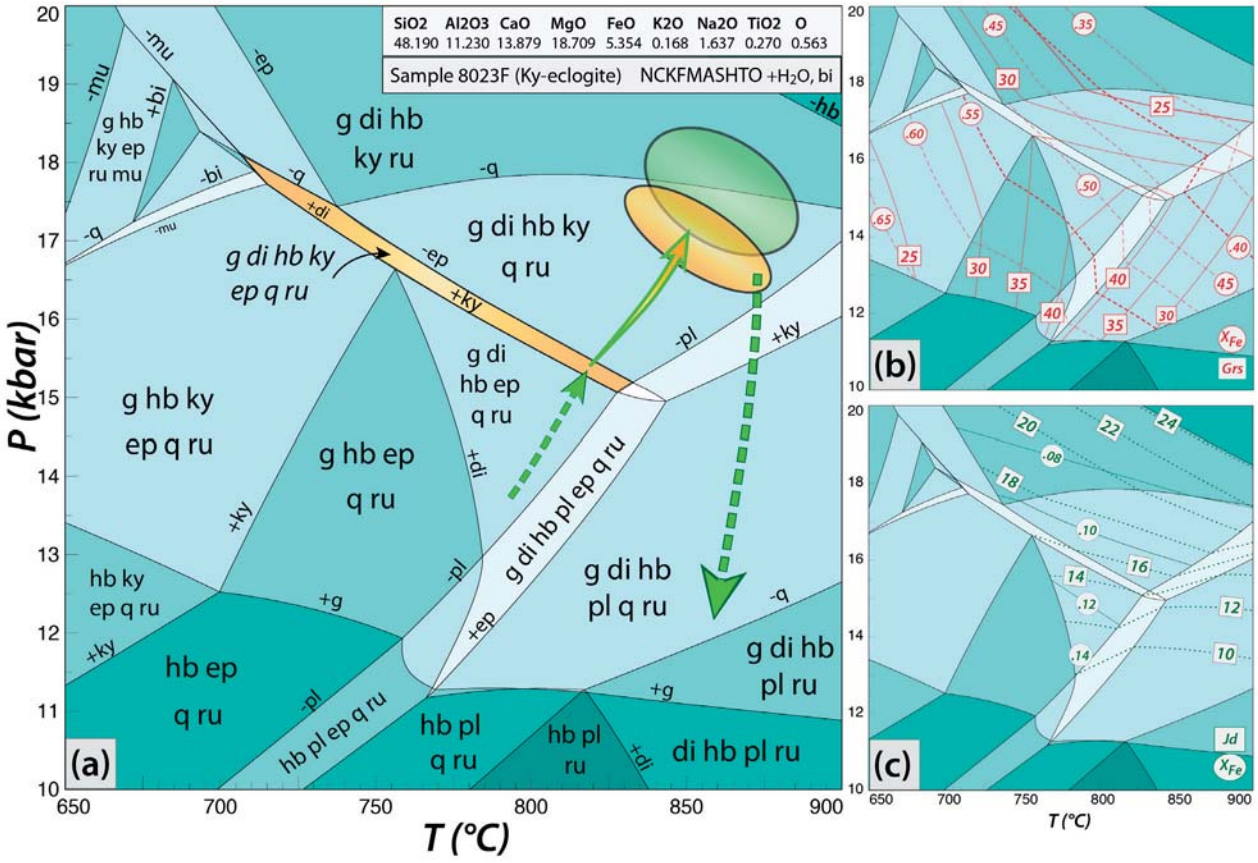

Figure 12: Pseudosection calculated for the kyanite eclogite (8023F). The rock composition is given as mole-% oxide. Ellipses corresponds to alternative location for the peak-pressure stage described in the text. Compositional isopleths for garnet and clinopyroxene are shown in (b) and (c), respectively.

The modelled grossular content (33-40 in the field g + di + hb + ky + ep + q + ru, decreasing to 24 in the epidote-absent field) is higher than the analyzed values (20-24) that would be approached only at the highest pressures of the latter field (Fig. 12b). It is therefore difficult to refine the peak *P–T* estimate using the compositional isopleths. On the other hand, the analysed X_{Fe} ratios of the garnet core (0.53-0.38) and the jadeite content of clinopyroxene (9-24, cluster around 20-22) are compatible with those modelled at these conditions (Fig. 12b,c). Furthermore, the analysed rimward decrease of X_{Fe}(g) is in agreement with the trend of the garnet compositions modelled along a prograde *P–T* path involving increasing pressure and/or temperature (Fig 12b and c). This path likely started in the kyanite-absent field g + di + hb + ep + q + ru, where modelled X_{Fe}(g) values are close to those analyzed in the garnet core (X_{Fe} = 53-50). Although the absolute modelled values are higher than those observed, the prograde *P–T* path shown in Fig. 12a qualitatively reproduces the observed grossular zoning (initial increase followed by a decrease). The best fit between observations and model (assemblage and mineral compositions) is reached in the field g + di + hb + ky + ru ± q, corresponding to the peak matrix assemblage, at 870 °C, 17-18 kbar. This value is interpreted to correspond to the metamorphic peak reached by the rock.

The development of plagioclase-bearing symplectites reflects the rock entering plagioclase-bearing fields along a *P–T* path dominated by decompression (dashed line in Fig. 12a) that also leads to decreasing the proportion of garnet and kyanite. The variable symplectitc textures associated with a strong chemical zoning suggest that they reflect conditions with inefficient diffusion, dominated by micro-scale local equilibria and different micro-scale chemical domains rather than homogeneous reequilibration (cf. Möller 1998, 1999; Pitra *et al.*, 2010). Consequently, they cannot be quantitatively interpreted in a pseudosection calculated for the whole-rock bulk composition.

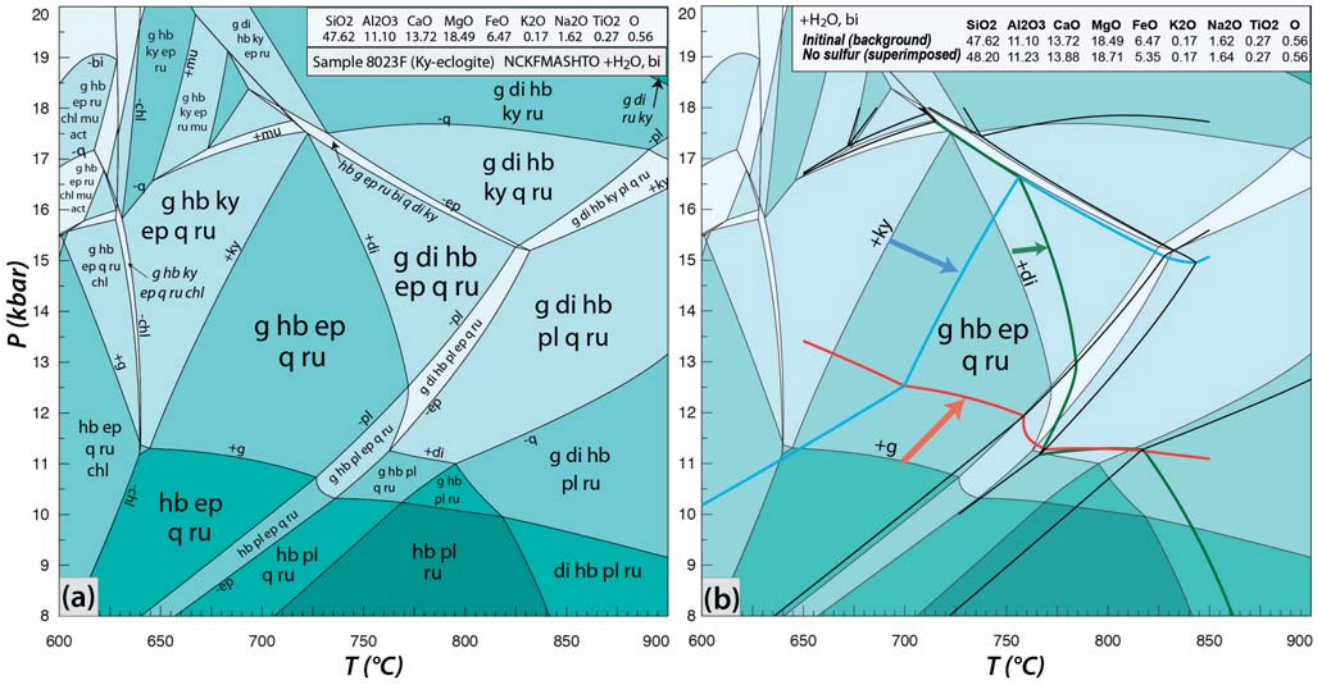

Figure 13: Effect of Fe^{2+} fractionation due to the presence of sulphides in the kyanite eclogite sample 8023F. (a) Pseudosection calculated with the analyzed whole-rock composition without taking into account the fractionation of Fe^{2+} in sulphides. (b) Pseudosection from (a) as a background image with superposition of kyanite-, garnet- and diopside-in lines for a composition of which Fe^{2+} contained in sulphides was subtracted. The main effect is the shift of kyanite-,and diopside-in lines to higher temperature (up to 40 °C) and the garnet-in line to higher pressure (up to 1.5 kbar).

DISCUSSION

Validity of the pseudosections

Pseudosections are phase diagrams calculated for a specific bulk composition. The estimation of this composition is subject to different sort of uncertainties and presumptions that merit a brief discussion. Pseudosections may be particularly sensitive to variations of the bulk X_{Fe} ([Fe/(Fe+Mg)] ratio, e.g., Powell & Holland, 1990; White *et al.*, 2001) as well as the amount of available H_2O (e.g., Guiraud *et al.*, 1996; Carson *et al.*, 1999; López-Carmona *et al.*, 2013).

Fe content in sulphides and consequences

Fe-sulphides are common, albeit accessory, constituents of silicate, in particular metabasic, rocks. However their influence on the bulk X_{Fe} ratio is rarely discussed. In the kyanite-eclogite (8023F) they are interpreted as part of the initial to early prograde metamorphic assemblage and do not appear to participate in reaction textures, apart from late-stage reequilibrations (chalcopyrite transformation to covellite and goethite). Although they only form around 2 vol.% of the thin section (estimated by point counting), they can fractionate a non-negligible amount of ferrous iron from the bulk composition. Therefore, a pseudosection for the kyanite-eclogite was calculated to test the effect of neglecting the iron fractionation in sulphides (Fig. 13a,b). In this case, it results in a modification of the bulk X_{Fe} ratio from 22 to 26 and causes a significant shift of the garnet-, kyanite- and clinopyroxene-in lines (Fig. 13b). As a consequence, the size of the central field (g + hb + ep + q + ru) is significantly modified, although the effect is less important for the field corresponding to the peak assemblage. The grossular isopleths are only little affected, but X_{Fe} isopleths are significantly displaced to lower P and T by up to 1.5 kbar and 20 °C, resulting in a poorer agreement between calculations and observations (Fig. S1). Clearly, taking the Fe fractionation in sulphides into account must not be neglected, even if they are present in apparently low proportions. Pseudosections including a full set of isopleths and P/T-XH_2O and -Fe_2O_3 content are provided in Fig. S1 & S2 for comparison.

Fe_2O_3 content

Beyond the effect of the Fe^{2+} fractionation in sulphides, bulk X_{Fe} is strongly influenced by the estimation of the amount of ferric iron. Although the analytical determination of the Fe^{3+} becomes common

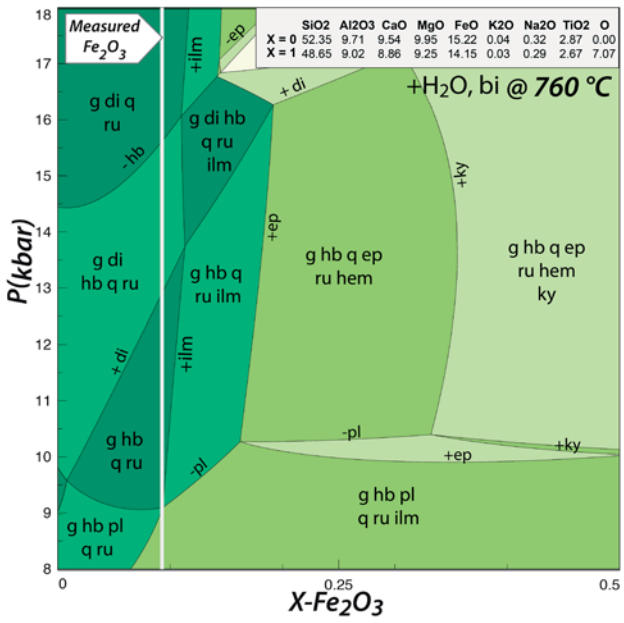

Figure 14: P-XFe_2O_3 pseudosection showing the effect of varying the proportion of Fe_2O_3 vs. FeO on assemblages at 760 °C, between 8 and 18 kbar, for the Fe-Ti eclogite sample MU6. The bulk rock compositions in mole-% oxide corresponding to minimum and maximum possible amounts of Fe_2O_3 (X = 0 and X = 1, respectively) are given in the upper right. The pseudosection is calculated in the range of X = 0 and X = 0.5. The white line shows the Fe_2O_3 value corresponding to the measured Fe_2O_3.

practice, López-Carmona *et al.* (2013) have shown that the proportion of Fe^{3+} can be easily modified by superficial alteration even in apparently fresh samples, and argued for a systematic use of *P*/*T*–XFe_2O_3 pseudosections [XFe_2O_3 = $2Fe_2O_3/(2Fe_2O_3+FeO)$ = $Fe^{3+}/(Fe^{3+}+ Fe^{2+})$]. In both samples studied, the amount of Fe^{3+} vs. Fe^{2+} was analysed (FeO by titration) and these values were used for calculating the pseudosections presented above.

For the Fe-Ti-eclogite, a *P*-XFe_2O_3 pseudosection was calculated to test the effect of Fe_2O_3 on the predicted assemblages and compositions, at 760 °C and from 8 to 18 kbar (Fig. 14). The analysed Fe_2O_3 content corresponds to XFe_2O_3 = 0.09. The assemblages do not substantially change from XFe_2O_3 = 0 to 0.09, therefore adjusting the Fe_2O_3 content to values lower than the one analyzed is unjustified. Slightly higher values of Fe_2O_3 result in the appearance of ilmenite up to 18 kbar and the stabilisation of epidote, which is incompatible with the observations. Consequently, using the analysed Fe_2O_3 content in the sample appears as the best option for the Fe-Ti-eclogite.

For the kyanite-eclogite, the main issue is the modelled high grossular content in garnet cores, which does not fit the analyzed composition. Therefore the calculations aimed particularly on investigating the influence of the Fe_2O_3 variation on the position of the garnet isopleths. In the *P*-XFe_2O_3 pseudosection calculated at 675 °C (Fig. 15), the increase of Fe_2O_3 content leads very abruptly to garnet not being stable in the assemblage. For lower values of Fe_2O_3, kyanite is not stable and grossular content increases, leading to even poorer agreement between the model and the observations. A similar effect is observed in pseudosections, where the fractionation of Fe^{2+} in sulphides was not taken into account – the variation of Fe_2O_3 does not provide better results (Fig. S2). Consequently, the analyzed amount of Fe_2O_3 was used.

H_2O content

Because of the dehydration character of a vast majority of metamorphic reactions (along a prograde evolution), most rocks are saturated in H_2O, which is then commonly considered in excess. Whereas this approach usually yields correct results, and is generally a good starting point, care is needed in some cases. These include rocks undergoing partial melting (e.g. Powell, 1983; White *et al.*, 2001), subduction-related metamorphism (e.g. Ballèvre *et al.* 2003; López-Carmona *et al.*, 2013), retrograde evolution (e.g. Guiraud *et al.*, 2001; Pitra *et al.*, 2010), and also the metamorphism of H_2O-poor protoliths. This is the case of rocks that have been previously

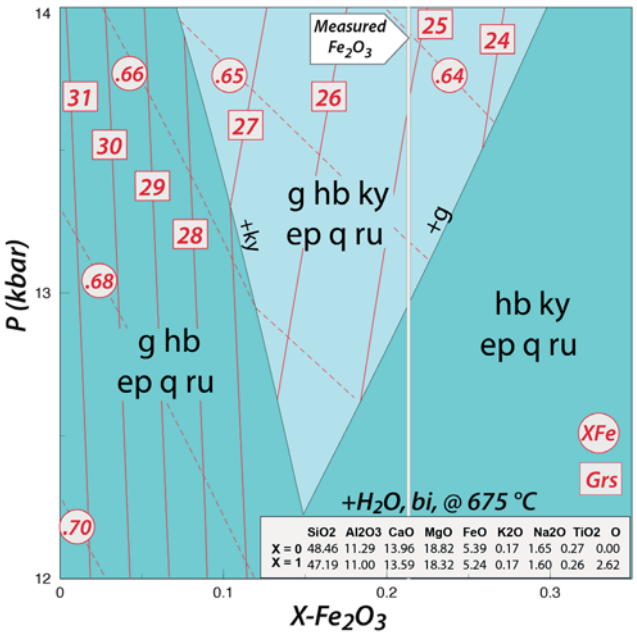

Figure 15: *P*-XFe_2O_3 pseudosection showing the effect of Fe_2O_3 on the paragenesis at 675 °C, between 12 and 14 kbar, for the kyanite-eclogite sample 8023F. The bulk rock compositions in mole-% oxide corresponding to minimum and maximum possible amount of Fe_2O_3 (X = 0 and X = 1, respectively) are given in the upper right. The pseudosection is calculated in the range of X = 0 and X = 0.35. The white line marks the Fe_2O_3 value corresponding to the measured Fe_2O_3.

dehydrated (polycyclic metamorphic rocks), but also unaltered magmatic rocks (granites, gabbros, dolerite dykes, etc.), and the studied samples may belong to one of the latter cases.

Although the H_2O-saturated pseudosection for the Fe-Ti eclogite yields a satisfactory agreement between the model and the observations, the imperfect fit of the kyanite-eclogite (in particular between the calculated and measured grossular content in garnet) calls for exploring this aspect. Figure 16a is a *T*-XH_2O diagram at 14.5 kbar, corresponding to the pressure inferred for the growth of the garnet core, for the bulk composition used in calculating Fig. 12. The *x* axis involves variation of the H_2O content from zero at x=0 to a value at x=1 sufficient to saturate the assemblages. When H_2O undersaturation is reached, at XH_2O ~ 0.85, both kyanite and diopside become rapidly stable over the entire temperature interval explored. At lower H_2O contents, first epidote, then quartz disappears from the stable assemblages at XH_2O ~ 0.45 and 0.25, respectively. Consequently, such conditions (XH_2O <0.45) appear inappropriate to account for the crystallisation of the garnet core, which contains quartz and epidote as inclusions. On the other hand, the calculated grossular isopleths become strongly H_2O-sensitive beyond the epidote-out line, decrease to a minimum of about 16 at XH_2O ~ 0.15, and encompass values analysed in the garnet core (*Grs* ~ 21). In order to explore these divergent signals, a *P*–*T* pseudosection has been calculated at XH_2O = 0.3 (Fig. 16b). Nevertheless, epidote is not stable in the entire *P*–*T* range explored (650-850 °C, 10-18 kbar). The grossular isopleths (Fig. 16b) fit the values observed in the garnet core, but fail to account for the zoning pattern observed (increase-decrease – see above). Consequently, despite the shortcomings, the H_2O-saturated pseudosection yields the best match between the model and observations for the prograde part of the *P*–*T* path of the kyanite-eclogite. Finally, H_2O-saturation is also compatible with the large size of the minerals forming the peak assemblage (garnet, clinopyroxene, amphibole, kyanite) that suggests fast diffusion and hence the presence of a free fluid during the prograde evolution of the rock.

The coarse-grained corundum conundrum

In most kyanite-bearing eclogite in the study area, clusters of acicular corundum grains were produced together with sapphirine and plagioclase in symplectites replacing kyanite (Fig 8b; see also Möller, 1999). Rarely in the field, corundum is also found as coarser (up to 1 mm) pinkish-violet (Cr-bearing) crystals. They occur as inclusions in 2-4 cm kyanite grains and are thus an earlier generation than the acicular corundum intergrown with plagioclase. Blocky 0.3 mm large corundum crystals found together with rutile and spinel in one micro-domain of the kyanite-eclogite sample 8023F are likely of that early generation. At the same time, however, quartz is

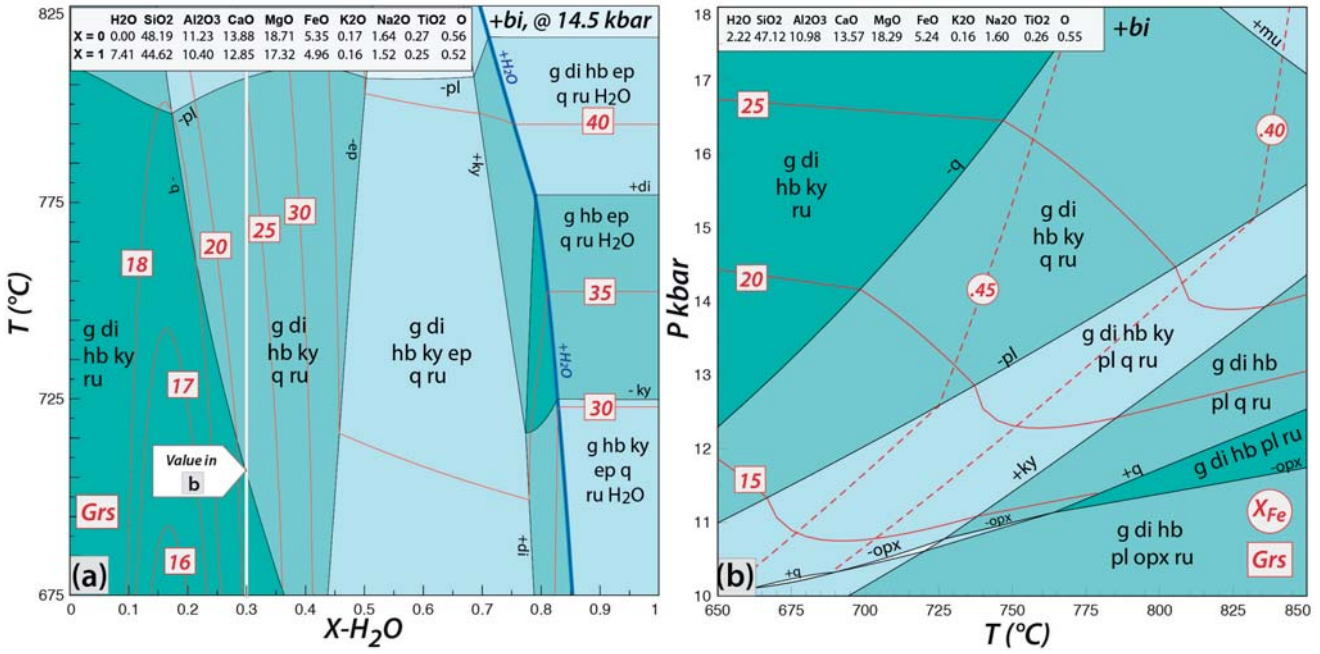

Figure 16: Effect of H_2O on the pseudosection of the kyanite-eclogite sample 8023F. (a) *T*-XH_2O pseudosection calculated between 675 and 825 °C at 14.5 kbar. The bulk rock compositions corresponding to H_2O-saturated and H_2O-undersaturated conditions (X = 0 and X = 1, respectively) are given in the upper left. The white line marks the H_2O value chosen to calculate the *P*–*T* pseudosection in (b). (b) *P*–*T* pseudosection calculated for an H_2O-undersaturated composition (X = 0.7 in (a)).

found locally in the matrix and can form large grains up to 1 mm, although generally confined in clinopyroxene and never in contact with sapphirine or symplectitic corundum. Kyanite, clinopyroxene and quartz are inferred to crystallise in equlibrium on the prograde *P–T* path (see above). Consequently, corundum could be considered as part of the peak mineral assemblage. Co-stability of quartz, corundum and kyanite implies unrealistic very high temperatures that are at variance with the other petrological evidence of the rock. Corundum is absent from our calculated pseudosections, even where we artificially increased the Al content. Aluminium is, however, a reputedly slowly diffusing element and can have very small equilibration volumes. Consequently, we consider that the local presence of coarse-grained corundum, although remaining enigmatic, does not affect the petrological interpretations presented above. It could be caused by (1) minor amounts of Cr and Fe that would stabilize a primary (prograde) corundum, or (2) a local excess of Al in the vicinity of kyanite that would lead to formation of primary corundum.

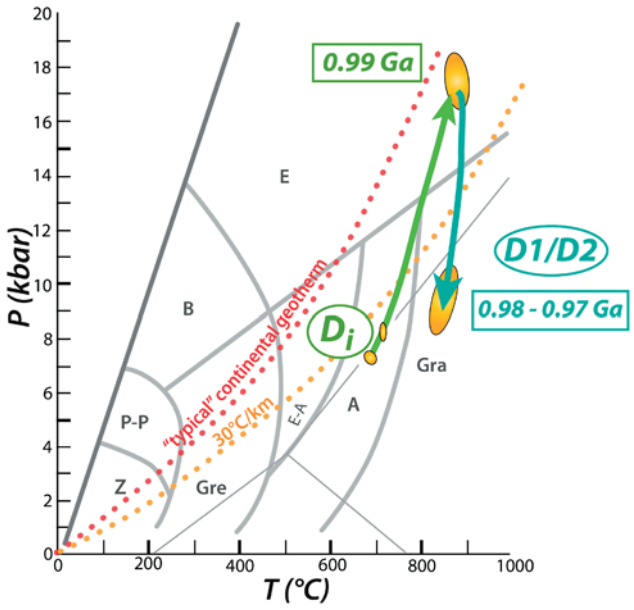

Figure 17: P–T path for Sveconorwegian eclogite, based on the modeling presented in this study. Di = internal foliation in garnet. Ages of eclogitization and D1-D2 deformation are from Möller et al. (2015). Metamorphic facies from Spear (1993), with "typical" continental geotherm from Brown & Musset (1993). Z = Zeolite; P-P = Prehnite-pumpellyite; B = Blueschist; Gre = Greenschist; E-A = Epidote-amphibolite; E = Eclogite; A = Amphibolite; Gra = Granulite.

Tectonic implications

The eclogite-bearing nappe represents a part of the Baltica continental crust that experienced westward tectonic burial to eclogite-facies conditions, beneath the Idefjorden Terrane, followed by eastward, foreland-directed, tectonic exhumation (Möller *et al.*, 2015). In the following section, we discuss the implications of the documented *P–T* path and the tectonic setting of the Sveconorwegian eclogites.

The first part of the *P–T* path, retrieved from the core of zoned garnet, shows a prograde metamorphic evolution from ~ 690 °C 7.5 kbar to 710 °C 8.5 kbar, at typical Barrovian-type conditions. Bent to sigmoidal inclusion trails, from the inner to the outer core of the Fe-Ti eclogite garnet, record syntectonic garnet growth during this stage. This was followed by burial to eclogite-facies depths at high temperature, reaching ~ 850-900 °C at 16-19 kbar, significantly higher than previously thought (Möller, 1998; 1999). Figure 17 illustrates that the peak pressure conditions coincide with a "normal" continental geotherm, reached along a steep prograde path (high d*P*/d*T*).

Subsequent near-isothermal decompression to granulite-facies conditions (810-875 °C, 8-11.5 kbar) is compatible with unpublished *P–T* estimates from below the footwall of the eclogite-nappe (C. Möller, unpublished data) and is in accordance with the regional occurrence of opx-bearing leucosome in garnet amphibolite in western parts of the Eastern Segment (Hansen *et al.*, 2015; C. Möller, unpublished field data). Granulite- and upper amphibolite-facies tectonites, including sapphirine-bearing mylonites, demonstrate that the decompression was coeval with deformation (Möller, 1999; Möller *et al.*, 2015; Tual *et al.*, 2015).

U-Pb zircon ages of prograde eclogitization and partial melt crystallization in orthogneiss place broad age brackets on the decompression at 988 ± 6 Ma and 976 ± 6 Ma, respectively (Möller *et al.*, 2015). However, the preservation of growth zoning in garnet, the near-isothermal decompression path, and the formation of symplectite suggest rapid exhumation and short residence at high temperatures (cf. Möller, 1998; 1999).

To summarize, eclogites in the Eastern Segment suggest both rapid burial to ~ 65 km and a rapid tectonic uplift (Fig. 17). From a tectonic point of view, this firstly requires a scenario with doubled crustal thickness at c. 1Ga. Secondly, given the geological setting in a migmatized nappe and the high temperatures at peak-pressure conditions and during decompression, it is likely that the exhumation was aided by the presence of partial melt (Möller *et al.*, 2015; Tual *et al.*, 2015).

The clockwise *P–T* path of the eclogites, associated with near isothermal decompression through granulite-facies conditions is typical of crustal overthickening and continental collision (e.g. Harley, 1989). This scenario is compatible with the setting of the eclogite-bearing nappe and enclosing rocks in the Eastern Segment, where H*P*-H*T* conditions, ductile deformation and foreland-vergent flow were widespread (Johansson *et al.*, 1991; Johansson & Kullerud 1993; Wang & Lindh, 1996; Möller *et al.*, 1997, 2007, 2015; Möller, 1998, 1999; Andersson *et al.*, 1999, 2002; Söderlund *et al.*, 2002; Bingen *et al.*, 2008b; Hansen *et al.*, 2015; Piñán-Lamas *et al.*, 2015; Tual *et al.*, 2015).

High-grade eclogite-facies terranes, petrologically almost identical to those in the Sveconorwegian orogen (carrying sapphirine-symplectitic high-temperature overprinted kyanite eclogite), are common in continental collision zones. Examples are found in the Trans-Hudson orogen (Baldwin *et al.*, 2007; 2015), the Grenville orogen (Grant, 1989; Davidson 1990), the Variscan orogen (O'Brien 1997; Godard & Mabit, 1998), the Caledonides (Johansson & Möller, 1986; Möller, 1988; Elvevold & Gilotti, 2000; Janák *et al.*, 2013), and the Alps (Liati & Siedel, 1994; 1996; Moulas *et al.*, 2013). The geodynamic setting varies from UH*P* metamorphism by continental subduction (e.g. Liou *et al.*, 2004 and references therein) to H*P* metamorphism by crustal thickening (e.g. Grujic *et al.*, 2011).

The classic markers of subduction of the continental crust into the mantle (Mg-Cr-rich mantle peridotite and UH*P* indicators), present e.g. in the Western Gneiss Region of Norway (Cuthbert *et al.*, 2000), are absent from the eclogite-bearing terrane in the Eastern Segment of the Sveconorwegian orogen. This and the fact that the peak-pressure estimate conforms to the continental thermal gradient (Fig. 17), speaks against subduction into the mantle and for a setting where the eclogite-facies metamorphism was instead caused by doubling of the thickness of the continental crust.

Among numerous specific models for the formation and exhumation of eclogites, one recently brought forward for the eastern Himalayan eclogites (Warren *et al.*, 2011; Grujic *et al.*, 2011) accounts for some tectonic and metamorphic features that are similar to the eclogites of the Eastern Segment. These similarities include (1) the metamorphic *P–T* path, with high temperatures (reaching ~ 850 °C) during eclogite-facies metamorphism (cf. also Kohn, 2014 and references therein); (2) similar compositions of the eclogite-bearing host gneisses and their surroundings (e.g. Hodges 2000), i.e. crustal affinity and lack of density contrast that could have promoted buoyancy-driven exhumation (Grujic *et al.*, 2011); (3) a ductile thrust at the base of the eclogite-bearing unit that has placed H*P* rocks on top of lower-*P* ones (Kelett *et al.*, 2010; Warren *et al.*, 2011; Grujic *et al.*, 2011). Eclogites in eastern Himalaya represent fragments of the lower overthickened crust and have been interpreted as exhumed over a crustal scale ramp within a weak lower crust (Warren *et al.*, 2011; Grujic *et al.*, 2011). This syn-convergence exhumation model involves tectonic extrusion (thrust below coupled with extension zone above) and does not require major extension or buoyancy forces (Grujic *et al.*, 2011). A major difference between the eclogite-bearing terranes exposed in the eastern Himalayas and in the Eastern Segment is that the Himalayan occurs in the upper crustal nappe stack, at the surface, whereas the Sveconorwegian eclogites studied in this paper stalled at a 40 km level. Nevertheless, this model constitutes an appealing mechanism for the formation and exhumation of the eclogites in the Eastern Segment (cf. Möller *et al.*, 2015). The similarities between Sveconorwegian and Himalayan eclogite occurrences (1-3 above) emphasize the modern style of Grenvillian-aged tectonics.

ACKNOWLEGEMENTS

L. Tual thanks Matthijs Smit for great assistance and fruitful discussions during EMPA analysis at Copenhagen University, DK. Discussions during an Erasmus teaching mobility of L. Tual at Rennes 1 University were appreciated. Jenny Andersson is thanked for numerous discussions and for the template of Figure 1. Research was funded by grants from the Geological Survey of Sweden (60-1655/2009, 61-1420/2010) and the Crafoord Foundation (20110817) to C. Möller.

REFERENCES

Andersson, J., Söderlund, U., Cornell, D., Johansson, L., & Möller, C. (1999). Sveconorwegian (-Grenvillian) deformation, metamorphism and leucosome formation in SW Sweden, SW Baltic Shield: constraints from a Mesoproterozoic granite intrusion. *Precambrian Research*, **98(1)**, 151-171.

Andersson, J., Möller, C.A. & Johansson, L. 2002. Zircon geochronology of migmatite gneisses along the Mylonite Zone (S Sweden): a major Sveconorwegian

terrane boundary in the Baltic Shield. *Precambrian Research*, **114**, 121–147.

Austin Hegardt, E., Cornell, D.H., Claesson, L., Simakov, S., Stein, H.J. & Hannah, J.L. 2005. Eclogites in the central part of the Sveconorwegian, Eastern Segment of the Baltic Shield: support for an extensive eclogite terrane. *Geologiska Föreningens i Stockholm Förhandlingar*, GFF, **127**, 221–232.

Baldwin, J. A., Powell, R., Williams, M. L., & Goncalves, P. 2007. Formation of eclogite, and reaction during exhumation to mid-crustal levels, Snowbird tectonic zone, western Canadian Shield. *Journal of Metamorphic Geology*, **25(9)**, 953-974.

Baldwin, J. A., Powell, R., White, R. W., & Štípská, P. 2015. Using calculated chemical potential relationships to account for replacement of kyanite by symplectite in high pressure granulites. *Journal of Metamorphic Geology*, **33(3)**, 311-330.

Ballevre, M., Pitra, P., & Bohn, M. 2003. Lawsonite growth in the epidote blueschists from the Ile de Groix (Armorican Massif, France): a potential geobarometer. *Journal of metamorphic Geology*, **21(7)**, 723-735.

Bingen, B. 1989. Geochemistry of Sveconorwegian augen gneisses from SW Norway at the amphibolite-granulite facies transition. *Norsk geologisk tidsskrift*, **69**, 177-189

Bingen, B., & van Breemen, O. 1998. U-Pb monazite ages in amphibolite-to granulite-facies orthogneiss reflect hydrous mineral breakdown reactions: Sveconorwegian Province of SW Norway. *Contributions to Mineralogy and Petrology*, **132(4)**, 336-353.

Bingen, B., Skår, Ø., Marker, M., Sigmond, E. M., Nordgulen, Ø., Ragnhildstveit, J., Mansfeld, J., Tucker, R. D. & Liégeois, J. P. 2005. Timing of continental building in the Sveconorwegian orogen, SW Scandinavia. *Norwegian Journal of Geology*, **85(1-2)**, 87-116.

Bingen, B. & Solli, A., 2009. Geochronology of magmatism in the Caledonian and Sveconorwegian belts of Baltica: synopsis for detrital zircon provenance studies. *Norwegian Journal of Geology,* **89 (4)**.

Bingen, B., Nordgulen, Ø., Viola, G., 2008a. A four-phase model for the Sveconorwegian orogeny, SW Scandinavia. Norwegian Journal of Geology 88, 43–72.

Bingen, B., Andersson, J., Soderlund, U., & Moller, C., 2008b. The Mesoproterozoic in the Nordic countries. *Episodes*, **31(1)**, 29-34.

Brown, G. C., & Mussett, A. E. 1993. The continental crust. In: *The Inaccessible Earth*. Springer Netherlands, 186-212

Carson, C. J., Powell, R. & Clarke, G. L. 1999. Calculated mineral equilibria for eclogites in CaO-Na_2O-FeO-MgO-Al_2O_3-SiO_2-H_2O: application to the Pouébo Terrane, Pam Peninsula, New Caledonia. *Journal of Metamorphic Geology*, **17**, 9-24.

Coggon, R. & Holland, T.J.B. 2002. Mixing properties of phengitic micas and revised garnet-phengite thermobarometers. *Journal of Metamorphic Geology*, **20**, 683-696.

Cuthbert, S.J., Carswell, D.A., Krogh-Ravna, E.J. & Wain, A. 2000. Eclogites and eclogites in the Western Gneiss Region, Norwegian Caledonides. *Lithos*, **52**, 165-195.

Dale, J., Powell, R., White, R. W., Elmer, F. L. & Holland, T. J. B. 2005. A thermodynamic model for Ca-Na clinoamphiboles in Na_2O-CaO-FeO-MgO-Al_2O_3-SiO_2-H_2O-O for petrological calculations. *Journal of Metamorphic Geology*, **23**, 771-791.

Davidson, A. 1990. Evidence for eclogite metamorphism in the southwestern Grenville Province. *Geological Survey of Canada*, Paper, **90–1C,** 113–118.

Diener, J. F. A., Powell, R., White, R. W. & Holland, T. J. B. 2007. A new thermo-dynamic model for clino- and orthoamphiboles in Na_2O-CaO-FeO-MgO-Al_2O3- SiO_2-H_2O-O. *Journal of Metamorphic Geology*, **25**, 631-656.

Elvevold, S. & Gilotti, J. A. 2000. Pressure–temperature evolution of retrogressed kyanite eclogites, Weinschenk Island, north–east Greenland Caledonides. *Lithos*, **53(2)**, 127-147.

Engvik, A. K., Bingen, B., & Solli, A. 2016. Localized occurrences of granulite: *P–T* modeling, U–Pb geochronology and distribution of early-Sveconorwegian high-grade metamorphism in Bamble, South Norway. *Lithos*, **240**, 84-103.

Godard, G., & Mabit, J. L. 1998. Peraluminous sapphirine formed during retrogression of a kyanite-bearing eclogite from Pays de Léon, Armorican Massif, France. *Lithos*, **43**, 15-29.

Grant, S. M. 1989. Tectonic implications from sapphirine-bearing lithologies, south-west Grenville Province, Canada. *Journal of Metamorphic Geology*, **7**, 583-598.

Grujic, D., Warren, C. J., & Wooden, J. L. 2011. Rapid synconvergent exhumation of Miocene-aged lower orogenic crust in the eastern Himalaya. *Lithosphere*, **3**, 346-366.

Guiraud, M., Powell, R. & Cottin, J. Y. 1996. Hydration of orthopyroxene—cordierite-bearing assemblages at Laouni, Central Hoggar, Algeria. *Journal of Metamorphic Geology*, **14**, 467-476.

Guiraud, M., Powell, R., & Rebay, G. 2001. H_2O in metamorphism and unexpected behaviour in the preservation of metamorphic mineral assemblages. *Journal of Metamorphic Geology*, **19(4)**, 445-454.

Hansen, E., Johansson, L., Andersson, J., LaBarge, L., Harlov, D., Möller, C., & Vincent, S. 2015. Partial melting in amphibolites in a deep section of the Sveconorwegian Orogen, SW Sweden. *Lithos*, **236**, 27-45.

Harley, S. L. 1989. The origins of granulites: a metamorphic perspective. *Geological Magazine*, **126**, 215-247.

Hodges, K. V. 2000. Tectonics of the Himalaya and southern Tibet from two perspectives. *Geological Society of America Bulletin*, **112(3)**, 324-350.

Holland, T. J. B. & Powell, R. 1998. *An* internally consistent thermodynamic dataset for phases of

petrological interest. *Journal of Metamorphic Geology*, **16**, 309-343.

Holland, T. J. B. & Powell, R. 2003. Activity-composition relations for phases in petrological calculations: an asymmetric multicomponent formulation. *Contributions to Mineralogy and Petrology*, **145**, 492-501.

Holland, T. J. B. & Powell, R. 2011. An improved and extended internally consistent thermodynamic dataset for phases of petrological interest, involving a new equation of state for solids. *Journal of Metamorphic Geology*, **29**, 333–383.

Holland, T. J. B., Baker, J. M. & Powell, R. 1998. Mixing properties and activity-composition relationships of chlorites in the system MgO-FeO-Al_2O_3-SiO_2-H_2O. *European Journal of Mineralogy*, **10**, 395-406.

Janák, M., Krogh Ravna, E. J., Kullerud, K., Yoshida, K., Milovský, R., & Hirajima, T. 2013. Discovery of diamond in the Tromsø Nappe, Scandinavian Caledonides (N. Norway). *Journal of Metamorphic Geology*, **31**, 691-703.

Johansson, L., & Möller, C. 1986. Formation of sapphirine during retrogression of a basic high-pressure granulite, Roan, Western Gneiss Region, Norway. *Contributions to Mineralogy and Petrology*, **94**, 29-41.

Johansson, L., & Kullerud, L., 1993. Late Sveconorwegian metamorphism and deformation in southwestern Sweden. *Precambrian Research*, **64**, 347-360.

Johansson, L., Lindh, A., & Möller, C. 1991. Late Sveconorwegian (Grenville) high-pressure granulite facies metamorphism in southwest Sweden. *Journal of Metamorphic Geology*, **9**, 283-292.

Johansson, L., Möller, C. & Söderlund, U. 2001. Geochronology of eclogite facies metamorphism in the Sveconorwegian Province of SW Sweden. *Precambrian Research*, **106**, 261-275.

Kellett, D. A., Grujic, D., Warren, C., Cottle, J., Jamieson, R., & Tenzin, T. 2010. Metamorphic history of a syn-convergent orogen-parallel detachment: The South Tibetan detachment system, Bhutan Himalaya. *Journal of Metamorphic Geology*, **28**, 785-808.

Kohn, M. J., 2014. Himalayan metamorphism and its tectonic implications. *Annual Review of Earth and Planetary Sciences*, **42**, 381-419.

Labrousse, L., Prouteau, G., & Ganzhorn, A. C., 2011. Continental exhumation triggered by partial melting at ultrahigh pressure. *Geology*, **39(12)**, 1171-1174.

Leake, B. E., Woolley, A. R., Arps, C. E. S., *et al.*, 1997. Nomenclature of amphiboles: Report of the Subcommittee on Amphiboles of the International Mineralogical Association, Commission on New Minerals and Mineral Names. *American Mineralogist*, **82**, 1019-1037.

Leake, B. E., Woolley, A. R., Birch, W. D., Burke, E. A., Ferraris, G., Grice, J. D., Hawthorne, F. C. Kisch, H. J., Krivovichev, V. G., Schumacher, J. C., Stephenson, N. C. N. & Whittaker, E. J. 2004. Nomenclature of amphiboles: additions and revisions to the International Mineralogical Association's amphibole nomenclature. *Mineralogical Magazine*, **68**, 209-215.

Liati, A., & Seidel, E. 1994. Sapphirine and högbomite in overprinted kyanite-eclogites of central Rhodope, N. Greece: first evidence of granulite-facies metamorphism. *European Journal of Mineralogy*, **6**, 733-737.

Liati, A., & Seidel, E. 1996. Metamorphic evolution and geochemistry of kyanite eclogites in central Rhodope, northern Greece. *Contributions to Mineralogy and Petrology*, **123**, 293-307.

Liou, J. G., Tsujimori, T., Zhang, R. Y., Katayama, I., & Maruyama, S. 2004. Global UHP metamorphism and continental subduction/collision: the Himalayan model. *International Geology Review*, **46(1)**, 1-27.

López-Carmona, A., Pitra, P. & Abati, J. 2013. Blueschist-facies metapelites from the Malpica-Tui Unit (NW Iberian Massif): phase equilibria modelling and H_2O and Fe_2O_3 influence in high-pressure assemblages. *Journal of Metamorphic Geology*, **31**, 263-280.

Moulas, E., Kostopoulos, D., Connolly, J. A., & Burg, J. P. 2013. *P–T* estimates and timing of the sapphirine-bearing metamorphic overprint in kyanite eclogites from Central Rhodope, northern Greece. *Petrology*, **21(5)**, 507-521.

Möller, C. 1988. Geology and metamorphic evolution of the Roan area, Vestranden, Western Gneiss region, central Norwegian Caledonides. *Norges Geologiske Undersøkelse*.

Möller, C., 1998. Decompressed eclogites in the Sveconorwegian (–Grenvillian) orogen of SW Sweden: petrology and tectonic implications. *Journal of Metamorphic Geology*. **16**, 641 656.

Möller, C., 1999. Sapphirine in SW Sweden: a record of Sveconorwegian (–Grenvillian) late-orogenic tectonic exhumation. *Journal of Metamorphic Geology*. **17**, 127–141.

Möller, C., Andersson, J., Lundqvist, I. & Hellström, F.A. 2007. Linking deformation, migmatite formation and zircon U–Pb geochronology in poly-metamorphic orthogneisses, Sveconorwegian Province, Sweden. *Journal of Metamorphic Geology*. **25**, 727–775.

Möller, C., Andersson, J., Dyck, B. & Antal Lundin, I., 2015. Exhumation of an eclogite terrane as a hot migmatitic fold nappe, Sveconorwegian orogen. Hirajama, T., Medaris, G. (Eds.), High- and ultrahigh-pressure metamorphism, from microscopic to orogenic scale. Lithos (Special Issue). *Lithos*, **226**, 147–168.

O'Brien, P. J. 1997. Garnet zoning and reaction textures in overprinted eclogites, Bohemian Massif, European Variscides: a record of their thermal history during exhumation. *Lithos*, **41(1)**, 119-133.

Pattison, D. R. M., 2003. Petrogenetic significance of orthopyroxene-free garnet + clinopyroxene + plagioclase ± quartz-bearing metabasites with respect to the amphibolite and granulite facies. *Journal of Metamorphic Geology*, **21**, 21-34.

Petersson, A., Scherstén, A., Bingen, B., Gerdes, A., & Whitehouse, M. J. 2015. Mesoproterozoic continental growth: U–Pb–Hf–O zircon record in

the Idefjorden Terrane, Sveconorwegian Orogen. *Precambrian Research*, **261**, 75-95.

Pinan-Llamas, A., Andersson, J. & Möller, C., 2015. Polyphasal foreland-vergent deformation in a deep parautochthonous section of the 1 Ga Sveconorwegian orogen, in: Roberts, N., Viola, G., Slagstad, T. (Eds.), The structural, metamorphic and magmatic evolution of Mesoproterozoic orogens. *Precambrian Research*, **265**, 121-149.

Pitra, P., Kouamelan, A. N., Ballèvre, M. & Peucat, J.-J., 2010. Palaeoproterozoic high-pressure granulite overprint of the Archean continental crust: evidence for homogeneous crustal thickening (Man Rise, Ivory Coast). *Journal of Metamorphic Geology*, **28**, 41-58.

Powell, R. & Holland, T. 1990. Calculated mineral equilbria in the pelite system, KFMASH. *American Mineralogist*, **75**, 367-380.

Powell, R., Holland, T. J. B. H. & Worley, B., 1998. Calculating phase diagrams involving solid solutions via non-linear equations, with examples using THERMOCALC. *Journal of metamorphic Geology*, **16**, 577-588.

Slagstad, T., Roberts, N. M., Marker, M., Røhr, T. S. & Schiellerup, H., 2012. A non-collisional, accretionary Sveconorwegian orogen. *Terra Nova*, **25(1)**, 30-37.

Spear, F. S., 1993 Metamorphic phase equilibria and pressure-temperature-time paths. Mineralogical Society of America, Washington, 799 pp.

Stephens, M. B., 2009. Synthesis of the bedrock geology in the Bergslagen region, Fennoscandian Shield, south-central Sweden. *Sveriges geologiska undersökning (SGU).*

Stephens, M. B. & Andersson, J. 2015. Migmatization related to mafic underplating and intra-or back-arc spreading above a subduction boundary in a 2.0–1.8 Ga accretionary orogen, Sweden. *Precambrian Research*, **264**, 235-257.

Söderlund, U., Jarl, L.G., Persson, P.O., Stephens, M.B. & Wahlgren, C.A.-H., 1999. Protolith ages and timing of deformation in the eastern, marginal part of the Sveconorwegian orogen, southwestern Sweden. *Precambrian Research*, **94**, 29–48.

Söderlund, U., Möller, C., Andersson, J., Johansson, L. & Whitehouse, M.J., 2002. Zircon geochronology in polymetamorphic gneisses in the Sveconorwgian orogen, SW Sweden: ion microprobe evidence for 1.46-1.42 Ga and 0.98-0.96 Ga reworking. *Precambrian Research*, **113**, 193-225.

Söderlund, U., Hellström, F. A. & Kamo, S. L., 2008. Geochronology of high-pressure mafic granulite dykes in SW Sweden: tracking the *P–T*–t path of metamorphism using Hf isotopes in zircon and baddeleyite. *Journal of Metamorphic Geology*, **26(5)**, 539-560.

Tual, L., Pinan-Llamas, A. & Möller, C. 2015. High-Temperature Deformation in the Basal Shear Zone of an Eclogite-Bearing Fold Nappe, Sveconorwegian Orogen, Sweden, in: Roberts, N., Viola, G., Slagstad, T. (Eds.), The structural, metamorphic and magmatic evolution of Mesoproterozoic orogens. *Precambrian Research*, **265**, 104-120.

Vander Auwera, J., Bolle, O., Bingen, B., Liégeois, J. P., Bogaerts, M., Duchesne, J. C. & Longhi, J. 2011. Sveconorwegian massif-type anorthosites and related granitoids result from post-collisional melting of a continental arc root. *Earth-Science Reviews*, **107**, 375-397.

Vielzeuf, D. & Schmidt, M. W. 2001. Melting relations in hydrous systems revisited: application to metapelites, metagreywackes and metabasalts. *Contributions to Mineralogy and Petrology*, **141**, 251-267.

Wahlgren, C. H., Cruden, A. R. & Stephens, M. B. 1994. Kinematics of a major fan-like structure in the eastern part of the Sveconorwegian orogen, Baltic Shield, south-central Sweden. *Precambrian Research*, **70**, 67-91.

Wang, X.-D. & Lindh, A., 1996. Temperature-pressure investigation of the southern part of the Southwest Swedish Granulite Region. *European Journal Mineralogy*, **8**, 51–67

Warren, C. J., Grujic, D., Kellett, D. A., Cottle, J., Jamieson, R. A., & Ghalley, K. S. 2011. Probing the depths of the India-Asia collision: U-Th-Pb monazite chronology of granulites from NW Bhutan. *Tectonics*, **30**, TC2004.

White, R. W., Powell, R., Holland, T. J. B. & Worley, B. A., 2000. The effect of TiO_2 and Fe_2O_3 on metapelitic assemblages at greenschist and amphibolite facies conditions: mineral equilibria calculations in the system K_2O-FeO-MgO-Al_2O_3-SiO_2-H_2O-TiO_2-Fe_2O_3. *Journal of Metamorphic Geology*, **18**, 497-511.

White, R. W., Powell, R. & Holland, T. J. B., 2001. Calculation of partial melting equilibria in the system Na_2O-CaO-K_2O-FeO-MgO-Al_2O_3-SiO_2-H_2O (NCKFMASH). *Journal of Metamorphic Geology*, **19**, 139-153.

White, R. W., Powell, R. & Clarke, G. L. 2002 The interpretation of reaction textures in Fe-rich metapelitic granulites of the Musgrave Block, central Australia: constraints from mineral equilibria calculations in the system K_2O-FeO-MgO-Al_2O_3-SiO_2-H_2O-TiO_2-Fe_2O_3. *Journal of Metamorphic Geology*, **20**, 41-55.

White, R. W., Powell, R. & Holland, T. J. B. 2007 Progress relating to calculation of partial melting equilibria for metapelites. *Journal of Metamorphic Geology*, **25**, 511-527.

Wolf, M. B. & Wyllie, P. J. 1994. Dehydration-melting of amphibolite at 10 kbar: the effects of temperature and time. *Contributions to Mineralogy and Petrology*, **115**, 369-383.

SUPPORTING INFORMATION

P–T evolution of Precambrian eclogite in the Sveconorwegian orogen, SW Sweden.

Lorraine Tual [1]*, Pavel Pitra [2], Charlotte Möller [1]

[1] Department of Geology, Lund University, Sölvegatan 12, SE-223 62 Lund, Sweden

[2] Géosciences Rennes, UMR CNRS 6118, Université Rennes 1, 35042 Rennes, Cedex, France

Short title: *P–T* evolution of Precambrian eclogite, SW Sweden.

** Corresponding author: lorraine.tual@gmail.com; +46729373025*

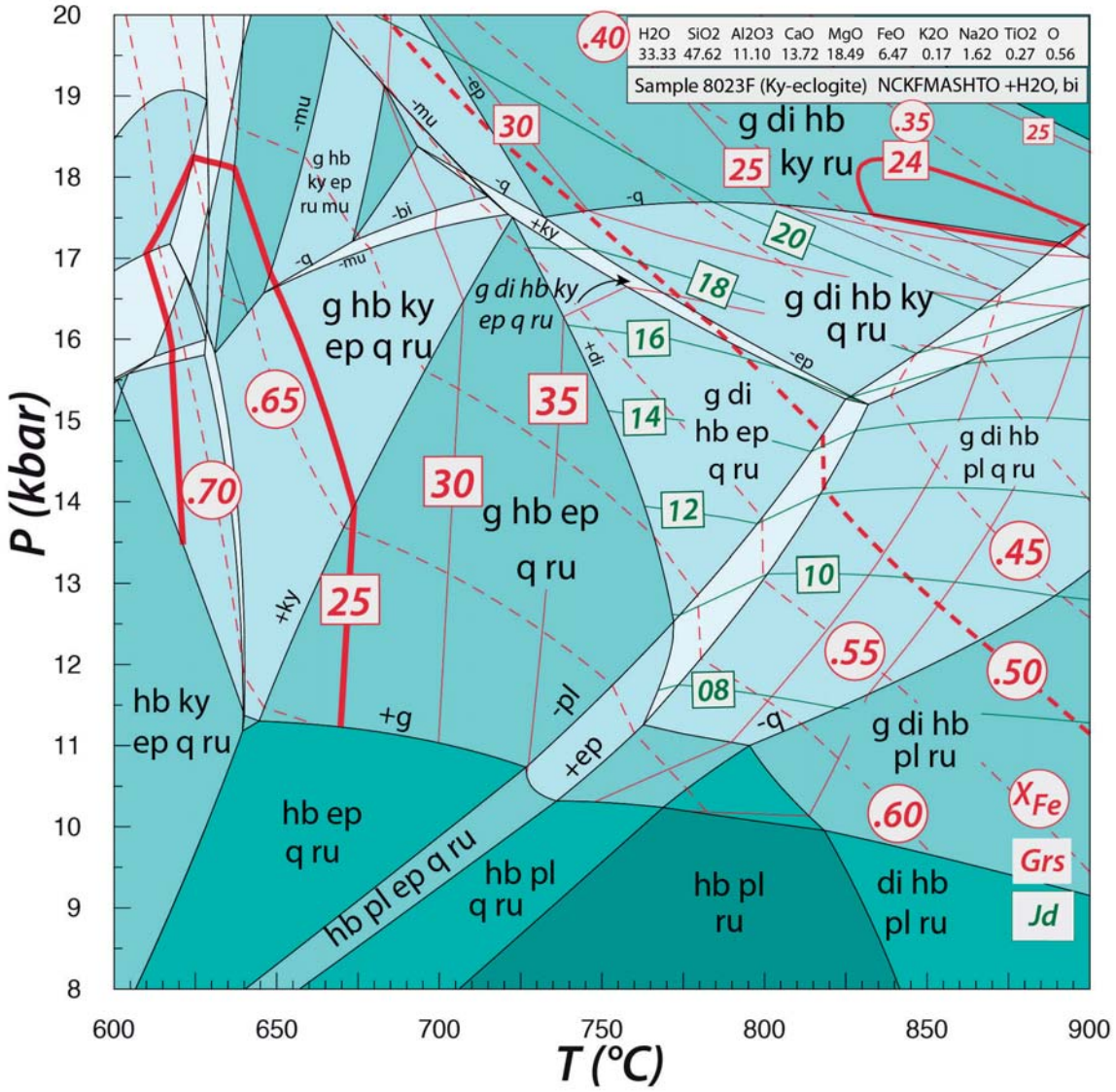

Figure S1: Pseudosection calculated for the kyanite eclogite (8023F), ignoring Fe fractionation in sulphide. The rock composition is given as mole-% oxide. Compositional isopleths for garnet and clinopyroxene are shown in red and green, respectively.

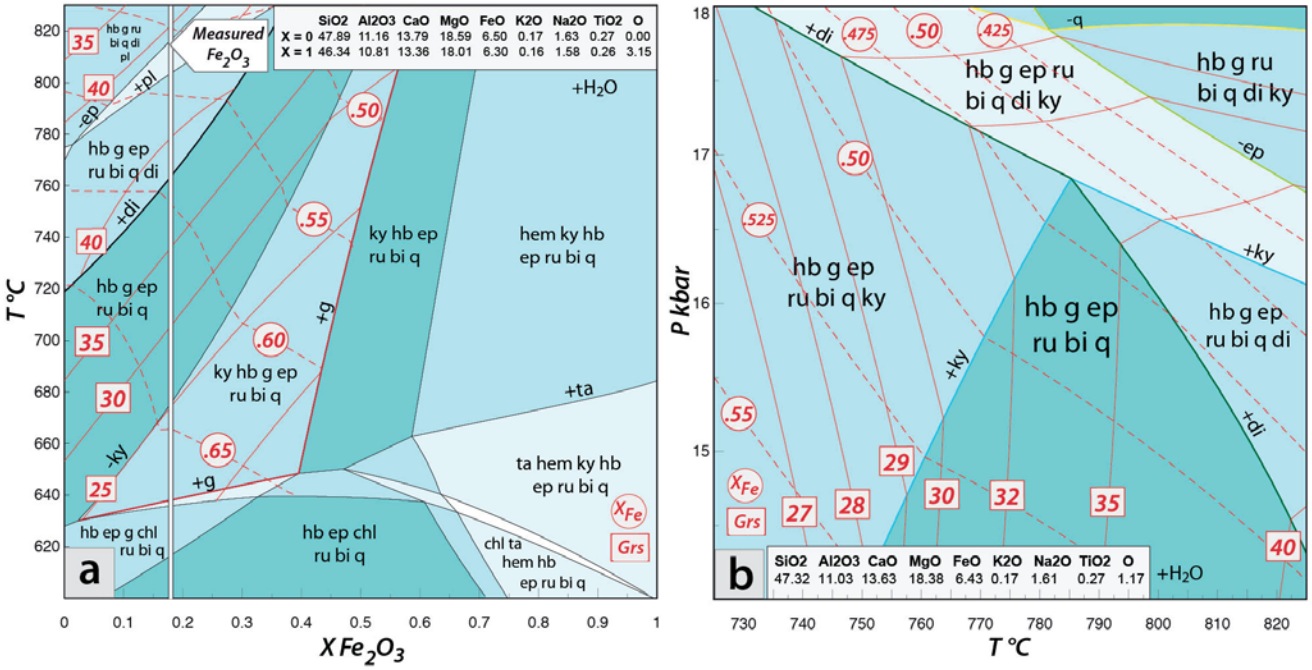

Figure S2: T-XFe2O3 pseudosection showing the effect of Fe2O3 (a) on the paragenesis at 14 kbar, between 610 and 830 °C, for the kyanite-eclogite sample 8023F – Fractionation of Fe in sulphide is not considered. The bulk rock compositions in mole-% oxide corresponding to minimum and maximum possible amount of Fe2O3 (X = 0 and X = 1, respectively) are given in the upper right. The pseudosection is calculated in the range of X = 0 and X = 1. The white line marks the Fe2O3 value corresponding to the measured Fe2O3. (b) *P–T* pseudosection showing the effect of increasing Fe2O3, using a value corresponding at X = 0.37 in (a).

PAPER III

Tracking the prograde P–T path of Precambrian eclogite using Ti-in-quartz and Zr-in-rutile thermobarometry.

Lorraine Tual [1]*, Charlotte Möller [1], Martin Whitehouse[2]

[1] Department of Geology, Lund University, Sölvegatan 12, SE-223 62 Lund, Sweden
[2] Swedish Museum of Natural History, Box 50 007, SE-104 05 Stockholm, Sweden

** Corresponding author: lorraine.tual@gmail.com; +46729373025*

ABSTRACT

Fe-Ti-rich eclogite from the 1.0 Ga Sveconorwegian orogen, SW Sweden, contains abundant quartz, rutile and zircon in distinct microtextural sites: garnet core, garnet rim, and matrix. In situ analyses of Ti-in-quartz and Zr-in-rutile record the temperatures of progressive crystallization of quartz and rutile during the prograde metamorphic path. Assemblages and compositions of minerals at different temperatures and pressures are constrained independently by a *P–T* pseudosection model for the same rock. Zr-in-rutile yields temperatures of 700–715 °C for the growth of the garnet core at 7 kbar, 760–790 °C for growth of the garnet rim at 12-18 kbar, and ~810 °C for equilibration of the matrix minerals at 18 kbar. Ti-in-quartz yield temperatures of ~635 °C for the growth of the garnet core, 740–890 °C for the growth of the garnet rim growth, and ~890 °C for the equilibration of the matrix minerals. For the early prograde stages (garnet core) the Zr-in-rutile temperature estimates are in accord with the pseudosection, but only a few grains record the metamorphic peak. Ti-in-quartz estimates for the metamorphic peak (garnet rim and matrix) conform to the pseudosection, but appear too low for the early prograde stage (garnet core). The pseudosection shows that rutile was produced by continuous ilmenite breakdown during the early stages of prograde metamorphism, a reaction that ran to completion at c. 730 °C. Rutile grains in the garnet rim and the matrix grew larger by recrystallization of previously produced rutile; this recrystallization is interpreted to have been particularly efficient at 775–815 °C, the stage during which hornblende was consumed and clinopyroxene produced (i.e. dehydration). The combination of Ti-in-quartz and Zr-in-rutile thermometry yields both pressure and temperature conditions in almost perfect agreement with the *P–T* path as deduced from the pseudosection. The variation in Ti concentration in quartz is small regardless of crystal size, and the Ti-in-quartz thermometer provides both precise and accurate peak temperatures of 875–910 °C, without significant diffusional reequilibration. The lack of significant Ti diffusion in quartz is consistent with a short residence time at high-temperature. Our study demonstrates that *P–T* pseudosection models provide insights on the crystallization sequences of metamorphic phases that are important in the interpretation of Ti-in-quartz and Zr-in-rutile temperature data. The combination of the three methods has the potential of yielding detailed information on the prograde *P–T* path.

Keywords: *Ti-in-quartz; Zr-in-rutile; eclogite; Sveconorwegian orogen; prograde P–T path*

INTRODUCTION

Trace element thermometers such as zirconium-in-rutile and titanium-in-quartz (hereinafter referred to as Zr-in-rutile and Ti-in-quartz, respectively; Zack *et al.*, 2004; Watson *et al.*, 2006; Wark & Watson, 2006; Ferry & Watson 2007, Thomas *et al*, 2010) have proven an independent means of *P–T* estimation for metamorphic terranes (e.g. Kooijman *et al.*, 2012; Ewing *et al.*, 2013; Ashley *et al.*, 2013). The Zr-in-rutile thermometer is particularly useful for determination of equilibration temperatures of high-grade metamorphic rocks such as granulite, for which Fe-Mg exchange thermometry is problematic (e.g. Zack *et al.*, 2004; Baldwin and Brown, 2008; Luvizotto & Zack, 2009; Zhang *et al.*, 2009; Jiao *et al.*, 2011; Kooijman *et al.*, 2012; Ewing *et al.*, 2013; Štípská *et al.*, 2014; Korhonen *et al.*, 2014; Liu *et al.*, 2015). The Ti-in-quartz thermometer is applicable over a wide range of temperatures (e.g.: Spear & Wark 2009; Menegon *et al.*, 2011; Spear

et al., 2012; Ashley *et al*; 2013; Kidder *et al.*, 2013). The cathodoluminescence (CL) intensity of quartz is strongly dependent on Ti content and can provide qualitative indications on chemical zoning during crystal growth or diffusion processes (e.g. Spear & Wark, 2009; Leeman *et al.*, 2012).

The Ti-in-quartz and Zr-in-rutile thermometers both rely on the equilibrium between quartz, rutile, and zircon. The Ti-in-quartz equilibrium is more dependent on pressure than Zr-in-rutile. Consequently, if Ti-in-quartz and Zr-in-rutile results are paired, P and T can be constrained from the intersection of the two equilibrium lines in the P–T field (Thomas *et al.*, 2010). Alternatively, if pressure can be determined by independent means (geobarometry or other constraints from phase equilibria), Ti-in-quartz and Zr-in-rutile can be used as two independent thermometers.

This study investigates the behavior of the Zr-in-rutile and Ti-in-quartz equilibria during prograde and peak metamorphism of quartz-bearing high-temperature eclogite in the Sveconorwegian orogen. The prograde P–T stages and peak P–T conditions have been independently constrained by pseudosection modelling coupled with phase equilibria and chemical zoning of garnet (Tual *et al.*, *submitted*). Our results show that whereas Zr-in-rutile accurately records the early stages of the prograde part of the P–T path, Ti-in-quartz records peak temperatures. The phase equilibria model shows that this is due to rapid rutile recrystallization during the main continuous dehydration reaction in the rock. We show that, when combined, the three independent methods Ti-in-quartz, Zr-in-rutile, and P–T pseudosection model yield robust constraints on temperature and insights on crystallization process during metamorphism.

2 TECTONIC SETTING

The Sveconorwegian orogen is a 500 km wide belt in SW Scandinavia (Fig. 1; parts of the Baltic Shield), which underwent accretion to collisional orogeny in the time period 1.14-0.92 Ga (Bingen *et al.*, 2005; Bingen *et al.*, 2008). Today the orogen is eroded and exposes deep sections of the mountain chain. Eclogite is present in the easternmost part of the orogen, the Eastern Segment, which is the lithological continuation of Baltica crust (Möller *et al.*, 2015 and references therein). The eclogites are bound within a recumbent fold nappe, which lies just underneath the contact with the Idefjorden Terrane (Fig. 1; Möller *et al.*, 2015). The nappe represents a part of the Baltica continental crust that experienced westward tectonic burial at eclogite-facies conditions beneath the western Sveconorwegian terranes, followed by eastward, foreland-directed, tectonic exhumation at granulite facies temperatures and stalling at c. 40 km depth (Möller, 1998, 1999; Möller *et al.*, 2015;

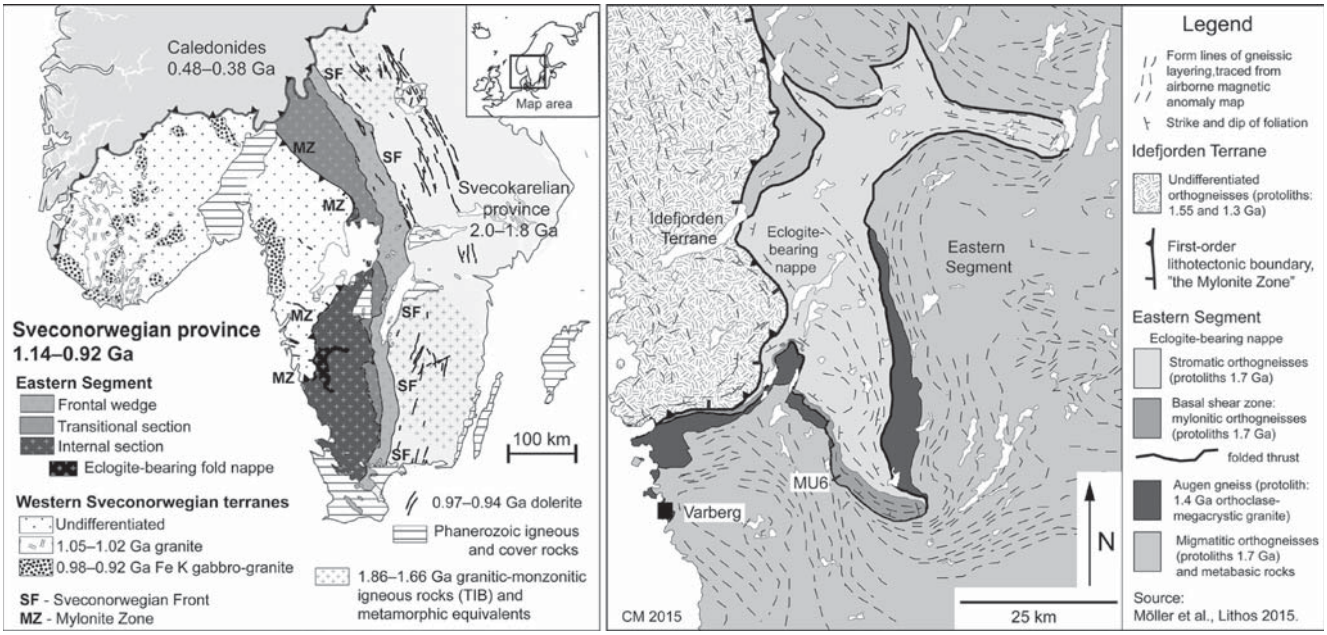

Figure 1: (a) Sketch map of the Sveconorwegian orogen showing the Eastern Segment (dark grey tones) and the western Sveconorwegian terranes, separated by ductile deformation zones (after Bingen *et al.*, 2008). Figure based on 1:5 M Fennoscandian map database and Geological Survey of Sweden (SGU) 1:1 M Bedrock map database (template provided by J. Andersson, SGU). TIB = Transcandinavian Igneous Belt. (b) Sketch map showing the location of the eclogite-bearing terrane after Möller *et al.* (2015). The location of the investigated sample (MU6) is indicated.

Tual *et al.*, 2015; Tual *et al.*, *submitted*). The timing of eclogite metamorphism (collision) and exhumation at 40 km depth is bracketed between 0.99 and 0.97 Ga (U-Pb ages of zircon; Johansson *et al.*, 2001; Möller *et al.*, 2015).

3 *P–T* EVOLUTION AND PETROGRAPHY

In addition to common garnet-clinopyroxene dominated rocks, some eclogite bodies in the Eastern Segment contain layers of Mg-Al-rich kyanite-bearing eclogite and Fe-Ti-rich eclogite. The two latter rock types provide detailed information on the *P–T* evolution (Möller 1998, 1999; Möller *et al*, 2015; Tual *et al*. 2015; Tual *et al.*, *submitted*). All eclogites were partially re-equilibrated during decompression at high-pressure granulite- and upper amphibolite-facies, but sizable garnet grains preserve records of the prograde metamorphic evolution, and remnant grains of other peak-pressure minerals (clinopyroxene, rutile, ± quartz, ± kyanite) are locally preserved in the matrix. The mineral assemblages, micro-textures, and chemical zoning of garnet in these rocks have allowed deduction of a sequence of metamorphic stages and a clockwise *P–T* evolution (Möller 1998, 1999; Tual *et al.*, *submitted*). Growth zoning in garnet is preserved despite high temperatures during peak metamorphism and decompression, which testifies to limited diffusion and short residence times at high-temperature (*op. cit.*).

The sample chosen for this study (MU6) is from a Fe-Ti-rich layer in a 2 x 1.5 km large mafic body (WGS84: 57°09'21.3"N 12°42'49.4"E; Lilla Ammås). The high-pressure assemblage is garnet + clinopyroxene + quartz + rutile + accessory apatite and zircon. Amphibole, ilmenite, and plagioclase are present in lower amounts, the two latter as early prograde and retrograde phases. The sample is rich in quartz, rutile, and zircon, and in this respect well suited for Zr-in-rutile and Ti-in-quartz thermobarometry. The calculated *P–T* pseudosection for this sample shows two prograde stages spanning from 670 to 880 °C (Fig. 2; Tual *et al.*, *submitted.*). Below we report the petrography and mineral chemistry of sample MU6; further details including pseudosection calculation for this sample are provided in Tual *et al.*, (*submitted).*

Mineral compositions are given in mole % unless stated otherwise. Cpfu = cations per formula unit. X_{Fe} = $Fe^{2+}/(Fe^{2+}+Mg)$; *Grs* = 100xCa/(Ca+Fe^{2+}+Mg+Mn); *Prp* = 100xMg/(Ca+Fe^{2+}+Mg+Mn); *Alm* = 100xFe^{2+}/(Ca+Fe^{2+}+Mg+Mn); *Sps* = 100xMn/(Ca+Fe^{2+}+Mg+Mn); *An* = 100xCa/(Ca+Na+K); *Jd* = 100xNa/(Na+Ca). The symbol "→" is used to describe the zoning from core to rim.

Garnet is 3-5 mm large, constitutes 70% of the sample and has a distinct core-and-rim structure. The core domains contain elongated inclusion trails of rutile, quartz, plagioclase, and locally hornblende, which follow straight, gently bent or locally sigmoidal patterns (Fig. 3a). An inclusion-poor zone in the inner rim of garnet separates the core from the outer rim; in the outer rim rutile and quartz grains are 5-10 times larger than in the core, and their orientations follow the garnet rim (Fig. 3a-d). Three garnet grains (A, C, E) with distinct core and rim domains were selected for Ti-in-quartz and Zr-in-rutile analysis. Garnet A has a comparably large core domain with abundant small rutile inclusions, and a distinct rim (especially in the upper part of the grain in Fig. 3b). The core of garnet C (Fig. 3c) has rounded quartz inclusions interspersed between elongated rutile trails, and contains a higher proportion of quartz inclusions than garnet A. Garnet E has inclusion trails with a sigmoidal shape (Fig. 3d), contains abundant rutile and quartz inclusions of various sizes, and elongated quartz in its core is unusually large (~100µm). Garnet is chemically zoned: *Alm*=55→46, *Prp*=17→32, *Sps*=3→1, X_{Fe}=0.76→0.61. The grossular content increases slightly from the garnet core to the inner rim (*Grs*=25→28), is uniform in the inner rim, and a decreases towards the outermost rim (*Grs*=25-26).

Rutile occurs as a relatively abundant matrix phase and as inclusions in garnet, quartz and clinopyroxene (2.5%; Figs. 3 & 4a-l). In garnet cores, elongated rutile grains define conspicuous inclusion trails (together with quartz) and are locally associated with minute ilmenite grains; straight grain boundaries indicate equilibrium between rutile and ilmenite. Matrix rutile grains are also associated with ilmenite, but show a contrasting texture, characterized by partial to complete replacement of rutile by ilmenite. This retrograde type of ilmenite often contain composite lamellae of ilmenite + quartz (cf "ilm*", Figs. 3b & 4i). The grain size of rutile increases progressively from a few µm in garnet cores, to a few hundred µm in garnet rims (Fig. 3a & d), and up to 2 mm in the matrix (Fig. 3).

Quartz constitutes nearly 20% of the matrix and individual grains are up to 3 mm large (Fig. 2). In garnet cores, 0.01-0.1 mm quartz grains form oriented inclusions, often spatially associated with apatite or rutile (Figs. 2 & 4a-e). By contrast, quartz inclusions in garnet rims are randomly orientated and of larger

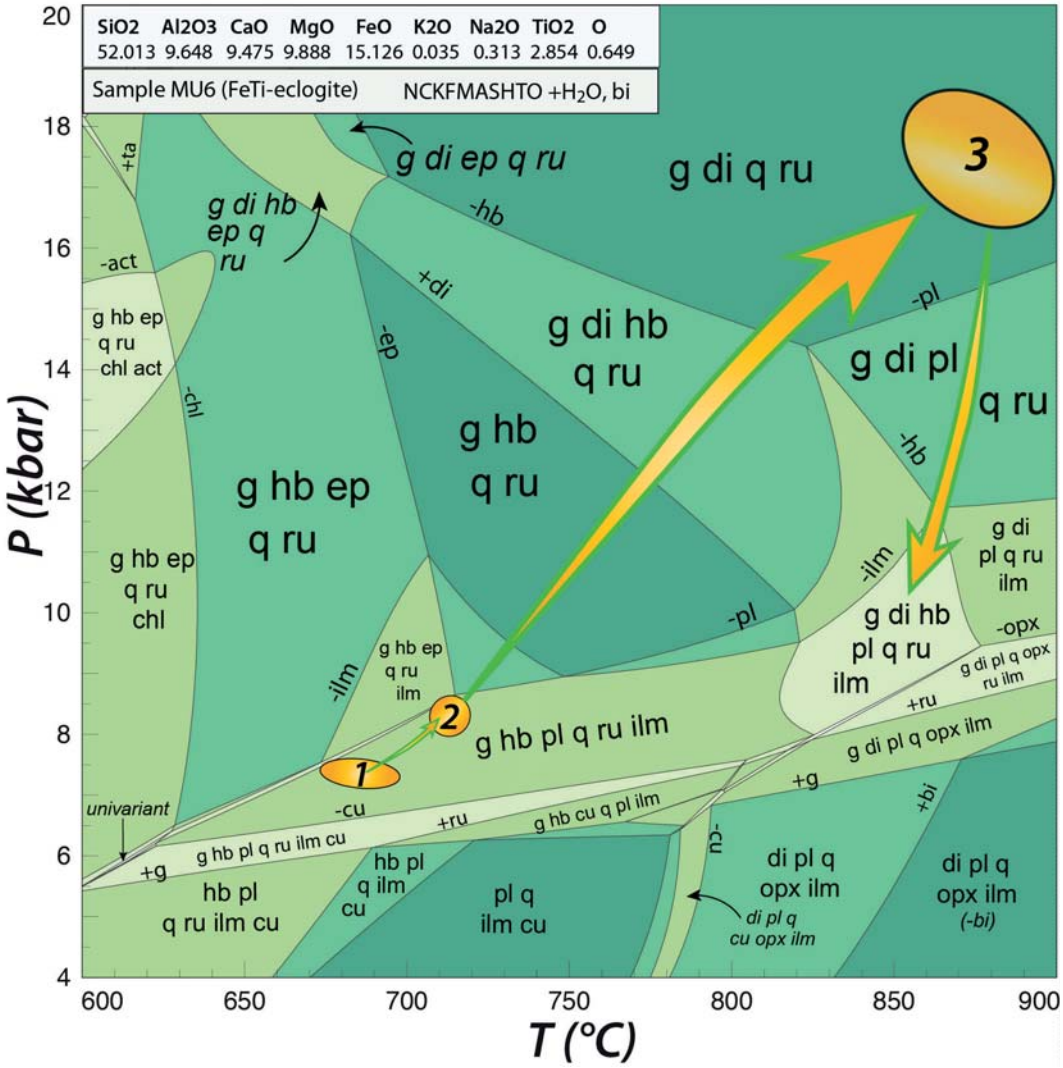

Figure 2: Pseudosection calculated for sample MU6 (from Tual *et al.* submitted). The rock composition is given as mole-% oxide. Ellipses correspond to the stages described in the text and used for Zr-in-rutile and Ti-in-quartz thermometry. Mineral abbreviations from Holland & Powell (2011).

size (0.05-0.3 mm; Figs. 2 & 4f-j). CL zoning has neither been detected in quartz inclusions (Fig. 4a-j), nor in the matrix quartz (Fig. 4a-m, with one oscillatory-zoning exception shown in Fig. 4n).

Zircon is present in all textural settings, in the garnet cores, garnet rims and in the matrix. More zircon is however found in garnet rims and in the matrix than in garnet cores. The grain size of zircon is generally <20 µm in garnet cores, and >30µm in garnet rims and in the matrix.

Matrix clinopyroxene grains can be up to 10mm large and constitute ~10% of the sample (Fig. 2a). Their composition is diopside with low jadeite content (X_{Fe}=0.10-0.22, *Jd*=2-10, Al = 0.05-0.32 cpfu) and they commonly contain abundant inclusions of expelled plagioclase (up to 50 vol.%; Fig. 2a). The Ca-Tschermak component ranges between 3 and 10%. Clinopyroxene is locally partly replaced by amphibole in the matrix (Fig. 2a). Amphibole is present in garnet cores; their composition classifies as hornblende, although some inclusions in garnet are pargasitic or tschermakitic. Plagioclase occurs as inclusions in the garnet core and expelled blebs in clinopyroxene (up to 50%). The composition of plagioclase in clinopyroxene is An = 45-55; inclusions in garnet core vary strongly from An= 40 to 81. Minor late hydration has led to local formation of chlorite and sericite.

In summary (from Tual *et al.*, *submitted),* the rock underwent prograde metamorphism at increasing pressures through the amphibolite-facies to the eclogite-facies. During the first stage garnet formed and grew in equilibrium with hornblende + rutile + quartz + plagioclase + ilmenite + zircon, concomitant with deformation (locally bent to sigmoidal

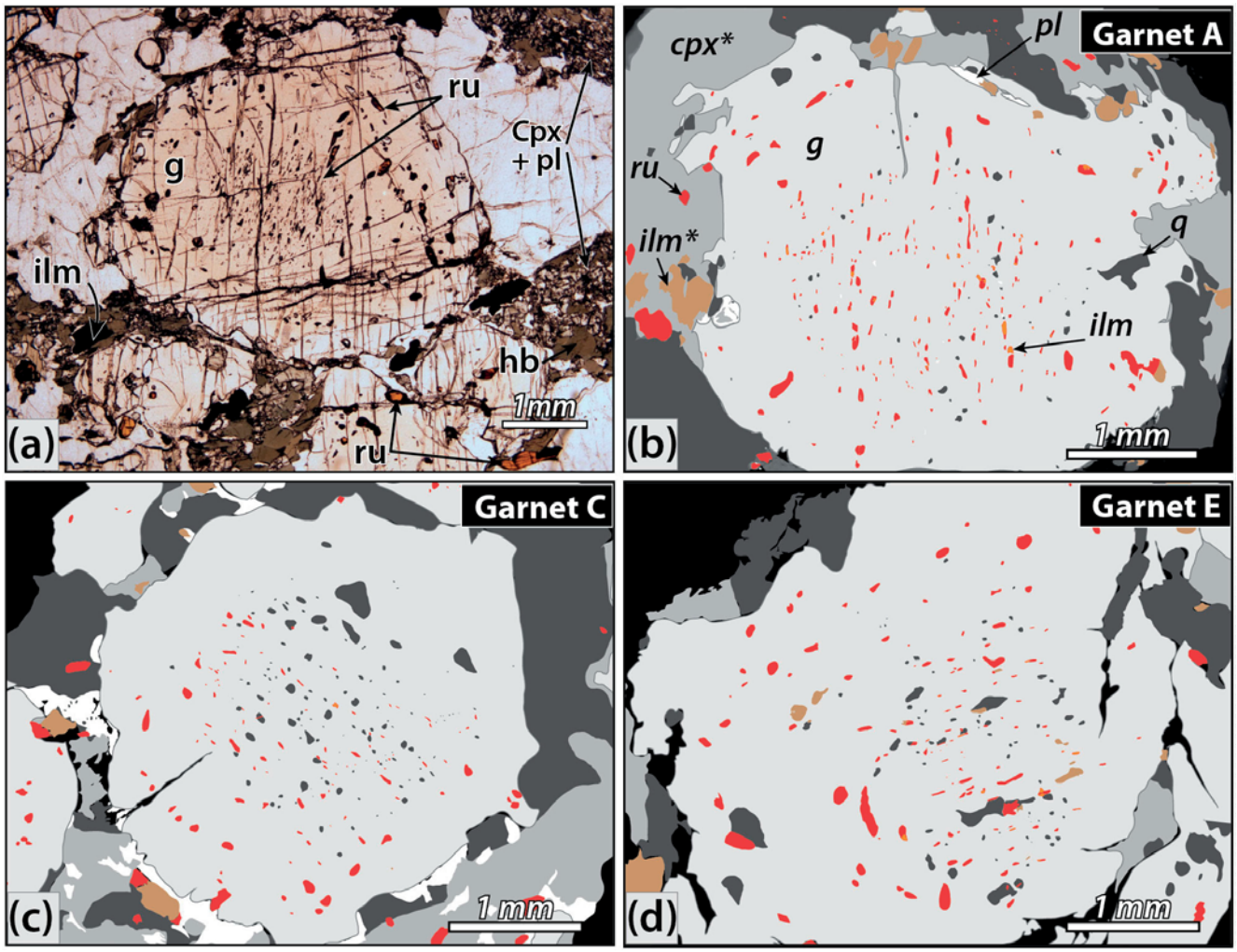

Figure 3: Garnet petrography, sample MU6. (a) Photomicrograph (plane light) of typical texture with garnet (g) + quartz (q) + clinopyroxene (cpx; now clinopyroxene + plagioclase (pl) ± hornblende (hb)) + rutile (ru; in the matrix partially replaced by ilmenite). (b-d) Sketches based on backscatterred electron (BSE) images of garnet grains A, C and E. Oriented trails rich in quartz and rutile are present in the garnet core, locally with sigmoidal shape (d). Inclusions are scarce in the inner rim of garnet; in the outer rim inclusions are larger than in the core and with a less pronounced orientation.

inclusion trails). Garnet continued to grow under eclogite-facies conditions (clinopyroxene-present and plagioclase-absent fields, Fig. 2) at higher *P–T* conditions. The matrix assemblage (garnet + clinopyroxene + quartz + rutile) equilibrated at the metamorphic peak, and was subsequently modified during decompression. Plagioclase + clinopyroxene intergrowths formed during decompression from a more sodic high-pressure clinopyroxene. A second generation of ilmenite formed at the expense of matrix rutile. Minor chlorite and sericite formed at a late stage by small-scale local fluid infiltration at low temperature.

4 METHODS

The Ti-in-quartz and Zr-in-rutile thermometer are both moderately and slightly pressure sensitive, respectively; hence the estimation of pressure by an independent method is preferable. The pseudosection model of sample MU6 (Fig. 2, Tual *et al.*, *submitted*) allows independent estimation of pressures associated with discrete metamorphic stages: garnet core, garnet rim and matrix equilibration.

4.1 Pseudosection calculation

Pseudosection calculation, with results and interpretation (Fig. 2), are given in detail by Tual *et al.* (*submitted*). Below we summarize the relevant data associated with constraining pressure for different metamorphic stages. The pseudosection was calculated using THERMOCALC 3.3 and database ds55 (Powell *et al.*, 1998) in the system NCKFMASHTO (Na_2O - CaO - K_2O - FeO - MgO - Al_2O_3 - SiO_2 - H_2O - TiO_2 - O). Mineral abbreviations are

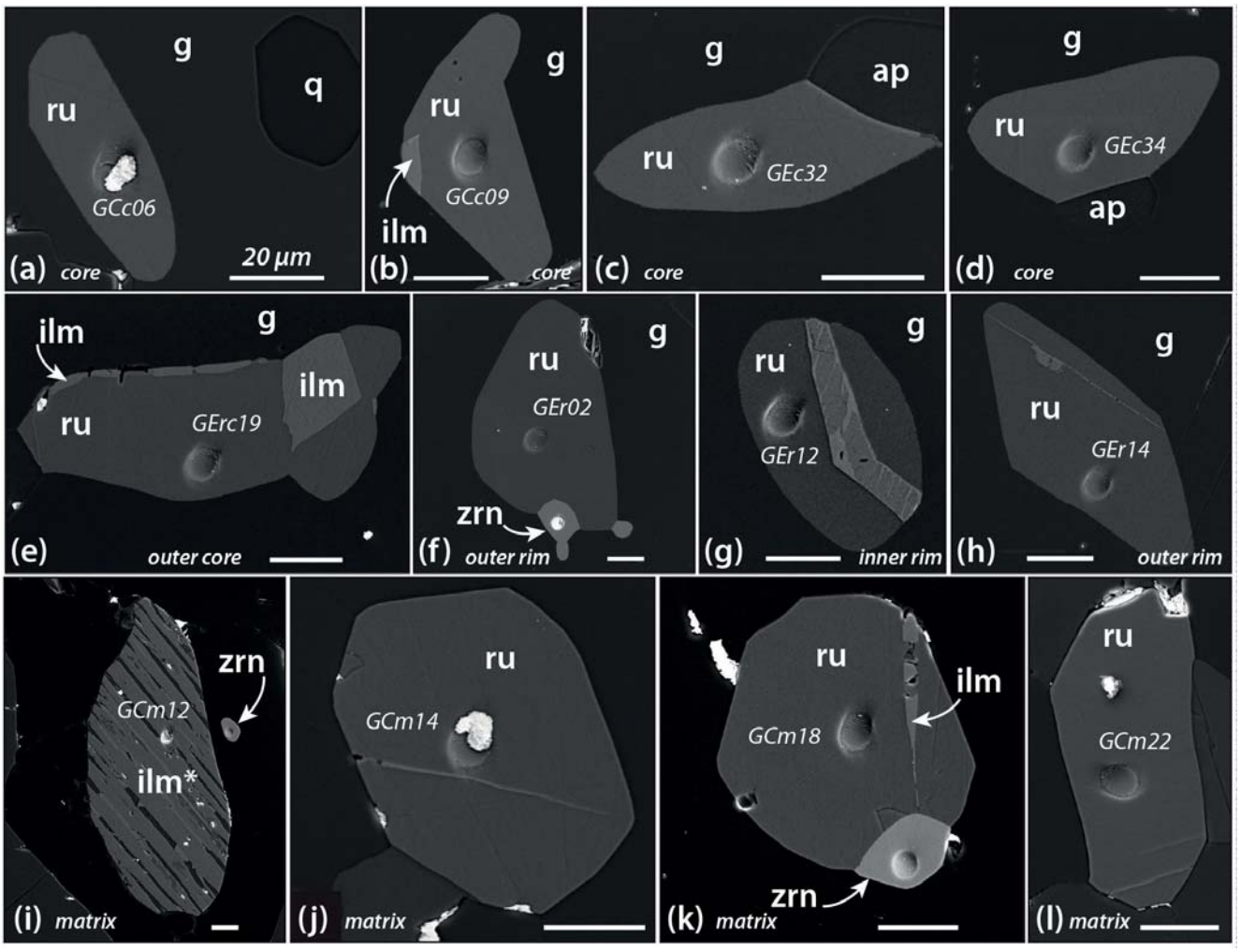

Figure 4: Secondary electron (SE) images of rutile grains, with analytical spots (Table S1), in (a-e) the cores of garnet, (f-h) the rims of garnet, and (i-l) the matrix. Ilmenite occurs as inclusions in the cores of garnet (b, e), while it has partly or entirely replaced rutile grains in the matrix (i).

those used by THERMOCALC (Holland & Powell, 2011).

The three ellipses in the pseudosection (Fig. 2) correspond to stages in the prograde history. The first stage, constrained by mineral inclusions and the *inner core* composition of garnet, shows the onset of garnet growth at c. 7–7.5 kbar and 675–700 °C. The assemblage is g + hb + ru + pl + q + ru + ilm (+ bi, Fig. 5). The second stage, at 8–8.5kbar and 705–720 °C, is constrained by the composition of the *outer core* of garnet in the presence of plagioclase. The inclusion-poor domains in the *inner rim* of garnet corresponds roughly to conditions from the second stage to ~12 kbar at 775 °C, based on the garnet composition. The garnet rim contains clinopyroxene inclusions; hence the rock is inferred to have passed through a clinopyroxene-in field during growth of the garnet rim. Finally, the third stage at ~16-18.5 kbar at 850–900 °C is based on the *matrix* minerals *and* the *outer rim* of garnet.

The pseudosection-based *P*–*T* estimates for the three stages of the *P*–*T* path provide pressure estimates for input in thermometry calculations; the temperatures estimates can also be compared with those from Zr-in-rutile and Ti-in-quartz thermometry. The pressure values entered in the equations are: (1) 7 kbar, inner garnet core; (2) 12 kbar, inclusion-poor domain in garnet and the uppermost limit for garnet core and lowermost limit for garnet rim; and (3) 18 kbar, outer garnet rim and matrix.

4.2 Sample preparation

Rock slabs of 0.5 mm were prepared and polished for *in situ* analyses. Four garnet grains and their surrounding matrixes were selected using reflected light binocular microscopy. The selection was based on (1) abundance of rutile and quartz inclusions in garnet, (2) distinct core and rim domains in garnet, (3) close proximity of matrix quartz and rutile, (4) garnet grain size: large round garnet grains were pre-

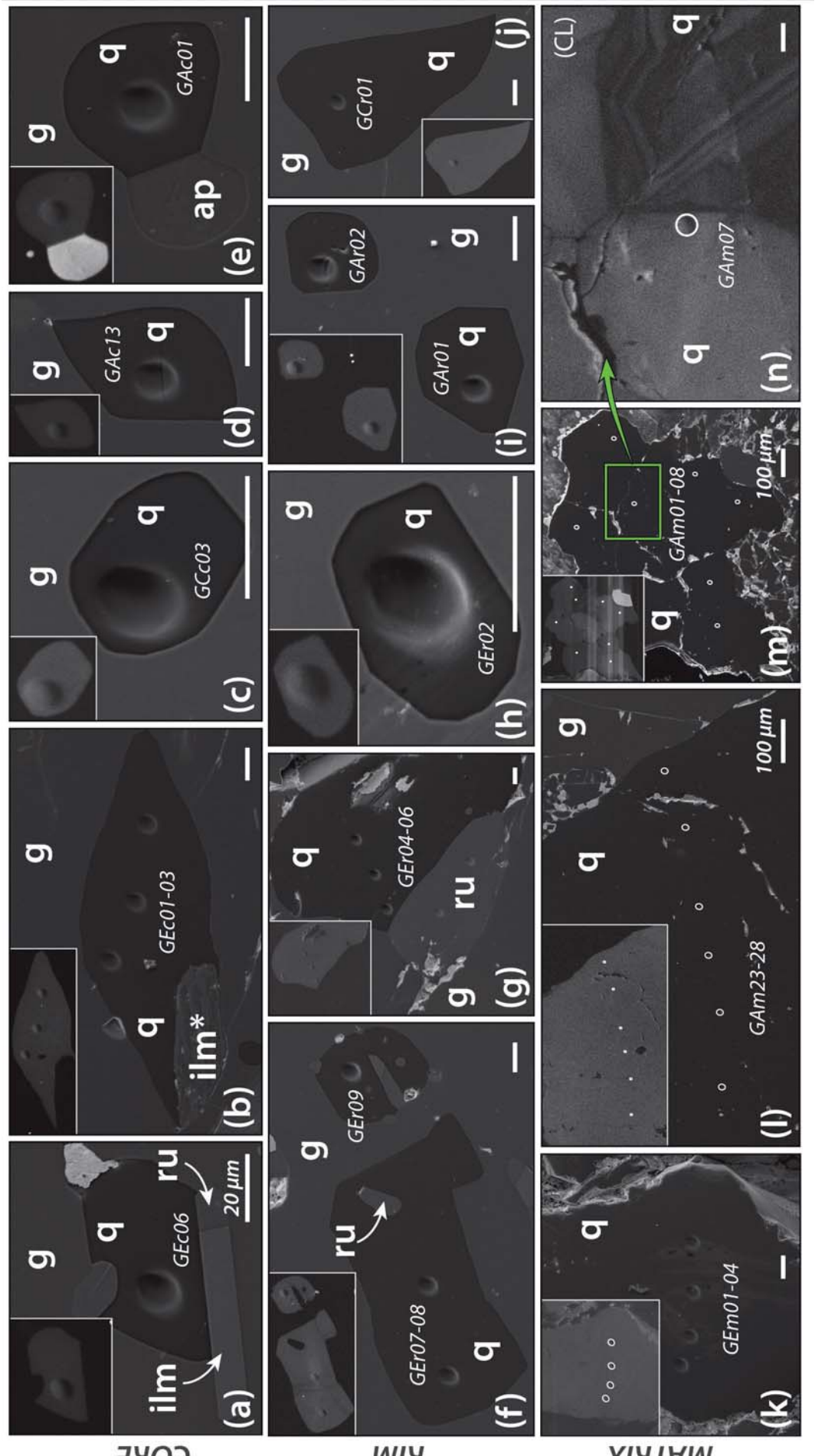

Figure 5: Secondary electron (SE) images of quartz grains with analytical spots (10 µm large). The insets in the upper left show the corresponding cathodoluminescence image. (a-e) quartz grains analyzed in the garnet core; (f-j) quartz grains analyzed in the garnet rim; (k-n) quartz grains analyzed in the matrix. Quartz grains do not show CL zoning; shades in the CL image in (m) reflect different grain orientations; (n) is the one exception of a grain with oscillatory zoning.

ferred (4 to 5 mm in diameter). Selected grains were cut off from the slab and mounted in the centermost part of a 25 mm epoxy disc. Gold coating (30 nm) was used for Secondary Ion Mass Spectrometry (SIMS) analyses; carbon coating for Scanning Electron Microscopy (SEM) analyses.

Ti concentrations in quartz and Zr concentrations in rutile were determined by SIMS using a CAMECA IMS1280 large-geometry instrument (Nordsim laboratory, Museum of Natural History in Stockholm). For both methods, an aperture projected O_2^- primary beam was used to generate analytical spots of either 10 µm or 15 µm on the sample, with corresponding beam currents of ca. 3 or 5nA. Positive secondary ions were optimized in a 45eV energy window, filtered at a mass resolution (M/ΔM) of 4000 to eliminate interfering species and detected in peak-hopping mode using an ion counting electron multiplier for trace elements at $<10^6$ cps or a Faraday cup.

For rutile, the species ^{48}Ti and ^{90}Zr were measured, Zr concentrations being derived from the relative ^{90}Zr/^{48}Ti ratio between the unknowns and a rutile reference material, R10b, which has a Zr content of 759 µg g^{-1} (Luvizotto *et al.*, 2009). Typical within-run uncertainties on the ^{90}Zr/^{48}Ti ratio were ~3% (s.e.) while an external precision of ~12% (RSD) was obtained from 12 measurements of R10b. These analytical uncertainties were propagated together with the reported ca. 1% uncertainty on the concentration in R10b and are clearly the dominant contribution to overall uncertainty (Table S1).

For quartz, the species ^{27}Al, ^{28}Si, ^{40}Ca, ^{47}Ti and ^{48}Ti were measured, Al and Ca being used to detect the possible presence of other minerals as inclusions that might adversely affect the measurement by contributing extraneous Ti. Ti concentrations were calibrated using the ^{47}Ti/^{28}Si ratio against a smoky quartz reference material from Shandong Province, China, which has a Ti concentration of 57 µg g^{-1} (Audétat *et al.*, 2015). Data exhibiting extreme excursions of ^{27}Al/^{28}Si (in some cases tripping the electron multiplier) or ^{40}Ca/^{28}Si ratio were excluded from consideration. In contrast to Zr in rutile, overall uncertainty in Ti concentration of quartz is dominated by the ~7% uncertainty in the content of the reference material, propagated together with typical within-run uncertainties of <1% and an external precision of ~2% (n = 10; Table S2).

4.3 Zr-in-rutile and Ti-in-quartz

Rutile and quartz grains were imaged using backscattered electron (BSE) and secondary electron (SE) image modes. BSE images are best to identify micro-inclusions and ilmenite exsolutions, whereas SE images show best micro-fractures, grain boundaries, and analytical pits (Fig. 4). Additionally, quartz grains were imaged using cathodoluminescence (CL) in order to identify discrete zoning pattern or grain boundaries in quartz. Imaging was performed using a Hitachi 3400N scanning electron microscope fitted with a miniGatan CL detector, and 10 to 15 kV acceleration voltage.

Temperature calculations from Zr-in-rutile were made using the calibration of Tomkins *et al.* (2007) and the three different and independently constrained pressure values (section 4.1). Temperature calculations for Ti-in-quartz follow the calibration of Thomas *et al.* (2010), using the independently constrained three pressure values (section 4.1).

5 RESULTS

5.1 Results of Zr-in-rutile

Analyses of Zr, Nb and Ta were performed on 147 spots (10 µm) in rutile grains. The full set of data is tabled in a supplementary file (Table S1). Forty-six analyses were discarded because the analytical spot was partly or entirely out of the grain or situated in ilmenite. In general, the core of each grain was targeted. Analyses are plotted in Fig. 6a according to their textural setting: inclusions in garnet core (garnet A, C and E), inclusions in garnet rim (garnet A, C and E), and matrix grains (in the vicinity of garnet C and E).

Zirconium contents generally range from ~500 to 1200 ppm for rutile inclusions in the core and rim of garnet, with outliers down to 250 and up to 1600 ppm (Fig. 6a). Matrix grains show a larger range: around garnet C from 750 to 1500 ppm Zr, with outliers down to 500 and up to 2500 ppm. The median of each set of analyses and microstructural setting (e.g. "C-core" compared to "C-rim" and "C-mat"; Fig. 6a) show a systematic increase of Zr (a few hundreds of ppm) from core to rim and matrix, consistent with the prograde evolution. Two rutile grains directly adjacent to zircon in garnet E (Fig. 4e) and C (Fig. 4k) have significantly lower Zr contents than

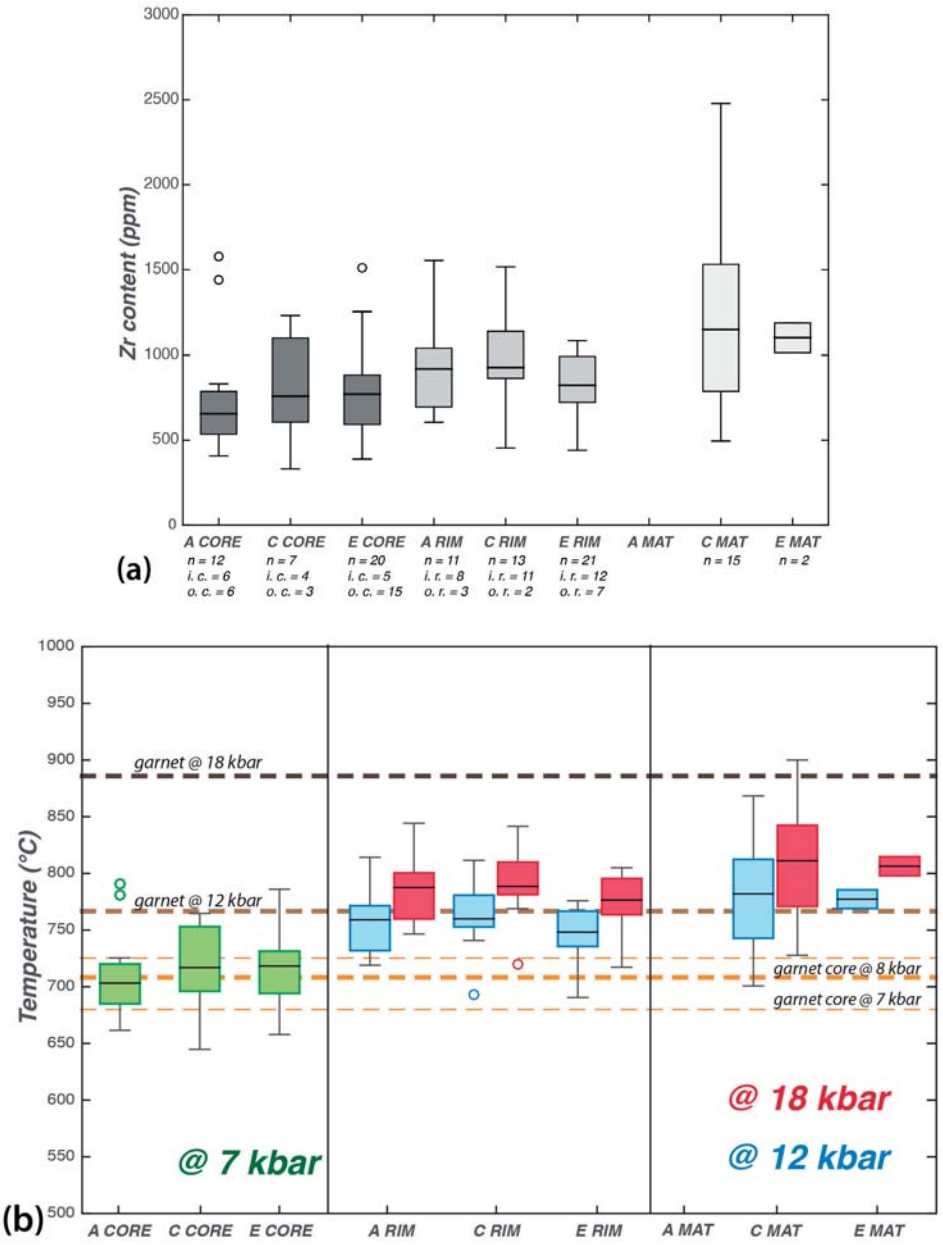

Figure 6: (a) Zr concentrations (ppm) in rutile grains from garnet A, C and E, organized after textural position. The box plots present the upper and lower interquartile range of the results separated by a median line (black). Circles = outliers. n = number of spots. CORE: inclusions in the core of garnet; RIM: inclusions in the rim of garnet; MAT: matrix grains. Textural positions in garnet: o. c.: outer core; o. r.: outer rim; i. r.: inner rim; o. r.: outer rim. (b) Zr-in-rutile temperatures calculated using the calibration of Tomkins *et al.* (2007): at 7 kbar (green boxes), 12 kbar (blue boxes), and 18 kbar (red boxes). All spots in rutile grains are considered and box plots are constructed as in (a). Dashed lines represent temperatures interpreted from the pseudosection model (Fig. 2): garnet core (7–8 kbar; orange), garnet at 12 kbar (light brown), garnet outer rim and matrix (18 kbar; dark brown).

other grains from the same garnet and setting (709 instead of ~871 ppm and 495 instead of ~1352 ppm, respectively). These analyses are included in the data set plotted in Fig. 6.

Temperatures range from 680 to 750 °C for rutile in garnet cores at 7 kbar, with a median between 700 and 715 °C. Temperatures obtained from rutile in the core of garnet A spread less than those from garnet C and E, and record slightly lower temperatures. The results are in agreement with the temperature range estimated from the pseudosection for the growth of the garnet core (i.e. from 675 to 720 °C between 7 and 8 kbar, Fig. 2).

Temperatures calculated for rutile in the garnet rim are slightly different for the three garnet grains. Rutile inclusions in garnet A yield temperatures between 730 and 770 °C at 12 kbar and 760–800 °C at 18 kbar. In the rim of garnet C, rutile temperature range between 750 and 780 °C at 12 kbar and 780–810 °C at 18 kbar; in the rim of garnet E, the values are 740–760 °C at 12 kbar and 765–800 °C at 18 kbar. Temperature predicted from the pseudosection at 12 kbar are similar to the results from the rutile thermometry (i.e. ~760 °C); however, at 18 kbar, temperatures calculated from Zr-in-rutile are ~80 °C lower than the temperature suggested by the pseudosection (~790 versus 880 °C).

Few matrix grains were successfully analyzed due to the retrograde partial replacement of rutile by ilmenite in the matrix. Temperature estimates range from 740 to 810 °C at 12 kbar with a lower limit at 700

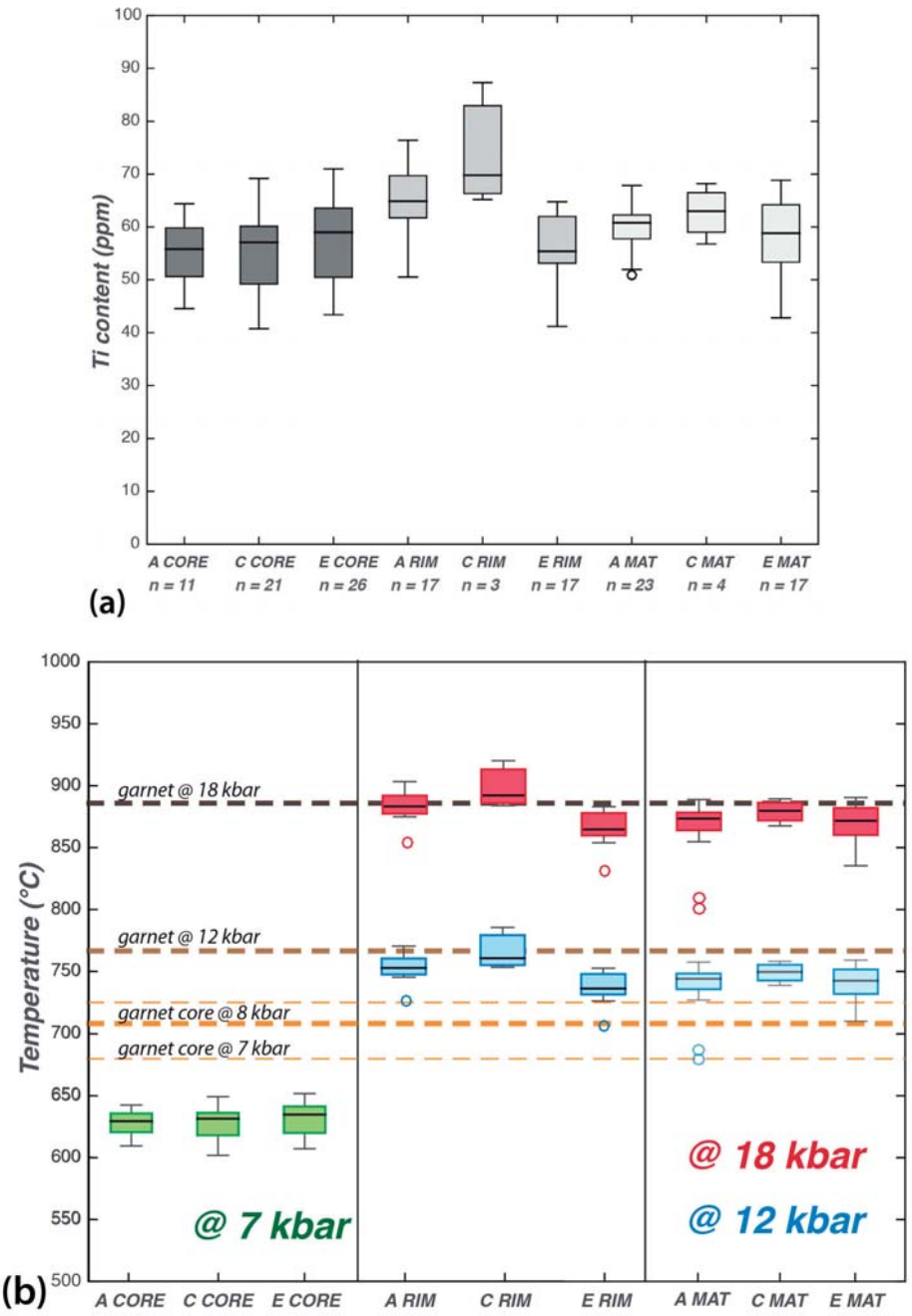

Figure 7: (a) Ti concentrations (ppm) in quartz grains from garnet A, C and E organized after textural position. The box plots represent the upper and lower interquartile range of the results separated by a median line (black). Circles = outliers. n = number of spots. CORE: inclusions in the garnet core; RIM: Inclusions in the garnet rim; MAT: matrix grains. (b) Ti-in quartz temperatures calculated using the calibration of Thomas *et al.* (2010): at 7 kbar (green boxes), 12 kbar (blue boxes), and 18 kbar (red boxes). All spots in quartz grains are considered and box plots are constructed as in (a). Dashed lines represent temperatures interpreted from the pseudosection model (Fig. 2): garnet core (7–8 kbar; orange), garnet at 12 kbar (light brown), garnet outer rim and matrix (18 kbar; dark brown).

°C and upper limit at 870 °C. At 18 kbar, which is considered as the equilibrium of the matrix minerals at peak *P–T* conditions, temperatures range from 770 to 850 °C, with the lowermost value at 725 °C at the highest at 900 °C, the latter calculated from three analyses out of fifteen. Although only two reliable analyses were obtained in the vicinity of garnet E, they are similar to the median result of matrix rutile surrounding garnet C (n=15), i.e. 780 °C at 12 kbar and 810 °C at 18 kbar.

5.2 Results of Ti-in-quartz

Spot analysis (10 µm) of quartz targeted crystal cores, but a few analyses were distributed as profiles across grains in the matrix. The absence of CL zoning (e.g. Fig. 5a-m) suggests that Ti is relatively homogeneously distributed within single grains. 155 analyses were performed; 16 were discarded, because the analytical spot hit outside the grain (Table S2).

Compared to the Zr-in-rutile temperatures (section 5.1), the temperatures calculated from Ti-in-quartz thermometry are more precise (Fig. 7a). The pressure influence is however greater for the Ti-in-quartz equilibrium than for Zr-in-rutile (~21.5 versus ~5 °C/ kbar). In garnet cores, Ti contents in quartz are 50–62 ppm. In quartz inclusions in garnet rims A and C, Ti range from 60 to 82 ppm with a median ~68, while inclusions in garnet rim E range from 52 to 60 ppm. In the matrix, Ti contents in quartz range from 52 to 68 ppm, with a median ~60 ppm.

The increase of Ti content in quartz is significant from the garnet cores to the garnet rims, but there is no significant difference between the values from the garnet rims to the matrixes.

Temperatures calculated from the Ti-content in quartz inclusions in *garnet cores* are similar for the three garnet grains and range from 620 to 640 °C with a median at 630 °C (Fig. 7b). These results are ~50 °C lower than expected from the pseudosection (at 7 kbar; Fig. 2). Even with an input of 8 kbar Ti-in-quartz temperatures are at least 30-60 °C lower than expected.

Ti-in-quartz temperatures calculated from inclusions in *garnet rims* vary slightly for the three different garnet grains. At 12 kbar, expected to correspond to the lowermost pressure for the growth of the garnet rims, estimates are ~745–760 °C for garnet A, 755 –775 °C for garnet B, and 730–750 °C for garnet E (Fig. 7b). The median is 755 °C for garnet A and C, respectively, and c. 15 °C lower for garnet E. These temperatures are in good agreement with the temperatures obtained from both Zr-in-rutile thermometry and the pseudosection model (Fig. 2). At 18 kbar, considered as the higher limit for the growth of the garnet rim, Ti-in-quartz temperatures are 885 °C, i.e. ~130 °C higher than at 12 kbar. These temperatures are also in nearly perfect agreement with the pseudosection (~890 °C at 18 kbar, Fig. 2).

Forty-four analyses performed in different positions in *matrix grains* yield a tight cluster of temperatures. At 18 kbar, the median temperature is ~880 °C, in perfect agreement with the peak pressure temperature suggested by the pseudosection (Figs. 7b & 2).

6 DISCUSSION

6.1 Statistical error

According to Ewing *et al.* (2013), an inherent uncertainty of ~3% can be taken as a reasonable estimation for Tomkins *et al.* (2007) calibration for Zr-in-rutile, while error on Ti-in-quartz calibration (Thomas *et al.*, 2010) is ~7%. The analytical error on single grain presented in this study is estimated at ~12% for Zr-in-rutile and ~7.2% on Ti-in-quartz.

Data are presented in the form of box plots (Fig. 6 and 7): the box is given by the lower and upper interquartile range of the data (middle half of the results) separated by the median of the data; the whiskers extend out to the furthest data point that is within 1.5 times the interquartile range from the box; outliers are represented by circles. Because the whole range of data is used for T calculation, both analytical and calibrations error are considered to be largely exceeded.

6.2 Petrological interpretation of Zr-in-rutile and Ti-in-quartz thermometry

Measured Zr contents in rutile grains vary with textural setting: they increase from the cores of garnet, to the rims of garnet, and further to the matrix (Fig. 6a). Ti contents in quartz show a similar increase from the cores to the rims of garnet, but the Ti contents in matrix quartz are similar or lower than in quartz inclusions in the rims of garnet (Fig. 7a). Adding appropriate values of pressure to the temperature calculations leads to marked differences in estimated temperature for the three different textural settings (Figs 6b, 7b), thus supporting the previously modelled P–T path (Fig. 2). The higher interquartile range of Ti-in-quartz temperatures from garnet cores overlaps the lower interquartile range from garnet rims and matrixes (Fig. 7b), which reflect the prograde continuous growth and recrystallization.

When compared with the pseudosection, the Zr-in-rutile and Ti-in-quartz estimates give information on crystallization and recrystallization processes in the rock. For example, Zr-in-rutile temperatures from inclusions in garnet cores match the temperature read off the pseudosection for that same stage. This suggests that the growth of rutile grains now included in the garnet core was synchronous with, rather than earlier than, the growth of the garnet core. In fact, calculation of modal proportions of rutile, quartz and ilmenite (Fig. 9) shows that *growth* (as opposed to recrystallization) of rutile and quartz is restricted within the field in which the garnet core grew, at 6–9 kbar. The equilibration of rutile and quartz during continued heating and compression must have taken place by recrystallization of existing grains.

Consequently, the results from Zr-in-rutile and Ti-in-quartz thermometry are consistent with continuous prograde crystallization, recrystallization, and reequilibration of the matrix phases during the growth of garnet, until the instance at which the grains were included in garnet and shielded from further reaction.

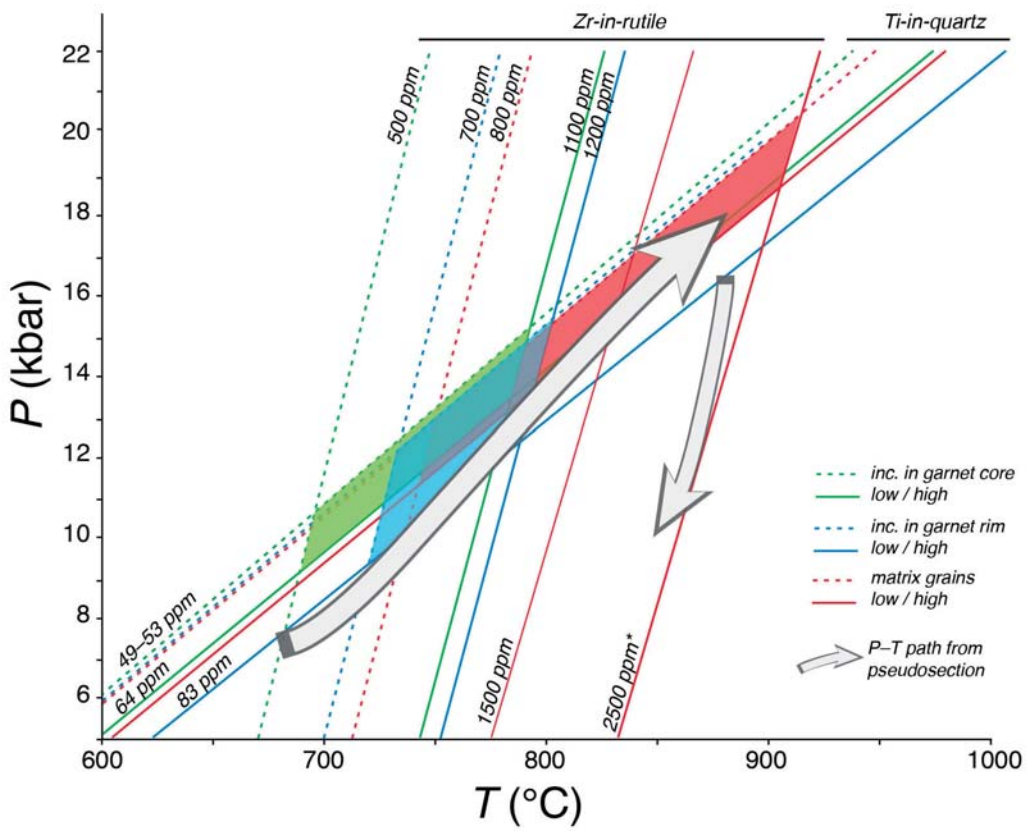

Figure 8: Isopleths calculated for Ti-in-quartz and Zr-in-rutile (method after Thomas *et al.*, 2010) based on the results from Zr-in-rutile and Ti-in-quartz for inclusions in the cores of garnet (green), inclusions in the rims of garnet (blue), and matrix grains (red). Lower values (dashed lines) correspond to the bottom of the lower interquartile range of the data; higher values correspond to the upper interquartile range of the data (solid lines). The three highest values of Zr-in-rutile (out of 15 analyses of rutile grains in the matrix) reached 2500 ppm. The boxes show that the full range of temperature estimates using Zr-in-rutile and Ti-in-quartz in each microstructural setting follows closely the *P–T* path deduced from pseudosection modelling (white arrows; Tual *et al.*, *submitted.*).

Several studies have reported findings of *lower* Zr contents in rutile grains that are in direct contact with zircon (e.g. Luvizotto & Zack, 2009; Jiao *et al.*, 2011; Kooijman *et al.*, 2012; Ewing *et al.*, 2013; Walsh *et al.*, 2014). Two analyses of rutile in contact with zircon are presented in this paper (Fig. 4f, k; inclusion in garnet rim and matrix grain, respectively). These two grains have significantly lower Zr contents than other rutile grains in the equivalent textural setting, similar to what has been found in previous studies. Zircon crystals directly adjacent to rutile grains can be reaction products from the recrystallization of rutile, e.g., by intragranular exsolution (Kooijman *et al.*, 2012), during post-peak cooling (Walsh *et al.*, 2014). During the prograde evolution of the rock studied in this paper, however, zircon should instead have dissolved during prograde growth of rutile (cp. Kohn *et al.*, 2015). The lower Zr contents of rutile grains in contact with zircon therefore remain enigmatic.

Whereas Zr-in-rutile temperatures from the garnet core are similar to the temperature range modelled in the pseudosection, Ti-in-quartz temperatures for this stage appear too low (tentatively attributed to incomplete Ti saturation of quartz). Ti-in-quartz temperatures for the garnet rim and matrix conditions are consistent with the pseudosection. The combination of Zr-in-rutile and Ti-in-quartz isopleths (e.g., Thomas *et al.*, 2010) can provide a way to qualitatively crosscheck results without other pressure constraints. Even when ignoring issues of apparent too low Ti-in-quartz temperatures for garnet cores and low Zr-in-rutile temperatures for garnet rims and matrix, pairing the results from Ti-in-quartz and Zr-in-rutile results in a prograde path from garnet core to rim and matrix (Fig. 8). If the highest values of Zr-in-rutile from the matrix grains are used (i.e. 2283, 2382, 2479 ppm), estimated peak conditions are 875–900 °C, 17–18.5 kbar, supporting estimates from the pseudosection (850–900 °C, 16.5–18.5 kbar, Tual *et al.*, *submitted.*). These results show that the combination of the three independent methods Zr-in-rutile, Ti-in-quartz, and pseudosection modelling are a robust and powerful tool in tracking a *P–T* history.

6.3 Interpretation of inconsistent Zr in rutile and Ti in quartz contents

Results presented in this study indicate two contrasting problems concerning apparent accuracy of the Ti-in-quartz and Zr-in-rutile thermometers: A) for the garnet core, at 7 kbar, Ti-in-quartz gives lower temperatures than Zr-in-rutile thermometry and the pseudosection; B) for matrix grains, inferred to equilibrate at ~18 kbar, Zr-in-rutile gives lower temperatures than Ti-in-quartz thermometry and the thermodynamic pseudosection model.

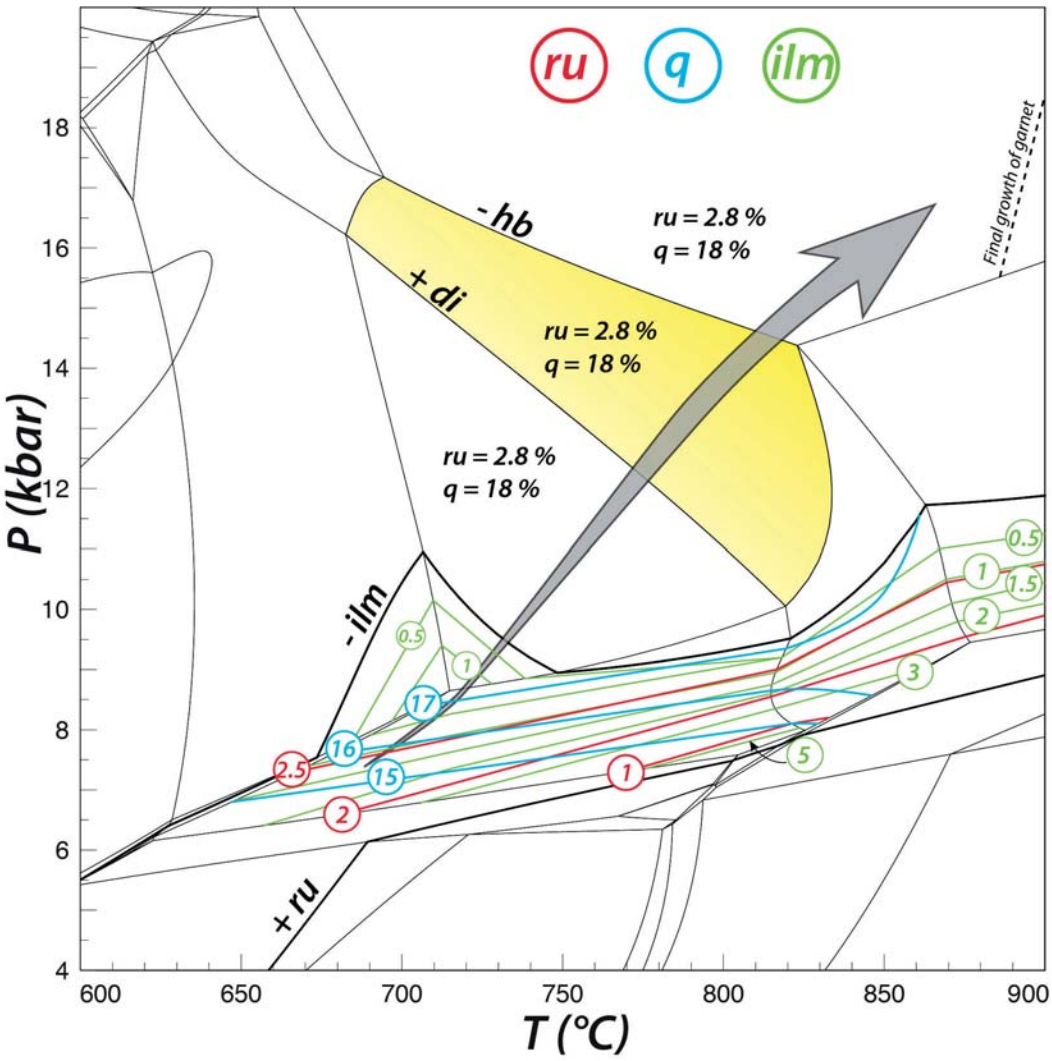

Figure 9: *P–T* pseudosection and *P–T* path (grey arrow) as presented in Fig. 2, contoured for modal proportions (in % for the mineral assemblage, ignoring H_2O) of quartz (blue), rutile (red), and ilmenite (green). The dashed line represents the final growth of garnet (along the corresponding X_{Fe} isopleth, cf. Tual *et al.*, *submitted*). Most changes in modal proportions occur between 6 and 9 kbar, and the steady proportions are given for each field (along the path). The modal proportions of minerals in the model correspond to those obtained from point counting of the thin section. The yellow area is the field of hornblende breakdown, clinopyroxene production, and fluid release.

The reliability of Ti-in-quartz and Zr-in-rutile thermometry results depends on the equilibrium between rutile, quartz, and zircon. In the studied rock there is textural evidence for co-stability of these three phases throughout the three metamorphic stages. Grain size is, however, larger in the garnet rim and in the matrix than in the garnet core.

The discrepancies described above can be the result of either: (1) inaccurate calibration of the thermometer, including the influence of pressure, (2) retrograde diffusion of Ti-in-quartz and Zr-in-rutile, at respective stages (above), (3) kinetics, leading to a *relatively* more efficient (faster) incorporation of Zr in rutile than Ti in quartz during growth of the garnet core, and the opposite scenario at matrix equilibration at peak conditions.

(1) Calibrations

The calibration and pressure dependence of Zr-in-rutile presented in Tomkins *et al.* (2007) has proven reliable in a number of studies (e.g. Racek *et al.*, 2008; Kooijman *et al.*, 2012; Ewing *et al.*, 2013; Štípská *et al.*, 2014). The Ti-in-quartz calibration (Thomas *et al.*, 2010) has, however, been a point of debate. Huang & Audétat (2012) showed that quartz which grew at slow rates and relatively "low" temperatures (600–800 °C) might result in underestimation of *T* and presented a recalibration of the Ti-in-quartz thermometer. In the rock subject to the present study, it is unlikely that the garnet core grew slower than the rim, because the surface/volume ratio decreases towards garnet rim growth. Instead, the garnet core can be expected to grow relatively "faster" than the rim, also allowing inclusions to get larger towards the rim. Moreover, as the Ti-in-quartz temperatures are similar to those obtained by Zr-in-rutile and the pseudosection at 12 kbar (775 °C), there is no justification for choosing another calibration. Finally, Thomas *et al.* (2015) confirmed that the initial calibration of Thomas *et al.* (2010) appear the most reliable one from 5 to 20 kbar.

(2) Diffusion

There is no clear CL-zoning in quartz grains (except for one occurrence of oscillatory zoning, Fig. 5)

and there is limited variation in Ti content (Fig. 7a) among quartz grains of different sizes, and across single large grains in the matrix. The Ti-in-quartz data presented in this study are precise and consistent over the sample scale for each textural setting, similarly to what has been described for other samples by Thomas *et al*. (2015). As shown in Fig. 8, the slope of the *P–T* path is similar to the slope of the Ti-in-quartz equilibrium line, which explains the small variation of Ti content in quartz during the prograde path. In this respect, our case differs from that of Ewing *et al*. (2013), who showed a larger range for Ti-in-quartz temperatures than for Zr-in-rutile temperatures, and inferred this difference to be the result of net loss of Ti in quartz. Experiments performed by Cherniak *et al*. (2007) showed that Ti in quartz will diffuse over a distance of 500 µm during a 1 Ma episode at 800 °C. We do not however observe net loss of Ti in quartz grains included in garnet core or in the matrix. Our results are consistent with those of Spear & Wark (2009) who showed that no systematic diffusion occurs even for small quartz grains (<70 µm), when quartz grains are shielded by garnet. Our study shows that neither did diffusion affect matrix grains, in turn suggesting short residence time at high temperature. Finally, the first part of the decompression path was near-isothermal and crosses higher values of Ti-in-quartz isopleths (Fig. 8); hence no Ti diffusion in quartz is expected until the rock starts to cool down (inferred to start from 10 kbar).

Partial replacement of rutile by ilmenite took place in the matrix, with accompanying recrystallization of rutile and resetting of Zr-in-rutile temperatures. Zr diffusion in (apparently) well-preserved grains cannot be ruled out without more detailed profiles over these single matrix grains. In granulite facies rocks, it is in theory expected that rutile grains would be affected by Zr loss, because the crystallization temperature might exceed the closure temperature of Zr diffusion (Cherniak *et al.*, 2007; Baldwin & Brown 2008). It is however unknown whether retrograde Zr resetting (by intracrystalline diffusion) in matrix rutile is more likely than Ti resetting in quartz under the same conditions. . Finally, similar than for quartz, the first part of the decompression path, coeval with the partial replacement of rutile by ilmenite, was near-isothermal and follows closely the Zr-in-rutile isopleths (Fig. 8); therefore no Zr diffusion in rutile is expected down to 10 kbar.

(3) Kinetics

Kinetics effects can result in chemical disequilibrium even though minerals appear in textural equilibrium. The relative diffusion rates of Ti and Zr and the growth rate of garnet are parameters that could influence Ti-in-quartz and Zr-in-rutile results.

At garnet core conditions, quartz, ilmenite, rutile and zircon coexisted, and Zr-in-rutile temperatures fit with the pseudosection. Zirconium is available, so to allow rutile to incorporate expected amount of Zr. Even though rutile is growing and ilmenite progressively breaking down and releasing Ti (Fig. 9), Ti-in-quartz estimates remain at least ~55 °C lower than what the pseudosection and Zr-in-rutile thermometry suggest. It is considered unlikely that rutile incorporates excess Zr, therefore the problem should lie in quartz incorporating too little Ti. Ashley *et al*. (2014) proposed that crystal plastic flow might hinder the incorporation of Ti in quartz. By contrast, Nachlas & Hirth (2015) demonstrated that ductile shearing improves the incorporation and equilibration of Ti and other trace elements in quartz. Moreover, Kidder *et al*. (2013) showed that Ti-in-quartz can be reliable at temperatures as low as greenschist facies. In the rock studied in this paper, the garnet cores grew under deformation, under the lowest temperature recorded by the rock (amphibolite facies), and must have grown relatively fast. Our preferred interpretation is that fast growth led to the incorporation of incompletely Ti-equilibrated quartz grains.

At the core-to-rim transition (12 kbar), both Zr-in-rutile and Ti-in-quartz results are in agreement with results from the pseudosection. This pressure is close to the terminal breakdown of ilmenite (Fig. 9; although extremely sensitive on whole-rock Fe^{3+} content, Tual *et al.*, *submitted.*). For this stage, all data suggest mutual equilibrium of rutile, quartz, and zircon.

At peak pressure and temperature, Ti-in-quartz temperatures, but only few Zr-in-rutile temperatures, in the studied sample fit well with the pseudosection. Zr-in-rutile has been considered the more reliable thermometer at high temperatures (e.g. Zack & Luvizotto, 2006; Zhang *et al.*, 2009; Kooijman *et al.*, 2012; Ewing *et al.*, 2013). Yet in our sample, most matrix rutile has incorporated too little Zr to match the peak *P–T* conditions. According to the pseudosection model (Fig. 9), quartz and rutile were produced in the ilmenite-bearing stability fields but thereafter remained in constant modal amounts. At 12 kbar, there is no discrepancy between Zr-in-rutile results and Ti-in-quartz results, but rutile appears only partially equilibrated between ~12 kbar and 18 kbar. Prograde reequilibration at 12-15 kbar was dominated by the progressive breakdown of hornblende and growth of clinopyroxene (yellow field,

Fig. 9); in the investigated sample this stage is also characterized by a substantial increase in grain size, including the grain size of rutile. Dehydration of amphibole and associated fluid transport through the matrix may have enhanced grain boundary diffusion of elements as well as recrystallization of matrix phases, including rutile. This process took place between 775 and 820 °C (Fig. 9, yellow field), well in line with Zr-in-rutile results presented in this study (Fig. 6b). Hydrous fluid production coming to an end at 820 °C and 15 kbar may have led to a cease of Zr incorporation in rutile. A few matrix grains do however record Zr concentrations up to ~2500 ppm, confirming a peak temperature ~900 °C (Fig. 8).

To conclude, our study shows that Ti concentration in quartz is remarkably constant regardless of crystal size and can provide both precise and accurate results at high temperatures. The use of the three independent methods Ti-in-quartz, Zr-in-rutile, and a *P–T* pseudosection model is a robust mean to constrain *P–T* evolution as well as provide insights on crystallization process during metamorphism.

ACKNOWLEDGEMENTS

L. Tual thanks M. Smit for inspiring discussions and preliminary Zr-in-rutile attempts at the EMP in Copenhagen and G. Fontorbe for Matlab tips. We gratefully acknowledge U. Söderlund for reviewing an early draft of this manuscript, Thomas Zack (University of Gothenburg) for providing the rutile standard, and Anne-Sophie Bouvier (Université de Lausanne) for providing the quartz standard. The technical support and guidance of K. Lindén and L. Ilyinsky at Nordsim was greatly appreciated. The Nordsim facility is operated under a contract between the research funding agencies of Denmark, Iceland, Norway, and Sweden, the Geological Survey of Finland, and the Swedish Museum of Natural History. This paper is Nordsim publication No XXX. Research was funded by a grant from Kungliga Fysiografiska Sällskapet i Lund to L. Tual.

REFERENCES

Ashley, K. T., Webb, L. E., Spear, F. S., & Thomas, J. B. (2013). P-T-D histories from quartz: A case study of the application of the Ti-in-quartz thermobarometer to progressive fabric development in metapelites. *Geochemistry, Geophysics, Geosystems*, *14*(9), 3821-3843.

Ashley, K. T., Carlson, W. D., Law, R. D., & Tracy, R. J. (2014). Ti resetting in quartz during dynamic recrystallization: Mechanisms and significance. *American Mineralogist*, *99*(10), 2025-2030.

Audétat, A., Garbe-Schönberg, D., Kronz, A., Pettke, T., Rusk, B., Donovan, J. J., & Lowers, H. A. (2015). Characterisation of a natural quartz crystal as a reference material for microanalytical determination of Ti, Al, Li, Fe, Mn, Ga and Ge. *Geostandards and Geoanalytical Research*, *39*(2), 171-184.

Baldwin, J. A., & Brown, M. (2008). Age and duration of ultrahigh-temperature metamorphism in the Anápolis–Itauçu Complex, Southern Brasília Belt, central Brazil–constraints from U–Pb geochronology, mineral rare earth element chemistry and trace-element thermometry. *Journal of Metamorphic Geology*, *26*(2), 213-233.

Bingen, B., Skår, Ø., Marker, M., Sigmond, E. M., Nordgulen, Ø., Ragnhildstveit, J., Mansfeld, J., Tucker, R. D. & Liégeois, J. P. (2005). Timing of continental building in the Sveconorwegian orogen, SW Scandinavia. *Norwegian Journal of Geology*, **85(1-2)**, 87-116.

Bingen, B., Nordgulen, Ø., Viola, G., (2008). A four-phase model for the Sveconorwegian orogeny, SW Scandinavia. Norwegian Journal of Geology 88, 43–72.

Cherniak, D. J., Watson, E. B., & Wark, D. A. (2007). Ti diffusion in quartz. *Chemical Geology*, *236*(1), 65-74.

Ewing, T. A., Hermann, J., & Rubatto, D. (2013). The robustness of the Zr-in-rutile and Ti-in-zircon thermometers during high-temperature metamorphism (Ivrea-Verbano Zone, northern Italy). *Contributions to Mineralogy and Petrology*, *165*(4), 757-779.

Ferry, J. M., & Watson, E. B. (2007). New thermodynamic models and revised calibrations for the Ti-in-zircon and Zr-in-rutile thermometers. *Contributions to Mineralogy and Petrology*, *154*(4), 429-437.

Hayden, L. A., & Watson, E. B. (2007). Rutile saturation in hydrous siliceous melts and its bearing on Ti-thermometry of quartz and zircon. *Earth and Planetary Science Letters*, *258*(3), 561-568.

Holland, T. J. B. & Powell, R. (2011). An improved and extended internally consistent thermodynamic dataset for phases of petrological interest, involving a new equation of state for solids. *Journal of Metamorphic Geology*, **29**, 333–383.

Huang, R., & Audétat, A. (2012). The titanium-in-quartz (Ti-in-quartz) thermobarometer: a critical examination and re-calibration. *Geochimica et*

Cosmochimica Acta, *84*, 75-89.

Jiao, S., Guo, J., Mao, Q., & Zhao, R. (2011). Application of Zr-in-rutile thermometry: a case study from ultrahigh-temperature granulites of the Khondalite belt, North China Craton. *Contributions to Mineralogy and Petrology*, *162*(2), 379-393.

Johansson, L., Möller, C. & Söderlund, U. (2001). Geochronology of eclogite facies metamorphism in the Sveconorwegian Province of SW Sweden. *Precambrian Research*, **106**, 261-275.

Kidder, S., Avouac, J. P., & Chan, Y. C. (2013). Application of titanium-in-quartz thermobarometry to greenschist facies veins and recrystallized quartzites in the Hsüehshan range, Taiwan. *Solid Earth*, *4*(1), 1-21.

Kohn, M. J., Corrie, S. L., & Markley, C. (2015). The fall and rise of metamorphic zircon. *American Mineralogist*, *100*(4), 897-908.

Kooijman, E., Smit, M. A., Mezger, K., & Berndt, J. (2012). Trace element systematics in granulite facies rutile: implications for Zr geothermometry and provenance studies. *Journal of Metamorphic Geology*, *30*(4), 397-412.

Korhonen, F. J., Clark, C., Brown, M., & Taylor, R. J. M. (2014). Taking the temperature of Earth's hottest crust. *Earth and Planetary Science Letters*, *408*, 341-354.

Leeman, W. P., MacRae, C. M., Wilson, N. C., Torpy, A., Lee, C. T. A., Student, J. J., ... & Vicenzi, E. P. (2012). A study of cathodoluminescence and trace element compositional zoning in natural quartz from volcanic rocks: Mapping titanium content in quartz. *Microscopy and Microanalysis*, *18*(06), 1322-1341.

Liu, Y. C., Deng, L. P., Gu, X. F., Groppo, C., & Rolfo, F. (2015). Application of Ti-in-zircon and Zr-in-rutile thermometers to constrain high-temperature metamorphism in eclogites from the Dabie orogen, central China. *Gondwana Research*, *27*(1), 410-423.

Luvizotto, G. L., & Zack, T. (2009). Nb and Zr behavior in rutile during high-grade metamorphism and retrogression: an example from the Ivrea–Verbano Zone. *Chemical Geology*, *261*(3), 303-317.

Luvizotto, G. L., Zack, T., Meyer, H. P., Ludwig, T., Triebold, S., Kronz, A., ... & Jacob, D. V. (2009). Rutile crystals as potential trace element and isotope mineral standards for microanalysis. *Chemical Geology*, *261*(3), 346-369.

Menegon, L., P. Nasipuri, H. Stünitz, H. Behrens, and E. Ravna (2011), Dry and strong quartz during deformation of the lower crust in the presence of melt, *Journal of Geophysical Research.*

Möller, C., (1998). Decompressed eclogites in the Sveconorwegian (–Grenvillian) orogen of SW Sweden: petrology and tectonic implications. *Journal of Metamorphic Geology*. **16**, 641 656.

Möller, C., (1999). Sapphirine in SW Sweden: a record of Sveconorwegian (–Grenvillian) late-orogenic tectonic exhumation. *Journal of Metamorphic Geology*. **17**, 127–141.

Möller, C., Andersson, J., Dyck, B. & Antal Lundin, I., (2015). Exhumation of an eclogite terrane as a hot migmatitic nappe, Sveconorwegian orogen. Hirajama, T., Medaris, G. (Eds.), High- and ultrahigh-pressure metamorphism, from microscopic to orogenic scale. Lithos (Special Issue). *Lithos*, **226**, 147–168.

Nachlas, W. O., & Hirth, G. (2015). Experimental constraints on the role of dynamic recrystallization on resetting the Ti-in-quartz thermobarometer. *Journal of Geophysical Research: Solid Earth*.

Powell, R., Holland, T. J. B. H. & Worley, B., (1998). Calculating phase diagrams involving solid solutions via non-linear equations, with examples using THERMOCALC. *Journal of metamorphic Geology*, **16**, 577-588.

Racek, M., Štípská, P., & Powell, R. (2008). Garnet–clinopyroxene intermediate granulites in the St. Leonhard massif of the Bohemian Massif: ultrahigh-temperature metamorphism at high pressure or not?. *Journal of Metamorphic Geology*, *26*(2), 253-271.

Spear, F. S., & Wark, D. A. (2009). Cathodoluminescence imaging and titanium thermometry in metamorphic quartz. *Journal of Metamorphic Geology*, *27*(3), 187-205.

Spear, F. S., Ashley, K. T., Webb, L. E., & Thomas, J. B. (2012). Ti diffusion in quartz inclusions: implications for metamorphic time scales. *Contributions to Mineralogy and Petrology*, *164*(6), 977-986.)

Štípská, P., Powell, R., & Racek, M. (2014). Rare eclogite-mafic granulite in felsic granulite in Blanský les: precursor of intermediate granulite in the Bohemian Massif?. *Journal of Metamorphic Geology*, *32*(4), 325-345.

Taylor-Jones, K., & Powell, R. (2015). Interpreting zirconium-in-rutile thermometric results. *Journal of Metamorphic Geology*, *33*(2), 115-122.

Thomas, J. B., Watson, E. B., Spear, F. S., Shemella, P. T., Nayak, S. K., & Lanzirotti, A. (2010). Ti-in-quartz under pressure: the effect of pressure and temperature on the solubility of Ti-in-quartz. *Contributions to Mineralogy and Petrology*, *160*(5), 743-759.

Thomas, J. B., Watson, E. B., Spear, F. S., & Wark, D. A. (2015). Ti-in-quartz recrystallized: experimental confirmation of the original Ti-in-quartz calibrations.

Contributions to Mineralogy and Petrology, *169*(3), 1-16.

Tomkins, H. S., Powell, R., & Ellis, D. J. (2007). The pressure dependence of the zirconium-in-rutile thermometer. *Journal of Metamorphic Geology*, *25*(6), 703-713.

Tual, L., Pinan-Llamas, A. & Möller, C. (2015). High-Temperature Deformation in the Basal Shear Zone of an Eclogite-Bearing Fold Nappe, Sveconorwegian Orogen, Sweden, in: Roberts, N., Viola, G., Slagstad, T. (Eds.), The structural, metamorphic and magmatic evolution of Mesoproterozoic orogens. *Precambrian Research*, **265**, 104-120.

Walsh, A. K., Kelsey, D. E., Kirkland, C. L., Hand, M., Smithies, R. H., Clark, C., & Howard, H. M. (2014). *P–T*–t evolution of a large, long-lived, ultrahigh-temperature Grenvillian belt in central Australia. *Gondwana Research*.

Wark, D. A., & Watson, E. B. (2006). TitaniQ: a titanium-in-quartz geothermometer. *Contributions to Mineralogy and Petrology*, *152*(6), 743-754.

Watson, E. B., Wark, D. A., & Thomas, J. B. (2006). Crystallization thermometers for zircon and rutile. *Contributions to Mineralogy and Petrology*, *151*(4), 413-433.

Zack, T., Moraes, R., & Kronz, A. (2004). Temperature dependence of Zr-in-rutile: empirical calibration of a rutile thermometer. *Contributions to Mineralogy and Petrology*, *148*(4), 471-488.

Zack, T., & Luvizottow, G. L. (2006). Application of rutile thermometry to eclogites. *Mineralogy and Petrology*, *88*(1-2), 69-85.

Zhang, R. Y., Iizuka, Y., Ernst, W. G., Liou, J. G., XU, Z. Q., Tsujimori, T., ... & Jahn, B. M. (2009). Metamorphic *P–T* conditions and thermal structure of Chinese Continental Scientific Drilling main hole eclogites: Fe–Mg partitioning thermometer vs. Zr-in-rutile thermometer. *Journal of Metamorphic Geology*, *27*(9), 757-772.

SUPPORTING INFORMATION : Tracking the prograde *P–T* path of Precambrian eclogite using Ti-in-quartz and Zr-in-rutile thermobarometry.

Lorraine Tual [1*], Charlotte Möller [1], Martin Whitehouse[2]

Table S1: Full set of Zr-in-rutile results. Grey analyses are discarded because the analytical spot was misplaced.

Mineral ID *Grey: Discarded analysis*	Setting	90Zr/48Ti EM/FC1	Zr ppm	±	Calculated Temperature @ 7 kbar	@ 12 kbar	@ 18 kbar
A_mt1405_c-01	garnet core	1,07E-02	8,63E+00	29908	4387	1246	1282	1325
A_mt1405_c-02	garnet core	1,45E-04	3,11E+00	407	50	662	684	710
A_mt1405_c-03	garnet core	2,03E-04	4,89E+00	567	73	690	713	740
A_mt1405_c-04	garnet core	5,15E-04	5,27E+00	1440	187	781	806	836
A_mt1405_c-05	garnet core	2,41E-04	3,56E+00	675	84	706	729	757
A_mt1405_c-06	garnet core	2,44E-04	4,58E+00	682	87	707	730	758
A_mt1405_c-07	garnet core	2,38E-04	3,43E+00	667	82	705	728	756
A_mt1405_c-08	garnet core	2,29E-04	3,91E+00	640	80	701	724	752
A_mt1405_c-09	garnet core	2,30E-04	4,07E+00	643	81	701	725	752
A_mt1405_c-10	garnet core	1,75E-04	3,23E+00	491	60	678	700	727
A_mt1405_c-11	garnet core	5,64E-04	3,76E+00	1578	196	791	816	846
A_mt1405_c-12	garnet core	2,65E-04	3,51E+00	743	92	715	738	766
A_mt1405_c-13	garnet core	1,80E-04	4,08E+00	504	63	680	702	729
A_mt1405_c-14	garnet core	2,97E-04	2,93E+00	831	102	725	749	777
C_mt1405_c-01	garnet core	2,43E-04	3,59E+00	680	84	707	730	758
C_mt1405_c-02	garnet core	3,74E-04	3,91E+00	1047	131	748	772	801
C_mt1405_c-03	garnet core	3,72E-04	2,94E+00	1040	127	747	771	800
C_mt1405_c-05	garnet core	1,18E-04	3,04E+00	331	41	645	666	692
C_mt1405_c-06	garnet core	2,08E-04	3,71E+00	581	72	692	715	743
C_mt1405_c-07	garnet core	2,47E-03	4,65E+00	6906	880	979	1009	1044
C_mt1405_c-08	garnet core	4,29E-04	2,20E+00	1200	145	762	786	816
C_mt1405_c-09	garnet core	4,41E-04	4,07E+00	1234	155	765	789	819
C_mt1405_c-10	garnet core	4,01E-04	4,81E+00	1122	144	755	779	808
C_mt1405_c-11	garnet core	2,71E-04	2,09E+00	759	91	717	740	768
E_mt1405_c-01	garnet core	3,02E-04	4,20E+00	846	106	727	751	779
E_mt1405_c-02	garnet core	1,64E-04	5,72E+00	460	61	672	694	721
E_mt1405_c-03	garnet core	4,43E-04	5,02E+00	1239	160	765	790	819
E_mt1405_c-04	garnet core	1,57E-04	5,28E+00	438	57	668	690	717
E_mt1405_c-05	garnet core	2,69E-04	4,53E+00	753	96	716	739	767
E_mt1405_c-06	garnet core	2,56E-05	4,58E+00	72	9	536	555	578
E_mt1405_c-07	garnet core	2,35E-04	4,81E+00	656	84	703	726	754
E_mt1405_c-08	garnet core	5,21E-03	1,07E+01	14581	2325	1102	1135	1174
E_mt1405_c-09	garnet core	2,00E-04	3,08E+00	559	69	689	712	739
E_mt1405_c-11	garnet core	3,80E-04	2,90E+00	1062	130	749	774	803
E_mt1405_c-12	garnet core	1,74E-04	4,31E+00	486	61	677	699	726
E_mt1405_c-13	garnet core	3,98E-04	3,87E+00	1115	139	754	779	808
E_mt1405_c-14	garnet core	2,97E-04	4,35E+00	831	105	725	749	777
E_mt1405_c-15	garnet core	1,41E-04	2,88E+00	394	48	659	681	707
E_mt1405_c-17	garnet core	4,48E-04	3,87E+00	1255	157	766	791	820
E_mt1405_c-20	garnet core	3,47E-04	4,81E+00	970	124	740	764	793
E_mt1405_c-21	garnet core	2,99E-04	4,01E+00	838	105	726	750	778
E_mt1405_c-22	garnet core	2,63E-04	3,58E+00	735	91	714	737	765
E_mt1405_c-23	garnet core	2,91E-04	1,17E+00	815	97	724	747	775
E_mt1405_c-24	garnet core	3,06E-04	4,03E+00	857	107	728	752	780
E_mt1405_c-25	garnet core	2,70E-04	2,16E+00	757	91	717	740	768
E_mt1405_c-26	garnet core	2,40E-04	3,61E+00	671	83	705	729	756
E_mt1405_c-27	garnet core	2,22E-04	4,39E+00	620	78	698	721	749
E_mt1405_c-29	garnet core	3,07E-04	2,51E+00	861	104	729	752	781
E_mt1405_c-30	garnet core	1,39E-04	3,34E+00	389	48	658	680	706
E_mt1405_c-31	garnet core	2,02E-04	4,76E+00	565	72	690	713	740
E_mt1405_c-32	garnet core	3,24E-04	5,72E+00	908	120	734	758	786
E_mt1405_c-33	garnet core	1,51E-04	3,66E+00	422	52	665	687	713
E_mt1405_c-34	garnet core	2,80E-04	4,09E+00	785	98	720	743	772
E_mt1405_c-36	garnet core	1,90E-04	3,49E+00	532	66	685	707	734
E_mt1405_c-37	garnet core	4,32E-04	3,98E+00	1209	151	763	787	816
E_mt1405_c-38	garnet core	5,40E-04	3,37E+00	1511	186	786	811	841
A_mt1405_r-01	garnet rim	3,29E-04	5,71E+00	919	121	735	759	788
A_mt1405_r-02	garnet rim	3,83E-04	1,97E+00	1071	129	750	774	803
A_mt1405_r-03	garnet rim	2,16E-04	4,56E+00	606	77	696	719	746
A_mt1405_r-04	garnet rim	3,40E-04	4,22E+00	951	120	739	762	791
A_mt1405_r-05	garnet rim	2,39E-04	2,27E+00	668	81	705	728	756
A_mt1405_r-06	garnet rim	2,59E-04	3,33E+00	726	89	713	736	764
A_mt1405_r-07	garnet rim	3,30E-04	3,65E+00	925	115	736	760	788
A_mt1405_r-08	garnet rim	4,82E-04	4,63E+00	1350	172	774	799	828
A_mt1405_r-09	garnet rim	5,55E-04	4,35E+00	1554	196	789	814	844
A_mt1405_r-10	garnet rim	3,14E-04	1,86E+00	879	106	731	755	783
A_mt1405_r-11	garnet rim	2,45E-04	5,60E+00	686	90	707	731	758
C_mt1405_r-01	garnet rim	5,03E-04	3,37E+00	1409	174	779	803	833
C_mt1405_r-02	garnet rim	4,99E-04	3,10E+00	1398	171	778	803	832
C_mt1405_r-03	garnet rim	2,73E-04	3,23E+00	763	94	717	741	769

Table S1: continued.

Mineral ID	**Setting**	**90Zr/48Ti**		**Zr ppm**	**±**	**Calculated Temperature**		
Grey: Discarded analysis		**EM/FC1**				**@ 7 kbar**	**@ 12 kbar**	**@ 18 kbar**
C_mt1405_r-04	garnet rim	3,62E-04	5,11E+00	1012	131	745	769	798
C_mt1405_r-05	garnet rim	3,45E-04	5,06E+00	966	125	740	764	793
C_mt1405_r-06	garnet rim	3,87E-04	4,66E+00	1083	138	751	776	805
C_mt1405_r-07	garnet rim	3,26E-04	4,51E+00	912	116	734	758	787
C_mt1405_r-08	garnet rim	2,99E-04	4,72E+00	837	107	726	750	778
C_mt1405_r-09	garnet rim	3,22E-04	3,26E+00	901	111	733	757	785
C_mt1405_r-10	garnet rim	5,42E-04	4,88E+00	1517	195	786	811	842
C_mt1405_r-11	garnet rim	1,82E-04	4,90E+00	509	65	681	703	730
C_mt1405_r-12	garnet rim	3,08E-04	3,50E+00	863	107	729	753	781
C_mt1405_r-13	garnet rim	3,31E-04	3,70E+00	927	115	736	760	788
C_mt1405_r-14	garnet rim	1,62E-04	2,76E+00	453	55	671	693	720
C_mt1405_r-15	garnet rim	3,12E-04	3,87E+00	873	109	730	754	782
C_mt1405_r-16	garnet rim	3,18E-04	4,87E+00	890	114	732	756	784
C_mt1405_r-17	garnet rim	3,45E-04	6,57E+00	966	131	740	764	793
C_mt1405_r-18	garnet rim	4,70E-04	5,70E+00	1316	173	771	796	826
E_mt1405_r-01	garnet rim	3,59E-04	4,90E+00	1005	129	744	768	797
E_mt1405_r-02	garnet rim	2,53E-04	4,17E+00	709	89	710	734	762
E_mt1405_r-03	garnet rim	3,66E-04	3,44E+00	1024	126	746	770	799
E_mt1405_r-04	garnet rim	3,88E-04	1,35E+00	1086	130	752	776	805
E_mt1405_r-05	garnet rim	4,02E-03	4,99E+00	11250	1448	1057	1088	1126
E_mt1405_r-06	garnet rim	3,24E-04	2,66E+00	907	110	734	758	786
E_mt1405_r-07	garnet rim	2,60E-04	2,09E+00	728	88	713	736	764
E_mt1405_r-08	garnet rim	2,50E-04	4,23E+00	700	88	709	733	760
E_mt1405_r-09	garnet rim	2,53E-04	3,39E+00	707	87	710	733	761
E_mt1405_r-10	garnet rim	2,34E-04	4,30E+00	655	83	703	726	754
E_mt1405_r-11	garnet rim	2,35E-03	3,76E+00	6572	818	972	1001	1036
E_mt1405_r-12	garnet rim	3,77E-04	4,30E+00	1055	133	749	773	802
E_mt1405_r-13	garnet rim	2,97E-04	2,79E+00	831	101	725	749	777
E_mt1405_r-14	garnet rim	2,88E-04	1,88E+00	805	97	722	746	774
E_mt1405_r-14@0	garnet rim	3,64E-04	4,59E+00	1018	129	745	769	798
E_mt1405_r-15	garnet rim	3,53E-04	4,91E+00	988	127	742	766	795
E_mt1405_r-16	garnet rim	NaN	NaN	#VALUE!	#VALUE!	#VALUE!	#VALUE!	#VALUE!
E_mt1405_r-17	garnet rim	2,93E-04	4,36E+00	820	104	724	748	776
E_mt1405_r-18	garnet rim	1,43E-04	4,93E+00	400	51	660	682	709
E_mt1405_r-19	garnet rim	2,99E-04	4,94E+00	838	108	726	750	778
E_mt1405_r-20	garnet rim	2,33E-04	3,87E+00	652	81	703	726	754
E_mt1405_r-21	garnet rim	3,46E-04	3,09E+00	969	119	740	764	793
E_mt1405_r-22	garnet rim	3,13E-04	4,13E+00	877	110	731	754	783
E_mt1405_r-23	garnet rim	2,64E-04	4,24E+00	739	93	714	738	766
E_mt1405_r-24	garnet rim	2,94E-04	4,15E+00	824	104	725	748	776
E_mt1405_r-25	garnet rim	2,66E-04	3,83E+00	744	93	715	738	766
E_mt1405_r-26	garnet rim	1,57E-04	3,92E+00	440	55	668	691	717
C_mt1405_m-01	matrix	2,42E-04	4,26E+00	677	85	706	729	757
C_mt1405_m-02	matrix	7,21E-06	7,89E+00	20	3	463	481	502
C_mt1405_m-03	matrix	1,52E-05	5,29E+00	43	6	504	523	545
C_mt1405_m-04	matrix	6,22E-06	5,70E+00	17	2	456	473	494
C_mt1405_m-05	matrix	8,22E-06	3,37E+00	23	3	470	488	509
C_mt1405_m-06	matrix	5,61E-06	5,47E+00	16	2	451	468	488
C_mt1405_m-07	matrix	3,89E-04	5,81E+00	1088	144	752	776	805
C_mt1405_m-08	matrix	4,06E-04	5,03E+00	1136	146	756	781	810
C_mt1405_m-09	matrix	1,88E-04	1,99E+00	527	63	684	706	733
C_mt1405_m-10	matrix	3,65E-04	3,94E+00	1021	128	746	770	798
C_mt1405_m-11	matrix	1,01E-05	4,01E+00	28	4	481	499	521
C_mt1405_m-12	matrix	5,69E-06	2,80E+00	16	2	451	468	489
C_mt1405_m-13	matrix	2,70E-06	5,04E+00	8	1	416	432	451
C_mt1405_m-14	matrix	4,11E-04	5,88E+00	1151	152	758	782	811
C_mt1405_m-15	matrix	4,41E-04	3,42E+00	1235	152	765	789	819
C_mt1405_m-16	matrix	5,09E-04	3,69E+00	1426	177	780	805	835
C_mt1405_m-17	matrix	1,36E-05	4,29E+00	38	5	498	516	538
C_mt1405_m-18	matrix	1,77E-04	3,25E+00	495	61	678	701	728
C_mt1405_m-19	matrix	5,58E-06	4,12E+00	16	2	450	467	488
C_mt1405_m-20	matrix	2,53E-04	4,53E+00	709	90	711	734	762
C_mt1405_m-21	matrix	8,16E-04	2,91E+00	2283	279	832	858	890
C_mt1405_m-22	matrix	5,60E-04	2,97E+00	1566	192	790	815	845
C_mt1405_m-23	matrix	8,51E-04	3,26E+00	2382	293	837	864	895
C_mt1405_m-24	matrix	8,86E-04	4,59E+00	2479	315	842	868	900
C_mt1405_m-25	matrix	1,14E-05	4,25E+00	32	4	488	506	528
C_mt1405_m-26	matrix	2,70E-06	3,57E+00	8	1	416	432	452
C_mt1405_m-28	matrix	4,47E-04	2,74E+00	1250	152	766	791	820
C_mt1405_m-27	matrix	NaN	NaN	#VALUE!	#VALUE!	#VALUE!	#VALUE!	#VALUE!
E_mt1405_m-01a	matrix	3,18E-05	4,65E+00	89	11	550	569	592
E_mt1405_m-02	matrix	1,83E-05	3,06E+00	51	6	515	534	556

Table S1: continued.

Mineral ID *Grey: Discarded analysis*	**Setting**	**90Zr/48Ti EM/FC1**		**Zr ppm**	**±**	**Calculated Temperature @ 7 kbar**	**@ 12 kbar**	**@ 18 kbar**
E_mt1405_m-03	matrix	6,85E-06	4,13E+00	19	2	461	478	499
E_mt1405_m-04	matrix	6,77E-06	3,37E+00	19	2	460	478	498
E_mt1405_m-05	matrix	2,53E-05	4,52E+00	71	9	535	554	577
E_mt1405_m-06	matrix	4,25E-04	3,32E+00	1190	147	761	785	815
E_mt1405_m-06@0	matrix	2,21E-05	3,99E+00	62	8	527	546	568
E_mt1405_m07	matrix	3,63E-04	4,22E+00	1015	128	745	769	798

	90Zr/48Ti EM/FC1			**Zr ppm**	**±**	
Standard						
R10b_20150202_@1	2,23E-04	3,51E+00				
R10b_20150202_@2	2,71E-04	2,51E+00				
R10b_20150202_@3	2,51E-04	4,12E+00		mean	2,71E-04	
R10b_20150202_@4	2,51E-04	3,77E+00		sd	3,20E-05	
R10b_20150202_@5	2,58E-04	2,83E+00		RSD (%)	1,18E+01	
R10b_20150202_@6	2,48E-04	4,15E+00		ppm	7,59E+02	Luvizotto et al., Chem. Geol. 200
R10b_20150202_@7	2,36E-04	3,98E+00		±	8,00E+00	
R10b_20150202_@8	2,84E-04	4,10E+00				
R10b_20150202_@9	3,19E-04	3,43E+00				
R10b_20150202_@10	3,21E-04	3,79E+00				
R10b_20150202_@11	3,02E-04	2,54E+00				
R10b_20150202_@12	2,90E-04	3,94E+00				
R13_20150202_@1	1,35E-04	3,52E+00		3,77E+02	4,66E+01	
R13_20150202_@2	1,11E-04	2,58E+00		3,10E+02	3,76E+01	
R13_20150202_@3	1,33E-04	2,27E+00		3,73E+02	4,50E+01	
R13_20150202_@4	1,46E-04	2,10E+00		4,10E+02	4,93E+01	
			mean	3,67E+02		
			sd	3,76E+01		
			not reported?			
R19_20150202_@1	9,58E-05	3,02E+00		2,68E+02	3,28E+01	
R19_20150202_@2	8,42E-05	4,19E+00		2,36E+02	2,96E+01	
R19_20150202_@3	8,37E-05	4,16E+00		2,34E+02	2,94E+01	
R19_20150202_@4	8,28E-05	2,50E+00		2,32E+02	2,81E+01	
			mean	2,42E+02		
			sd	1,92E+01		
			Luvizotto	249 ± 6		
Diss_20150202_@1	3,80E-05	2,81E+00		1,06E+02	1,30E+01	
Diss_20150202_@2	3,89E-05	4,89E+00		1,09E+02	1,40E+01	
Diss_20150202_@3	4,03E-05	4,06E+00		1,13E+02	1,42E+01	
Diss_20150202_@4	3,43E-05	3,49E+00		9,60E+01	1,19E+01	
Diss_20150202_@5	3,36E-05	3,41E+00		9,41E+01	1,16E+01	
Diss_20150202_@6	3,59E-05	3,19E+00		1,01E+02	1,24E+01	
			mean	1,03E+02		
			sd	8,19E+00		
			Luvizotto	128 ± 5		

Table S2: Full set of Ti-in-quartz results. Grey analyses are discarded because the analytical spot was misplaced.

Mineral ID	**Setting**	**47Ti/28Si**		**27Al/28Si**		**40Ca/28Si**		**28Si/Coeff**			**Ti ppm**	**±**	**Calculated Temperature**		
Grey : Discarded analysis		**EM/FC2**		**EM/FC2**		**EM/FC2**		**FC2**					**@ 7 kbar**	**@ 12 kbar**	**@ 18 kbar**
A_qtz_mt1405_c-01	garnet core	1,31E-05	0,36	1,52E-04	0,22	3,73E-06	18,90	1,64E+08	0,69		46	3	612	717	843
A_qtz_mt1405_c-02	garnet core	1,49E-05	0,41	1,60E-04	0,33	3,54E-06	14,51	1,69E+08	1,02		52	4	623	729	857
A_qtz_mt1405_c-03	garnet core	1,81E-05	0,40	6,07E-03	1,95	2,84E-03	1,75	1,71E+08	0,85		63	5	641	750	881
A_qtz_mt1405_c-04	garnet core	1,27E-05	0,38	3,36E-04	0,46	5,47E-05	2,84	1,72E+08	0,82		45	3	609	714	840
A_qtz_mt1405_c-05	garnet core	1,61E-05	0,36	2,02E-04	0,67	2,02E-05	2,45	1,71E+08	0,82		57	4	630	738	867
A_qtz_mt1405_c-06	garnet core	1,71E-05	0,36	1,72E-04	0,27	2,80E-06	13,61	1,74E+08	0,78		60	4	636	744	874
A_qtz_mt1405_c-07	garnet core	1,70E-05	0,40	2,19E-04	0,25	3,28E-06	13,40	1,71E+08	0,75		59	4	635	743	873
A_qtz_mt1405_c-09	garnet core	1,84E-05	1,61	1,24E-04	1,56	4,59E-06	16,63	1,62E+08	0,84		64	5	643	752	882
A_qtz_mt1405_c-10	garnet core	1,50E-05	0,39	2,58E-04	0,81	4,59E-05	1,68	1,65E+08	0,81		52	4	623	730	858
A_qtz_mt1405_c-11	garnet core	1,59E-05	0,36	1,61E-04	0,25	3,00E-06	14,83	1,70E+08	0,76		56	4	629	737	866
A_qtz_mt1405_c-12	garnet core	1,11E-07	4,88	5,49E-03	0,20	4,43E-05	6,89	1,40E+08	1,02		0	0	325	396	481
A_qtz_mt1405_c-13	garnet core	1,43E-05	0,34	3,51E-04	5,04	3,51E-04	6,39	1,71E+08	0,77		50	4	619	726	853
C_qtz_mt1405_c-01	garnet core	1,92E-05	0,52	2,07E-04	0,41	5,73E-06	18,93	1,46E+08	0,36		67	5	647	756	888
C_qtz_mt1405_c-03	garnet core	1,70E-05	0,34	2,20E-04	0,83	8,01E-06	16,94	1,41E+08	0,28		60	4	635	744	873
C_qtz_mt1405_c-03@0	garnet core	1,77E-05	0,36	1,80E-04	0,33	2,67E-05	4,28	1,40E+08	0,42		62	5	639	748	878
C_qtz_mt1405_c-05	garnet core	1,68E-05	0,33	2,09E-04	0,25	5,72E-06	13,34	1,49E+08	0,42		59	4	634	742	872
C_qtz_mt1405_c-06	garnet core	1,63E-05	0,36	2,09E-04	0,27	7,96E-06	13,89	1,49E+08	0,36		57	4	631	739	868
C_qtz_mt1405_c-07	garnet core	1,23E-05	0,51	1,50E-04	0,56	5,94E-06	12,25	1,51E+08	0,39		43	3	606	711	836
C_qtz_mt1405_c-08	garnet core	1,97E-05	0,46	1,46E-04	0,22	5,26E-06	11,32	1,55E+08	0,57		69	5	650	759	891
C_qtz_mt1405_c-09	garnet core	1,42E-05	0,36	1,73E-04	0,35	5,32E-06	10,88	1,62E+08	0,48		50	4	619	725	852
C_qtz_mt1405_c-10	garnet core	1,91E-05	0,37	2,09E-04	0,25	3,86E-06	13,53	1,58E+08	0,40		67	5	647	756	887
C_qtz_mt1405_c-16	garnet core	1,33E-05	0,35	1,45E-04	0,30	3,81E-06	12,90	1,66E+08	0,48		47	3	613	719	845
C_qtz_mt1405_c-19	garnet core	2,47E-04	0,30	-9,78E-01	0,00	-1,19E+00	0,01	2,88E+07	0,22		864	63	982	1131	1310
C_qtz_mt1405_c-20	garnet core	1,35E-05	0,52	1,63E-04	0,42	7,66E-06	14,35	1,41E+08	0,48		47	3	614	720	847
C_qtz_mt1405_c-21	garnet core	1,35E-05	0,43	1,49E-04	0,29	6,46E-06	14,16	1,40E+08	0,46		47	3	614	720	846
C_qtz_mt1405_c-23	garnet core	1,43E-05	0,48	1,78E-04	0,27	6,80E-06	14,54	1,45E+08	0,47		50	4	620	726	853
C_qtz_mt1405_c-24	garnet core	1,72E-05	0,38	2,31E-04	0,30	6,95E-06	12,99	1,51E+08	0,69		60	4	636	744	874
C_qtz_mt1405_c-25	garnet core	1,71E-05	0,37	2,31E-04	0,58	2,69E-05	1,80	1,51E+08	0,48		60	4	636	744	874
C_qtz_mt1405_c-26	garnet core	1,54E-05	0,52	1,79E-04	0,26	1,24E-05	10,36	1,47E+08	0,40		54	4	626	733	862
C_qtz_mt1405_c-27	garnet core	1,61E-05	0,34	2,04E-04	0,23	4,48E-06	13,95	1,52E+08	0,42		56	4	630	738	867
C_qtz_mt1405_c-28	garnet core	1,16E-05	0,55	1,18E-04	0,28	7,90E-06	13,29	1,48E+08	0,32		41	3	601	705	830
C_qtz_mt1405_c-29	garnet core	1,72E-05	0,47	2,39E-04	0,32	2,41E-05	15,22	1,49E+08	0,54		60	4	636	745	875
C_qtz_mt1405_c-30	garnet core	1,71E-05	0,37	2,23E-04	0,31	1,38E-05	11,46	1,49E+08	0,44		60	4	636	744	874
C_qtz_mt1405_c-31	garnet core	1,57E-05	0,38	1,91E-04	0,75	2,93E-05	12,00	1,47E+08	0,44		55	4	628	735	864
C_qtz_mt1405_c-32	garnet core	2,21E-05	0,30	1,65E-01	2,50	5,39E-02	2,34	1,59E+08	0,78		77	6	661	772	905
E_qtz_mt1405_c-01	garnet core	1,68E-05	0,29	2,40E-04	0,23	2,53E-06	13,04	1,95E+08	0,63		59	4	634	742	871
E_qtz_mt1405_c-02	garnet core	1,76E-05	0,39	2,72E-04	0,20	1,01E-05	12,88	1,87E+08	0,46		62	4	639	747	877
E_qtz_mt1405_c-03	garnet core	1,76E-05	1,54	2,83E-04	6,62	5,85E-06	6,48	1,91E+08	0,62		62	5	639	747	877
E_qtz_mt1405_c-04	garnet core	1,44E-05	0,34	1,91E-04	0,15	2,80E-06	12,20	1,86E+08	0,55		50	4	620	726	854
E_qtz_mt1405_c-05	garnet core	1,80E-05	0,38	4,59E-02	0,69	1,84E-02	0,45	1,90E+08	0,91		63	5	641	749	880
E_qtz_mt1405_c-06	garnet core	1,40E-05	0,32	1,98E-04	0,26	2,69E-06	12,95	1,93E+08	0,60		49	4	618	724	851
E_qtz_mt1405_c-07	garnet core	1,97E-05	0,43	3,34E-01	2,23	7,76E-02	0,40	1,85E+08	1,11		69	5	649	759	891
E_qtz_mt1405_c-08	garnet core	1,35E-05	0,44	2,09E-04	0,23	2,44E-06	14,13	1,90E+08	0,61		47	3	614	719	846
E_qtz_mt1405_c-09	garnet core	1,26E-05	0,34	4,54E-02	3,21	1,83E-02	2,44	1,86E+08	0,85		44	3	608	713	839
E_qtz_mt1405_c-10	garnet core	2,15E-04	0,30	-6,75E-01	0,00	-7,82E-01	0,00	3,94E+07	0,33		752	55	957	1104	1280
E_qtz_mt1405_c-11	garnet core	1,26E-05	0,34	1,72E-04	0,22	5,33E-06	7,69	1,91E+08	0,64		44	3	608	713	839
E_qtz_mt1405_c-12	garnet core	1,83E-05	0,86	2,28E-03	5,34	6,44E-04	6,82	1,96E+08	0,91		64	5	642	751	882
E_qtz_mt1405_c-13	garnet core	1,81E-05	0,32	1,81E-04	0,23	1,18E-05	2,84	1,94E+08	0,53		64	5	641	750	881
E_qtz_mt1405_c-14	garnet core	1,69E-05	0,37	2,52E-04	0,18	3,89E-06	11,70	1,90E+08	0,59		59	4	635	743	873
E_qtz_mt1405_c-15	garnet core	1,24E-05	0,61	1,59E-04	0,64	4,24E-06	14,06	1,81E+08	0,47		43	3	606	711	837
E_qtz_mt1405_c-17	garnet core	1,78E-05	0,29	3,45E-03	1,21	1,46E-03	1,10	1,91E+08	0,66		62	5	640	748	879
E_qtz_mt1405_c-18	garnet core	3,51E-05	0,84	-2,88E-01	0,00	-8,63E-01	0,00	1,38E+08	1,11		123	9	709	826	966
E_qtz_mt1405_c-19	garnet core	1,85E-05	0,38	5,48E-02	4,04	2,37E-02	3,78	1,97E+08	1,17		65	5	643	752	883
E_qtz_mt1405_c-20	garnet core	7,65E-05	0,22	-3,24E-01	0,00	-4,09E-01	0,00	8,82E+07	0,45		268	19	802	930	1084
E_qtz_mt1405_c-21	garnet core	1,85E-05	0,38	-8,15E-01	0,00	2,79E-01	1,79	1,77E+08	1,04		65	5	643	752	883
E_qtz_mt1405_c-22	garnet core	1,42E-05	0,33	2,26E-04	0,90	9,04E-06	6,62	1,93E+08	0,63		50	4	619	725	852
E_qtz_mt1405_c-23	garnet core	1,46E-05	0,31	1,98E-04	0,24	4,05E-06	12,40	1,96E+08	0,61		51	4	621	728	856
E_qtz_mt1405_c-24	garnet core	1,42E-05	0,34	1,70E-04	0,23	1,10E-05	13,24	1,90E+08	0,56		50	4	618	725	852
E_qtz_mt1405_c-25	garnet core	1,78E-05	0,40	2,18E-04	0,72	1,52E-05	12,56	2,00E+08	0,68		63	5	640	748	879
E_qtz_mt1405_c-26	garnet core	2,31E-04	0,28	-6,51E-01	0,00	-7,40E-01	0,00	4,05E+07	0,51		810	59	970	1118	1296
E_qtz_mt1405_c-27	garnet core	1,45E-05	0,40	2,20E-04	0,46	3,25E-04	15,24	1,82E+08	0,74		51	4	620	727	854
E_qtz_mt1405_c-28	garnet core	1,82E-05	0,29	2,07E-04	0,25	2,56E-06	9,30	1,81E+08	0,58		64	5	642	751	881
E_qtz_mt1405_c-29	garnet core	1,74E-05	0,45	2,04E-04	0,23	4,90E-06	12,72	1,78E+08	0,57		61	4	638	746	876
E_qtz_mt1405_c-30	garnet core	1,66E-05	0,38	6,76E-04	0,70	1,03E-04	2,63	1,78E+08	0,77		58	4	633	741	870
E_qtz_mt1405_c-31	garnet core	1,51E-05	0,36	1,53E-04	0,32	2,79E-06	9,69	1,87E+08	0,72		53	4	625	731	860
E_qtz_mt1405_c-32	garnet core	1,84E-05	0,34	1,64E-04	0,28	4,34E-06	6,60	1,80E+08	0,67		64	5	643	752	882
E_qtz_mt1405_c-33	garnet core	1,81E-05	0,40	1,69E-04	0,28	3,38E-06	12,49	1,81E+08	0,63		64	5	641	750	881
E_qtz_mt1405_c-34	garnet core	1,45E-05	0,35	1,63E-04	1,49	2,07E-06	13,54	1,78E+08	0,63		51	4	621	727	855
E_qtz_mt1405_c-35	garnet core	2,02E-05	0,28	1,91E-04	0,26	2,76E-06	14,77	1,78E+08	0,67		71	5	652	762	894
E_qtz_mt1405_c-36	garnet core	2,03E-05	0,37	2,00E-04	0,20	2,19E-06	11,38	1,78E+08	0,64		71	5	652	762	894
E_qtz_mt1405_c-37	garnet core	1,88E-05	0,29	2,34E-04	0,25	4,45E-06	12,15	1,78E+08	0,81		66	5	645	754	885
A_qtz_mt1405_r-01	garnet rim	2,18E-05	2,28	1,91E-04	1,49	7,17E-06	13,66	1,64E+08	0,84		76	6	659	770	903
A_qtz_mt1405_r-02	garnet rim	1,73E-05	0,35	3,29E-04	1,56	1,71E-04	5,77	1,65E+08	0,91		61	4	637	745	875
A_qtz_mt1405_r-03	garnet rim	3,47E-05	0,39	-4,05E-01	0,00	1,91E+00	2,59	1,22E+08	0,80		122	9	708	824	964
A_qtz_mt1405_r-04	garnet rim	2,15E-05	0,48	2,36E-04	0,63	3,46E-02	7,06	1,74E+08	1,17		75	5	658	769	902

Table S2: continued

Mineral ID	Setting	47Ti/28Si		27Al/28Si		40Ca/28Si		28Si/Coeff		Ti ppm	±	Calculated Temperature		
Grey : Discarded analysis		EM/FC2		EM/FC2		EM/FC2		FC2				@ 7 kbar	@ 12 kbar	@ 18 kbar
A_qtz_mt1405_r-05	garnet rim	2,11E-05	0,27	3,73E-04	1,63	9,01E-05	3,16	1,75E+08	0,69	74	5	656	766	899
A_qtz_mt1405_r-06	garnet rim	1,77E-05	0,45	1,87E-03	4,58	8,39E-05	3,94	1,85E+08	0,95	62	5	639	747	878
A_qtz_mt1405_r-07	garnet rim	1,82E-05	0,41	2,52E-04	0,27	3,45E-06	14,75	1,78E+08	0,81	64	5	642	751	882
A_qtz_mt1405_r-08	garnet rim	2,01E-05	0,35	2,01E-04	0,24	2,95E-06	12,17	1,79E+08	0,73	70	5	651	761	893
A_qtz_mt1405_r-09	garnet rim	1,78E-05	0,29	2,26E-04	0,25	4,31E-06	15,04	1,80E+08	0,76	62	5	640	748	879
A_qtz_mt1405_r-10	garnet rim	1,75E-05	0,38	1,82E-04	0,23	4,80E-06	11,83	1,76E+08	0,71	61	4	638	746	877
A_qtz_mt1405_r-11	garnet rim	1,94E-05	0,31	2,52E-04	0,30	1,41E-05	14,13	1,92E+08	0,93	68	5	648	758	889
A_qtz_mt1405_r-12	garnet rim	1,44E-05	4,34	2,08E-04	7,82	3,90E-05	27,27	1,83E+08	0,81	51	4	620	726	854
A_qtz_mt1405_r-13	garnet rim	1,73E-05	0,54	2,08E-04	0,32	2,37E-05	15,39	1,72E+08	0,64	60	4	637	745	875
A_qtz_mt1405_r-14	garnet rim	1,77E-05	0,33	2,29E-04	0,19	2,70E-05	12,77	1,66E+08	0,62	62	4	639	747	878
A_qtz_mt1405_r-15	garnet rim	1,87E-05	0,41	2,58E-04	0,17	1,03E-05	13,70	1,55E+08	0,61	66	5	644	754	885
A_qtz_mt1405_r-16	garnet rim	1,88E-05	0,29	3,02E-04	0,21	5,34E-06	15,66	1,71E+08	0,70	66	5	645	754	885
A_qtz_mt1405_r-17	garnet rim	1,85E-05	0,36	2,92E-04	0,33	1,46E-05	18,86	1,69E+08	0,55	65	5	643	752	883
A_qtz_mt1405_r-18	garnet rim	1,98E-05	0,40	2,67E-04	0,26	7,11E-06	18,00	1,76E+08	0,59	69	5	650	760	892
C_qtz_mt1405_r-01	garnet rim	1,99E-05	0,35	2,11E-04	0,26	4,77E-06	13,69	1,55E+08	0,58	70	5	650	760	892
C_qtz_mt1405_r-03	garnet rim	2,49E-05	0,40	2,10E-04	0,28	1,62E-05	13,50	1,57E+08	0,63	87	6	673	785	920
C_qtz_mt1405_r-04	garnet rim	1,86E-05	0,39	4,49E-04	1,38	6,57E-05	5,56	1,71E+08	0,45	65	5	644	753	884
E_qtz_mt1405_r-01	garnet rim	1,55E-05	0,31	1,67E-04	0,25	2,59E-06	12,39	1,92E+08	0,57	54	4	627	734	862
E_qtz_mt1405_r-02	garnet rim	1,85E-05	0,32	1,44E-04	0,28	3,57E-06	6,62	1,95E+08	0,52	65	5	643	752	883
E_qtz_mt1405_r-04	garnet rim	1,54E-05	0,32	2,43E-04	0,29	5,85E-06	11,35	1,79E+08	0,82	54	4	626	733	861
E_qtz_mt1405_r-05	garnet rim	1,52E-05	0,38	3,17E-04	0,26	4,16E-06	11,23	1,72E+08	0,67	53	4	625	732	860
E_qtz_mt1405_r-06	garnet rim	1,44E-05	0,36	3,91E-04	0,40	2,04E-05	3,98	1,75E+08	0,66	50	4	620	726	854
E_qtz_mt1405_r-07	garnet rim	1,45E-05	0,34	1,95E-04	0,43	2,18E-06	10,84	1,77E+08	0,83	51	4	621	727	855
E_qtz_mt1405_r-08	garnet rim	1,18E-05	0,50	1,30E-04	0,22	4,74E-06	7,29	1,77E+08	0,75	41	3	602	706	831
E_qtz_mt1405_r-09	garnet rim	1,50E-05	0,34	2,02E-04	0,30	3,91E-02	4,37	1,77E+08	0,77	52	4	623	730	858
E_qtz_mt1405_r-10	garnet rim	1,72E-05	0,33	2,36E-04	0,26	1,09E-05	14,51	1,78E+08	0,67	60	4	636	745	875
E_qtz_mt1405_r-11	garnet rim	1,72E-05	0,42	2,68E-04	0,81	1,04E-05	6,44	1,82E+08	0,57	60	4	637	745	875
E_qtz_mt1405_r-12	garnet rim	1,78E-05	0,47	2,70E-04	0,23	1,49E-05	5,60	1,82E+08	0,59	62	5	640	748	879
E_qtz_mt1405_r-13	garnet rim	1,80E-05	0,36	1,92E-04	0,36	2,69E-06	11,80	1,88E+08	0,82	63	5	641	750	880
E_qtz_mt1405_r-13b	garnet rim	1,66E-05	0,31	2,22E-04	0,16	2,85E-06	13,40	1,80E+08	0,63	58	4	633	741	870
E_qtz_mt1405_r-14	garnet rim	1,76E-05	0,40	2,65E-04	0,23	4,01E-06	13,61	1,77E+08	0,63	62	4	639	747	878
E_qtz_mt1405_r-15	garnet rim	1,58E-05	0,47	2,69E-04	0,28	5,39E-05	27,73	1,80E+08	0,61	55	4	629	736	865
E_qtz_mt1405_r-16	garnet rim	1,78E-05	0,29	3,11E-04	0,62	1,09E-04	18,04	1,81E+08	0,60	62	5	640	748	879
E_qtz_mt1405_r-17	garnet rim	1,55E-05	0,47	9,19E-04	4,56	1,58E-04	5,73	1,82E+08	0,59	54	4	626	734	862
A_qtz_mt1405_m-01	matrix	1,66E-05	0,37	2,67E-04	0,38	3,78E-05	11,59	1,69E+08	0,78	58	4	633	741	871
A_qtz_mt1405_m-02	matrix	1,77E-05	0,36	2,24E-04	0,17	1,69E-05	18,37	1,68E+08	0,61	62	4	639	747	878
A_qtz_mt1405_m-03	matrix	1,76E-05	0,40	2,46E-04	0,25	2,11E-05	14,86	1,74E+08	0,81	62	4	639	747	877
A_qtz_mt1405_m-04	matrix	1,65E-05	0,41	2,32E-04	0,27	2,58E-05	13,60	1,72E+08	0,48	58	4	632	740	869
A_qtz_mt1405_m-05	matrix	1,45E-05	0,42	1,73E-04	0,30	2,84E-05	14,30	1,84E+08	0,58	51	4	621	727	855
A_qtz_mt1405_m-06	matrix	1,94E-05	0,28	2,73E-04	0,23	4,65E-04	3,60	1,79E+08	0,76	68	5	648	757	889
A_qtz_mt1405_m-07	matrix	8,84E-06	0,43	1,69E-04	0,63	2,68E-05	10,57	1,82E+08	0,77	31	2	578	679	801
A_qtz_mt1405_m-08	matrix	1,81E-05	0,30	2,85E-04	0,78	4,17E-05	10,95	1,73E+08	0,81	63	5	641	750	880
A_qtz_mt1405_m-09	matrix	1,78E-05	0,32	2,86E-04	0,17	6,42E-06	13,24	1,75E+08	0,68	62	5	640	748	878
A_qtz_mt1405_m-09@0	matrix	1,96E-04	0,30	-8,00E-01	0,00	-1,04E+00	0,00	3,43E+07	0,50	687	50	942	1087	1260
A_qtz_mt1405_m-10@0	matrix	1,65E-05	0,32	2,25E-04	0,22	3,51E-06	13,86	1,61E+08	0,43	58	4	633	740	870
A_qtz_mt1405_m-10	matrix	1,45E-05	0,35	3,40E-04	1,59	1,17E-04	24,06	1,88E+08	0,70	51	4	621	727	855
A_qtz_mt1405_m-11	matrix	1,69E-05	0,29	2,61E-04	0,18	9,17E-06	14,75	1,90E+08	0,85	59	4	635	743	872
A_qtz_mt1405_m-12	matrix	1,45E-05	0,54	2,09E-04	0,32	9,02E-06	7,98	1,86E+08	0,77	51	4	621	727	855
A_qtz_mt1405_m-17	matrix	1,60E-05	0,49	2,37E-04	0,28	4,38E-06	13,65	1,70E+08	0,75	56	4	630	737	866
A_qtz_mt1405_m-18	matrix	1,70E-05	0,37	3,13E-04	0,75	1,69E-04	12,28	1,74E+08	0,81	60	4	636	744	873
A_qtz_mt1405_m-19	matrix	1,84E-05	0,35	3,40E-04	0,39	4,31E-05	4,82	1,72E+08	0,70	65	5	643	752	883
A_qtz_mt1405_m-20	matrix	1,92E-05	0,54	4,30E-04	1,77	5,59E-05	7,89	1,80E+08	0,99	67	5	647	756	888
A_qtz_mt1405_m-21	matrix	1,69E-05	0,35	3,05E-04	0,21	3,93E-06	16,47	1,68E+08	0,58	59	4	635	743	872
A_qtz_mt1405_m-22	matrix	1,48E-05	0,32	2,50E-04	0,56	5,80E-06	9,44	1,83E+08	0,75	52	4	623	729	857
A_qtz_mt1405_m-23	matrix	1,78E-05	0,30	3,30E-04	0,23	6,11E-06	9,25	1,72E+08	0,81	62	5	640	748	879
A_qtz_mt1405_m-24	matrix	1,77E-05	0,32	6,33E-04	0,87	3,16E-05	2,14	1,75E+08	0,66	62	5	639	748	878
A_qtz_mt1405_m-25	matrix	1,74E-05	0,38	5,28E-04	0,19	9,41E-06	11,28	1,72E+08	0,70	61	4	637	746	876
A_qtz_mt1405_m-26	matrix	1,73E-05	0,37	5,53E-04	0,16	2,34E-05	12,40	1,72E+08	0,80	61	4	637	746	876
A_qtz_mt1405_m-27	matrix	9,59E-06	1,71	3,67E-04	1,35	9,13E-06	6,70	1,71E+08	0,74	34	3	585	687	809
A_qtz_mt1405_m-28	matrix	1,76E-05	0,31	5,50E-04	0,31	1,27E-05	17,07	1,59E+08	0,63	62	4	639	747	878
C_qtz_mt1405_m-15	matrix	1,85E-05	0,42	3,07E-04	0,27	6,67E-06	13,74	1,48E+08	0,39	65	5	643	752	883
C_qtz_mt1405_m-16	matrix	1,95E-05	0,39	3,94E-04	0,24	1,43E-05	13,73	1,54E+08	0,56	68	5	648	758	889
C_qtz_mt1405_m-18	matrix	1,75E-05	0,37	4,54E-04	0,58	8,32E-05	3,43	1,43E+08	0,29	61	4	638	746	876
C_qtz_mt1405_m-36	matrix	1,62E-05	0,53	1,62E-04	0,31	4,49E-06	13,55	1,63E+08	0,49	57	4	631	738	868
E_qtz_mt1405_m-01	matrix	1,49E-05	0,40	9,02E-04	0,35	2,57E-04	2,24	1,59E+08	0,78	52	4	623	730	858
E_qtz_mt1405_m-02	matrix	1,44E-05	0,38	3,10E-04	0,34	3,35E-05	3,64	1,54E+08	0,72	51	4	620	726	854
E_qtz_mt1405_m-03	matrix	1,45E-05	0,41	2,37E-04	0,28	1,43E-05	12,87	1,65E+08	0,66	51	4	621	727	855
E_qtz_mt1405_m-04	matrix	1,64E-05	0,47	2,35E-04	0,90	7,20E-05	8,52	1,69E+08	0,63	58	4	632	740	869
E_qtz_mt1405_m-05	matrix	1,69E-05	0,30	4,74E-04	0,71	5,25E-05	6,07	1,80E+08	0,72	59	4	635	743	873
E_qtz_mt1405_m-06	matrix	1,94E-05	0,33	1,87E-03	0,98	2,67E-04	3,16	1,84E+08	0,70	68	5	648	757	889
E_qtz_mt1405_m-07b	matrix	1,68E-05	0,34	1,96E-04	0,70	5,10E-06	9,93	1,93E+08	0,68	59	4	634	742	872
E_qtz_mt1405_m-08b	matrix	1,22E-05	0,80	1,52E-04	1,37	1,20E-04	23,52	1,99E+08	0,81	43	3	605	710	835
E_qtz_mt1405_m-09	matrix	1,66E-05	0,47	2,35E-04	0,26	8,83E-06	10,97	1,95E+08	0,56	58	4	633	741	871
E_qtz_mt1405_m-10	matrix	1,53E-05	0,37	1,92E-04	0,95	4,95E-05	9,87	1,95E+08	0,61	54	4	626	733	861

Table S2: continued

Mineral ID	**Setting**	**47Ti/28Si**		**27Al/28Si**		**40Ca/28Si**	**28Si/Coeff**			**Ti ppm**	**±**	**Calculated Temperature**		
Grey : Discarded analysis		**EM/FC2**		**EM/FC2**		**EM/FC2**	**FC2**					**@ 7 kbar**	**@ 12 kbar**	**@ 18 kbar**
E_qtz_mt1405_m-11	matrix	1,75E-05	0,33	1,85E-04	0,18	1,01E-05	7,27	1,91E+08	0,59	61	4	638	747	877
E_qtz_mt1405_m-12	matrix	1,85E-05	0,45	1,92E-04	0,22	1,04E-05	10,20	1,95E+08	0,71	65	5	643	752	883
E_qtz_mt1405_m-13	matrix	1,92E-05	0,31	2,76E-04	1,30	2,11E-05	5,25	1,86E+08	0,55	67	5	647	756	887
E_qtz_mt1405_m-14	matrix	1,96E-05	0,31	3,19E-04	0,14	1,82E-06	7,63	1,99E+08	0,61	69	5	649	759	891
E_qtz_mt1405_m-15	matrix	1,67E-05	0,31	2,36E-04	0,20	6,45E-05	4,63	2,09E+08	0,60	59	4	634	742	871
E_qtz_mt1405_m-16	matrix	1,73E-05	0,38	2,53E-04	0,24	3,03E-06	9,29	1,96E+08	0,61	61	4	637	745	875
E_qtz_mt1405_m-17	matrix	1,83E-05	0,34	3,89E-04	1,40	4,88E-05	5,22	1,97E+08	0,57	64	5	642	751	882
Standard														
Aud_qtz_20150203_@1		1,69E-05	0,46	1,38E-03	0,24	2,43E-06	15,45	1,30E+08	0,98					
Aud_qtz_20150203_@2		1,63E-05	0,55	1,32E-03	3,03	4,02E-06	14,86	1,28E+08	0,95					
Aud_qtz_20150203_@3		1,65E-05	0,42	1,37E-03	0,22	1,81E-06	14,99	1,31E+08	0,99					
Aud_qtz_20150203_@4		1,63E-05	0,50	1,11E-03	0,24	2,79E-06	14,63	1,31E+08	0,96					
Aud_qtz_20150203_@5		1,62E-05	0,47	1,35E-03	4,98	4,41E-06	12,84	1,30E+08	0,93					
Aud_qtz_20150203_@6														
Aud_qtz_20150204_@1		1,63E-05	0,49	1,22E-03	1,26	5,12E-06	12,03	1,20E+08	0,43					
Aud_qtz_20150204_@2		1,58E-05	0,46	1,10E-03	4,26	4,48E-06	13,97	1,20E+08	0,46					
Aud_qtz_20150204_@3		1,61E-05	0,48	1,25E-03	2,96	6,44E-06	22,12	1,19E+08	0,50					
Aud_qtz_20150204_@4		1,61E-05	0,41	1,31E-03	1,97	4,93E-06	11,18	1,20E+08	0,37					
	average	1,63E-05		1,27E-03		4,05E-06								
	sd	3E-07		1,07E-04		1,47E-06								
	RSD (%)	1,845735		8,47E+00		36,22794								
	ppm	57		1,54E+02			Audétat et al, GGR 2014							
	±	4		1,50E+01										
omitted std														
Aud_qtz_20150203_@6		1,93E-05	0,46	1,24E-03	0,88	2,42E-06	16,18	1,25E+08	0,88					

Litholund Theses

Dissertations

1. *Emma F. Rehnström, 2003:* Geography and geometry of pre-Caledonian western Baltica : U-Pb geochronology and palaeomagnetism.

2. *Oskar Paulsson, 2003:* U-Pb geochronology of tectonothermal events related to the Rodinia and Gondwana supercontinents : observations from Antarctica and Baltica.

3. *Ingela Olsson-Borell, 2003:* Thermal history of the Phanerozoic sedimentary succession of Skåne, southern Sweden, and implications for applied geology.

4. *Johan Lindgren, 2004:* Early Campanian mosasaurs (Reptilia; Mosasauridae) from the Kristianstad Basin, southern Sweden.

5. *Audrius Cecys, 2004:* Tectonic implications of the ca. 1.45 Ga granitoid magmatism at the southwestern margin of the East European Craton.

6. *Peter Dahlqvist, 2005:* Late Ordovician-Early Silurian facies development and stratigraphy of Jämtland, central Sweden.

7. *Mårten Eriksson, 2005:* Silurian carbonate platform and unconformity development, Gotland, Sweden.

8. *Jane Wigforss-Lange, 2005:* The effects of Late Silurian (mid-Ludfordian) sea-level change : a case study of the Öved-Ramsåsa Group in Skåne, Sweden.

9. *Erik Eneroth, 2006:* Nanomagnetic and micromagnetic properties of rocks, minerals and sulphide-oxidation products.

10. *Niklas Axheimer, 2006:* The lower and middle Cambrian of Sweden : trilobites, biostratigraphy and intercontinental correlation.

11. *Fredrik Terfelt, 2006:* Upper middle Cambrian through Furongian of Scandinavia with focus on trilobites, paleoenvironments and correlations.

12. *Andrius Rimsa, 2007:* Understanding zircon geochronology : constraints from imaging and trace elements.

13. *Mårten Eriksson 2007:* Silurian carbonate platforms of Gotland, Sweden : archives of local, regional and global environmental changes.

14. *Jane Wigforss-Lange, 2007:* Geochemical and sedimentary signatures of Phanerozoic events.

15. *Tobias Hermansson, 2007:* The tectonic evolution of the western part of the Svecofennian orogen, central Sweden : Insight from U/Pb and $^{40}Ar/^{39}Ar$ geochronology at Forsmark.

16. *Pia Söderlund,* 2008: ^{40}Ar-^{39}Ar, AFT and (U-Th)/He thermochronologic implications for the low-temperature geological evolution in SE Sweden.

17. *Anders Cronholm,* 2009: The flux of extraterrestrial matter to Earth as recorded in Paleogene and Middle Ordovician marine sediments.

18. *Carl Alwmark,* 2009: Traces in Earth's geological record of the break-up of the L-chondrite parent body 470 Ma.

19. *Linda Larsson-Lindgren,* 2009: Climate and vegetation during the Miocene : evidence from Danish palynological assemblages.

20. *Ingemar Bergelin,* 2010: $^{40}Ar/^{39}Ar$ whole-rock geochronology of Mesozoic basalts in Scania : evidence for episodic volcanism over an extended period of ca. 80 Myr.

21. *Johanna Mellgren,* 2011: Conodont biostratigraphy, taxonomy and palaeoecology in the Darriwilian (Middle Ordovician) of Baltoscandia : with focus on meteorite and extraterrestrial chromite-rich strata.

22. *Johan Olsson,* 2012: U-Pb baddeleyite geochronology of Precambrian mafic dyke swarms and complexes in southern Africa : regional-scale extensional events and the origin of the Bushveld complex.

23. *Kristina Mehlqvist,* 2013: Early land plant spores from the Paleozoic of Sweden : taxonomy, stratigraphy and paleoenvironments.

24. *Andreas Petersson,* 2015: Evolution of continental crust in the Proterozoic : growth and reworking in orogenic systems.

25. *Karolina Bjärnborg,* 2015: Origin of the Kleva Ni-Cu sulphide mineralisation in Småland, southeast Sweden.

26. Lorraine Tual, 2016: P–T evolution and high-temperature deformation of Precambrian eclogite, Sveconorwegian orogen.

Printed by Media-Tryck, Lund University, 2016

Lithosphere and Biosphere Science
Department of Geology
Lund University
Sölvegatan 12
SE-223 62 Lund, Sweden
Telephone +46 46 222 78 80

ISSN 1651-6648
ISBN 978-91-87847-14-1